An investigation into the characterisation and modelling of the impact response of CFRP

Justus Hoffmann



Exeter College
Department of Engineering Science
University of Oxford

A thesis submitted for the degree of
Doctor of Philosophy

Trinity Term, 2018

Abstract

An investigation into the characterisation and modelling of the impact response of CFRP

Justus Hoffmann
Exeter College, University of Oxford
Trinity Term, 2018

Following the general trend in the aviation sector, aerospace turbine engine manufacturers are making increasing use of advanced composite materials for key structures and components. Of these, the outcome of this work is specifically meant to aid the design and analysis process of a fan blade made of carbon-fibre-reinforced plastic (CFRP).

The simulation-based design and analysis process of a fan blade is driven by its design-critical load case, which is *bird strike*. There are two key challenges faced when modelling this impact event: (i) a very high finite element count arising from a *ply-by-ply* representation of the composite laminate, which, in turn, can result in uneconomically high model run times, and, (ii) the wide range of strain-rates experienced by a fan blade over the course of its deformation, failure, and damage evolution process, which, in turn, necessitates the composite's rate-dependency to be adequately accounted for.

To date, no model exists that addresses this set of challenges. The aim of this work, thus, is to develop a constitutive model that reflects a composite laminate's rate-dependent deformation, failure, and damage evolution behaviour across a multitude of plies within a single *representative volume element* (RVE). The model's key premise is that delamination between those individual plies is entirely driven by the RVE's out-of-plane stresses σ_{33}, σ_{23}, and σ_{31}, whereas any failure and damage evolution within the plies is exclusively linked to the RVE's in-plane stresses σ_{11}, σ_{22}, and σ_{12}. This, in turn, then allows for the RVE's treatment on the basis of two separate 'submodels': a *delamination model* for its out-of-plane, and a *ply model* for its in-plane behaviour. Particular emphasis is placed on allowing for a realistic strain-rate history experienced by the finite elements without sacrificing the simulation's numerical stability. This is achieved through the development of a *low-pass filter*-like strain-rate smoothing algorithm, which is shown to exceed the performance of a conventional *running average* approach.

In addition to the modelling work, this study also makes contributions to selected rate-dependent datasets required for the model's calibration. The contributions made to the *in-plane transverse compressive deformation mode* consists of: (i) a comparative

specimen design study, demonstrating that a *waisted block* should be preferred over a *block* design, (ii) its characterisation across two loading rate regimes, and, (iii) a comprehensive study investigating the influence of key split-Hopkinson bar setup and testing parameters on the achievability of valid high-rate testing conditions for this deformation mode.

The contributions made to the *in-plane transverse tensile deformation mode* consist of: (i) its characterisation across two loading rate regimes, and, (ii) a study similar to the one for the in-plane transverse compressive deformation mode investigating the achievabiliy of valid high-rate testing conditions. In particular, this study demonstrates the general infeasibility to achieve a specimen deformation under a (nearly) constant strain-rate at failure for this deformation mode.

The contributions made to the *out-of-plane tensile deformation mode* consist of: (i) the development of a form-fit specimen design, particularly with high-rate testing in mind, and, (ii) its characterisation across two loading rate regimes.

The contributions made to the *energy release rate under tensile loading in fibre direction* are as follows: (i) characterisation under high-rate loading based on valid force history data, which has not been achieved before, showing a pronounced drop in G_{Ic}^{f+} at an elevated loading rate, and, (ii) the utilisation of a modified split-Hopkinson bar setup for the corresponding material characterisation process, involving refinements on aspects of the experimental setup, data acquisition, and data reduction.

In the final part of this study, the modelling and experimental strands are drawn together through a model calibration and validation exercise, which also includes a direct comparison between the proposed constitutive model and a state-of-the-art ply-by-ply model (*LS-Dyna MAT 261*). It is ultimately shown that the developed model is able to achieve a sufficiently accurate representation of a composite laminate's mechanical behaviour, while at the same time clocking drastically lower computation times in comparison to a ply-by-ply modelling approach.

Acknowledgements

First and foremost I want to express my gratitude towards *Nik Petrinic*, without whom– no doubt—I would have never gotten the opportunity to come to Oxford. In the same breath I want to thank *Rolls-Royce plc* for the financial support via its *University Technology Centre* in Oxford.

Moreover, I would like to thank all members, past and present, of the *Impact Engineering Laboratory* team, and in particular, *Jens Wiegand* and *Hao Cui*, for their invaluable feedback as well as the innumerable technical discussions we have had over the last few years. Special thanks also to *Giulia Macaro* and *Mattia Montanari* for sharing the LaTeX template used for the preparation of this thesis.

My gratitude is also due to all the individuals that make the *Department of Engineering Science* such a well-oiled machine; in particular I want to thank *Stuart Carter*, *Graham Hillsdon*, *Jeffrey Fullerton* and *Andy Bateman* from the technical end of things, and *Karen Bamford* and *Hisham Elamin* from the administrative and IT end of things. Furthermore, I want to thank *Kalin Dragnevski* and *Chak Lui* for their technical support for the post-mortem analysis of the specimens in Chapter 3. I also want to thank *Daniel Eakins* for stepping in when others had to deal with life's unforeseen adversities.

Last, but not least, I want to thank my family across all continents, my lovely wife *Mahima*, and all the friends that made Oxford, *Oxford*.

Ausdauer wird früher oder später belohnt - meistens aber später.

Wilhelm Busch

Contents

Abstract i

Acknowledgements iii

List of Figures vii

List of Tables xiii

Notation xiv

1 Introduction 1
- 1.1 Background and motivation . . . 1
- 1.2 Brief introduction to composite materials . . . 7
- 1.3 Thesis outline and structure . . . 10
  - 1.3.1 Aim, objectives, and novelties . . . 10
  - 1.3.2 Thesis structure . . . 15

2 High-rate material characterisation of *22-c*, *22-t*, and *33-t* 17
- 2.1 Introduction . . . 19
  - 2.1.1 Split-Hopkinson bar testing: Setup, working principle, and validity conditions . . . 19
  - 2.1.2 Pulse shaping . . . 25
  - 2.1.3 Generation of a spectrum of linearly rising incident pulses for an SHPB and SHTB system . . . 28
- 2.2 In-plane compression testing transverse to the fibre direction (*22-c*) . . . 30
  - 2.2.1 Specimen design study: *block* vs. *waisted block* . . . 31
  - 2.2.2 Material characterisation under high-rate loading . . . 38
  - 2.2.3 Influences on the achievement of valid high-rate testing conditions 42
- 2.3 In-plane tensile testing transverse to the fibre direction (*22-t*) . . . 56
  - 2.3.1 Material characterisation across two strain-rate regimes . . . 56
  - 2.3.2 Influences on the achievement of valid high-rate testing conditions 61
- 2.4 Form-fit specimen design for dynamic out-of-plane tensile testing (*33-t*) 74
  - 2.4.1 Background and motivation . . . 74
  - 2.4.2 Form-fit design . . . 76
  - 2.4.3 Experimental setup, results and discussion . . . 77
  - 2.4.4 Potential improvements and further considerations . . . 80
- 2.5 Summary . . . 82

3 Strain-energy release rate under high-rate tensile loading in fibre direction 85
- 3.1 Introduction and motivation . . . 87
- 3.2 Literature review . . . 93
  - 3.2.1 Micro-mechanical background . . . 93

3.2.2 Known influences on the measured value of G_{Ic}^{f+} . . . 96
3.2.3 Approaches to obtaining G_{Ic}^{f+} . . . 97
3.2.4 Outline of *McCarroll*'s approach to determining $G_{Ic,dyn}^{f+}$ . . . 104
3.3 Specimen, experimental setup, and data acquisition . . . 107
3.3.1 Specimen geometry and ply configuration . . . 107
3.3.2 Specimen manufacturing, machining, and preparation . . . 108
3.3.3 Setup, loading conditions, and data acquisition for quasi-static testing . . . 109
3.3.4 Setup, loading conditions, and data acquisition for high-rate testing 110
3.4 Validity checks for the high-rate experiments . . . 114
3.4.1 Convergence towards force equilibrium . . . 115
3.4.2 Mode I loading . . . 118
3.4.3 Stress wave interferences with the crack tip stress field . . . 122
3.5 Elements of the data reduction process . . . 123
3.5.1 Rationale for determining G_{Ic}^{f+} as an averaged value over a series of crack tip propagations . . . 123
3.5.2 Relationship between G_{Ic}^{f+} and G_{Ic}^{lam} . . . 125
3.5.3 Association of G_{Ic}^{f+} with strain-rate . . . 126
3.6 Experimental results and discussion . . . 127
3.6.1 Experimental results . . . 127
3.6.2 Strain field analysis via DIC . . . 132
3.6.3 Fractography via SEM . . . 135
3.6.4 Attempt to explain the discrepancy between the present and *McCarroll*'s study . . . 141
3.7 Recommendations for improvements for further high-rate testing . . . 142
3.8 Summary and conclusion . . . 146

4 Constitutive model **148**
4.1 Motivation and aim of the model . . . 149
4.2 Main premise of the model and overview of its structure . . . 150
4.3 Elastic properties, ply and homogenised stiffness tensors . . . 155
4.4 Stress calculation and detection of failure . . . 160
4.4.1 Conceptual considerations . . . 160
4.4.2 Delamination model . . . 161
4.4.3 Ply model . . . 163
4.5 Damage evolution . . . 166
4.5.1 Conceptual considerations . . . 166
4.5.2 Delamination model . . . 169
4.5.3 Ply model . . . 172
4.6 Rate-dependency . . . 175
4.7 Strain-rate smoothing . . . 176
4.7.1 Motivation . . . 177
4.7.2 A *low-pass filter*-like algorithm for smoothing the strain-rate . . . 178
4.7.3 Numerical study . . . 180
4.8 Quantification of the limitations of damage modelling via CDM . . . 184
4.8.1 Background and motivation . . . 184
4.8.2 Study outline, results, and conclusions . . . 185

4.9 Key merits and limitations of the model . . . 188
4.10 Summary . . . 189

5 Model calibration and validation 191
5.1 Model calibration . . . 192
5.1.1 Calibration of the model's rate-dependent behaviour under normal deformation and failure . . . 192
5.1.2 Calibration of the model's rate-dependent behaviour under shear deformation and failure . . . 196
5.1.3 Calibration of the set of rate-dependent energy release rates . . . 200
5.2 Validation experiment and its model . . . 202
5.2.1 Experimental setup . . . 202
5.2.2 Model of the validation experiment . . . 203
5.3 Constitutive model validation . . . 207
5.3.1 Outline of *LS-Dyna MAT 261* . . . 207
5.3.2 Influence of the model's level of homogenisation and comparison to *MAT 261* . . . 210
5.3.3 Influence of the model's individual rate-dependent effects . . . 214
5.4 Summary . . . 216

6 Summary, conclusions, and suggestions for future work 217
6.1 Experimental work . . . 218
6.1.1 High-rate modulus and strength for *22-c*, *22-t*, *33-t*, and *12-shear* 218
6.1.2 Strain-energy release rate under high-rate tensile loading in fibre direction . . . 221
6.2 Constitutive model . . . 222

Bibliography 227

List of Figures

1.1 Usage of composite materials in the *Boeing 787 Dreamliner* 3
1.2 *Rolls-Royce*'s upcoming *UltraFan* engine generation 3
1.3 Modelling a composite laminate by (a) representing each ply individually, and (b) reflecting a multitude of plies within a representative volume element 6
1.4 Specific strength, shown in (a), and modulus, shown in (b), of composite materials in relation to the other material classes 8
1.5 (a) coordinate systems used to describe a laminated composite material's deformation behaviour; (b) material coordinate system with its individual deformation modes 10
1.6 Chart of the sets of modelling and experimental objectives of the thesis 14

2.1 Range of experimental setups to cover different segments of the strain-rate spectrum 20
2.2 SHPB setup with a visualisation of the propagating stress wave 21
2.3 Example of the discrepancy between the strain history determined via the SHB vs. a DIC-based analysis 23
2.4 Incident, reflected, and transmitted parts of the loading pulse 24
2.5 (a) determination of force disequilibrium and strain-rate history based on the gauge volume's end faces; (b) idealised force disequilibrium and strain-rate history including SE and CSR conditions 25
2.6 Spectrum of linearly rising loading pulses generated on an SHPB system using cardboard and neoprene rubber of various thicknesses 29
2.7 Spectrum of linearly rising loading pulses generated on an SHTB system using neoprene rubber of various thicknesses 30
2.8 Specimen geometries for *22-c* testing: (a) *block*, and (b) *waisted block* design (dimensions in mm) 33
2.9 (a) failure originating at one of the *block* design specimen's end faces; (b) DIC-analysis of a *block* design specimen showing failure plane localisation in the direct vicinity of one of the specimen's end faces; (c) DIC-analysis of a *waisted block* design specimen showing failure plane localisation at due distance from the specimen's end faces 34
2.10 DIC-based measurement of the strains transverse to the loading direction at different cross-sections of the specimens' gauge section for (a) the *block* design, and (b) the *waisted block* design 37
2.11 Stress-strain curves for *22-c* testing under quasi-static and high-rate loading conditions 40
2.12 Assessment of the validity of the dynamic *22-c* material characterisation tests 41

2.13 Subset of the experimental setup reflected by the FE model 45
2.14 (a) FE model of the experimental setup; (b) end faces of the gauge volume for obtaining the sample's force disequilibrium (FE/GS model) and strain-rate history 47
2.15 Convergence behaviour towards force equilibrium employing a range of modelling approaches 49
2.16 (a) experimentally-measured incident pulse and its idealisation; (b) force at the specimen's input bar end when subjecting the model to the idealised incident pulse; (c) force at the specimen's input bar end when subjecting the model to the experimentally-obtained incident pulse; (d) force at the specimen's output bar end when subjecting the model to the experimental incident pulse 50
2.17 Convergence behaviour towards force equilibrium employing the specimen's quasi-static and dynamic material properties for each modelling approach 51
2.18 Convergence towards force equilibrium for a range of bar materials and diameters 52
2.19 Evaluation of the specimen's strain-rate history for a range of modelling approaches 53
2.20 Evaluation of the specimen's strain-rate history for a ⌀16 mm titanium bar system and the range of available incident pulse rising slopes 54
2.21 Limiting strain-rate histories for testing under CSR conditions for ⌀16 mm and ⌀12 mm bar systems made of Mg, Al, Ti, and St, respectively . . 54
2.22 (a) specimen geometry for *22-t* testing (dimensions in mm); (b) CAD model of a *22-t* specimen with its mounted end sleeves 57
2.23 Stress-strain curves for *22-t* testing under quasi-static and high-rate loading conditions 59
2.24 Assessment of the validity of the dynamic *22-t* material characterisation tests 60
2.25 'Impedance profile' as encountered by a planar stress wave traversing through a specimen for dynamic *22-t* testing 62
2.26 (a) FE model of the experimental setup; (b) end faces of the gauge volume for obtaining the sample's force disequilibrium (FE/GS model) and strain-rate history 64
2.27 Evaluation of the convergence behaviour towards force equilibrium employing a range of modelling approaches 66
2.28 (a) experimentally-obtained and idealised incident pulse rising slopes; (b) force at the specimen's input bar end when subjecting the model to the idealised incident pulse; (c) force at the specimen's input bar end when subjecting the model to the experimentally-obtained incident pulse; (d) force at the specimen's output bar end when subjecting the model to the experimentally-obtained incident pulse 67
2.29 Convergence towards force equilibrium for a range of bar and sleeve material combinations 69
2.30 Evaluation of the specimen's strain-rate history for a range of model input parameter sets 70

2.31 Evaluation of the specimen's strain-rate history for a range of bar and end sleeve material combinations 71
2.32 Evaluation of the specimen's strain-rate history for an aluminium bar/sleeve system and the range of incident pulse rising slopes as determined in Chapter 2.1.3 72
2.33 (a) form-fit specimen design with mounted grips; (b) alignment fixture used for the assembly process of the specimen and grips 76
2.34 (a) geometry of the *adhesively-bonded waisted block* specimen; (b) geometry of the form-fit specimen (dimensions in mm) 77
2.35 Comparison of the measured strength and modulus between an *adhesively-bonded waisted block* and a form-fit design (results are normalised with respect to the form-fit design) 78
2.36 (a) prevalent failure cross-section for the form-fit design specimens; (b) prevalent failure cross-section for the *adhesively-bonded waisted block* specimens; (c) FE simulation of an *adhesively-bonded waisted block* specimen indicating slight stress concentrations in this particular cross-section 79
2.37 Results of the characterisation of strength and modulus across two loading rate regimes for *33-t* testing employing a form-fit specimen design (results are normalised with respect to the quasi-static tests) 80
2.38 Evaluation of the dynamic tests' force disequilibrium and strain-rate history for the form-fit specimen design 81

3.1 Fracture modes to describe crack propagation within the framework of fracture mechanics 88
3.2 Idealised fracture planes associated with a composite's failure modes on macro scale 88
3.3 Energy dissipation mechanisms on micro scale of a composite under tensile loading in fibre direction 94
3.4 Determination of G_{Ic}^{lam} based on the *area method* for (a) stable crack propagation, and (b) stick-slip crack propagation 100
3.5 Illustration of *McCarroll*'s model of the CT specimen (specimen dimensions were identical to the ones used in the present study) 106
3.6 Geometry of the CT specimen (dimensions in mm) 109
3.7 Comparison of the simulation results for the SHTB setup without any additional support to the ones employing additional brass bearings in the specimen's immediate vicinity; the plotted transverse displacement refers to the load introduction bolts' respective centre line 111
3.8 Experimental setup for the tests under (a) quasi-static, and (b) high-rate loading conditions 112
3.9 Loading pulse in conjunction with the (time-shifted) specimen response of a representative dynamic test 112
3.10 (a) 'displacement tracker' to allow for a DIC-based determination of the opening displacement; (b) comparison between an opening displacement measurement based on a conventional SHB analysis and a DIC-based approach 114
3.11 Modified split-Hopkinson tension bar and data acquisition setup for the high-rate experiments 114

3.12 Model of the SHTB setup to investigate the specimen's convergence behaviour towards force equilibrium 115
3.13 Forces measured at the load introduction bolts of input and output bar based on an FE simulation of the entire high-rate testing setup in conjunction with an unshaped incident pulse 116
3.14 Forces measured at the load introduction bolts of input and output bar based on an FE simulation of the entire high-rate testing setup in conjunction with a shaped incident pulse 117
3.15 Selected states of the stress fields pertaining to (a) σ_{xx} and (b) τ_{xy} . . 120
3.16 State of the max. principal stress field corresponding to 'timestamp 4' in Figure 3.14 121
3.17 Ratio γ of shear stress to the sum of axial and shear stresses for selected elements in direct vicinity of the crack tip 121
3.18 Determination of the relevant strain-rate for constitutive model calibration: experimental basis and its relation to FE modelling 127
3.19 Input bar, output bar, and averaged force history with the corresponding force disequilibrium of a representative high-rate experiment 128
3.20 Representative force vs. opening displacement curves for both loading rate regimes 129
3.21 Determined strain-rate values for (a) quasi-static loading, and (b) high-rate loading for a range of reference lengths 132
3.22 Strain field surrounding the crack tip for several stages of crack tip advancement under (a) quasi-static loading, and (b) high-rate loading (the times associated with the timestamps 1–3 for the latter can be found in Figure 3.19 in the preceding section) 134
3.23 SEM images of multiple 0° plies across the specimen's through-thickness direction for quasi-static loading (covering the total crack length from approx. 0 to 10 mm from image (a) to (d)) 137
3.24 SEM images of multiple 0° plies across the specimen's through-thickness direction for quasi-static loading (covering the total crack length from approx. 10 to 20 mm from image (a) to (d)) 138
3.25 SEM images of multiple 0° plies across the specimen's through-thickness direction for high-rate loading (covering the total crack length from approx. 0 to 10 mm from image (a) to (d)) 139
3.26 SEM images of multiple 0° plies across the specimen's through-thickness direction for high-rate loading (covering the total crack length from approx. 10 to 20 mm from image (a) to (d)) 140
3.27 SEM images of a single 0° ply, showing the constraining effect of 90° layers on adjacent 0° plies for (a) quasi-static loading, and (b) high-rate loading 141

4.1 Graphical representation of the constitutive model's main premise of obtaining the RVE's out-of-plane stresses via a delamination and the in-plane stresses via a ply model 153
4.2 Flowchart of the constitutive algorithm's main elements 154
4.3 Qualitative shape of the modelled stress-strain curve under in-plane shear deformation 158

4.4 Shear stress-strain behaviour for unloading and reverse loading in the elastoplastic and strain-softening domain 158
4.5 Comparison between the delamination failure criterion proposed by *Hou et al.* and its modification for the present study against the background of *Gan et al.*'s experimentally-generated data points in σ_{33}-σ_{31}^{+}-space . 163
4.6 Differing treatment of the stress return to the updated failure envelope depending on a stress state in the normal tensile or compression domain 171
4.7 Unprocessed out-of-plane normal strain-rate history of a finite element in direct vicinity of a projectile impacting on a panel 178
4.8 Illustration of a *low-pass filter*-like algorithm for preventing the strain-rate from deviating excessively across successive time steps 180
4.9 Force vs. deflection curves for a ball/plate impact model employing a range of strain-rate smoothing approaches 182
4.10 Force values at a deflection of 2 mm for all rate-smoothing approaches to highlight the convergence behaviour in case of an appropriate choice of the *low-pass filter*-like algorithm's governing parameters $\Delta\dot{\epsilon}_{tsh}$ and $\Delta\dot{\epsilon}_{lim}$ (strain-rate values in s^{-1}; running average values in number of cycles) 182
4.11 Illustration of the dependency of the stress-strain curve's softening slope on the finite element's volume for a given energy release rate value . . . 185
4.12 Quantification of the limiting finite element dimensions for basing the damage evolution process on the experimentally-determined energy release rate value for each failure mode 187

5.1 Normalised sets of data points and their corresponding fit functions for each relevant Young's modulus reflecting the composite's rate-dependent normal deformation behaviour 194
5.2 Normalised sets of data points and their corresponding fit functions for each relevant strength parameter reflecting the composite's rate-dependent normal deformation behaviour 195
5.3 Sets of stress-strain curves obtained under in-plane shear deformation across two loading rate regimes and their respective reflection by the constitutive model 198
5.4 Normalised sets of data points and their corresponding fit functions for each material property and empirical parameter reflecting the composite's rate-dependent in-plane shear behaviour 199
5.5 Example of an array of stress-strain curves of the modelled in-plane shear behaviour across the full range of relevant strain-rate values . . . 200
5.6 Essential geometric dimensions of the validation experiment (in mm) . 203
5.7 (a) mesh bias for the FE mesh of the panel; (b) deflection history for the range of investigated in-plane mesh densities; (c) juxtaposition of the meshes' maximum deflection against the number of finite elements for the range of investigated in-plane mesh densities; (d) deflection histories for the range of investigated out-of-plane discretisations 206
5.8 Increasing moment of resistance caused by higher levels of discretisation in the panel's through-thickness direction 207
5.9 Tractions acting on the potential fracture plane associated with IFF . . 208

5.10 (a) energy dissipated by the panel against impact velocity, and (b) model run time against impact velocity 212
5.11 Perforation of the panel for the super-critical impact velocity $v_{init} = 164$ m/s213
5.12 Dissipated energy against impact velocity for taking into account the individual rate-dependency of the model's elastic, failure, and damage evolution behaviour 215

List of Tables

2.1 Obtained material properties for *22-c* testing under quasi-static loading employing a *block* and a *waisted block* specimen design 35
2.2 Obtained material properties for *22-c* testing under quasi-static and high-rate loading conditions 42
2.3 Obtained material properties for *22-t* testing under quasi-static and high-rate loading conditions 60

3.1 Summary of the current state-of-the-art capabilities for determining the (dynamic) strain-energy release rate values of UD-reinforced carbon-fibre/epoxy composites 91
3.2 Summary of the approaches documented in literature to determine G_{Ic}^{f+} 104
3.3 Summary of determined energy release rate values across both loading rate regimes 130
3.4 Results of literature sources having determined G_{Ic}^{f+} for *IM7/8552* under quasi-static loading 131

5.1 Quasi-static material properties and their corresponding fit function parameters to reflect the composite's rate-dependent Young's moduli under normal deformation 195
5.2 Quasi-static material properties and their corresponding fit function parameters to reflect the composite's strength properties under normal deformation 196
5.3 Quasi-static values and their corresponding fit function parameters for all material properties and empirical parameters under in-plane shear deformation 199
5.4 Calibration of the model's set of rate-dependent energy release rates . . 202

Notation

The following contains an account of the set of symbols used throughout this work. Symobls which appear only in a specific context are excluded here; those symbols are explained in their relevant passages. As far as possible, symbols are kept identical to general conventions in the literature, or, if refering to a specific literature source, identical to the particular source.

Mathematical symbols representing scalar values are denoted in regular italic typeface, e.g. σ or ϵ, and vectors and tensors in bold italic typeface, e.g. $\boldsymbol{\sigma}$ or $\boldsymbol{\epsilon}$.

Abbreviations and shorthand symbols (also as super- or subscript)

2D	two-dimensional
3D	three-dimensional
1-dir.	in fibre direction
11-c	in-plane compressive deformation mode, in fibre direction
11-t	in-plane tensile deformation mode, in fibre direction
11	in-plane deformation mode, in fibre direction
12-shear	in-plane shear deformation mode (also used as '*12*')
2-dir.	transverse to fibre direction, in-plane
22-c	in-plane compressive deformation mode, transverse to the fibre direction
22-t	in-plane tensile deformation mode, transverse to the fibre direction
22	in-plane deformation mode, transverse to the fibre direction
23-shear	out-of-plane shear deformation mode (also used as '*23*')
3-dir.	transverse to fibre direction, out-of-plane
31-shear	out-of-plane shear deformation mode (also used as '*31*')
33-c	out-of-plane compressive deformation mode
33-t	out-of-plane tensile deformation mode
33	out-of-plane deformation mode
ASM	American Society for Metals

ASTM	American Society for Testing and Materials
IM7/8552	a particular carbon-fibre/epoxy composite material produced by *Hexcel*
Al	aluminium
CAD	computer-aided design
CC	compact compression (specimen), *OR* compliance calibration (method)
CDM	continuum damage mechanics
CFRP	carbon-fibre-reinforced plastic
CSR	constant strain-rate
CT	compact tension (specimen)
CV	coefficient of variation
DAQ	data acquisition
DEN	double edge notched (specimen)
DIC	digital image correlation
dyn	dynamic (loading conditions)
FE	finite element
FEM	finite element method
GS	gauge section
IFF	inter-fibre failure
LED	light-emitting diode
MCC	modified compliance calibration (method)
Mg	magnesium
QS	quasi-static (loading conditions)
RVE	representative volume element
SD	standard deviation
SE	stress equilibrium
SEM	scanning electron microscopy
SG	strain gauge
SHB	split-Hopkinson bar
SHPB	split-Hopkinson pressure bar
SHTB	split-Hopkinson tension bar
St	steel
symm.	symmetric

Ti	titanium
UD	unidirectional

Greek symbols

$\Delta\dot{\epsilon}_{lim}$	a governing parameter of the *low-pass filter*-like strain-rate smoothing algorithm
$\Delta\dot{\epsilon}_{proc}$	processed strain-rate difference between the current and previous time step
$\Delta\dot{\epsilon}_{raw}$	unprocessed strain-rate difference between the current and previous time step
$\Delta\dot{\epsilon}_{tsh}$	a governing parameter of the *low-pass filter*-like strain-rate smoothing algorithm
$\Delta\epsilon$	strain increment (laminate coord. sys.)
$\Delta\epsilon_{ij}$	strain tensor component ij increment (laminate coord. sys.)
$\Delta\omega$	stiffness damage increment
$\Delta\omega_i$	increment of the stiffness damage component i
$\Delta\omega_i^k$	increment of the stiffness damage component i of the k-th ply
$\Delta\sigma_{ij}$	increment of stress tensor component ij (laminate coord. sys.)
$\Delta\tilde{\epsilon}$	strain increment (material coord. sys.)
$\Delta\tilde{\epsilon}_{ij}^k$	increment of strain tensor component ij (k-th ply, material coord. sys.)
$\Delta\tilde{\sigma}_{ij}^k$	increment of stress tensor component ij (k-th ply, material coord. sys.)
Δ_F	force disequilibrium
$\dot{\epsilon}$	strain-rate
$\dot{\epsilon}_{proc}$	processed (i.e. 'smoothed') strain-rate
$\dot{\epsilon}_{t,raw}$	unprocessed strain-rate calculated for the current time step
$\dot{\epsilon}_{t-\Delta t}$	strain-rate pertaining to the previous time step
ϵ	strain
ϵ_0	strain value marking the onset of damage propagation
ϵ_f	strain value marking the end of the stress-strain curve
ϵ_p	plastic strain
ϵ_{ij}	strain tensor component ij
ϵ_{ij}^k	strain tensor component ij (k-th ply, laminate coord. sys.)
ϵ_{tsh}	strain value corresponding to the limiting slope of the stress-strain curve's softening domain
ϵ_{ult}	strain-to-failure

κ	scale factor for rate-dependent elastic properties
λ	scale factor for rate-dependent strength properties
ν	Poisson's ratio
ω	stiffness damage
ω_i	stiffness damage component i
ω_i^k	stiffness damage component i of the k-th ply
$\omega_i^{k,pr}$	stiffness damage component i of the k-th ply of the previous time step
ω_i^{pr}	stiffness damage component i of the previous time step
ρ	density
σ	stress
σ_0	stress value marking the onset of damage propagation
σ_{ij}	stress tensor component ij (laminate coord. sys.)
σ_{ij}^{tr}	trial stress tensor component ij (laminate coord. sys.)
σ_{in}	stress at the end of the gauge section facing the input bar
σ_{out}	stress at the end of the gauge section facing the output bar
$\tilde{\epsilon}_{ij}$	strain tensor component ij (material coord. sys.)
$\tilde{\sigma}_{ij}$	stress tensor component ij (material coord. sys.)
$\tilde{\sigma}_{ij}^{k,tr}$	trial stress tensor component ij (k-th ply, material coord. sys.)
$\tilde{\sigma}_{ij}^{k}$	stress tensor component ij (k-th ply, material coord. sys.)

Roman symbols

$\boldsymbol{C}$	stiffness tensor of the RVE (laminate coord. sys.)
Δa	crack tip advancement
Δr	increment of the damage evolution parameter
$\tilde{\boldsymbol{C}}$	stiffness tensor of a single ply (material coord. sys.)
$\tilde{C}_{ij}$	stiffness tensor component ij of a single ply (material coord. sys.)
A	cross-section
a	crack length
A_0	initial cross-section
c	wave velocity
C_{ij}	stiffness tensor component ij of the RVE (laminate coord. sys.)
E	Young's modulus
e	material exposure

E_{11c}	Young's modulus under in-plane compressive deformation in fibre direction
E_{11t}	Young's modulus under in-plane tensile deformation in fibre direction
$E_{22c,0}$	initial Young's modulus under in-plane compressive deformation transverse to the fibre direction
E_{22c}	Young's modulus under in-plane compressive deformation transverse to the fibre direction
E_{22t}	Young's modulus under in-plane tensile deformation transverse to the fibre direction
E_{33c}	Young's modulus under out-of-plane compressive deformation
E_{33t}	Young's modulus under out-of-plane tensile deformation
e_{del}	material exposure for delamination
E_{dissip}	dissipated energy
e^k_{f+}	material exposure for failure in fibre tensile direction (k-th ply)
e^k_{f-}	material exposure for failure in fibre compressive direction (k-th ply)
e^k_{IFF}	material exposure for inter-fibre failure (k-th ply)
E_{init}	kinetic energy of the projectile before interacting with the panel
E_{resid}	kinetic energy of the projectile after interacting with the panel
F	force
F_c	critical force causing a crack to propagate
F_{in}	force at the input bar end of a specimen
F_{max}	force at failure
F_{out}	force at the output bar end of a specimen
f_{res}	reserve factor
G	energy release rate, *OR* shear modulus
$G_{12,0}$	initial modulus under in-plane shear deformation
$G_{12,f}$	limiting modulus under in-plane shear deformation
G_{23}	out-of-plane shear modulus
G_{31}	out-of-plane shear modulus
G_{Ic}	energy release rate under mode I fracture
G^{del}_{Ic}	energy release rate for delamination failure under mode I fracture
G^{f+}_{Ic}	energy release rate for fibre tensile failure under mode I fracture
G^{f-}_{Ic}	energy release rate for fibre compressive failure under mode I fracture
G^{IFF}_{Ic}	energy release rate for inter-fibre failure under mode I fracture

G_{Ic}^{lam}	energy release rate of a laminate under mode I fracture
G_{IIc}^{del}	energy release rate for delamination failure under mode II fracture
G_{IIc}^{IFF}	energy release rate for inter-fibre failure under mode II fracture
H	fit function parameter for reflecting rate-dependency
K	fit function parameter for reflecting rate-dependency
K_{Ic}	critical stress intensity factor
l	length
l_c	characteristic element length
l_{ref}	reference length for strain-rate measurement
m	softening slope
m_f	softening slope pertaining to fibre tensile failure
m_{del}	softening slope pertaining to delamination failure
m_{IFF}	softening slope pertaining to inter-fibre failure
m_{proj}	mass of the projectile
r	damage evolution parameter
r^{pr}	damage evolution parameter pertaining to the previous time step
r_d	damage evolution parameter pertaining to delamination
r_f	damage evolution parameter pertaining to fibre damage
r_m	damage evolution parameter pertaining to inter-fibre failure
S_d	out-of-plane shear strength: representing both, S_{23} and S_{31}
S_m	in-plane shear strength: used synonymously with S_{12}
S_Y	yield strength under in-plane shear deformation
S_{12}	in-plane shear strength
S_{23}	out-of-plane shear strength
S_{31}	out-of-plane shear strength
S_{Yp}	empirical hardening parameter
t	time, *OR* thickness
t_{lam}	thickness of a laminate
t_{ply}	thickness of an individual ply
v	velocity
v_{init}	velocity of the projectile before interacting with the panel
v_{resid}	velocity of the projectile after interacting with the panel

x	distance, OR opening displacement
X_c	in-plane compressive strength in fibre direction
X_t	in-plane tensile strength in fibre direction
Y_c	in-plane compressive strength transverse to fibre direction
Y_t	in-plane tensile strength transverse to fibre direction
Z_c	out-of-plane compressive strength
Z_t	out-of-plane tensile strength

Chapter 1

Introduction

This chapter first presents the background to and motivation for this thesis. Thereafter, a brief introduction to composite materials is provided. Finally, the ultimate aim of this thesis, its breakdown into individual objectives, and the novelties generated within the context of each objective are presented, followed by an outline of the thesis structure.

1.1 Background and motivation

The commercial aviation sector is marked by an intense competition for market shares, which propels the development of evermore economical airplane and turbine models [61, 98]. One key avenue for achieving higher economic viability is by decreasing mass, which, in turn, directly translates to a decrease in fuel consumption. The reduction of an aircraft's components' mass in recent years has primarily been achieved by substituting metals with composite materials [131]. This substitution is based on the

exceptional mechanical properties of composites, most notably their very high specific modulus and strength. This increasing trend of material substitution, over the last few commercial airplane generations, has now reached a stage where approximately half of an airplane's mass consists of composite materials. As an illustration, the material composition for *Boeing*'s latest model, the *787 Dreamliner*, is given in **Figure 1.1**. A similarly high use of composite materials can also be seen in the *Airbus A350 XWB* [97]. Such an extensive use of composite materials has led to a roughly 20% reduction in total airplane mass when compared to a primarily aluminium-based construction [57].

The aircraft subsystem of particular interest to this study is the turbofan engine. It is hoped that the results of the present work will eventually aid the design and analysis process of a fan blade made of *carbon-fibre-reinforced plastic* (CFRP). A depiction of *Rolls-Royce*'s upcoming *UltraFan* turbofan engine generation is provided in **Figure 1.2**.

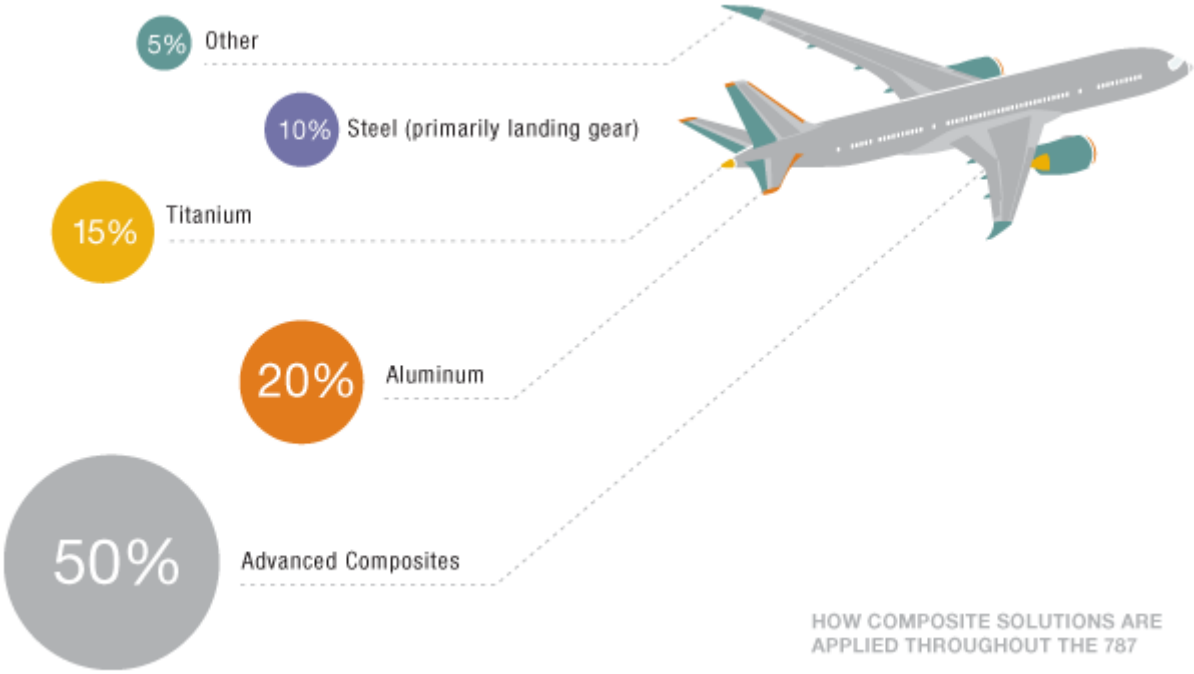


Figure 1.1: Usage of composite materials in the *Boeing 787 Dreamliner* (source: [57])

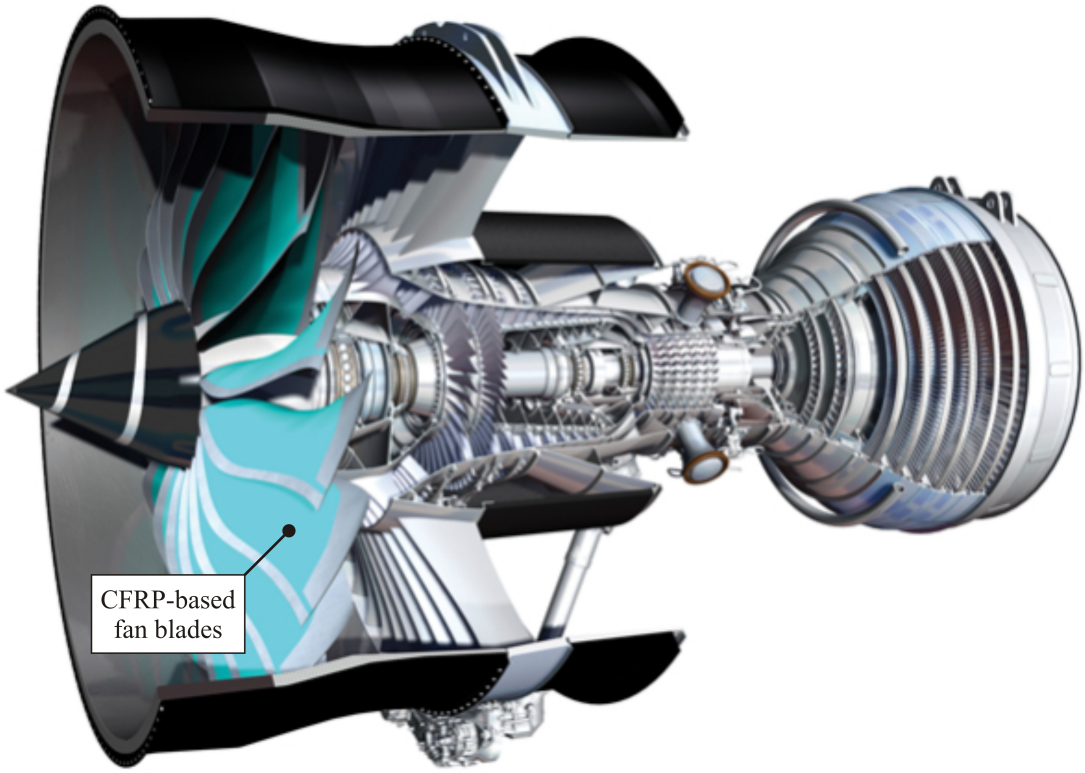


Figure 1.2: *Rolls-Royce*'s upcoming *UltraFan* engine generation (source of original image: [123])

In the recent past, the design and analysis process of aerospace components has experienced a shift from an essentially experimentally-based, to a mainly simulation-based procedure [3, 62]. The forces that have been driving this transition are:

- The need to reduce the high costs associated with an experimentally-based approach.
- The need to reduce the time required for the design and analysis process, and thus ultimately, the time-to-market.
- The need to cope with the vastly extended design space that has emerged as a consequence of employing composite materials due to their broad range of (i) fibre and matrix materials (including additives, nano-reinforcement, fibre surface treatments, etc.), and, (ii) fibre architectures (e.g., unidirectionally (UD) reinforced, woven, braided, 3D-reinforced, etc.). In order to fully exploit the potential that this material class has to offer, iterating through various design options in a time-efficient manner has become a necessity.
- A design process *in silico* allows for the analysis of processes that are not (readily) obtainable in an experiment, most notably those in the material volume's interior, and of entities that are very useful for the design and analysis process but not directly measurable in an experiment, such as the *material exposure*.

A key driver in the context of the design process of a turbofan engine's fan blade is *bird strike* [62]. Simulating this design-critical impact loading event poses two major challenges:

- **Involvement of large structural components, or at least substantial sections of those**. Discretising these large structures by employing a conventional

composite material model that relies on a ply-by-ply discretisation of the laminate results in a total finite element count that may easily render the model's computation time to be uneconomically high. This issue is likely to become even more pressing in the near future considering that laminates composed of very thin plies have recently been demonstrated to yield significant improvements in some of their key mechanical properties over the current generation of prepregs [2, 127, 147].

- **High-rate loading of the composite laminate**. The composite structure experiences a wide range of strain-rates over the course of its deformation, failure, and damage evolution process as a result of the rapidly applied loading. As CFRPs are known to exhibit a pronounced strain-rate-dependency for the majority of their mechanical properties[1], the composite's constitutive model, therefore, has to adequately account for this strain-rate-dependency in order to realistically capture the material's mechanical behaviour under impact loading.

Against the background of these two challenges, the ultimate aim of this thesis is to develop a constitutive model that captures a composite laminate's rate-dependent elastic, failure, and damage evolution behaviour across a multitude of plies within a single *representative volume element* (RVE). In doing so, the total number of finite elements required to discretise a given laminated composite structure can then be substantially reduced in comparison to a conventional ply-by-ply discretisation, see **Figure 1.3**, thus ultimately leading to economically viable model run times for the design and analysis process.

[1] see, for instance, the extensive range of literature sources quoted in the context of the constitutive model's calibration in **Chapter 5.1**, or the results of the characterisation of selected deformation, failure, and fracture modes in **Chapter 2** and **Chapter 3**

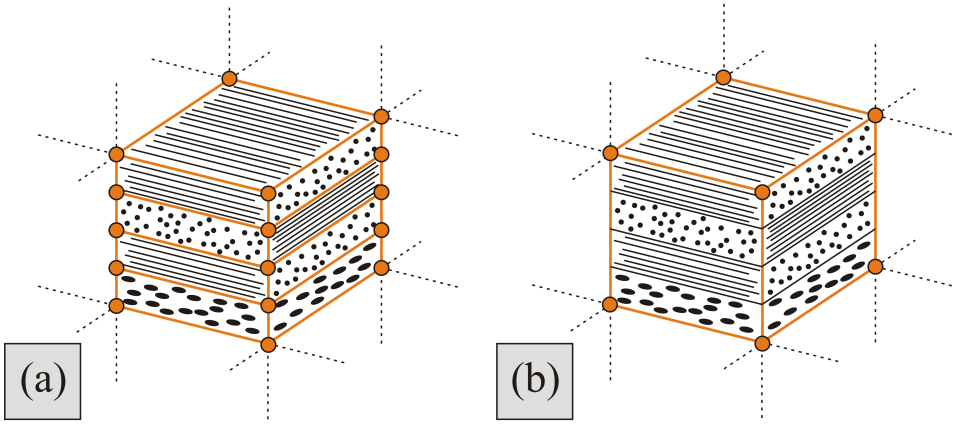


Figure 1.3: Modelling a composite laminate by (a) representing each ply individually, and (b) reflecting a multitude of plies within a representative volume element

For the constitutive model to adequately reflect a composite's rate-dependency, an input of rate-dependent datasets for each one of its strain-rate-dependent material properties is required. Consequently, aside from the modelling work, this thesis also incorporates an 'experimental branch', the purpose of which is to: (i) establish unavailable or extend existing rate-dependent model input datasets for selected material properties, and (ii) address critical aspects of the (high-rate) material characterisation procedure of selected deformation, failure, or fracture modes in order to ultimately obtain material properties generated under valid testing conditions.

A detailed description of each of the thesis objectives, their relation to its overall aim and one another, and the individual novelties generated by them will be presented in **Chapter 1.3.1**.

1.2 Brief introduction to composite materials

Outline of composites as a material class. Composite materials are characterised by consisting of a combination of two or more constituent materials forming a new material that exhibits favourable properties that exceed those of its individual constituents. In contrast to, for example, a metal alloy, constituent materials retain their individual chemical, physical, and mechanical characteristics. Composites commonly consist of a reinforcing material embedded in a matrix material [1, 122].

The geometry of the reinforcing material can range from particles to fibres of various lengths [1]. Semi-finished products based on continuous fibres exist in a wide array of ($2D$ or $3D$) architectures, such as unidirectional tapes, or woven, braided, or knitted fabrics [47]. The most commonly used fibre materials are carbon, glass, and aramid [47]. The fibres' key function is to carry tensile loading.

Matrix materials exist for all major material classes: polymers, metals, and ceramics [47, 122]. The matrix's key functions are: (i) retention of the fibres' position, (ii) transmission of forces to and between fibres, (iii) support of the fibres under compressive loading, (iv) energy absorption in case of impact and/or fracture, and (v) protection of the fibres from environmental influences [120, 130].

The composite material employed in the present study consists of layers of non-crimped, unidirectionally-oriented (UD) carbon fibres embedded in an epoxy matrix. The key characteristics of this type of composite are: (i) its very high specific strength and modulus (in fibre direction), (ii) its excellent chemical resistance, and (iii) its fatigue resistance [47, 131]. An illustration of the first aspect is provided in **Figure 1.4**, which

shows the composites' specific strength and modulus in relation to the other material classes.

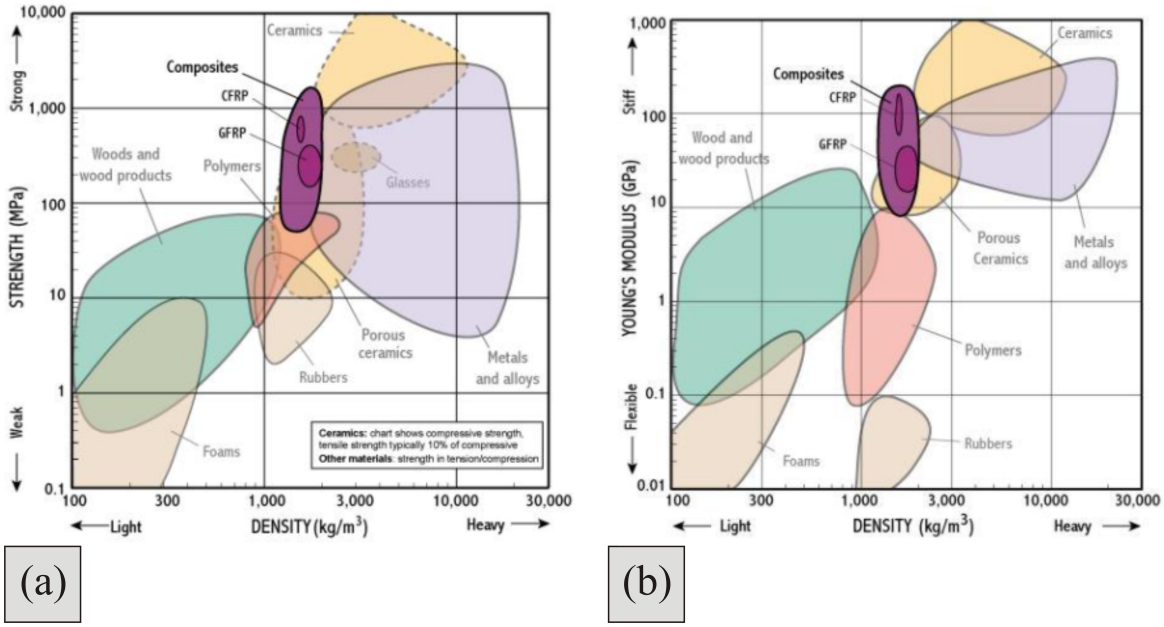


Figure 1.4: Specific strength, shown in (a), and modulus, shown in (b), of composite materials in relation to the other material classes (source: [142])

Length scale. The starting point for modelling a given material is the choice of an appropriate length scale. All features of the material's heterogeneous nature below this chosen scale are then not explicitly reflected by the model. The choice of the appropriate length scale is primarily driven by the need to find a suitable compromise between capturing the essential mechanisms that drive the deformation and failure behaviour of a material or structure under a given (thermo-)mechanical loading on the one hand, and the available computing power to solve the corresponding model within an economically viable timeframe on the other.

With respect to composite laminates consisting of UD plies, three scales are commonly distinguished: (i) *micro scale*, where individual fibres and the matrix are modelled as separate entities, (ii) *meso scale*, where individual plies are considered as homogenised

entities, and, (iii) *macro scale*, where a multitude of plies is considered as a homogenised entity. The developed constitutive model in the present work considers the macro and, to a certain extent, the meso scale. As this model derives its behaviour on macro scale on the basis of material properties determined on meso scale, the latter is the relevant scale for the material characterisation experiments required for the model's calibration.

The coordinate systems employed to describe a composite structure's deformation and failure behaviour are introduced in **Figure 1.5(a)**. A detailed description of the *material coordinate system* is given in **Figure 1.5(b)**. The *1-dir.* coincides with the fibre direction of a given ply, the *2-dir.* is oriented orthogonally to the fibres' direction within a ply's plane, and the *3-dir.* coincides with the laminate's through-thickness direction. The normal deformation modes, *11*, *22*, and *33*, are furthermore distinguished with regard to loading in tension or compression, e.g. *11-t* or *22-c*. In view of the stiffness tensor's symmetry [134], indices specifying entities associated with shear deformation are used interchangeably in the present thesis, e.g. $G_{12} = G_{21}$.

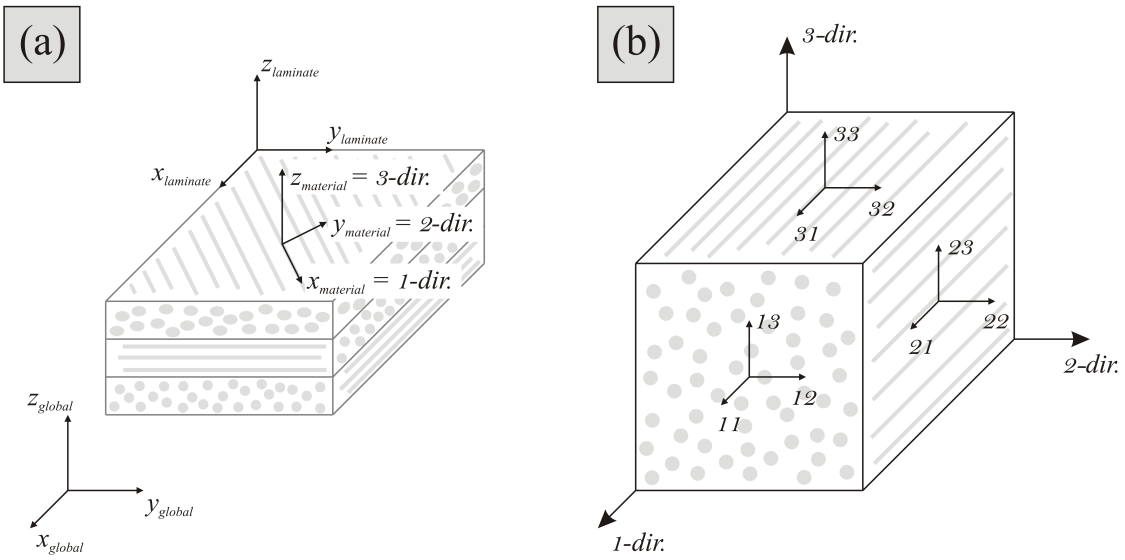


Figure 1.5: (a) coordinate systems used to describe a laminated composite material's deformation behaviour; (b) material coordinate system with its individual deformation modes

1.3 Thesis outline and structure

This subchapter first presents the overall aim of this thesis in conjunction with the individual objectives to reaching it. An emphasis is placed on highlighting the contributions to the body of knowledge. This is followed by a description of the thesis structure.

1.3.1 Aim, objectives, and novelties

The ultimate aim of this thesis is to develop a fully rate-dependent composite material model operating on macro scale to eventually support the design and analysis process of a fan blade made of CFRP. In order to facilitate a qualitatively and quantitatively accurate reflection of the composite's rate-dependency by the model, the modelling

work is complemented by experiments addressing selected gaps and shortcomings in the data and procedures documented in the literature.

Modelling work. The constitutive modelling work took an existing model coded by *Jens Wiegand* [145] as its starting point. The individual objectives then consisted of implementing the missing key features as follows:

- The in-plane shear deformation's non-linear behaviour.
- The rate-dependency for all relevant elastic, strength, and energy release rate properties.
- A novel strain-rate smoothing algorithm which enforces the model's numerical stability under impact loading without excessively 'damping' the strain-rate history experienced by the finite elements.

Apart from the strain-rate smoothing algorithm, the key novelty associated with the constitutive model consists of the model's range of capabilities in conjunction with its substantially reduced computation time requirements when compared to a conventional ply-by-ply representation of a laminate. These economical run times originate from representing the composite's deformation, failure, and damage evolution behaviour in a homogenised manner with an RVE on macro scale.

Experimental work. The experimental work's purpose is twofold: (i) to establish unavailable, or extend existing rate-dependent model input datasets for selected material properties, and (ii) to address critical aspects of the (high-rate) material characterisation procedure of selected deformation, failure, or fracture modes in order to ultimately

obtain material properties generated under valid testing conditions.[2] With regard to the composite's sets of rate-dependent moduli and strengths, this thesis focusses on the resin-dominated normal deformation modes *22-t*, *22-c*, and *33-t*. In contrast to said deformation modes, their fibre-dominated counterparts, *11-t* and *11-c*, are, apart from X_c, rate-insensitive[3], and the strength associated with *33-c*, Z_c, is not required by the constitutive model proposed in this thesis. In addition to the above normal deformation modes, the experimental work also addresses the characterisation of the composite's rate-dependent in-plane shear deformation behaviour (*12-shear*) in order to allow for the constitutive model's calibration of this deformation mode. With regard to the composite's set of rate-dependent energy release rate properties, this thesis focusses on the one associated with failure in fibre tensile direction under high-rate loading conditions, $G^{f+}_{Ic,dyn}$. In contrast to the dynamic energy release rates associated with fibre compressive failure, delamination, and inter-fibre failure (IFF), which have either been successfully determined experimentally or can be reasonably approximated, $G^{f+}_{Ic,dyn}$ is the only one that has not yet been *satisfactorily*[4] addressed.[5]

The individual objectives pertaining to the experimental work of this thesis are as follows:

- ***22-c***. The following facets of this deformation mode's characterisation process

[2]The validity conditions pertaining to high-rate material testing will be outlined in **Chapter 2.1** from a general point of view, and further detailed in **Chapter 3.4** for the particularities relevant in the context of determining the energy release rate under high-rate tensile loading.

[3]A more detailed discussion of each deformation mode's rate-dependency will be given in the context of the constitutive model's calibration in **Chapter 5.1**.

[4]A single attempt at determining $G^{f+}_{Ic,dyn}$ was made in the past, see *McCarroll (2011)* [100]. Said study, however, encountered issues in the form of heavy oscillations in the measured force signal. In order to overcome this issue, an alternative data reduction scheme was developed, which, in turn, relied on a set of far-reaching assumptions. *McCarroll*'s [100] approach and its shortcomings will be outlined and discussed in detail in the context of **Chapter 3**.

[5]A concise review of the state-of-the-art of determining the (high-rate) energy release rates for each failure mode will be presented in **Chapter 3.1.**

are addressed: (i) *specimen design*: an original study is presented which quantifies the deviation of the measured (initial) modulus and strength from their correct values when employing the most commonly used *block* specimen design as opposed to a *waisted block* design, (ii) *material characterisation*: the composite's modulus and strength are determined across two strain-rate regimes, and (iii) an original comprehensive simulation-based study is presented which investigates the influence of key split-Hopkinson bar (SHB) setup and testing parameters with respect to the achievability of valid high-rate testing conditions.

- ***22-t***. The work pertaining to this deformation mode is identical to the last two facets of deformation mode *22-c* above.
- ***33-t***. A novel form-fit specimen design is developed in order to overcome the issues associated an *adhesively-bonded waisted block* design commonly used for characterising this deformation mode. Emphasis is placed on the form-fit design's suitability for testing under high-rate loading conditions.
- ***12-shear***. This deformation mode is characterised across two strain-rate regimes in order to allow for the calibration of the constitutive model's rate-dependent non-linear in-plane shear behaviour.
- **Energy release rate under high-rate tensile loading in fibre direction**. The first novel aspect of this objective consists of the determination of the high-rate value of G_{Ic}^{f+}, which has not been *satisfactorily* accomplished before. The second facet of this objective's novelty consists of employing a modified SHB setup for the corresponding material characterisation process, involving refinements to aspects of the experimental setup, data acquisition, and data reduction. Furthermore, an extensive post-mortem analysis seeks to provide an interpret-

ation of the change in the material's measurable behaviour across the covered loading rate spectrum.

More extensive descriptions of the individual objectives' backgrounds, their motivation, or a review of the relevant literature will be given in the context of each objective's corresponding subchapter. **Figure 1.6** presents a chart of the sets of modelling and experimental objectives in order to ultimately reach this thesis' desired aim. The items containing novel contributions to the body of knowledge are highlighted in red.

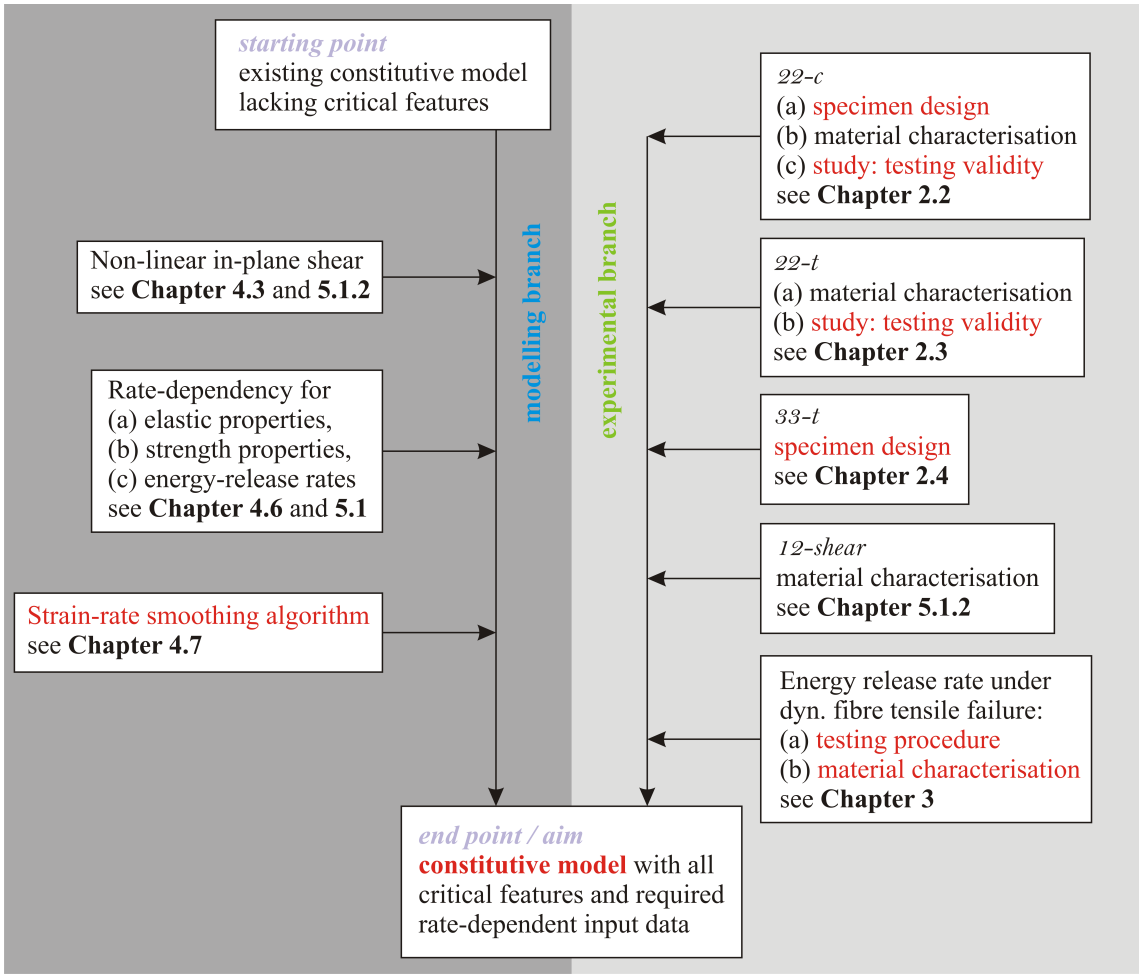


Figure 1.6: Chart of the sets of modelling and experimental objectives of the thesis (original contributions to the body of knowledge are highlighted in red)

1.3.2 Thesis structure

As a broad outline, the structure of this thesis consists of first presenting the developments, results, and improvements generated in the context of the experimental work, followed by a detailed description of the developed constitutive model. Subsequently, the model's calibration is detailed, based, in part, on the data generated in the context of the experimental work. Finally, the calibrated constitutive model is subjected to an extensive validation exercise.

Because this thesis covers several thematically distinct topics under the umbrella of achieving its ultimate aim, see outline in above **Chapter 1.3.1**, no 'centralised' literature review is provided. Instead, each distinct topic, where appropriate, is accompanied by a dedicated description of its background and motivation, and a review of the relevant literature.

The remainder of this thesis is structured as follows:

Chapter 2 focusses on the determination of the high-rate modulus and strength for the deformation modes *22-c*, *22-t*, and *33-t*. The study for *22-c* involves: (i) an investigation into its specimen design, (ii) its characterisation across two loading rate regimes, and, (iii) a comprehensive simulation-based study investigating the influence of key SHB setup and testing parameters with respect to the achievability of valid high-rate testing conditions. The corresponding study for *22-t* covers the identical range of topics except for (i). The study for *33-t* encompasses an investigation into its specimen design and its characterisation across two loading rate regimes.

Chapter 3 presents a study aimed at determining the energy release rate under high-

rate tensile loading of a laminate in fibre direction. Apart from obtaining the dynamic material data itself, this study places a particular focus on the determination procedure and its validity, covering aspects such as the experimental setup, loading conditions, and the data reduction method. An accompanying post-mortem analysis seeks to link the change in the measurable material property on macro scale across the examined loading rate spectrum to the corresponding underlying changes in the material's deformation and failure mechanisms on micro scale.

Chapter 4 presents an improved constitutive model reflecting a composite laminate's rate-dependent deformation, failure, and damage evolution behaviour on macro scale. The model's description encompasses its main premise, an outline of its governing constitutive equations, its incorporation of rate-dependent effects, a strain-rate smoothing algorithm, and a discussion of its key merits and limitations.

Chapter 5 details the constitutive model's calibration against openly available and generated strain-rate-dependent datasets for each one of its deformation, failure, and damage evolution parameters. Thereafter, the results of an extensive model validation exercise are presented and discussed.

Chapter 6 provides a concise summary for each of the main topics covered by this thesis. Each of these summaries culminates with a corresponding set of key conclusions, particularly highlighting the generated novelties. With the aim of providing possible starting points for future research, each set of conclusions is accompanied by suggestions for further work.

Chapter 2

Improvements to the high-rate material characterisation of the deformation modes *22-c*, *22-t*, and *33-t*

This chapter is divided into four subchapters. The first begins with an introduction to dynamic material characterisation employing a split-Hopkinson bar setup, followed by a description of the necessary conditions for the generation of valid high-rate material data and the various means to tailor the incident pulse in order to meet these conditions. Subsequently, a range of experimentally-generated incident pulse profiles featuring a linearly rising slope for an SHPB and SHTB system, respectively, is presented. The second subchapter examines three aspects of the *22-c* deformation mode: (i) a specimen design study comparing a *block* to a *waisted block* design, (ii) its character-

isation under high-rate loading conditions, and, (iii) a study investigating the influence of key SHB setup and testing parameters on the achievability of valid high-rate testing conditions. The third subchapter examines two aspects of the *22-t* deformation mode: (i) its characterisation across two loading rate regimes, and, (ii) a study similar to the last item of the aforementioned *22-c* testing. Finally, the fourth subchapter presents a specimen design study for the *33-t* deformation mode, in which a form-fit design suitable for high-rate testing on an SHB system is investigated.

Main contributions to the body of knowledge contained in the present chapter at a glance:

- A specimen design study for *22-c* testing which demonstrates that the deviations of the obtained material properties on the basis of the commonly used *block* design from their correct values measured via a *waisted block* design are not negligible. A subset of the experimental data from this study was published as: Thomson, D. M., Erice, B., Cui, H., Hoffmann, J., Wiegand, J., and Petrinic, N. (2018). A Puck-based localisation plane theory for rate- and pressure-dependent constitutive modelling of unidirectional fibre-reinforced polymers. *Composite Structures*, 184:299–305.
- A study investigating the influence of key split-Hopkinson bar setup and testing parameters on the achievability of valid high-rate testing conditions for the deformation modes *22-c* and *22-t*. One key conclusion from this study is that the deformation mode *22-t* cannot be characterised under a nearly constant strain-rate at failure in a high-rate loading experiment.
- The development of a form-fit specimen design for *33-t* testing, which is demon-

strated to be applicable for testing under high-rate loading conditions.

- The generation of rate-dependent data for *22-c* and *22-t* testing of *IM7/8552*, which add to their respective datasets documented in literature.

2.1 Introduction

This subchapter first provides a brief introduction to dynamic material characterisation employing a split-Hopkinson bar setup. An emphasis is placed on the conditions underlying the obtained high-rate material data's validity. This is followed by an overview of the various existing means for shaping the incident pulse profile in order to meet these conditions. The subchapter concludes by presenting a range of experimentally-generated incident pulse profiles featuring a linearly rising slope for an SHPB and SHTB system, respectively.

2.1.1 Split-Hopkinson bar testing: Setup, working principle, and validity conditions

Structures under design-critical load cases of a dynamic nature experience a range of strain-rates over the course of their deformation and fracture process. A constitutive model needs to adequately reflect this rate-dependency for all relevant mechanical properties in order to be able to facilitate a successful simulation-based design process. To this end, the model requires calibration against experimentally-obtained data points that cover a reasonably large section of the strain-rate range of interest. As illustrated in **Figure 2.1**, various experimental setups exist to cover the different sections of the

strain-rate spectrum. For the strain-rate regime between the order of magnitude of 10 to 1000 s^{-1}, the split-Hopkinson bar (SHB) technique has been firmly established over the last few decades as a reliable experimental setup for testing a wide range of materials and deformation modes (e.g. [5]).

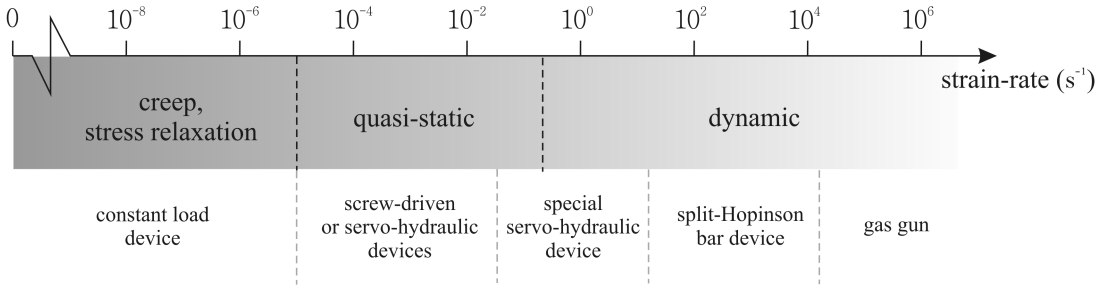


Figure 2.1: Range of experimental setups to cover different segments of the strain-rate spectrum (based on [5] and [39])

Experimental setup and DAQ. The setup[1] of an SHB experiment consists of a specimen sandwiched between two slender bars, termed the *input* (or *incident*) and *output* (or *transmission*) bar. These bars are aligned along their respective longitudinal axes, sufficiently supported in the transverse direction, and free to move longitudinally. A projectile is commonly used to generate the loading pulse by impacting the input bar. Each bar is instrumented with strain gauges in order to measure the magnitude of the stress wave passing through the bar at a particular cross-section. Data acquisition is realised via an amplifier, an oscilloscope, and a high-speed camera in case of a DIC-based strain measurement.

The generated loading pulse travels down the input bar until it encounters the input bar/specimen interface. Due to the impedance mismatch across this interface, only a part of the loading pulse is transmitted to the specimen, whilst the remaining part

[1] An SHPB setup is assumed for the following explanations; however, the given outline, in essence, also applies to setups for testing other deformations modes.

is reflected. Upon traversing the specimen, the pulse again encounters an impedance mismatch at the output bar/specimen interface, resulting in a similar split in transmitted and reflected wave parts. A depiction of the SHB setup in conjunction with a visualisation of the stress wave propagation is presented in **Figure 2.2**, where α_{in} and α_{out} denote the forward-travelling stress wave in the input and output bar, respectively, and β_{in} and β_{out} the corresponding backwards-travelling waves.

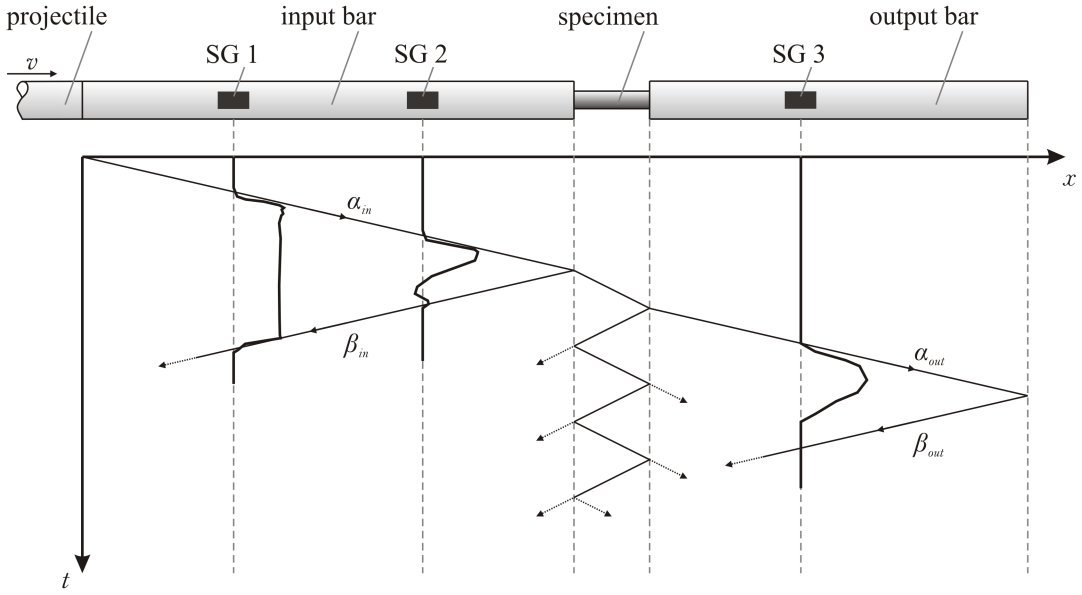


Figure 2.2: SHPB setup with a visualisation of the propagating stress wave

Data reduction. The evaluation process of an SHB experiment is based on the assumption of one-dimensional wave propagation, and consists of three major steps: (i) obtaining the bar stress in the cross-sections at the strain-gauge positions, (ii) time-shifting and superimposing, where appropriate, these stress histories to obtain the stress history at the bar/specimen interfaces, and, (iii) calculating the specimen's (engineering) strain-rate (**Equ. 2.1**), strain (**Equ. 2.2**)[2], and stress (**Equ. 2.3**)[3]. As this

[2]the equations for the calculation of strain and strain-rate assume the force equilibrium to be already established, i.e. $\epsilon_t(t) = \epsilon_i(t) + \epsilon_r(t)$ (see **Figure 2.4** for an illustration of the individual wave parts)

[3]the equation provided here is for the *1–wave analysis*; for the *2–* or *3–wave analysis*, see [5]

analysis cannot readily account for the compliance of a specimen's 'shoulder' section, fixtures connecting the specimen to the bar system, or adhesive layers between the specimen and those fixtures, other means for determining the specimen's strain (and strain-rate) are often employed such as affixing strain-gauges to the specimen or optical measurement using a high-speed camera. An example of the considerable deviation of the specimen's strain history as determined by the SHB analysis from that obtained via DIC analysis is shown in **Figure 2.3** for *22-t* testing.[4]

$$\dot{\epsilon}_s(t) = \frac{-2c_b}{l_{s,0}}\epsilon_r(t) \tag{2.1}$$

$$\epsilon_s(t) = \frac{-2c_b}{l_{s,0}}\int_0^t \epsilon_r(\tau)d\tau \tag{2.2}$$

$$\sigma_s(t) = \frac{E_b A_b}{A_{s,0}}\epsilon_t(t) \tag{2.3}$$

In the above equations E_b, A_b, c_b denote the bars' Young's modulus, cross-sectional area, and wave propagation velocity; $l_{s,0}$, $A_{s,0}$ the specimen's initial length and cross-sectional area; σ_s, ϵ_s, $\dot{\epsilon}_s$ the specimen's stress, strain, and strain-rate; ϵ_r, ϵ_t the loading pulse's reflected and transmitted wave parts according to **Figure 2.4**, respectively.

Validity of the obtained results. In order for an SHB experiment to yield valid material characterisation data, two key conditions need to be fulfilled:[5]

- The establishment of a uniaxial and uniform stress field across and along the specimen's gauge volume. This condition implies that inertia effects must be suf-

[4]The reader is referred to **Chapter 2.3.1** for details regarding the generation of this data.

[5]For the sake of completeness it should be mentioned that further conditions such as the sample material's representative nature (condition, volume, and freedom from machining-induced defects), the negligibility of wave dispersion effects (or their consideration in the evaluation process), as well as a host of requirements concerning the bar system (geometry, material, spatial arrangement, and behaviour under load) have to be fulfilled. For a more detailed outline of the last aspect, see *Gama et al. (2004)* [44] or the relevant *ASM handbook* [5].

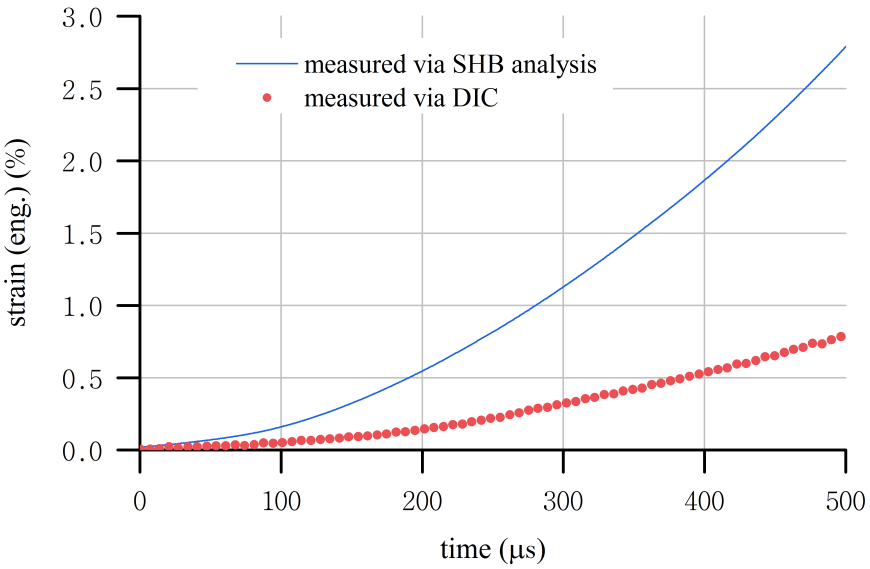


Figure 2.3: Example of the discrepancy between the strain history determined via the SHB vs. a DIC-based analysis

ficiently small when compared to the specimen's visco-elastic(-plastic) material response. Inertia effects result in a force gradient (and thus, a force disequilibrium) along the specimen's gauge volume. This time-dependent disequilibrium can be approximated by considering the two resultant forces, F_{in} and F_{out}, acting on the end faces of the specimen's gauge volume, see **Figure 2.5(a)**. The state of force disequilibrium, Δ_F, can then be quantified according to[6]

$$\Delta_F = \left| \frac{F_{in} - F_{out}}{\frac{1}{2}(F_{in} + F_{out})} \right| \cdot 100 \, . \tag{2.4}$$

The idealised convergence behaviour towards force equilibrium is depicted in **Figure 2.5(b)**. For the purpose of the present study, equilibrium was considered to be reached when Δ_F had stabilised below a threshold value of 10%. In the literature dedicated to SHB pulse shaping, the state of force equilibrium is commonly referred to as 'stress equilibrium' (SE); the present study follows this

[6]The force disequilibrium metric employed in the present study follows the general idea introduced by *Ravichandran et al. (1994)* [119].

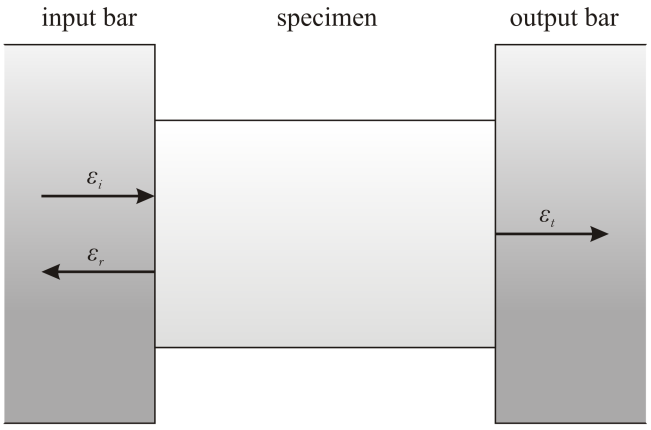


Figure 2.4: Incident, reflected, and transmitted parts of the loading pulse

convention.

- The occurrence of specimen failure under the influence of a nearly constant strain-rate along the sample's gauge volume. Analogous to the derivation of the force disequilibrium metric above, the strain-rate of the specimen's gauge section can be understood by considering the particle velocities of the respective end faces of the gauge volume, v_{in} and v_{out}, see **Figure 2.5(a)**. On the basis of these two velocities, the gauge volume's (engineering) strain-rate can then be calculated according to $\dot{\epsilon}_s = \frac{v_{in} - v_{out}}{l_{s,0}}$. Ideally, after an initial 'ringing-up period', this strain-rate converges asymptotically towards a desired strain-rate value with specimen failure occurring in the 'plateau section' of the strain-rate history; this idealised strain-rate history is illustrated in **Figure 2.5(b)**. In accordance with the literature, this state of a nearly constant strain-rate at specimen failure is abbreviated as CSR from hereon. In contrast to the establishment of SE, associating the state of CSR with a particular threshold value is more difficult as the asymptotic value against which the sample's strain-rate converges is only readily determinable for SHPB testing (see **Equ. 2.7** in **Chapter 2.2.3** for $\dot{\epsilon}_s|_{t\to\infty}$). In this particular

case, CSR was considered to be achieved when the sample's strain-rate reached 95% of its asymptotic value. Apart from this exception, however, the evaluation of CSR relied on assessing the specimen's strain-rate history in a more qualitative manner. Finally, it should be mentioned that achieving CSR is not, strictly speaking, required for the data's validity but for its *meaningfulness*. In other words, only if a dynamically obtained material property can be unambiguously associated with a particular strain-rate value can it be confidently used for model calibration.

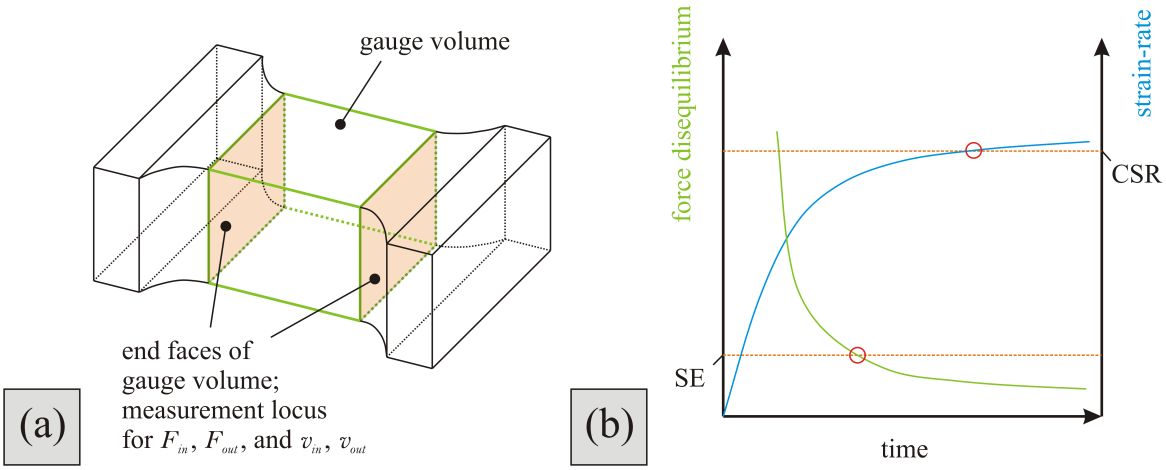


Figure 2.5: (a) determination of force disequilibrium and strain-rate history based on the gauge volume's end faces; (b) idealised force disequilibrium and strain-rate history including SE and CSR conditions

2.1.2 Pulse shaping

The incident pulse profile generated in a conventional SHB experiment is of a nearly rectangular shape, featuring a very steep rising flank. This particular pulse profile is known to cause several issues, thereby necessitating the shaping of the incident pulse:

Very rapid loading of the specimen. Especially for materials featuring a comparatively low strain-to-failure, such as most deformation modes of carbon-fibre/epoxy composites, failure can occur prior to reaching a state of reasonable force equilibrium along the specimen's gauge section, rendering the experiment invalid as a consequence. Decreasing the specimen's loading rate via pulse shaping thus aims to ensure the establishment of SE prior to sample failure.

Effects of wave dispersion. One aspect of this phenomenon is the development of pronounced high-frequency oscillations, known as *Pochhammer-Chree* oscillations, that trail the initial rising slope [35]. These oscillations, in turn, are prone to causing premature failure in comparatively brittle materials such as carbon-fibre/epoxy composites. Furthermore, wave dispersion also causes the incident wave profile to 'broaden' and slopes to decrease in steepness as the wave travels along the bar. If a conventional pulse is employed, wave dispersion should be addressed, e.g. by employing an additional step in the SHB analysis procedure in order to take this phenomenon into account (e.g. [54, 90]). This additional effort, however, becomes unnecessary when the incident pulse is sufficient shaped, as this results in the loading pulse's high-frequency content being substantially reduced (e.g. [118]).

Strain-rate history. A nearly constant strain-rate at specimen failure is desirable for yielding useful data for constitutive model calibration (see preceding section). Following *Vecchio et al.*'s [143] line of reasoning, the necessary requirement for meeting this condition can be derived analytically, ultimately resulting in

$$E_b A_b \epsilon_i(t) - A_s \sigma_s(t) = \frac{l_s E_b A_b}{2 c_b} \dot{\epsilon}_s(t) \ . \tag{2.5}$$

The authors argue that for $\dot{\epsilon}_s(t)$ to be constant, the incident pulse $\epsilon_i(t)$ and the

specimen's mechanical response $\sigma_s(t)$ must exhibit similar rates of change (assuming all coefficients in **Equ. 2.5** remain reasonably constant throughout the test). In other words, the incident pulse needs to reflect the qualitative behaviour of the specimen material's dynamic response. From the perspective of achieving a nearly constant strain-rate, then, a rectangular incident pulse is only suitable for materials exhibiting perfect plasticity. Unidirectionally-reinforced carbon-fibre/epoxy composites, however, exhibit a linear elastic behaviour up to failure for the vast majority of their deformation modes, thus requiring a ramp-like incident pulse.

Several approaches to shaping the incident pulse's profile have been developed over the last few decades: (i) employing a shaped projectile, e.g. [12, 30, 87, 88], (ii) using an additional rod in the loading train that features a series of recesses [49], (iii) using a pre-loading bar [109], and, (iv) employing a sacrificial *pulse shaper* that is placed on the impact surface of the input bar, e.g. [37, 42, 102, 143]. It is the last of these, i.e. pulse shapers, that were used in the present study, based on the following merits. First, this approach is the most versatile: (i) incident pulse profiles can be tailored over an extraordinarily large range, and (ii) pulse shapers are applicable to both, SHPB and SHTB testing. Second, using pulse shapers is comparatively easy to implement as no additional retooling of the experimental setup is required.[7]

[7] provided the input bar's impact surface is readily accessible in the case of the SHTB setup

2.1.3 Generation of a spectrum of linearly rising incident pulses for an SHPB and SHTB system

The SHPB system employed in the present study consisted of a ⌀16 mm titanium input ($l = 2510$ mm) and output bar ($l = 2510$ mm), and a ⌀20 mm titanium projectile ($l = 2715$ mm). The SHTB system featured a crescent-shaped projectile; for a detailed outline of this particular bar system, see *Gerlach et al. (2012)* [48]. The SHTB setup was composed of a ⌀16 mm titanium input ($l = 3057$ mm) and output bar ($l = 2974$ mm); its titanium projectile was 2500 mm in length. The following paragraphs present the generation of a range of incident pulses featuring a linearly rising slope for each of those SHB systems. These spectra of generable loading pulses form one of the key inputs for the *22-c* and *22-t* modelling studies that will be presented in **Chapter 2.2.3** and **2.3.2**, respectively.

SHPB. For the SHPB setup, discs made of hard or annealed copper are most commonly employed to achieve a gradually rising incident pulse (e.g. [42, 43, 44, 79, 107, 149]). For the present study, neoprene rubber and cardboard were used to generate linearly rising pulse profiles. Employing these materials instead of copper (or any other metal, for that matter) offered the advantage of not requiring any additional time and effort for machining and annealing in preparation of the pulse shapers.

A spectrum of incident pulse profiles was generated by employing a range of projectile velocities in conjunction with using cardboard and neoprene rubber of various thicknesses. A selection of the generated incident pulse profiles is presented in **Figure 2.6**, with only the incident pulses' rising flank shown for the sake of clarity. The rising flanks' slope ranged from 0.017 to 10.6 MPa/µs, thus covering well above 2.5 orders

of magnitude.

The generated incident pulse profiles exhibited a brief initial period during which the overall linear rise was disturbed by oscillations. It is recommended to search for means to eliminate these disturbances in future work.

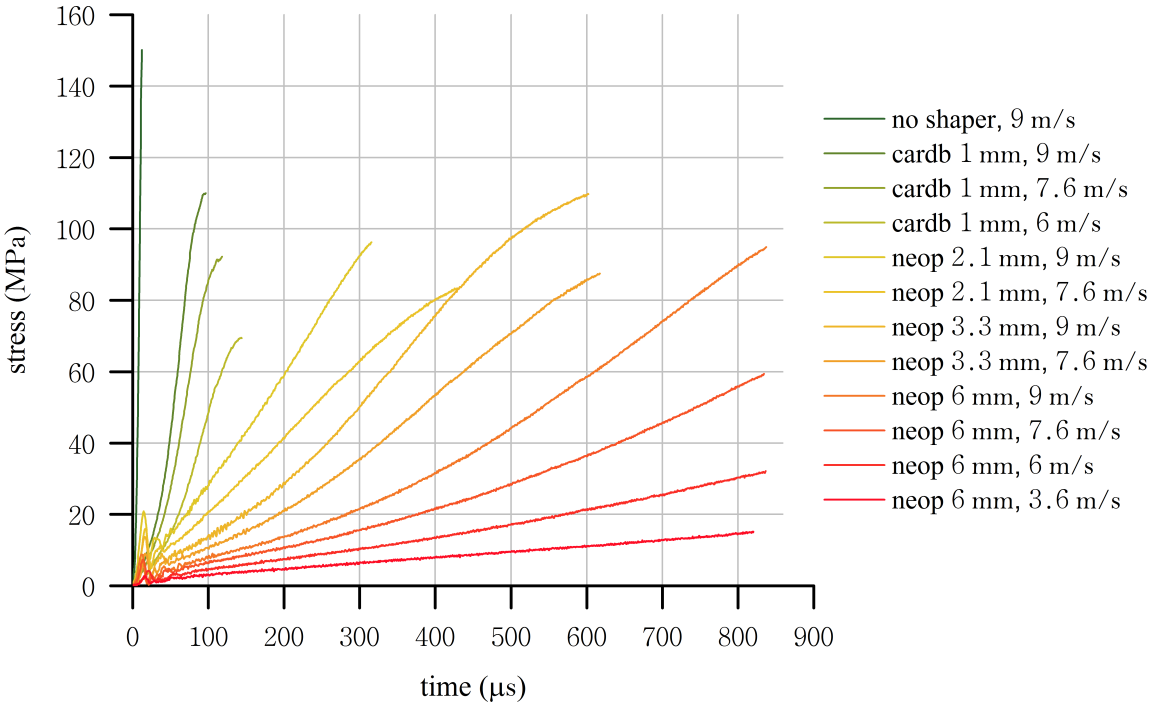


Figure 2.6: Spectrum of linearly rising loading pulses generated on an SHPB system using cardboard and neoprene rubber of various thicknesses

SHTB. Similar to the SHPB system, a spectrum of incident pulses featuring a linearly rising flank was generated for the SHTB system by employing neoprene rubber of various thicknesses in conjunction with a range of projectile velocities. A selection of thus generated incident pulse profiles is presented in **Figure 2.7**, with only the incident pulses' rising flank shown for the sake of clarity. The rising flanks' slope ranged from 0.063 to 5.7 MPa/µs, thus covering roughly two orders of magnitude.

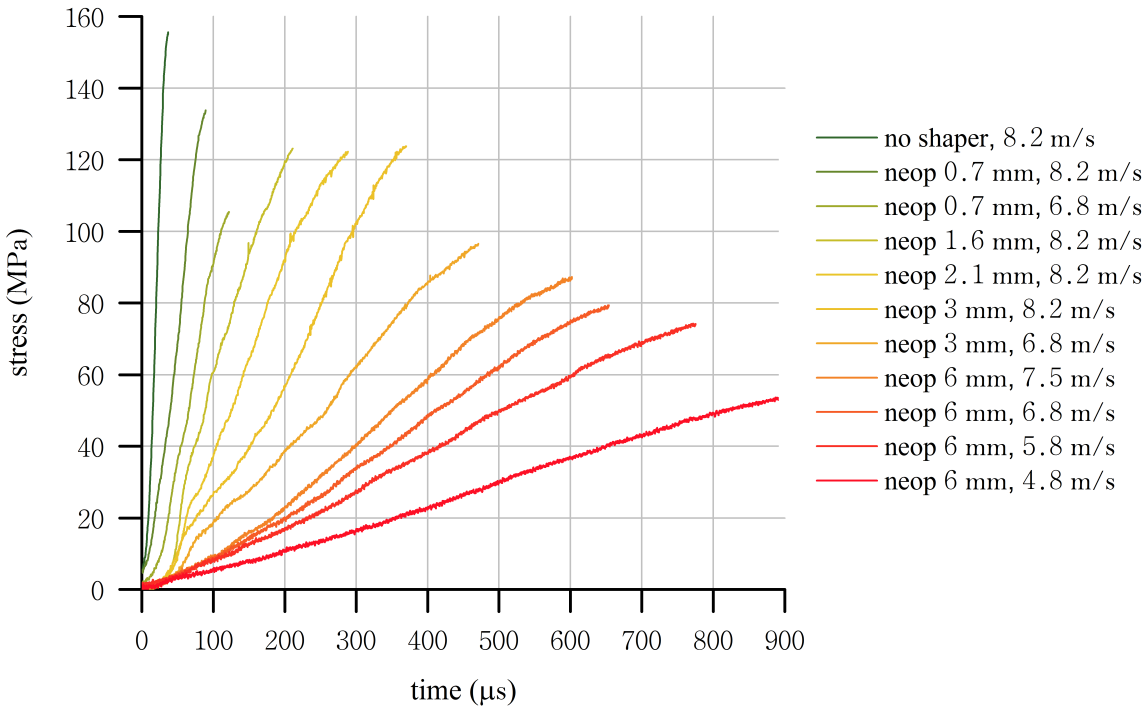


Figure 2.7: Spectrum of linearly rising loading pulses generated on an SHTB system using neoprene rubber of various thicknesses

2.2 In-plane compression testing transverse to the fibre direction (*22-c*)

This subchapter examines three aspects of the material characterisation of the *22-c* deformation mode. These are: (i) a specimen design study comparing a *block* to a *waisted block* design, (ii) its characterisation under high-rate loading conditions, and, (iii) a simulation-based investigation into the influences of key SHB setup and testing parameters on the achievement of valid high-rate testing conditions.

2.2.1 Specimen design study: *block* vs. *waisted block*

Motivation. A range of specimen designs for characterising the *22-c* deformation mode can be found in existing literature: (i) a *block* design [68, 79, 124, 139], (ii) a *waisted block* design [86], (iii) a *dog-bone* design in conjunction with threaded 'end sleeves' [144], (iv) a *beam* design [21], and, (v) a *strip* design with 'end tabs' [126]. In the context of testing at elevated loading rates, the *block* design appears to be the most commonly employed specimen design due to its simplicity, material economy, and comparatively short specimen length, which allows for a quick establishment of force equilibrium. *Block* design specimens, however, show a strong tendency to initiate failure in direct vicinity of the load introduction interfaces. The susceptibility to fail in this particular section of the specimen is caused by the friction-induced (partial) hindrance of the sample material's lateral expansion as the compressive load increases. Lubrication to reduce the interfacial friction is commonly applied to mitigate this phenomenon; however, this does not consistently eliminate the issue. Consequently, a three-dimensional stress field develops in the vicinity of the loading interfaces, which, in turn, is prone to triggering specimen failure. Strictly speaking, this non-negligible influence of additional stress components other than the one in loading direction should render the corresponding test invalid (see **Chapter 2.1.1**). Using the experimental data in spite of this deviation from a uniaxial and uniform stress field along and across the sample's gauge volume may lead to: (i) inaccuracies in the determined material properties (as the data reduction assumes deformation and failure under a one-dimensional stress field), and, (ii) an (undesired) influence on the fracture plane's

inclination angle.[8] The commonly practiced approach to resolve this issue is to employ a *waisted block* specimen design. This design allows the failure plane localisation to be shifted away from the loading interface region towards the specimen's mid-section, which, in turn, is governed by a reasonably one-dimensional and undisturbed stress field.

Despite the issues associated with the *block* design's tendency to initiate failure in the load introduction region of the specimen, it remains the specimen design most commonly used for *22-c* testing. The aim of this study was thus to quantify the difference between a *block* and a *waisted block* design in terms of the measured ultimate strength Y_c and initial modulus $E_{22c,0}$. Ultimately, this comparison was meant to determine if the *waisted block* design's influence on the measured material properties is significant enough to justify its use over the commonly used *block* design.

Material, specimen geometry, manufacturing, and preparation. A composite panel was produced by manually stacking *IM7/8552* unidirectionally-reinforced prepreg plies following the ply-book $[90]_{36}$, and subsequently curing this laminate according to *Hexcel*'s recommended temperature/pressure regime [63]. The resulting laminate measured approximately 4.5 mm in through-thickness direction. The specimen geometries for the *block* and *waisted block* design are provided in **Figure 2.8**. No additional machining was performed in the specimens' thickness direction. In order to facilitate a DIC-based analysis of the specimens' deformation and failure behaviour, a black speckle pattern on a white background was applied to one of the specimens' lateral faces.

[8] Measuring the failure plane's inclination might be of interest for calibration and/or validation purposes of 3D IFF failure theories, such as [117]. As this is not the case in the present study, the failure plane's inclination was not evaluated.

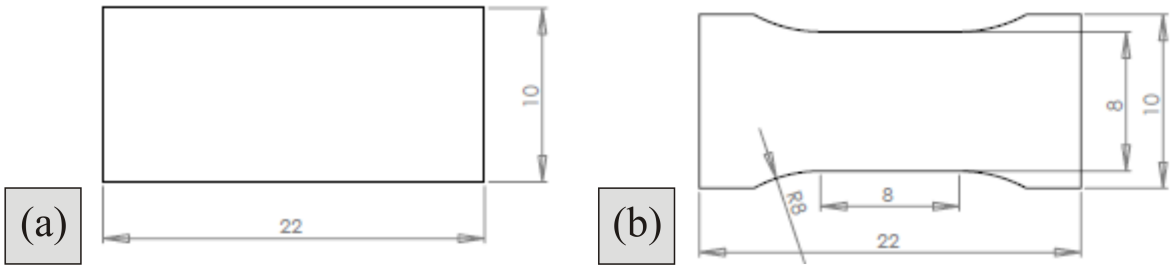


Figure 2.8: Specimen geometries for *22-c* testing: (a) *block*, and (b) *waisted block* design (dimensions in mm)

Experimental setup, data reduction, and bending check. Testing was carried out on a screw-driven *Zwick/Roell Z250* testing machine at a displacement rate of 0.008 mm/s. Force was measured by the machine's 20 kN load cell. The specimens' deformation and failure were recorded using a camera (*jAi BM-500GE*) in conjunction with a *Schneider-Kreuznach Xenoplan 0.14/11* lens. Strain (and thus strain-rate) was measured via DIC analysis of the recorded series of images. Friction between the interface of the specimen and the testing machine was minimised by applying a thin film of silicone grease. Five *block* and seven *waisted block* design specimens were tested in total. Strength was determined according to $Y_c = \frac{F_{max}}{A_0}$. The initial modulus $E_{22c,0}$ was obtained via a linear fit to the stress-strain data across a range of engineering strain values from 0.005 to 0.01. Each test's validity was ensured by checking for the absence of excessive specimen bending over the course of its deformation according to *ASTM D3410/D3410M-03* [6], see **Equ. 2.6**. This calculation was based on the strain measured via DIC in close vicinity of the respective surfaces.

$$B_y = \frac{\epsilon_{sideA} - \epsilon_{sideB}}{\epsilon_{sideA} + \epsilon_{sideB}} \cdot 100 \tag{2.6}$$

In the above equation, B_y denotes the bending metric, and ϵ_{sideA} and ϵ_{sideB} the specimen's surface strains in loading direction on opposite sides of the sample, respectively.

According to [6], the validity of an experiment requires B_y to remain below a value of 10%.

Results and discussion. In contrast to the *block* design, the *waisted block* design specimens consistently failed in the specimens' (waisted) mid-section. Failure plane localisation thus reliably occurred in sufficient distance to the specimen/testing machine interfaces. To illustrate this, **Figure 2.9** shows: (a) failure initiation at one of the *block* design specimen's end faces, (b) a DIC-analysis of a *block* design specimen with the failure plane localisation being triggered in the direct vicinity of one of the testing machine's interfaces, and, (c) a DIC-analysis of a *waisted block* design specimen exhibiting the desired shift of failure plane localisation to the specimen's mid-section.

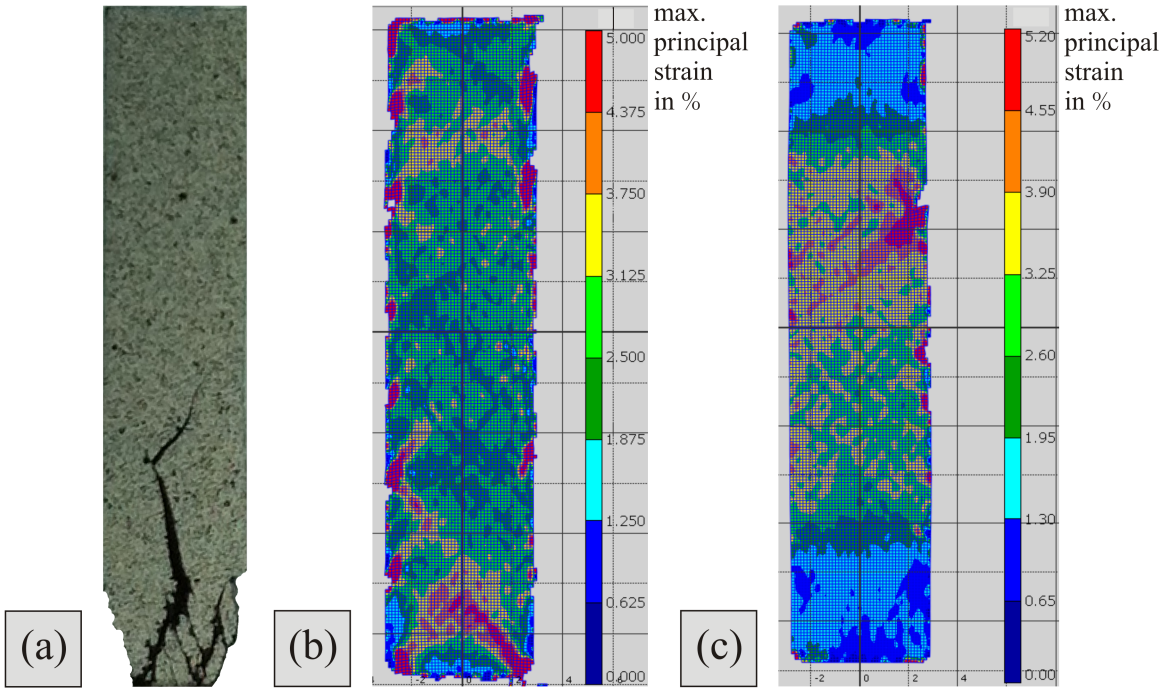


Figure 2.9: (a) failure originating at one of the *block* design specimen's end faces; (b) DIC-analysis of a *block* design specimen showing failure plane localisation in the direct vicinity of one of the specimen's end faces; (c) DIC-analysis of a *waisted block* design specimen showing failure plane localisation at due distance from the specimen's end faces

A summary of the material properties obtained from the tests of both specimen designs is presented in **Table 2.1**. The stress-strain curves pertaining to the tests of the *waisted block* design specimens will be presented in the context of the subsequent section.

Table 2.1: Obtained material properties for *22-c* testing under quasi-static loading employing a *block* and a *waisted block* specimen design

			block design	*waisted block* design
ultimate strength Y_c	mean	MPa	252	266
	SD	MPa	5	9
	CV	%	2.2	3.3
initial modulus $E_{22c,0}$	mean	MPa	8.9	8.5
	SD	MPa	0.1	0.2
	CV	%	1.3	2.4

The measured ultimate strength Y_c for the *waisted block* design showed an increase of 5.5% with respect to the *block* design specimens. The obtained value for the latter was very close to data found in literature: *Koerber et al. (2010)* [79] tested *IM/8552* using a *block* design employing almost identical specimen dimensions to the ones used in the present study, determining Y_c to be 255 MPa.

Compared to the *block* design tests, the measured initial modulus $E_{22c,0}$ of the *waisted block* design specimens showed a decrease of 4.6%. The stiffer response of the *block* design specimens may have been caused by the (partially) hindered expansion of the material transverse to the loading direction due to the interfacial friction between specimen and loading device. **Figure 2.10** presents the results of a DIC-based measurement of the strains transverse to the loading direction at the ends and middle of the gauge section for both specimen designs. This analysis provides an indication regarding the extent to which the lateral specimen expansion is hindered in case of the *block* design

specimen, thus clearly indicating a deviation from the desired one-dimensional state of stress in the specimen's gauge section. In contrast, the uniform lateral expansion of the material along the *waisted block* design specimen's gauge section is in accordance with the tenets of valid material characterisation.

The experimental scatter associated with the obtained material properties for both specimen designs was low.

In conclusion, a *waisted block* specimen design is recommended for the characterisation of the *22-c* deformation mode. The slightly higher specimen machining effort involved is deemed to be justified by the observation that both material properties, i.e. initial modulus and ultimate strength, are clearly affected by the specimen design choice.

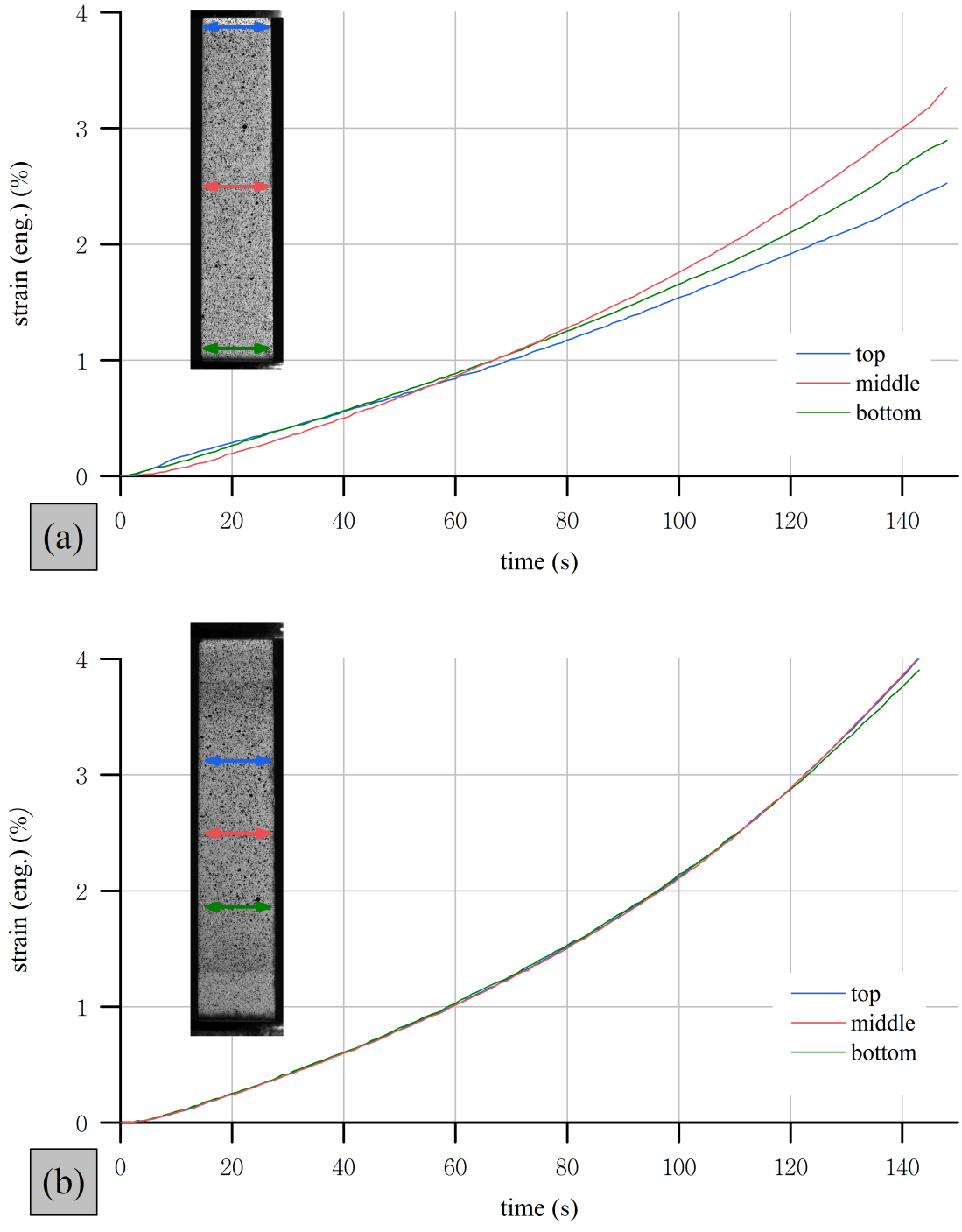


Figure 2.10: DIC-based measurement of the strains transverse to the loading direction at different cross-sections of the specimens' gauge section for (a) the *block* design, and (b) the *waisted block* design

2.2.2 Material characterisation under high-rate loading

Specimen, experimental setup, data reduction, and bending check. The specimens' material, design, manufacturing, and preparation were identical to what has been described in **Chapter 2.2.1**. High-rate testing was carried out employing the SHPB system outlined in **Chapter 2.1.3** in conjunction with a high-speed camera (*Specialised Imaging*, model: *Kirana*). The loading pulse was generated using a projectile velocity of 8.2 m/s together with a 3.3 mm thick neoprene pulse shaper. Strain (and thus strain-rate) was measured via DIC analysis of the recorded series of images. Strength was determined identically to what has been outlined in **Chapter 2.2.1**; the evaluation of the initial modulus will be discussed below. As for the tests under quasi-static loading, a thin film of silicone grease was used as a lubricant. Seven specimens in total were tested under high-rate loading conditions. Each tested specimen was checked for excessive bending based on **Equ. 2.6** given in the preceding section.

Results and discussion. The sets of stress-strain curves pertaining to quasi-static and high-rate testing are presented in **Figure 2.11**. This plot shows a markedly different behaviour of this deformation mode under an elevated loading rate regime. In particular, the loading rate's effect on the material's ultimate strength Y_t is immediately noticeable. Furthermore, the degree of this deformation mode's non-linearity appears to decrease under dynamic loading.[9] The validity of the high-rate tests can be deduced from **Figure 2.12**, which shows that failure occurred under SE and CSR conditions.

The dynamic initial modulus $E_{22c,0}$ could not be obtained based on a strain range

[9]It should be noted, however, that the steadily increasing strain-rate across the specimen's gauge section over the course of its deformation may contribute to this phenomenon.

identical to that used for the quasi-static tests (i.e. 0.005 to 0.01), since the force disequilibrium at that point had not yet dropped below the threshold value of 10%. Instead, its determination was based on a linear fit to the range of engineering strain values between $\epsilon_I = \epsilon(180\ \mu s)$ and $\epsilon_{II} = \epsilon_I + 0.005$. Apart from corresponding to a state of reasonable force equilibrium ($\Delta_F \approx 10\%$, see **Figure 2.12**), the thus defined bounds for the determination of $E^{dyn}_{22c,0}$ resulted in values of ϵ_I and ϵ_{II} of approx. 0.009 and 0.014, respectively, thus rendering its measurement still reasonably comparable to its counterpart obtained under quasi-static loading conditions.

From the perspective of assessing the quality of the obtained material properties under high-rate loading, it must be noted that the determination of the dynamic initial modulus was based on a section of the stress-strain curve that is not associated with specimen deformation under a nearly constant strain-rate. This, in turn, implies that the obtained value for $E^{dyn}_{22c,0}$ should be considered as having a degree of uncertainty associated with it. In contrast, the determination of Y_c^{dyn} was based on a state of specimen deformation under a nearly constant strain-rate.

Finally, it is worth mentioning that the material's high-rate strength measured in the present study employing a *waisted block* design ($Y_c^{dyn} = 413 \pm 15$ MPa at $\dot{\epsilon} = 127\ s^{-1}$) exceeds the ones measured by *Koerber et al. (2010)* [79] ($Y_c^{dyn} = 371 \pm 9$ MPa at $\dot{\epsilon} = 227\ s^{-1}$), and *Schaefer et al. (2014)* [124] ($Y_c^{dyn} = 393$ MPa at $\dot{\epsilon} = 800\ s^{-1}$), both of which having tested *block* design specimens made of *IM7/8552* at a higher strain-rate than the one in the present study. This, in turn, may be taken as further evidence that the higher degree of stress uniformity across the gauge section of the *waisted block* design yields a result closer to the 'real' material property due to not triggering the

fracture plane localisation process 'prematurely'.

A detailed investigation into the influences on the achievement of valid testing conditions for *22-c* testing using an SHB setup will be undertaken in the next section.

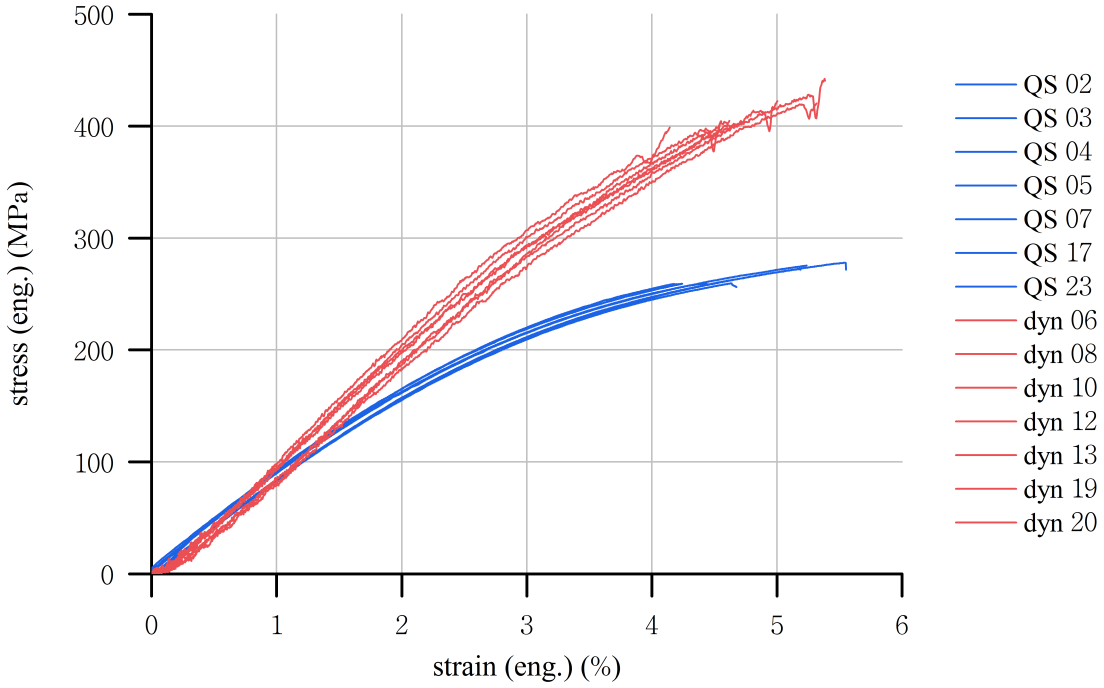


Figure 2.11: Stress-strain curves for *22-c* testing under quasi-static and high-rate loading conditions

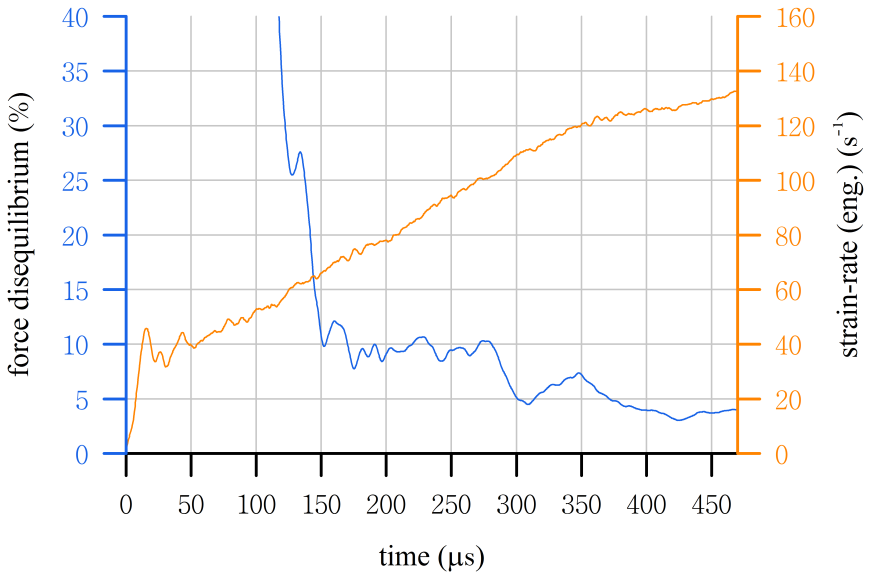


Figure 2.12: Assessment of the validity of the dynamic *22-c* material characterisation tests

Table 2.2 summarises the obtained material properties for *22-c* testing under high-rate loading conditions. The quasi-static testing results generated in the context of the above specimen design study are also reproduced in order to allow for a direct comparison across both loading rate regimes. The results indicated that the material's ultimate strength Y_c experiences an increase of 55%, and the initial modulus $E_{22c,0}$ of 28%, when compared to the data obtained under quasi-static loading. The overall level of experimental scatter was low, with the data obtained under dynamic loading conditions showing a slightly higher level of scatter than its quasi-static counterpart. The gauge section's strain-rate at the point of reaching the material's ultimate strength Y_c^{dyn} was measured to be 127 s^{-1}. The strain-rate associated with the initial modulus $E_{22c,0}^{dyn}$ was determined to be 83 s^{-1}.

Table 2.2: Obtained material properties for *22-c* testing under quasi-static and high-rate loading conditions

			quasi-static loading	high-rate loading
ultimate strength Y_c	mean	MPa	266	413
	SD	MPa	9	15
	CV	%	3.3	3.6
initial modulus $E_{22c,0}$	mean	MPa	8.5	10.9
	SD	MPa	0.2	0.6
	CV	%	2.4	5.1
strain-to-failure ϵ_{ult}	mean	%	4.79	4.82
	SD	%	0.53	0.44
	CV	%	11.1	9.2
strain-rate: Y_c	mean	s^{-1}	0.00036	127
strain-rate: $E_{22c,0}$				83

2.2.3 Influences on the achievement of valid high-rate testing conditions

Introduction. The aim of this modelling-based study was to investigate a range of split-Hopkinson bar setup and testing parameters for their effect on achieving valid high-rate testing conditions for the characterisation of the *22-c* deformation mode. The validity of testing conditions is understood here as the establishment of SE and CSR prior to specimen failure. The reader is referred to **Chapter 2.1.1** for a detailed description of these two conditions. The study presented here took the dynamic material characterisation data generated in **Chapter 2.2.2** as a reference point for the modelling process. The following aspects of high-rate *22-c* testing were of particular interest:

- *To what degree does the force disequilibrium history determined via the SHB analysis represent the force disequilibrium history measured directly at the end faces of the specimen's gauge section?*
- *What is the influence of the bar material and diameter, and the incident pulse's rising slope on the achievability of valid testing conditions?*
- *Which parameters does a model of the SHB experiment have to consider in order to achieve a satisfactory reflection of the specimen's force disequilibrium and strain-rate history?*

What follows is a brief outline of the two types of models employed in the present study, and the range of model input parameters and evaluation approaches considered by them.

Outline of the analytical model. The analytical model was based on the work of *Frew et al. (2001)* [42], who tested limestone samples on an SHPB system. In this context these authors proposed an analytical model to calculate the specimen's strain-rate (**Equ. 2.7**) and strain history (**Equ. 2.8**), as well as the stress histories at the input (**Equ. 2.9**) and output bar/specimen interface (**Equ. 2.10**). In deriving the former two equations, *Frew et al.* assumed a state of reasonable force equilibrium to have already been established. The incident pulse's profile was assumed to be a ramp function with the slope M.

$$\dot{\epsilon}_s = \frac{\gamma M}{E_s}\left[1 - e^{\frac{-2t}{rt_0}}\right] \tag{2.7}$$

$$\epsilon_s = \frac{\gamma M}{E_s}\left[t - \frac{rt_0}{2}\left[1 - e^{\frac{-2t}{rt_0}}\right]\right] \tag{2.8}$$

$$\sigma_{in} = \underbrace{\begin{array}{ll}
\frac{2\gamma M}{r+1} \cdot t & \text{for} \quad 0 \leq t < 2t_0 \\
\frac{2\gamma M}{r+1}\left[t + \left[\left(\frac{r-1}{r+1}\right) + \left(\frac{r-1}{r+1}\right)^2\right] \cdot (t-2t_0)\right] & \text{for} \quad 2t_0 \leq t < 4t_0 \\
\frac{2\gamma M}{r+1}\left[t + \left[\left(\frac{r-1}{r+1}\right) + \left(\frac{r-1}{r+1}\right)^2\right] \cdot (t-2t_0) + \left[\left(\frac{r-1}{r+1}\right)^3 + \left(\frac{r-1}{r+1}\right)^4\right] \cdot (t-4t_0)\right] & \text{for} \quad 4t_0 \leq t < 6t_0 \\
\ldots & \text{for} \quad 6t_0 \leq t < \ldots
\end{array}} \tag{2.9}$$

$$\sigma_{out} = \underbrace{\begin{array}{ll}
0 & \text{for} \quad 0 \leq t < t_0 \\
\frac{2\gamma M}{r+1}\left[\left[1 + \left(\frac{r-1}{r+1}\right)\right] \cdot (t-t_0)\right] & \text{for} \quad t_0 \leq t < 3t_0 \\
\frac{2\gamma M}{r+1}\left[\left[1 + \left(\frac{r-1}{r+1}\right)\right] \cdot (t-t_0) + \left[\left(\frac{r-1}{r+1}\right)^2 + \left(\frac{r-1}{r+1}\right)^3\right] \cdot (t-3t_0)\right] & \text{for} \quad 3t_0 \leq t < 5t_0 \\
\ldots & \text{for} \quad 5t_0 \leq t < \ldots
\end{array}} \tag{2.10}$$

The above equations use the following abbreviations:

$$\gamma = \frac{A_b}{A_s}, \qquad r = \frac{A_b \rho_b c_b}{A_s \rho_s c_s}, \qquad t_0 = \frac{l_{s,0}}{c_s} \; . \tag{2.11}$$

In the above equations, σ_{in} denotes the stress at the input bar/specimen interface, σ_{out} the stress at the output bar/specimen interface, and t_0 the wave transit time across the specimen, respectively; the subscript b refers to all bar-, and the subscript s to all specimen-related entities.

Outline of the FE model. The finite element model reflected the SHB setup from the input bar's cross-section, where the first strain-gauge station was located, up until the end of the output bar, see **Figure 2.13**. The geometric representation of the input bar, specimen, and output bar was meshed employing a *structured mesh* consisting of 3D reduced integration continuum elements (C3D8R) with a mesh size of roughly 0.3 mm in the specimen's gauge volume, and 1 mm for the bulk of the bars, with a continuous transition between these two mesh densities. The model assumed no friction between the specimen and bars. A depiction of the central section of the FE model for *22-c* testing is provided in **Figure 2.14(a)**.

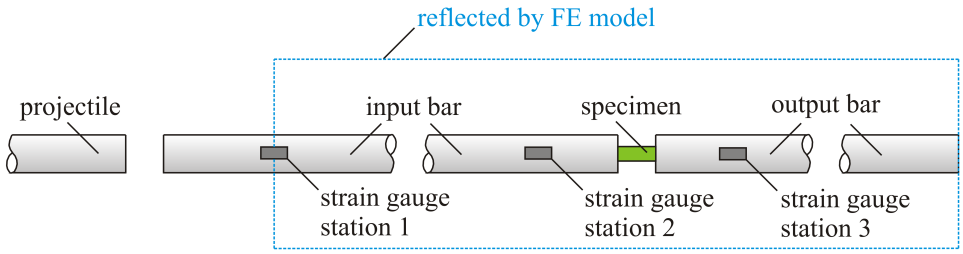


Figure 2.13: Subset of the experimental setup reflected by the FE model

Model input parameters and evaluation approaches. The modelling study considered the following range of input parameters:

- **Bar material**: Titanium vs. steel vs. aluminium vs. magnesium. The following material properties were used: $E_{Ti} = 114$ GPa, $E_{St} = 205$ GPa, $E_{Al} = 70$ GPa, $E_{Mg} = 45$ GPa, and $\rho_{Ti} = 4.4$ g/cm^3, $\rho_{St} = 7.9$ g/cm^3, $\rho_{Al} = 2.7$ g/cm^3, $\rho_{Mg} = 1.8$ g/cm^3, respectively.
- **Bar diameter**: 16 mm vs. 12 mm.
- **Specimen material properties**: Quasi-static vs. dynamic. The material properties were taken from the characterisation experiments reported in the previous two sections. As a simplification, these properties were assumed to remain constant throughout the specimen's deformation process.
- **Incident pulse**: As measured in the experiment vs. idealised (i.e. perfectly linear).
- **Incident pulse rising slope**: Range of available rising slopes as determined in **Chapter 2.1.3**.

The FE model considered two evaluation approaches for investigating the convergence behaviour towards force equilibrium. The first, abbreviated as FE/GS, was based on a force measurement directly at the gauge volume's end faces (see **Figure 2.14(b)** for illustration). The second, abbreviated as FE/SHB, was based on obtaining the bars' stress history, as measured at the cross-sections where the strain gauges were located in the experiment, and calculating the specimen/bar interface forces via the classical SHB analysis. With respect to obtaining the specimen's strain-rate history, only a measurement based on the gauge volume's end faces was considered. The reader is referred to **Chapter 2.1.1** for a description of the classical SHB analysis' inadequacy for obtaining the sample's strain-rate history.

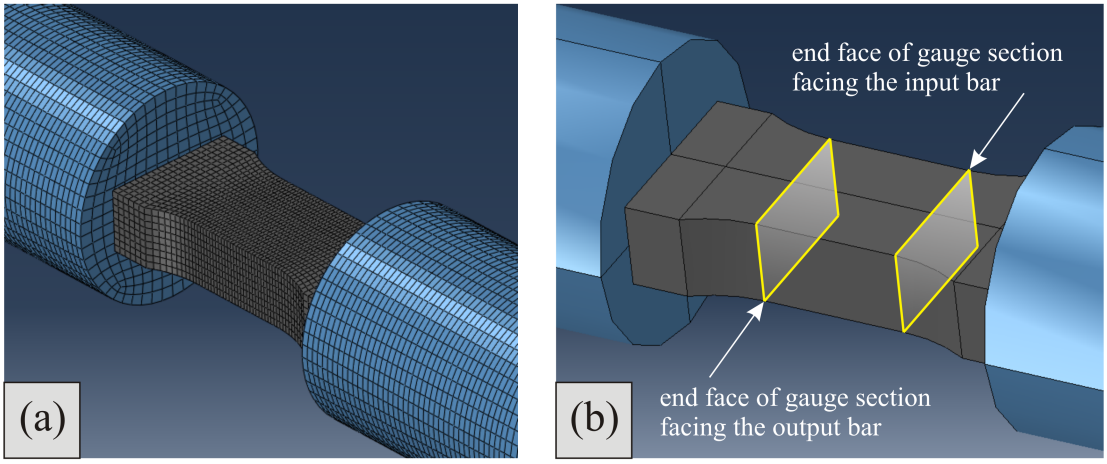


Figure 2.14: (a) FE model of the experimental setup; (b) end faces of the gauge volume for obtaining the sample's force disequilibrium (FE/GS model) and strain-rate history

Results and discussion: Convergence behaviour towards force equilibrium. A comparison between the results of the range of modelling approaches and the experimental data is presented in **Figure 2.15**. The reproducibility of the experimental data using the FE/SHB model in conjunction with the experimentally-determined incident pulse was satisfactory. In comparison to the FE/SHB approach, its FE/GS counterpart exhibited a considerably quicker convergence towards force equilibrium. This discrepancy became even more pronounced when employing an idealised incident pulse (see **Figure 2.16(a)** for a depiction of the experimentally-obtained and idealised incident pulses). Two conclusions were drawn from this: (i) The force disequilibrium history, as determined by the SHB analysis, overpredicts the actual disequilibrium along the specimen's gauge section. One reason for this discrepancy could be the differing distances across which the respective approaches measure the specimen's force convergence behaviour (FE/SHB: 22 mm, FE/GS: 8 mm). (ii) Fluctuations and disturbances in the incident pulse have a marked effect on the force disequilibrium history. This effect appeared to be particularly strong for the FE/GS model. The incident pulse's influence

on the force convergence behaviour could be traced back to its pronounced effect on the determined force associated with the input bar/specimen interface in case of the SHB analysis, and its corresponding counterpart, the force associated with the gauge volume's end face facing the input bar, in case of the FE/GS analysis. The graph of these force histories for employing the idealised incident pulse is shown in **Figure 2.16(b)**, and for the experimentally-obtained pulse in **Figure 2.16(c)**, respectively. A stark contrast between these force histories, depending on the nature of the incident pulse, is immediately noticeable. The corresponding forces at the opposite end of the specimen, however, did not show any such strong dependency on the incident pulse's fluctuations and disturbances, see **Figure 2.16(d)**.

In comparison to the FE/GS model, the analytical approach predicted a slightly higher level of the force disequilibrium history, see **Figure 2.15**. This, however, was to be expected, since the analytical model evaluated the force histories with respect to the bar/specimen interfaces, whereas the FE/GS analysis determined these force histories with respect to the sample's (shorter) gauge length.

A comparison between the results of the different modelling approaches employing the specimen's quasi-static and dynamic material properties is presented in **Figure 2.17**. This juxtaposition suggested that the consideration of the sample material's dynamic properties has no significant influence on the models' force disequilibrium history prediction.

The convergence behaviour towards force equilibrium is not a function of the steepness of the loading pulse's rising slope but merely depends on the magnitude of the imped-

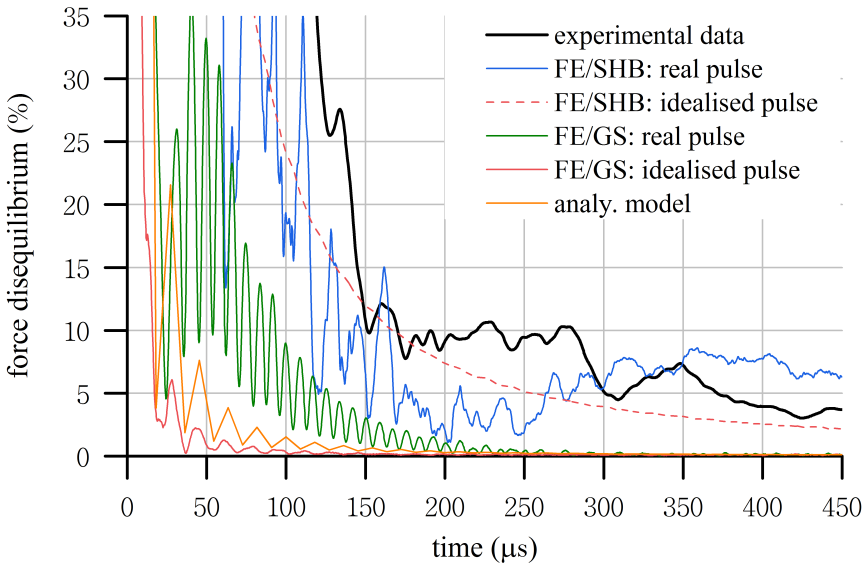


Figure 2.15: Convergence behaviour towards force equilibrium employing a range of modelling approaches

ance mismatch between the specimen and bars, see *Ravichandran et al. (1994)* [119].[10] The investigation of the influences on the achievability of SE therefore focused on the parameters determining the impedance mismatch, viz., the bar material (titanium, steel, aluminium, magnesium) and diameter (16 mm and 12 mm). The calculated force disequilibrium histories for the range of input parameter combinations employing the analytical model are presented in **Figure 2.18**. On the basis of these results it was concluded that employing a setup exhibiting a lower impedance mismatch between the specimen and bar system does not noticeably improve the time required to reach an acceptable state of force equilibrium. More specifically, the results indicated that the 10% mark of the force disequilibrium metric was reached by all investigated setups after around 36 µs. It is noteworthy that this duration is roughly in the order of magnitude of the time-to-failure of the specimen when subjected to an unshaped incident

[10] provided the incident pulse's qualitative shape is identical

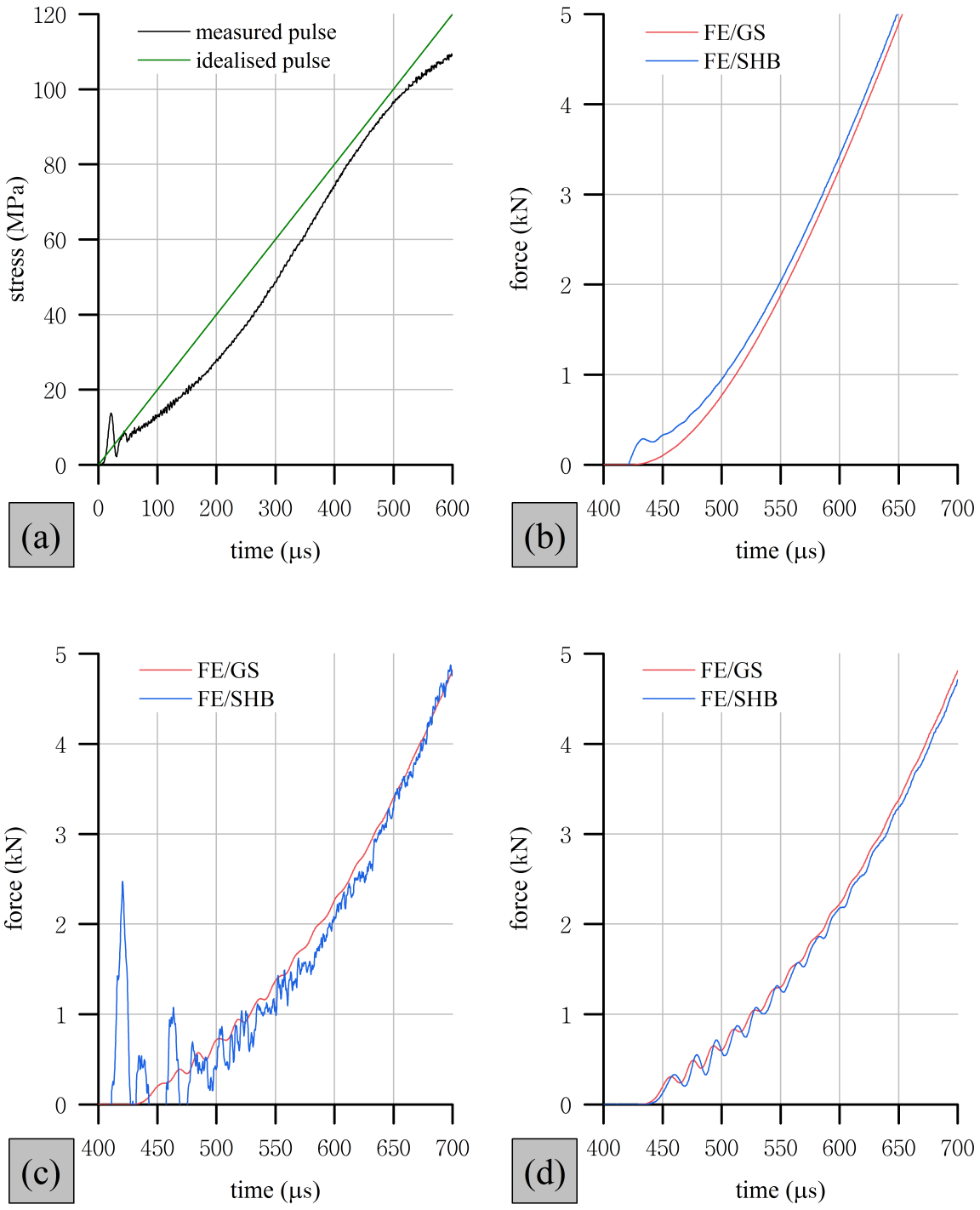


Figure 2.16: (a) experimentally-measured incident pulse and its idealisation; (b) force at the specimen's input bar end when subjecting the model to the idealised incident pulse; (c) force at the specimen's input bar end when subjecting the model to the experimentally-obtained incident pulse; (d) force at the specimen's output bar end when subjecting the model to the experimental incident pulse

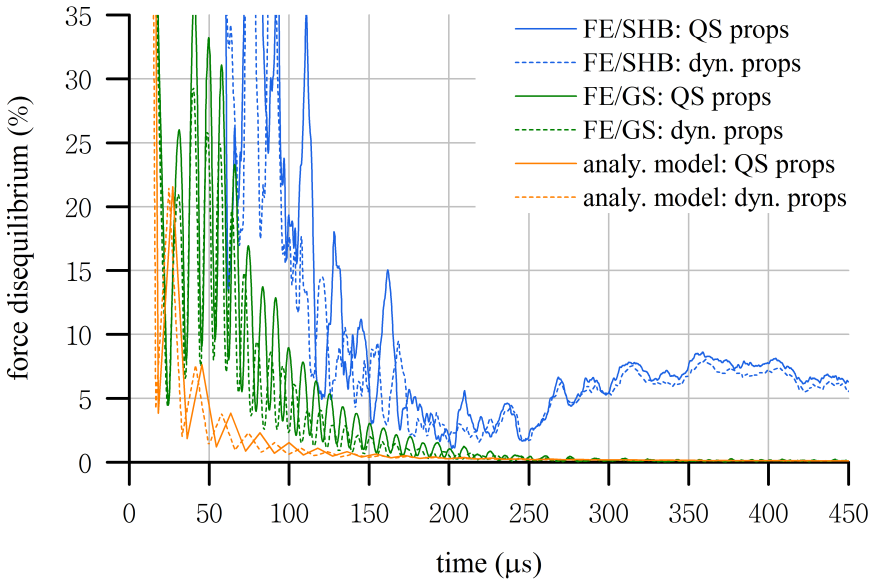


Figure 2.17: Convergence behaviour towards force equilibrium employing the specimen's quasi-static and dynamic material properties for each modelling approach

pulse: Ti: 48 µs, St: 65 µs, Al: 38 µs, Mg: 31 µs.[11] It was, therefore, concluded that the driving force limiting the establishment of SE in the specimen's gauge volume does not primarily arise from the magnitude of the impedance mismatch between the specimen and bar system but from the degree to which fluctuations and disturbances can be removed from the incident pulse.

Results and discussion: Strain-rate history. A comparison between the strain-rate histories based on the FE model, the analytical model, and the experimental data is presented in **Figure 2.19**. The following aspects are noteworthy:

- The reproducibility of the experimental data using the FE/GS model in conjunction with QS specimen properties and the experimentally-obtained incident pulse was satisfactory.
- The analytical model slightly underpredicted the specimen's strain-rate history.

[11] The calculation of the time-to-failure was based on the assumption of a rate-independent strain-to-failure (see experimental results in **Chapter 2.2.2** for justification). The durations given here are based on calculations for a ⌀16 mm bar system.

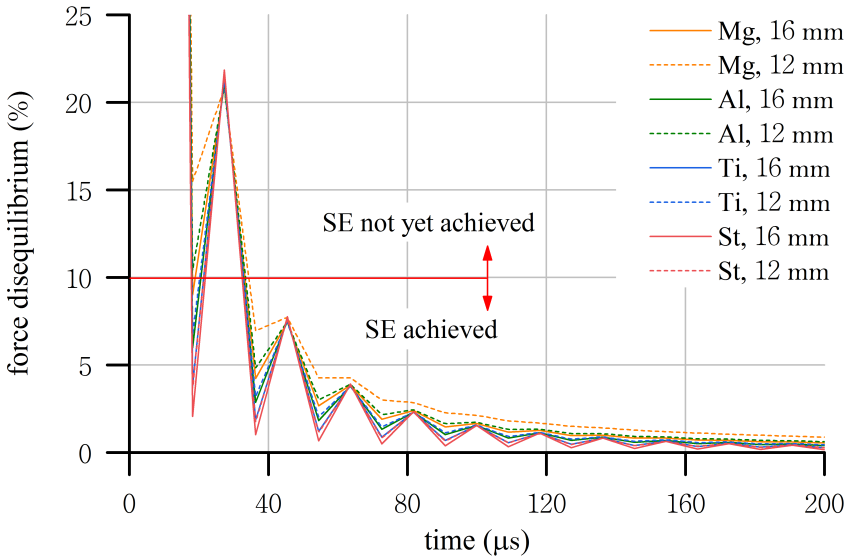


Figure 2.18: Convergence towards force equilibrium for a range of bar materials and diameters

This discrepancy between the analytical model and experimental data, however, was to be expected, as whilst the analytical model calculated the strain-rate between the specimen/bar interfaces, the experimental data was based on a DIC analysis of the deformation of the sample's (waisted) gauge section. As the strain-rate history prediction of the analytical model and the FE model were reasonably similar when run with the idealised incident pulse, it was concluded that part of the discrepancy between the analytical model and the experimental data was caused by the analytical model's inability to reflect the experimentally-obtained incident pulse.

- Taking into account the specimen's dynamic material properties resulted in a slight decrease in the predicted strain-rate history. The reader is, however, reminded that both modelling approaches exaggerated this influence due to the assumption of constancy in the sample material's properties over the course of its deformation.

- Existing fluctuations and disturbances in the incident pulse exhibited a marked influence on the FE model's strain-rate history prediction.

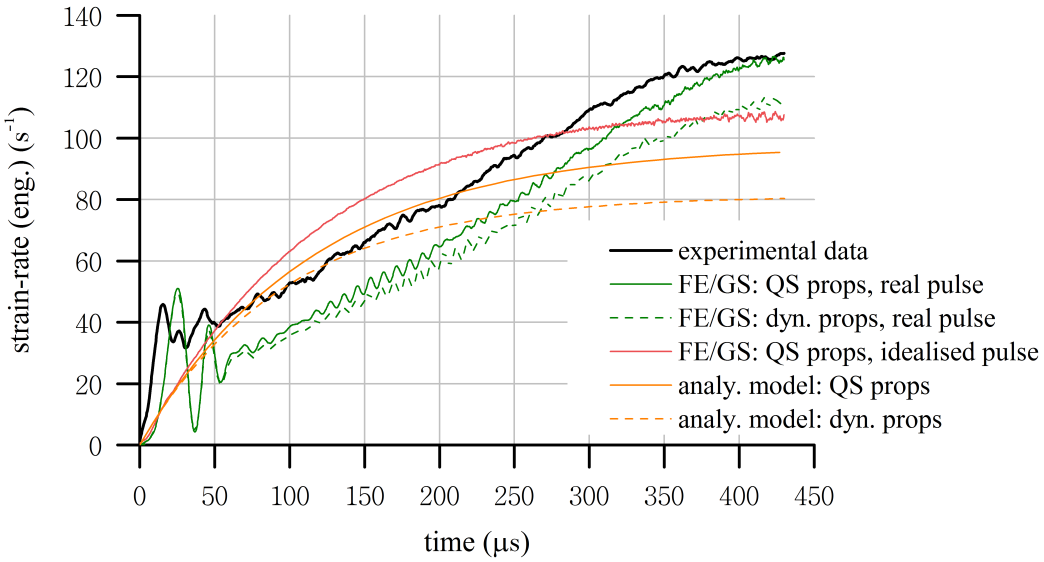


Figure 2.19: Evaluation of the specimen's strain-rate history for a range of modelling approaches

In order to investigate the limitations of the SHPB system employed for the dynamic *22-c* material characterisation tests in **Chapter 2.2.2**, the analytical model was successively run with the entire spectrum of generable incident pulses according to **Chapter 2.1.3**. The results, shown in **Figure 2.20**, indicated that this particular experimental setup limits the achievable specimen strain-rate, which satisfies CSR at failure, to approximately 200 s^{-1}.[12] Higher strain-rate values at failure can be attained only by abandoning the constraint of specimen deformation under a nearly constant strain-rate prior to failure (indicated by the dashed lines in **Figure 2.20**).

A comparison of the limiting strain-rate histories satisfying CSR for a range of commonly used bar materials and diameters is shown in **Figure 2.21**. On the basis of these results it can be concluded that the bar material and diameter have a profound

[12]Calculation of the time-to-failure for the individual curves was based on the assumption of a rate-independent strain-to-failure (see experimental results in **Chapter 2.2.2** for justification).

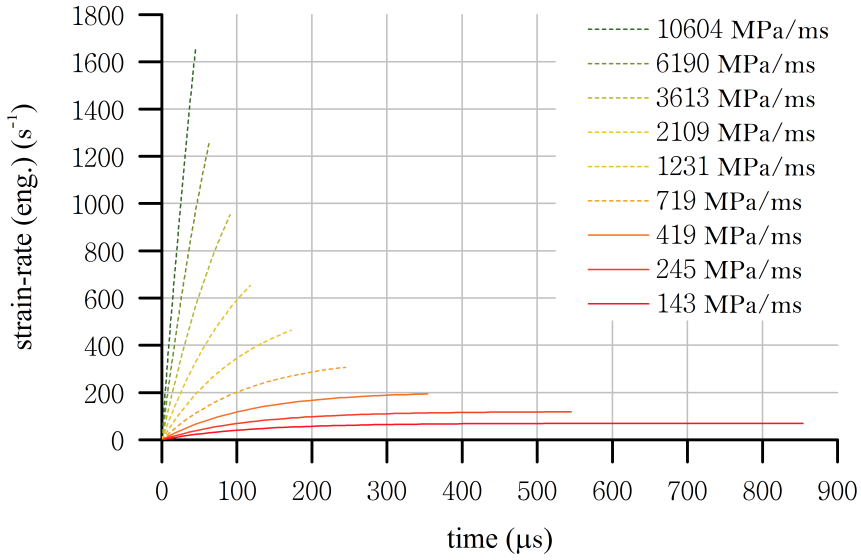


Figure 2.20: Evaluation of the specimen's strain-rate history for a ⌀16 mm titanium bar system and the range of available incident pulse rising slopes

influence on the highest achievable specimen strain-rate satisfying CSR at failure. In particular, strain-rates in the order of magnitude of several 100 s^{-1} require a careful choice of the employed SHPB system to be made.

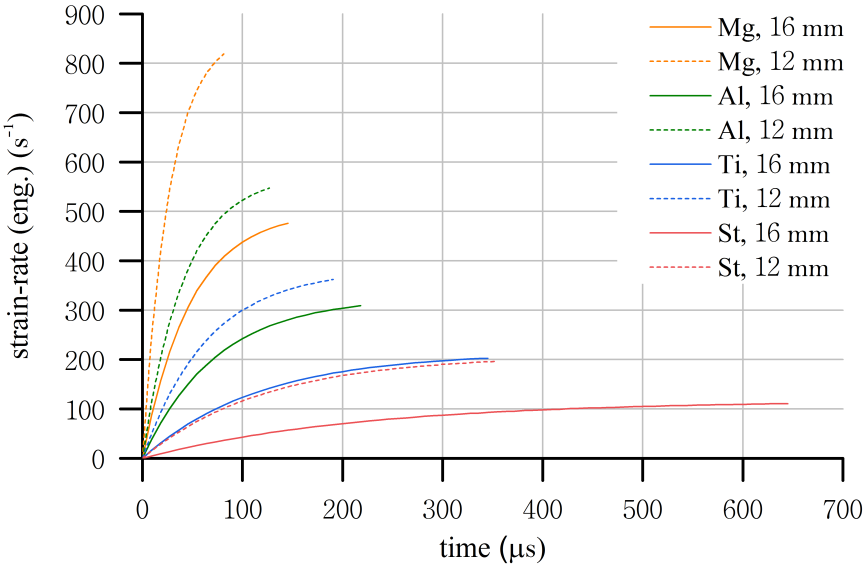


Figure 2.21: Limiting strain-rate histories for testing under CSR conditions for ⌀16 mm and ⌀12 mm bar systems made of Mg, Al, Ti, and St, respectively

Conclusions: Achievability of SE for *22-c* testing. The convergence behaviour towards force equilibrium, as measured at the end faces of the sample's gauge volume, was found to be much more benign than what the SHB analysis of the experimental data suggested. This implies that the evaluation of experimental data based on the latter method provides a very conservative estimate for the state of force disequilibrium along the specimen's gauge section. Furthermore, the force convergence behaviour towards a state of acceptable equilibrium was shown to: (i) depend strongly on fluctuations and disturbances in the incident pulse, and, (ii) barely depend on the choice of bar material and diameter. Lastly, for a reasonably linear and fluctuation-free incident pulse, all bar material and diameter combinations investigated in this study showed the establishment of SE long before reaching failure under a nearly constant deformation rate (compare the *time-to-failure* associated with the investigated bar systems in **Figure 2.20** to the time required to establish SE in **Figure 2.18**).

Conclusions: Achievability of CSR for *22-c* testing. Achieving specimen strain-rates in the order of magnitude of several hundred per second under the constraint of satisfying CSR prior to sample failure was shown to require a careful choice of bar material and diameter.

Conclusions: Model reflecting the force disequilibrium and strain-rate history. The FE-based modelling approach was found to satisfactorily capture the specimen's force convergence and strain-rate history. In particular, the possibility to directly obtain the force histories at the gauge section's end faces and the option to account for the experimentally-measured incident pulse were found to be critical features for the correct assessment of the experiment's validity. Employing the specimen material's quasi-static elastic properties for model input was shown to not influence the resultant

force convergence history in any substantial way, and to affect the sample's strain-rate history in only a mild way. The analytical approach employed in the present study was found to yield reasonably similar results to the FE model when the latter considered a perfectly linear incident pulse. Consequently, the analytical model can be considered as an efficient alternative to the FE-based modelling approach if a lower model fidelity is acceptable and a fluctuation-free range of loading pulses can be generated.

2.3 In-plane tensile testing transverse to the fibre direction (*22-t*)

This subchapter examines two aspects of the material characterisation of the *22-t* deformation mode. These are: (i) its characterisation under quasi-static and high-rate loading conditions, and, (ii) a simulation-based investigation into the influences of key SHB setup and testing parameters on the achievement of valid high-rate testing conditions.

2.3.1 Material characterisation across two strain-rate regimes

Material, specimen geometry, manufacturing, and preparation. The specimens were produced from the same *IM7/8552* panel that was used to manufacture the *22-c* specimens employed in the context of **Chapter 2.2.1**. **Figure 2.22** depicts the specimen's geometry and illustrates the specimen with its mounted 'end sleeves'. The threaded end sleeves were made of mild steel and adhesively bonded to the specimen using *Scotch-Weld DP 490*. In order to facilitate a DIC-based analysis of the specimens'

deformation and failure behaviour, a black speckle pattern on a white background was applied using a paintbrush.

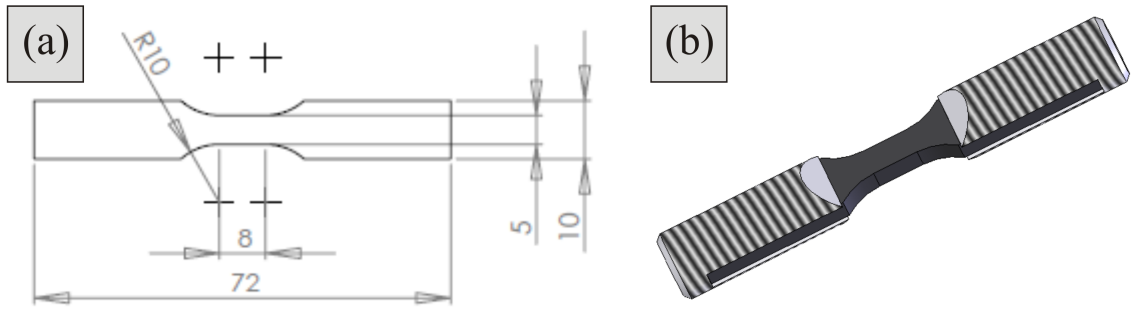


Figure 2.22: (a) specimen geometry for *22-t* testing (dimensions in mm); (b) CAD model of a *22-t* specimen with its mounted end sleeves

Experimental setup, DAQ, and data reduction. The experimental setup and data acquisition system for testing under quasi-static loading were identical to the ones described in **Chapter 2.2.1** for *22-c* testing. Dynamic testing was carried out by employing the SHTB system outlined in **Chapter 2.1.3** in conjunction with a high-speed camera (*Specialised Imaging*, model: *Kirana*). The loading pulse was generated using a projectile velocity of 4.8 m/s together with a 6 mm thick neoprene pulse shaper. Strain (and thus strain-rate) was measured optically. Strength was obtained according to $Y_t = \frac{F_{max}}{A_0}$; the determination of the modulus will be discussed below. Ten specimens were tested under quasi-static loading, three were tested dynamically.

Results and discussion. The generated sets of stress-strain curves for testing under the two loading rate regimes are presented in **Figure 2.23**. The curves for both strain-rate regimes showed a linear behaviour up to failure, which simplified the modulus determination in that the segment of the stress-strain curve used for obtaining E_{22t} did not have to be identical across both loading rate regimes. Consequently, E_{22t}^{QS} was obtained as the linear fit to a range of engineering strain values between 0.001 and

0.003, whereas E_{22t}^{dyn} was determined based on the linear fit to a range of engineering strain values between $\epsilon_I = \epsilon_{ult} - 0.001$ and $\epsilon_{II} = \epsilon_{ult}$. Obtaining the dynamic modulus based on the segment of the stress-strain curve leading up to specimen failure offered the advantage of minimising the influence of any remaining force disequilibrium on the determined high-rate modulus, as well as, being able to associate the thus obtained modulus with a comparatively higher strain-rate value (see **Figure 2.24**).

From the perspective of assessing the quality of the obtained modulus and strength under high-rate loading, it must be noted that the determination of both material properties was associated with a specimen deformation under a non-constant strain-rate, see **Figure 2.24**. This implies that the obtained values for Y_t^{dyn} and E_{22t}^{dyn} should be considered as having a degree of uncertainty associated with them. A detailed investigation into the influences on achieving valid high-rate testing conditions for the characterisation of the *22-t* deformation mode will be undertaken in the subsequent section. Against the background of the inability to establish CSR conditions at failure for the high-rate tests carried out in the present section, a special emphasis will be placed on examining the *general* feasibility of reaching a state of CSR at failure for dynamic *22-t* testing.

A summary of the determined material properties for the *22-t* material characterisation is provided in **Table 2.3**. The properties determined under quasi-static loading conditions are nearly identical to the corresponding values documented in literature (strength: [19, 63, 80, 96]; modulus: [19, 80, 96, 124]). The material's ultimate strength Y_t experienced an increase of 38%, and the modulus of 28%, with respect to the data obtained under quasi-static loading. The level of experimental scatter associated with

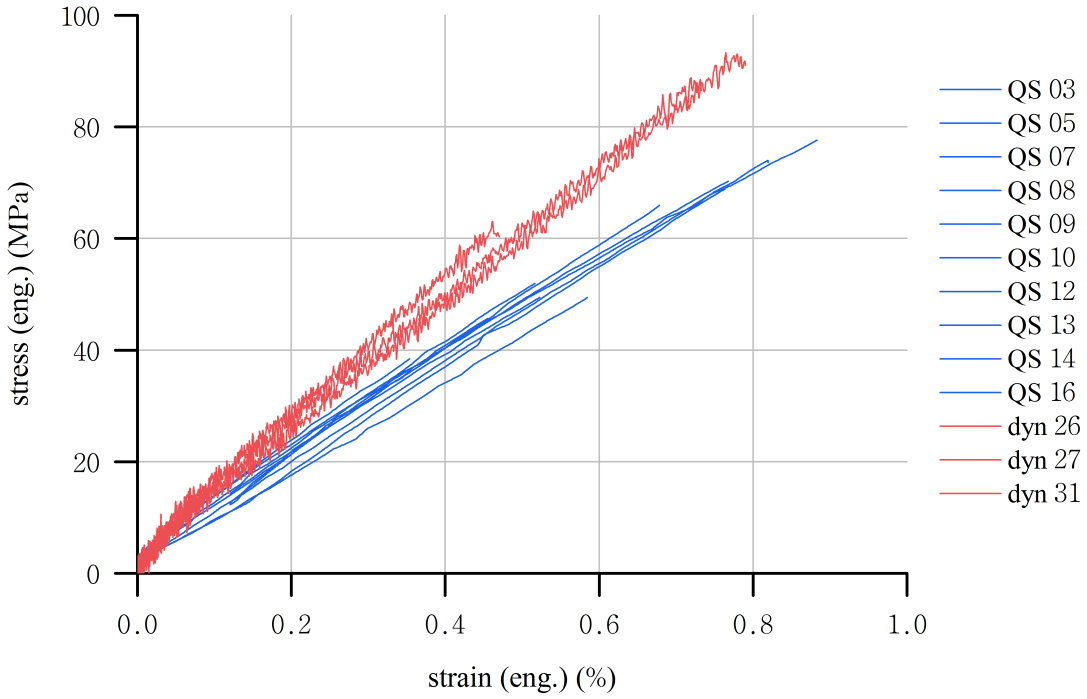


Figure 2.23: Stress-strain curves for *22-t* testing under quasi-static and high-rate loading conditions

Y_t was high, whereas for E_{22t}, was moderate. The gauge section's strain-rate at the point of reaching the material's ultimate strength Y_t^{dyn} was measured to be 28 s^{-1}. The strain-rate associated with E_{22t}^{dyn} was determined to be 27 s^{-1}.

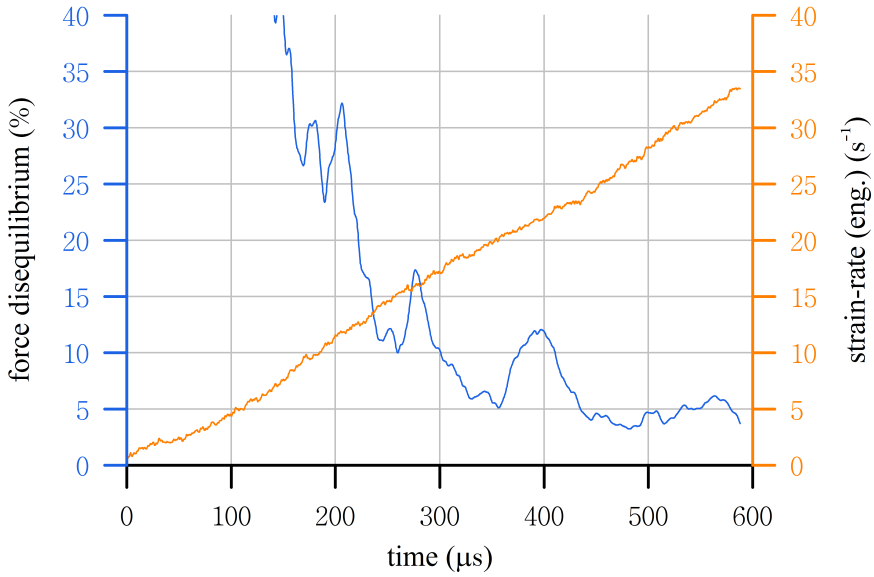


Figure 2.24: Assessment of the validity of the dynamic *22-t* material characterisation tests

Table 2.3: Obtained material properties for *22-t* testing under quasi-static and high-rate loading conditions

			quasi-static loading	high-rate loading
ultimate strength Y_t	mean	MPa	59	82
	SD	MPa	14	16
	CV	%	23.1	20.1
modulus E_{22t}	mean	MPa	9.4	12.0
	SD	MPa	0.6	0.5
	CV	%	5.9	3.9
strain-to-failure ϵ_{ult}	mean	%	0.62	0.66
	SD	%	0.18	0.17
	CV	%	28.7	26.1
strain-rate: Y_t	mean	s^{-1}	0.00024	28
strain-rate: E_{22t}				27

2.3.2 Influences on the achievement of valid high-rate testing conditions

Introduction. The aim of this modelling-based study was to investigate a range of split-Hopkinson bar setup and testing parameters for their effect on achieving valid high-rate testing conditions for the characterisation of the *22-t* deformation mode. The validity of testing conditions is understood here as the establishment of SE and CSR prior to specimen failure. The reader is referred to **Chapter 2.1.1** for a detailed description of these two conditions. The study presented here took the dynamic material characterisation data generated in **Chapter 2.3.1** as a reference point for the modelling process. The following aspects of high-rate *22-t* testing were of particular interest:

- *To what degree does the force disequilibrium history determined via the SHB analysis represent the force disequilibrium history measured directly at the end faces of the specimen's gauge section?*
- *What is the influence of the bar and end sleeve material, and the incident pulse's rising slope on the achievability of valid testing conditions? In particular, under what circumstances is it possible to achieve specimen failure in a deformation state satisfying CSR?*
- *Which parameters does a model of the SHB experiment have to consider in order to achieve a satisfactory reflection of the specimen's force disequilibrium and strain-rate history?*

In contrast to the modelling study for dynamic *22-c* testing, the corresponding study for *22-t* testing did not consider an analytical modelling approach due to the exper-

imental setup's higher level of complexity, which entailed a multitude of impedance jumps. This is depicted in **Figure 2.25**, which provides an illustration of the series of impedance jumps experienced by a stress wave traversing through the specimen for *22-t* testing.[13] This 'impedance profile' is in marked contrast to dynamic *22-c* testing, which is essentially governed by its two impedance jumps across the specimen/bar interfaces. Consequently, the modelling study for dynamic *22-t* testing relied on an FE representation of the experimental setup.

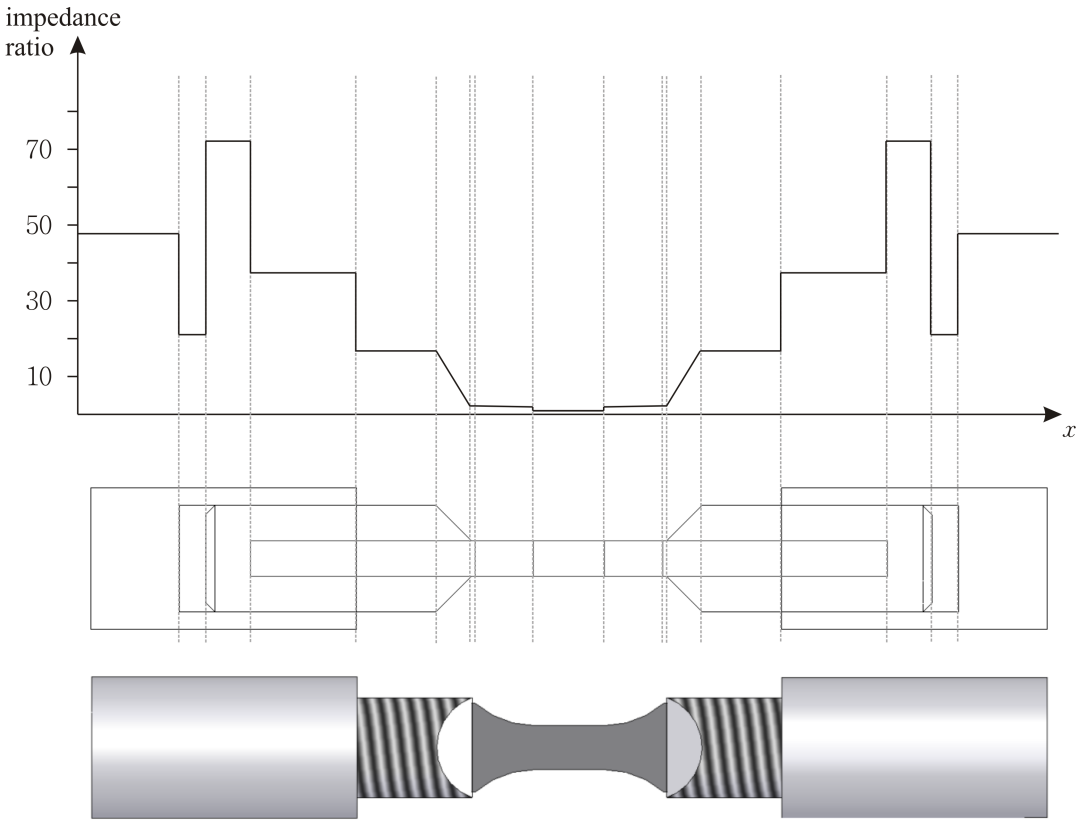


Figure 2.25: 'Impedance profile' as encountered by a planar stress wave traversing through a specimen for dynamic *22-t* testing

[13]The stated *impedance ratio* refers to the acoustic impedance of a particular cross-section with respect to the specimen's gauge section. The setup's geometry and material for this calculation were based on the dynamic *22-t* material characterisation tests described in **Chapter 2.3.1**.

Outline of the FE model. The finite element model reflected the SHB setup from the input bar's cross-section, where the first strain-gauge station was located, up until the end of the output bar, see **Figure 2.13** in **Chapter 2.2.3**. The geometric representation of the input bar, specimen, and output bar was meshed employing a *structured mesh* consisting of 3D reduced integration continuum elements (C3D8R) with a mesh size of roughly 0.3 mm in the specimen's gauge volume, and 1 mm for the bulk of the bars, with a continuous transition between these two mesh densities. The end sleeves' threads, as well as the adhesive layer between the specimen and end sleeves, were not reflected explicitly. Instead, the bars and sleeves, and the sleeves and specimen shared common nodes along their respective interfaces. A depiction of the central section of the FE model for *22-t* testing is provided in **Figure 2.26(a)**.

Model input parameters and evaluation approaches. The modelling study considered the following range of input parameters:

- **Bar and end sleeve material**: Titanium vs. steel vs. aluminium. The following material properties were used: $E_{Ti} = 114$ GPa, $E_{St} = 205$ GPa, $E_{Al} = 70$ GPa, and $\rho_{Ti} = 4.4$ g/cm^3, $\rho_{St} = 7.9$ g/cm^3, $\rho_{Al} = 2.7$ g/cm^3, respectively.
- **Specimen material properties**: Quasi-static vs. dynamic. The material properties were taken from the characterisation experiments carried out in the previous section. As a simplification, these properties were assumed to remain constant throughout the specimen's deformation process.
- **Incident pulse**: As measured in the experiment vs. idealised (i.e. perfectly linear).
- **Incident pulse rising slope**: Range of available rising slopes as determined in

Chapter 2.1.3.

The evaluation approaches were identical to the ones employed in the corresponding modelling study for *22-c* testing, see **Chapter 2.2.3**.

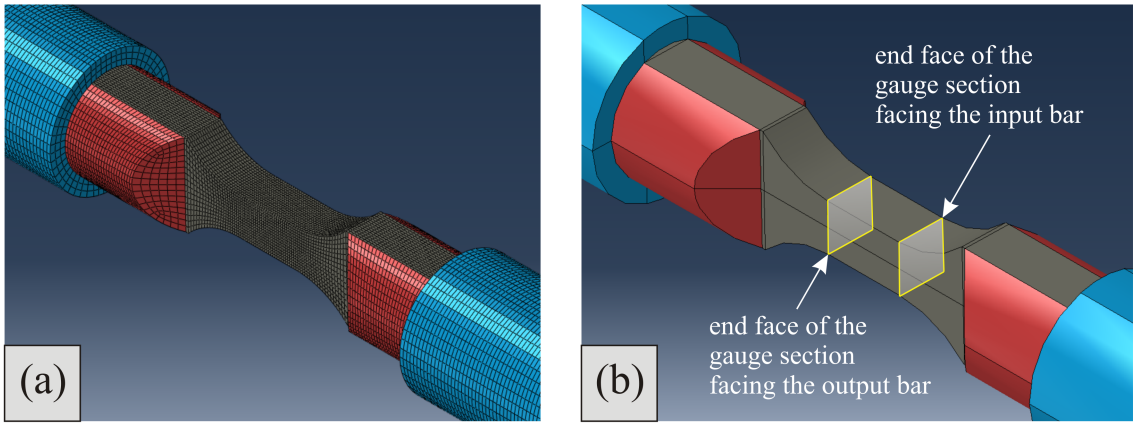


Figure 2.26: (a) FE model of the experimental setup; (b) end faces of the gauge volume for obtaining the sample's force disequilibrium (FE/GS model) and strain-rate history

Results and discussion: Convergence behaviour towards force equilibrium. A comparison between the range of employed modelling approaches and the experimental data is presented in **Figure 2.27**. The following aspects are noteworthy:

- The FE/SHB model did not capture the experimentally-generated data sufficiently well. It is assumed that this discrepancy is the result of the FE model not accounting for the additional system compliance caused by the adhesive layer between the specimen and end sleeves. In order to achieve a more satisfactory predictive capability of the model, it is recommended to insert a cohesive zone in this particular region.
- In comparison to the FE/SHB model, the FE/GS approach showed a much quicker convergence towards force equilibrium. One reason for this overprediction of disequilibrium by the SHB analysis may be the differing distances across which

the respective approaches determined the sample's force convergence behaviour (FE/SHB: 49 mm, FE/GS: 8 mm).

- Considering the specimen material's dynamic properties did not substantially affect the obtained force convergence behaviour.
- Although the incident pulse rising slopes for the experimentally-obtained and idealised pulses were nearly identical, see **Figure 2.28(a)**, minute fluctuations and disturbances in the former exerted a considerable influence on the force disequilibrium history. The root cause of this phenomenon was identical to the one outlined in the context of the modelling study for *22-c* testing, see **Chapter 2.2.3**. The corresponding plots of the forces acting on the specimen's input bar end for the FE/SHB and FE/GS model are provided in **Figure 2.28(b)** for the idealised loading pulse, and in **Figure 2.28(c)** for the experimentally-obtained pulse. Analogous to the modelling study of *22-c* testing, the forces acting on the specimen's output bar end did not show any such sensitivity to fluctuations and disturbances in the incident pulse, see **Figure 2.28(d)**.

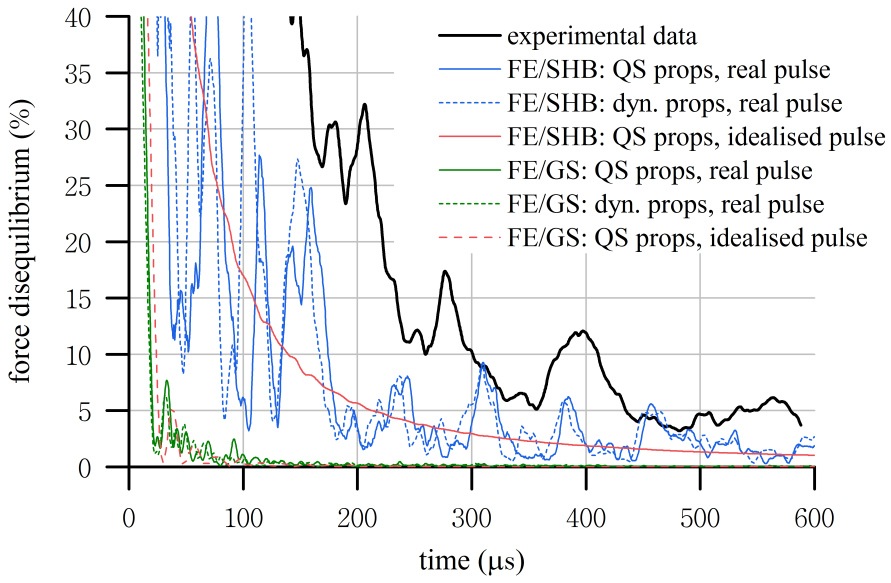


Figure 2.27: Evaluation of the convergence behaviour towards force equilibrium employing a range of modelling approaches

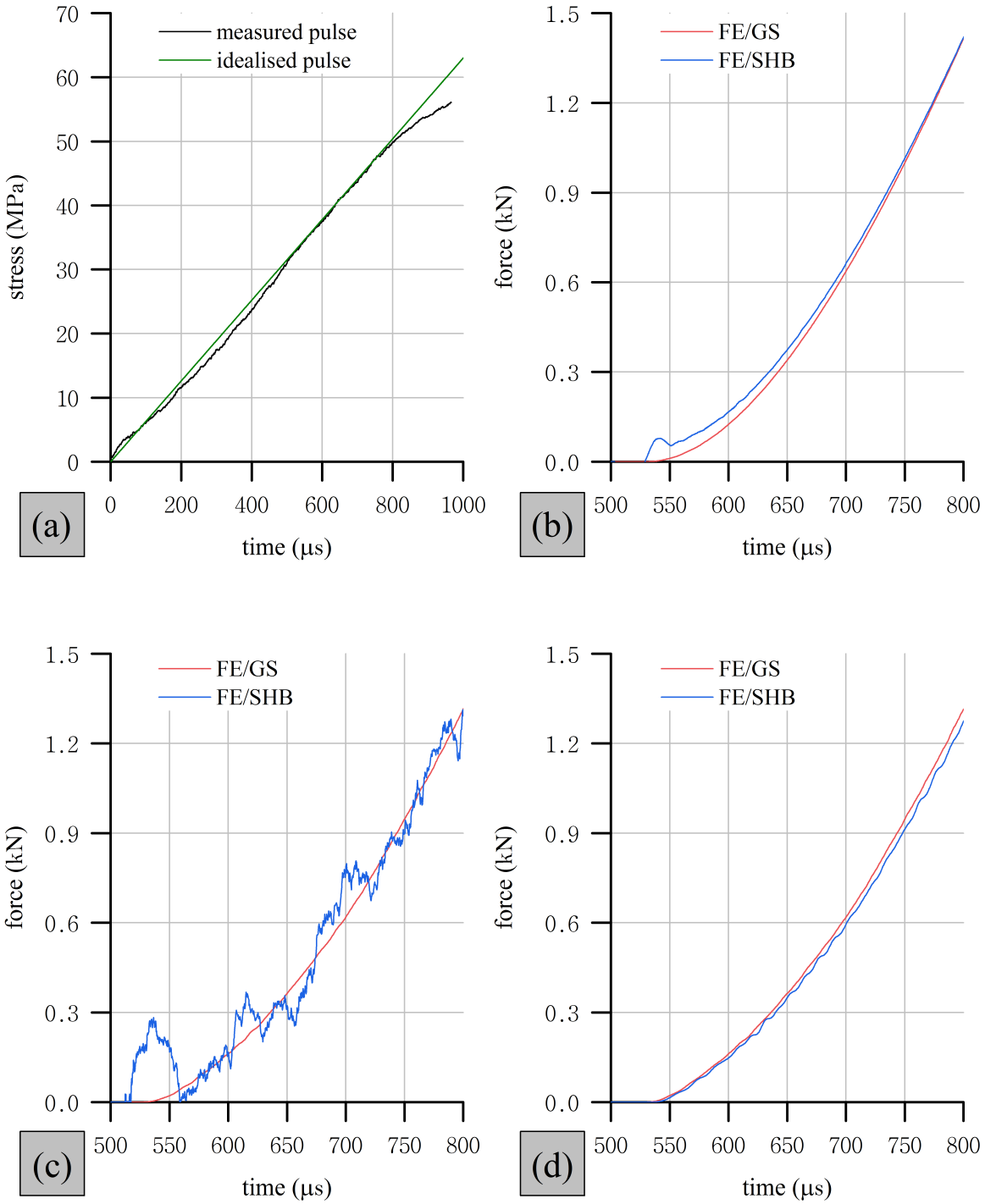


Figure 2.28: (a) experimentally-obtained and idealised incident pulse rising slopes; (b) force at the specimen's input bar end when subjecting the model to the idealised incident pulse; (c) force at the specimen's input bar end when subjecting the model to the experimentally-obtained incident pulse; (d) force at the specimen's output bar end when subjecting the model to the experimentally-obtained incident pulse

As was mentioned in the context of the modelling study for *22-c* testing, force convergence does not depend on the steepness of the incident pulse's slope. The SE achievability study for *22-t* testing, therefore, focused on the different material combinations for the bars and sleeves. The results generated for employing the FE/GS model in conjunction with the idealised loading pulse indicate that the gauge section's force convergence behaviour does not substantially depend on the choice of bar and sleeve material, see **Figure 2.29**. In particular, swapping the mild steel end sleeves used in the experiments with ones made of titanium did not result in any noticeable improvement. Moreover, the results indicate that the 10% mark of the force disequilibrium metric was reached by all investigated setups after around 30 µs. It is noteworthy that this duration is roughly in the order of magnitude of the time-to-failure of the specimen when subjected to an unshaped incident pulse: Ti: 28 µs, St: 36 µs, Al: 26 µs.[14] It was, therefore, concluded that the convergence towards a state of force equilibrium for the high-rate material characterisation of *22-t* is not as much of a concern as the very low strain-to-failure of this deformation mode might initially suggest. The reader is reminded, however, that fluctuations and disturbances in the incident pulse may delay the establishment of a state of SE in experiments compared to the results generated here based on simulations employing an idealised incident pulse.

[14]Calculation of the time-to-failure was based on the assumption of a rate-independent strain-to-failure (see experimental results in **Chapter 2.3.1** for justification).

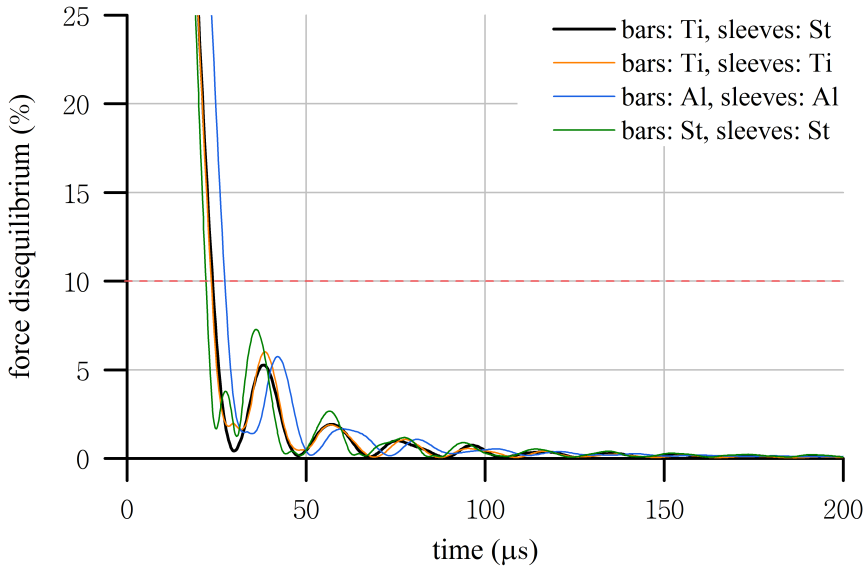


Figure 2.29: Convergence towards force equilibrium for a range of bar and sleeve material combinations

Results and discussion: Strain-rate history. A comparison between the generated strain-rate histories employing a range of sets of input parameters for the FE model and the experimental data is presented in **Figure 2.30**. The following aspects of this juxtaposition are noteworthy:

- The model in its current configuration did not capture the experimentally-generated data sufficiently well. The higher strain-rate level predicted by the model was likely the result of not accounting for the additional system compliance caused by the adhesive layer between the specimen and end sleeves. It is recommended to insert a cohesive zone in this particular region in order to achieve a more satisfactory predictive capability of the model.[15]
- Taking into account the specimen's dynamic material properties resulted in a slight decrease in the predicted strain-rate history. The reader is, however, re-

[15]For all remaining sets of simulations in this study, a calibration factor was applied to the models' strain-rate output in order to account for the effect of the additional system compliance.

minded that **Figure 2.30** exaggerates this influence due the assumption of constancy of the sample material's properties over the course of its deformation.

- Bearing in mind the nearly perfect linearity of the experimentally-obtained incident pulse, see **Figure 2.16(a)**, considering the said pulse for model input resulted in a strain-rate history featuring a surprising amount of fluctuations. It can thus be inferred that even minute fluctuations and disturbances in the incident pulse have a non-negligible influence on the model's strain-rate history prediction. The absence of any noteworthy fluctuations in the experimental data, then, may be attributed to the adhesive's ability to dampen such minor loading pulse disturbances.

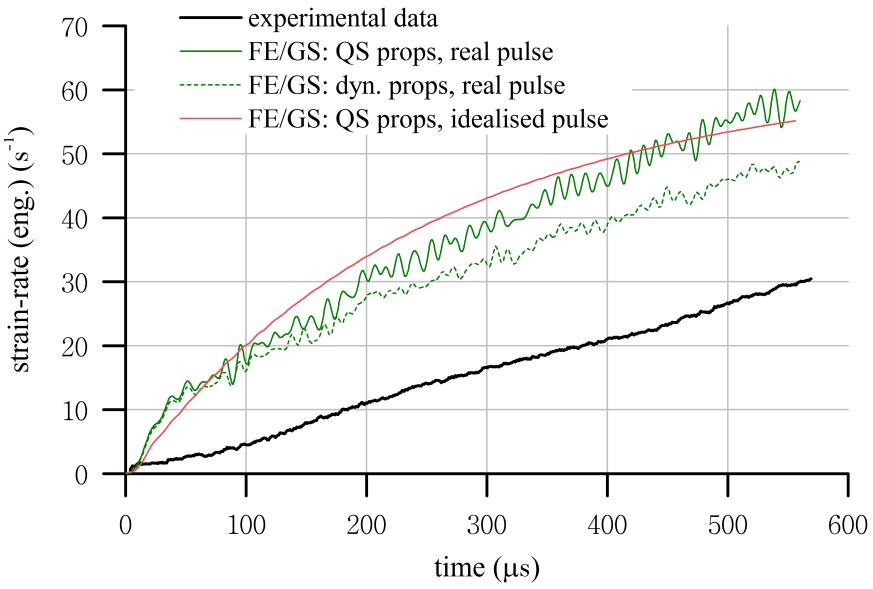


Figure 2.30: Evaluation of the specimen's strain-rate history for a range of model input parameter sets

A comparison between the strain-rate histories for a range of commonly employed bar and end sleeve materials is presented in **Figure 2.31**.[16] The generated model results

[16]The corresponding simulations were based on the experimentally-determined incident pulse and the specimen's quasi-static material properties.

suggest that the choice of the bar material only has a minor effect on the specimen's strain-rate history. In particular, swapping the end sleeves made of mild steel, as employed in the experiments, with ones made of titanium has practically no effect on the strain-rate history.

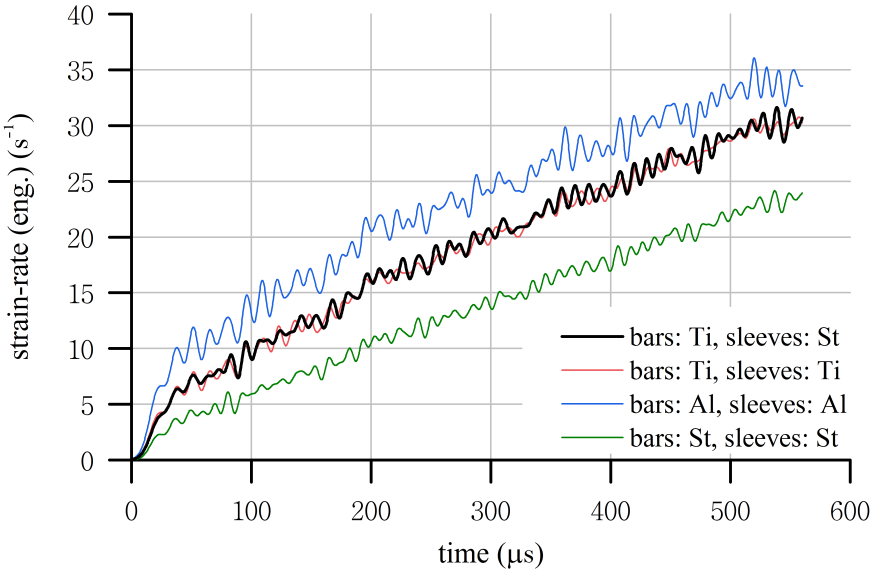


Figure 2.31: Evaluation of the specimen's strain-rate history for a range of bar and end sleeve material combinations

The general feasibility of achieving a specimen deformation state satisfying CSR prior to specimen failure was investigated by successively subjecting the FE model of the SHTB system, comprised of aluminium bars and sleeves, to the full range of available incident pulse rising slopes (see **Chapter 2.1.3**). The choice for an aluminium-based system over the other available material options was motivated by its property to minimise the impedance mismatch between the bars, sleeves, and specimen, thus resulting in the SHB system that should be able to establish a specimen deformation under CSR the quickest. The resulting plot for this set of simulations, presented in **Figure 2.32**, shows that none of the strain-rate histories, even for the lowest available incident pulse

rising slope, reached a state of CSR prior to sample failure.[17] Considering that this CSR-achievability study was based on the SHB system resulting in the least realistic impedance mismatch between the bars, sleeves, and specimen, and that high-rate testing commonly aims at strain-rates at failure well above 100 s^{-1}, it was thus concluded that the low strain-to-failure of the *22-t* deformation mode renders the establishment of CSR prior to specimen failure impossible.

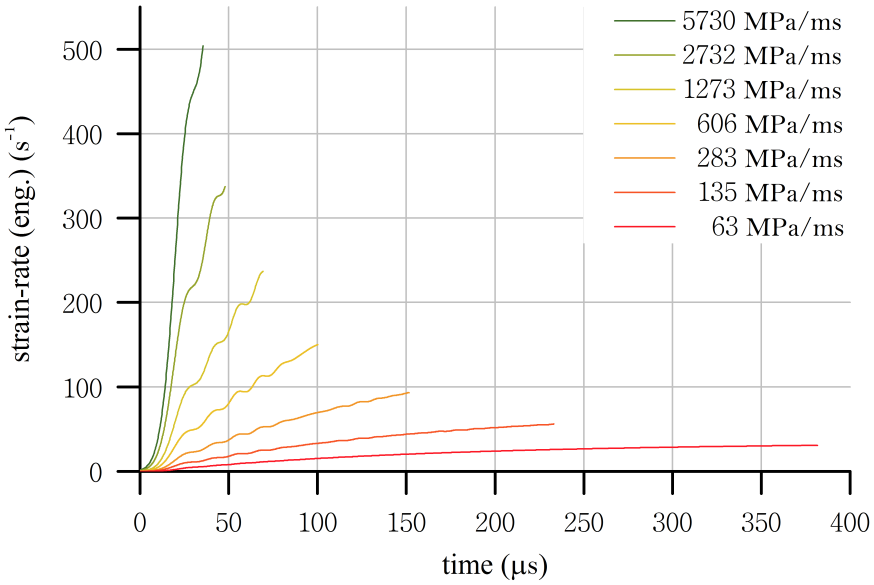


Figure 2.32: Evaluation of the specimen's strain-rate history for an aluminium bar/sleeve system and the range of incident pulse rising slopes as determined in **Chapter 2.1.3**

Conclusions: Achievability of SE for *22-t* testing. The convergence behaviour towards force equilibrium, as measured at the end faces of the sample's gauge volume, was found to be much more benign than what the SHB analysis of the experimental data suggested. This implies that the evaluation of experimental data based on the latter method provides a very conservative estimate of the state of force disequilibrium along the specimen's gauge section. Moreover, the modelling study indicated that

[17] Calculation of the time-to-failure for the individual curves was based on the assumption of a rate-independent strain-to-failure (see experimental results in **Chapter 2.3.1** for justification).

achieving a state of SE for the high-rate material characterisation of *22-t* is not as much of a concern as the very low strain-to-failure of this deformation mode might initially suggest. While employing different materials for the bar system and/or end sleeves was found to barely affect the force disequilibrium history, fluctuations and disturbances in the incident pulse were shown to exert a pronounced influence.

Conclusions: Achievability of CSR for *22-t* testing. This study demonstrated that it is not possible to achieve a state of specimen deformation satisfying CSR prior to failure, even when employing an experimental setup that minimises the impedance mismatches between the bars, end sleeves, and specimen, and subjecting the sample to a very low incident pulse rising slope. This, in turn, implies that the experimentally-obtained value for Y_t^{dyn} is unavoidably subject to a degree of uncertainty in terms of its association with a definite strain-rate value.

Conclusions: Model reflecting the force disequilibrium and strain-rate history. The FE model, in its current configuration, was unable to capture the specimen's force disequilibrium and strain-rate history sufficiently well. It is, therefore, recommended to extend the model by adding a cohesive zone between the specimen and end sleeves in order to account for the adhesive layer's considerable compliance. Accounting for the specimen material's dynamic elastic properties was shown to not influence the resultant force disequilibrium history in a substantial way, and to only mildly affect the sample's strain-rate history.

2.4 Form-fit specimen design for dynamic out-of-plane tensile testing (*33-t*)

This subchapter develops a form-fit design for *33-t* testing to overcome the issue of adhesive bond failure faced when using a conventional *adhesively-bonded waisted block* specimen design in conjunction with a composite material that features a comparatively inert matrix material. Experiments are described which aimed at demonstrating: (i) the comparability of results generated using a *form-fit* versus an *adhesively-bonded waisted block* design, and (ii) the form-fit design's suitability for high-rate testing.

2.4.1 Background and motivation

A major weakness of laminated composites is the comparatively low level of their mechanical out-of-plane properties, particularly if no through-thickness reinforcement is present. The increasing utilisation of composite materials for high-tech applications means that thicker laminates, more complicated geometries, as well as more complex load cases have become more and more commonplace [38, 65, 106]. This development, in turn, entails an increasing importance of accounting for the composite's out-of-plane properties for the modelling process, and, by extension, for the material characterisation tests underlying the models' calibration. Of these out-of-plane properties, this subchapter focuses on the tensile properties, particularly under dynamic loading.

The *33-t* properties of unidirectionally-reinforced composites are roughly similar to their in-plane counterpart (*22-t*). However, differences exist, particularly in the form of a slightly lower out-of-plane tensile strength in the case of *33-t* (e.g. [65, 76]). Ex-

haustive material characterisation programmes, therefore, tend to cover this deformation mode separately by employing a dedicated experiment.

Three specimen design types for determining the *33-t* properties can be found in literature: (i) a *waisted block* or *cylinder* type (subjected to axial loading) (references to follow), (ii) a *curved beam* type (subjected to a bending load), e.g. [26, 71], and, (iii) a *cross-specimen* type (subjected to axial loading), e.g. [50, 133]. Although dynamic testing has also been carried out employing specimen types (ii) [71] and (iii) [50], using an *adhesively-bonded waisted block* (e.g. [27, 75]) or *cylinder* (e.g. [101, 103, 104]) design is by far the most commonly employed approach for determining the high-rate out-of-plane tensile properties.

In the context of the present study a carbon-fibre/thermoplastic matrix composite[18] was characterised by employing an *adhesively-bonded waisted block* specimen design. Testing, however, revealed the adhesive bond to not be strong enough to ensure reproducible load introduction, which caused a substantial number of specimens to fail due to detachment of the adhesive from the specimen. This issue, which was already very pronounced when testing under quasi-static loading, proved to be even more salient for dynamic testing. Despite attempts to improve the adhesive bond through the use of alternate adhesives, no viable substitute was found. As a consequence, a form-fit design for *33-t* testing was investigated in order to provide a means to facilitate a reproducible load introduction for composite materials featuring a comparatively inert matrix material. Special emphasis was placed on assessing this design's suitability for testing under high-rate loading conditions using an SHB setup. Although approaches

[18]The exact composition of the composite cannot be given here for proprietary reasons. Consequently, the experimental results presented in **Chapter 2.4.3** will be given in normalised form.

to employing a form-fit design for *33-t* testing under quasi-static loading have been made in the past [60, 65, 141], no such study for high-rate testing exists yet.

2.4.2 Form-fit design

The form-fit specimen design chosen for the present study with its mounted grips is presented in **Figure 2.33(a)**. The specimen's dimensions will be provided in the next section. As shown in **Figure 2.33(b)**, the mounting process of the grips used a dedicated fixture in order to prevent any misalignment between the longitudinal axes of the specimen and grips. This, in turn, ensured the absence of spurious bending moments during testing which could have otherwise caused premature specimen failure. The axial alignment was retained over the course of the specimens' handling by a set screw located in the body of each grip. The grips were made of stainless steel.

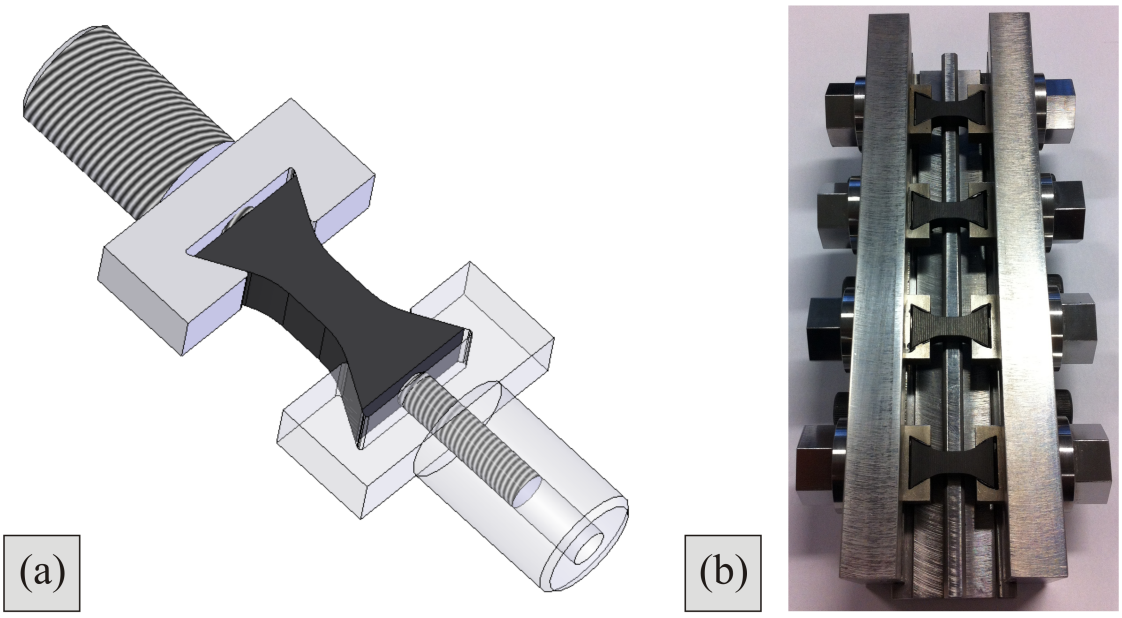


Figure 2.33: (a) form-fit specimen design with mounted grips; (b) alignment fixture used for the assembly process of the specimen and grips

2.4.3 Experimental setup, results and discussion

Comparison between the *adhesively-bonded waisted block* and form-fit design. The geometries of the *adhesively-bonded waisted block* and form-fit specimen employed in the present study are presented in **Figure 2.34**. The gauge length and cross-section of both specimen designs were kept identical to ensure comparability.

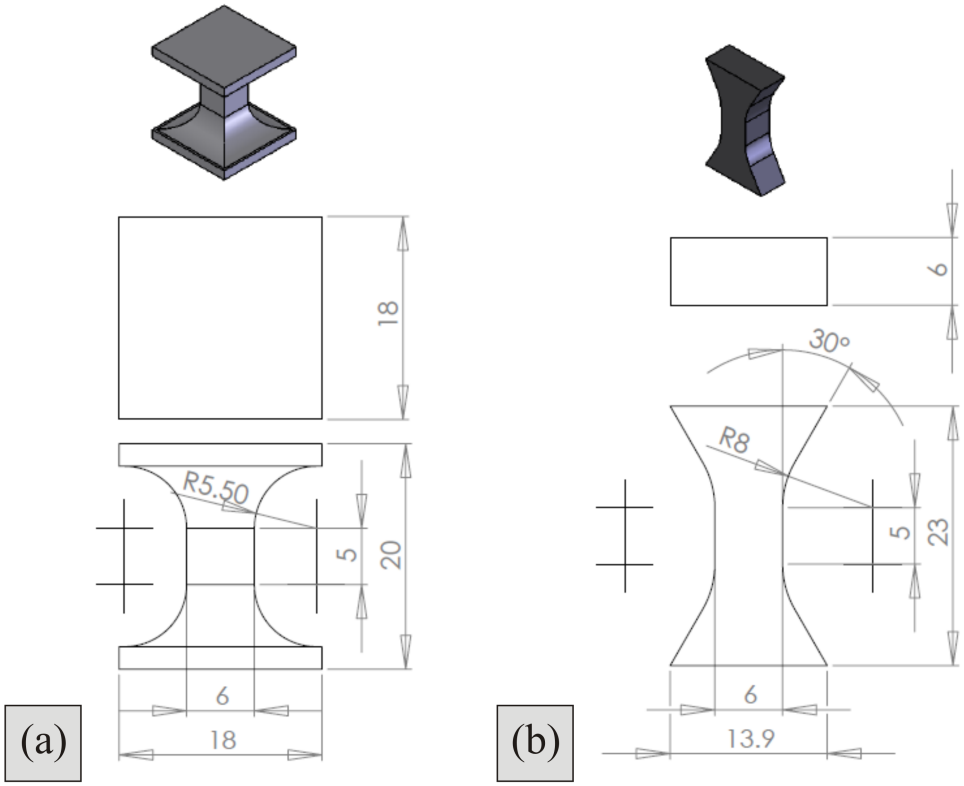


Figure 2.34: (a) geometry of the *adhesively-bonded waisted block* specimen; (b) geometry of the form-fit specimen (dimensions in mm)

Eight specimens of each design were tested under quasi-static loading on a *Zwick/Roell Z*250 screw-driven testing machine.[19] Load application was displacement-controlled at a rate of 0.008 mm/s. Force was measured via the testing machine's 20 kN load cell, displacement (and thus strain) was measured optically.

[19]For the *adhesively-bonded waisted block* specimen design, 18 specimens were tested, however, only 8 exhibited valid failure (i.e. they did not fail due to adhesive bond failure).

The normalised results are presented in **Figure 2.35**. Overall, the experimental scatter was significant. However, in comparison, the form-fit design performed better with regard to this aspect. Considering the magnitude of the experimental scatter, the mean values of strength and modulus across both specimen designs were deemed to be sufficiently close to render the form-fit design a valid alternative to the conventional *adhesively-bonded waisted block* specimen.

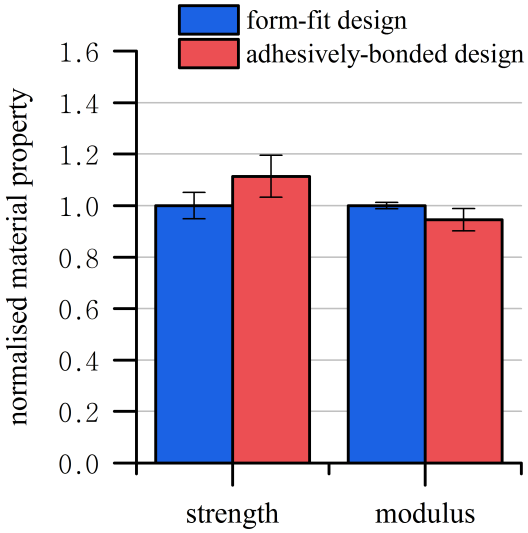


Figure 2.35: Comparison of the measured strength and modulus between an *adhesively-bonded waisted block* and a form-fit design (results are normalised with respect to the form-fit design)

The tests also showed that specimens of both designs failed overwhelmingly in the cross-section at the very end of their respective gauge volume, see **Figure 2.36(a,b)**. This might be attributed to the slight stress concentrations in this particular cross-section, which, in case of the *adhesively-bonded waisted block* specimen design, are a known feature (see, for instance, *Ferguson et al. (1998)* [38]). **Figure 2.36(c)** provides the stress plot of an FE model of an *adhesively-bonded waisted block* specimen to illustrate these stress concentrations.

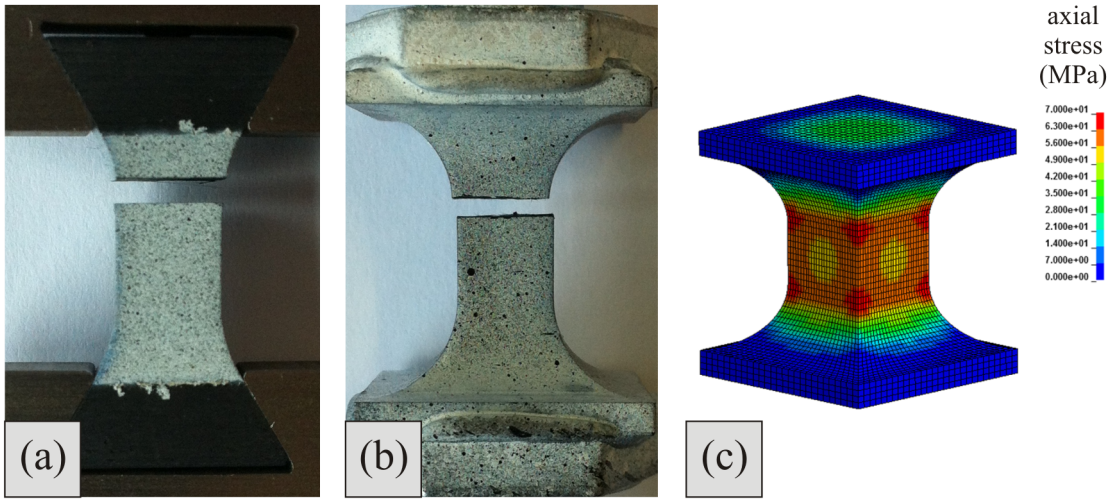


Figure 2.36: (a) prevalent failure cross-section for the form-fit design specimens; (b) prevalent failure cross-section for the *adhesively-bonded waisted block* specimens; (c) FE simulation of an *adhesively-bonded waisted block* specimen indicating slight stress concentrations in this particular cross-section (taken from [146])

Suitability of the form-fit design for dynamic testing. Split-Hopkinson bar experiments were carried out to assess the form-fit design's suitability for testing at elevated loading rates. The reader is referred to **Chapter 2.1.3** for an outline of the employed SHTB system. A total of six specimens were tested using a 3 mm neoprene pulse shaper in conjunction with a projectile velocity of 4.8 m/s. Displacement (and thus strain) was measured optically.

A comparison of the high-rate testing results with those obtained from testing under quasi-static loading is presented in **Figure 2.37** in normalised form. It can be seen that both, strength and modulus, exhibit an increase under an elevated loading rate regime. The experimental scatter was more pronounced for high-rate testing.

The validity of the high-rate tests was assessed by means of the force disequilibrium metric Δ_F introduced in the context of **Chapter 2.1.1**. As shown in **Figure 2.38**, the value of Δ_F remained below the desired 10%-mark well ahead of specimen failure, thus

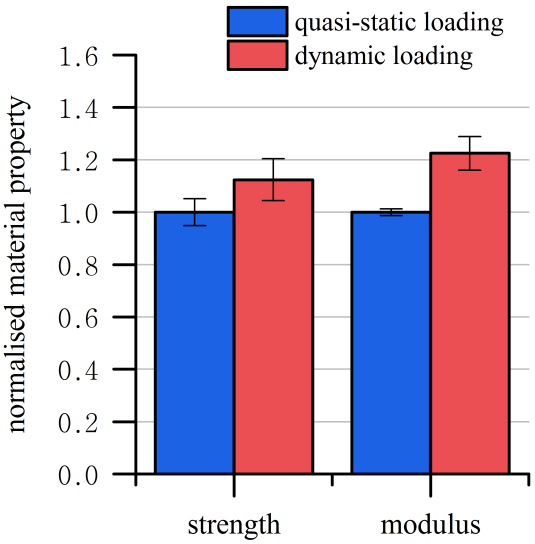


Figure 2.37: Results of the characterisation of strength and modulus across two loading rate regimes for *33-t* testing employing a form-fit specimen design (results are normalised with respect to the quasi-static tests)

indicating the validity of the high-rate testing results. The strain-rate at failure was approximately 35 s^{-1}, see **Figure 2.38**. Similar to the material characterisation tests for the *22-t* deformation mode in **Chapter 2.3.1**, the obtained material properties for *33-t* are also associated with a specimen deformation at a non-constant strain-rate. As these two deformation modes strongly resemble each other, the reader is referred to **Chapter 2.3.1** for a more in-depth description of this phenomenon and its ramifications.

2.4.4 Potential improvements and further considerations

Potential improvements. The form-fit specimen and grip design employed for dynamic *33-t* testing may be improved in multiple ways:

- **Higher quality surface finish**. As materials failing in a brittle manner are especially susceptible to surface irregularities and defects introduced by the ma-

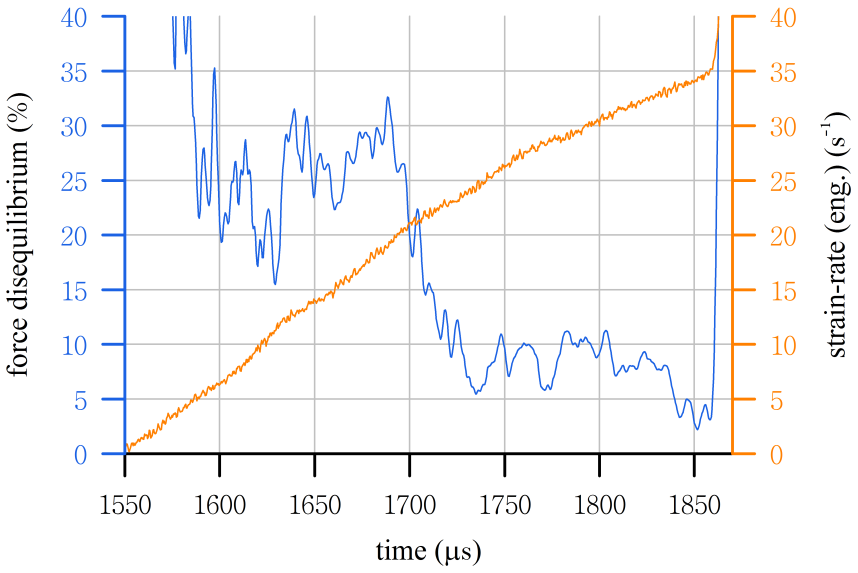


Figure 2.38: Evaluation of the dynamic tests' force disequilibrium and strain-rate history for the form-fit specimen design

chining process (e.g. [51]), a higher quality surface finish could lower the high degree of experimental scatter encountered in the present study.

- **Failure locus**. The reason for the majority of specimens failing at the very end of their gauge section should be further investigated. As was mentioned above, slight stress concentrations inevitably exist in this particular cross-section, however, the radius of the specimen's 'shoulder region' as well as the machining process (e.g. [65]) are further influences that could be investigated in order to eventually shift the failure locus statistically more towards the gauge section's centre.
- **Grip material and geometry**. The present study employed stainless steel grips for high-rate testing on a titanium-based SHTB system. Matching the grip and bar material would lessen the impedance mismatches between the bar system, grips, and specimen, thereby facilitating testing at higher loading rates whilst maintaining valid testing conditions.[20] A more slender grip design could also be

[20]The overall effect of this, however, should not be overestimated: see **Chapter 2.3.2** for a study exploring a range of end sleeve materials for dynamic *22-t* testing.

investigated with the same aim in mind.

Usage of the form-fit design for 'unproblematic' matrix materials. Besides enabling load introduction without relying on a strong adhesive bond between the specimen and 'end caps', the form-fit design offers the following additional advantages over the conventional *adhesively-bonded waisted block* specimen design:

- It requires substantially less material. Taking the specimen geometries presented in **Chapter 2.4.3** as a reference, only 30% of the material volume that was used to produce an *adhesively-bonded waisted block* specimen was required to machine a form-fit specimen.[21] As the very thick panels required for out-of-plane tensile testing are costly to produce, this material economy offers a considerable advantage.
- It simplifies and expedites specimen assembly, since there is no adhesive bond application involved and, therefore, no curing time needed.
- The grips are reusable, in contrast to the 'end caps' required for the *adhesively-bonded waisted block* design.

2.5 Summary

22-c. The following aspects of this deformation mode's characterisation process were addressed:

- *Specimen design.* An original study was presented which quantified the deviation of the measured strength and (initial) modulus from their correct values when

[21] This value refers to the material block cut from the panel prior to any further machining.

employing the most commonly used *block* specimen design opposed to a *waisted block* design. It was thus demonstrated that the deviations from a reasonably one-dimensional stress field along a *block* specimen design's gauge volume result in non-negligible deviations in the obtained material properties. Consequently, it was recommended to favour a *waisted block* over a *block* specimen design.

- *Material characterisation.* The composite's (initial) modulus and strength for this deformation mode were determined across two strain-rate regimes as follows: $E_{22c,0}^{QS} = 8.5 \pm 0.2$ GPa and $Y_c^{QS} = 266 \pm 9$ MPa at $\dot{\epsilon} = 0.00036$ s^{-1}, $E_{22c,0}^{dyn} = 10.9 \pm 0.6$ GPa at $\dot{\epsilon} = 83$ s^{-1}, and $Y_c^{dyn} = 413 \pm 15$ MPa at $\dot{\epsilon} = 127$ s^{-1}. Both properties thus showed a significant dependency on the applied loading rate.
- A comprehensive simulation-based study investigated the influence of key SHB setup and testing parameters on the achievability of valid high-rate testing conditions. This study's key findings were as follows: (i) compared to a direct force measurement at the gauge volume's end faces, the conventional SHB analysis provides a very conservative measure for the determination of the establishment of SE, (ii) fluctuations and disturbances in the incident pulse exert a pronounced influence on the force disequilibrium and strain-rate history of the sample's gauge section, and, (iii) the influence of the choice of the bar material and diameter has an almost negligible influence on the establishment of SE, but a pronounced effect on reaching a deformation state satisfying CSR.

22-t. The following aspects of this deformation mode's characterisation process were addressed:

- *Material characterisation.* The composite's modulus and strength for this deform-

ation mode were determined across two strain-rate regimes as follows: $E_{22t}^{QS} = 9.4 \pm 0.6$ GPa and $Y_t^{QS} = 59 \pm 14$ MPa at $\dot{\epsilon} = 0.00024$ s^{-1}, $E_{22t}^{dyn} = 12.0 \pm 0.5$ GPa at $\dot{\epsilon} = 27$ s^{-1}, and $Y_t^{dyn} = 82 \pm 16$ MPa at $\dot{\epsilon} = 28$ s^{-1}. Both properties thus showed a significant dependency on the applied loading rate.

- A comprehensive simulation-based study investigated the influence of key SHB setup and testing parameters on the achievability of valid high-rate testing conditions. The key findings of this modelling study were similar to the corresponding *22-c* study's findings for its statements (i), (ii), and the first aspect of (iii). With respect to the establishment of CSR for high-rate *22-t* testing, however, it was found that this condition cannot be met, irrespective of the material employed for the bars and end sleeves.

33-t. Motivated by the goal of overcoming adhesive bond failure observed when employing a conventional *adhesively-bonded waisted block* specimen design for testing a composite featuring a comparatively inert matrix material, a form-fit specimen design was developed for (high-rate) out-of-plane tensile testing. This form-fit design was shown to be an appropriate substitute for the conventional *adhesively-bonded waisted block* design and its suitability for testing under high-rate loading conditions was demonstrated. Apart from not relying on an adhesive bond between 'end caps' and specimen, the form-fit design offered additional advantages: (i) a substantially reduced material volume requirement, (ii) a simplification and foreshortening of the specimen assembly process, and, (iii) the reusability of the grips connecting the specimen to the testing machine.

Chapter 3

Determination of the strain-energy release rate under high-rate tensile loading in fibre direction

The goal of this chapter is to experimentally determine the energy release rate of a composite laminate under high-rate tensile loading in fibre direction in order to provide the dataset pertaining to $G_{Ic}^{f+}(\dot{\epsilon})$ for constitutive model calibration. First, a brief overview of a composite laminate's set of (rate-dependent) energy release rates is presented, which leads to the motivation to focus on the experimental determination of $G_{Ic}^{f+}(\dot{\epsilon})$. Then, an outline of the relevant literature is provided, covering: (i) a composite's failure in fibre tensile direction from a micro-mechanical perspective, (ii) the known dependencies of G_{Ic}^{f+} on various parameters, (iii) an outline of the data reduction approaches documented in literature including an assessment of their respective suitability for high-rate testing, and, (iv) an overview of the only other study dedicated

to determining $G_{Ic}^{f+}(\dot{\epsilon})$ including a discussion of its shortcomings. Next, a description of the material, specimen design, experimental setups, and data acquisition systems employed for the material characterisation programme is given. Then, a critical assessment of the high-rate testing conditions, specifically their ability to ensure the validity of the high-rate tests is presented, followed by an outline of all relevant aspects of the data reduction procedure. Subsequently, the experimental results are presented and an interpretation of the observed rate-dependent trend is offered on the basis of an extensive post-mortem analysis of the specimens. The chapter concludes by providing a list of recommendations that can serve as a starting point for further improving the characterisation of $G_{Ic}^{f+}(\dot{\epsilon})$.

Main contributions to the body of knowledge contained in the present chapter at a glance:

- Characterisation of the energy release rate of a composite laminate under high-rate tensile loading in fibre direction based on valid force history data.
- Modification of an existing SHTB setup in order to facilitate carrying out the experiments under valid testing conditions, which includes the refinement of various aspects such as the experimental setup, loading conditions, and data reduction method.
- Extensive post-mortem analysis of the specimens with the aim of linking the change in the experimentally-observable material behaviour on macro scale to the corresponding changes in the governing mechanisms on micro scale.
- The key contents of this chapter were published as: Hoffmann, J., Cui, H., and Petrinic, N. (2018). Determination of the strain-energy release rate of a compos-

ite laminate under high-rate tensile deformation in fibre direction. *Composites Science and Technology*, 164:110–119.

3.1 Introduction and motivation

Modelling design-critical impact events on an aircraft's composite material structures, such as in the case of *bird strike*, necessitates an accurate reflection of the composite's strain-rate-dependent deformation, failure, and damage propagation behaviour. While **Chapter 2** focussed on the rate-dependency of a composite's elastic and strength properties, the present chapter deals with its rate-dependent strain-softening behaviour, which, in turn, is governed by the material's set of strain-energy release rates.

Within the framework of *fracture mechanics*, the propagation of cracks is described in terms of the three *fracture modes* illustrated in **Figure 3.1** (e.g. [122]). This set of fracture modes is defined with respect to a particular *fracture plane*. The *idealised* fracture planes associated with a composite's failure modes on macro scale are depicted in **Figure 3.2**. In contrast to delamination and IFF, fibre failure in mode I encompasses tensile and compressive failure. In order to readily distinguish between these two in the following, the terms *fibre tensile failure* and *fibre compressive failure* are used instead of mode I.

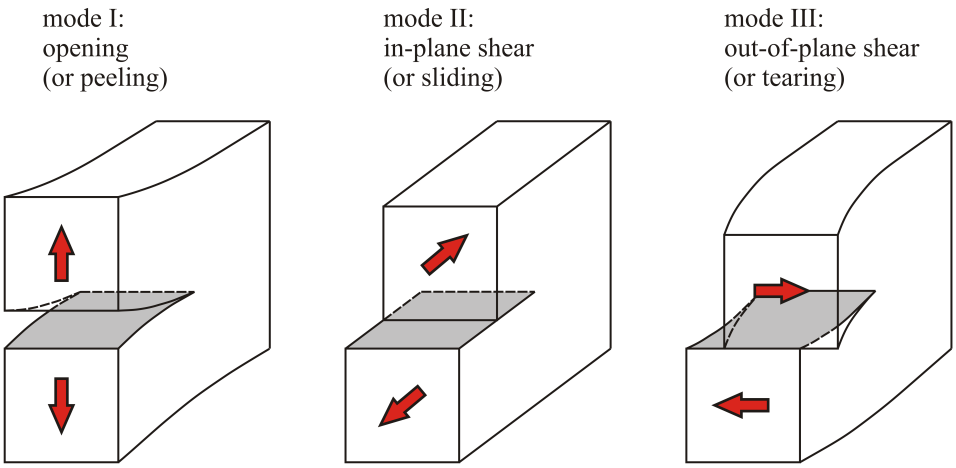


Figure 3.1: Fracture modes to describe crack propagation within the framework of fracture mechanics

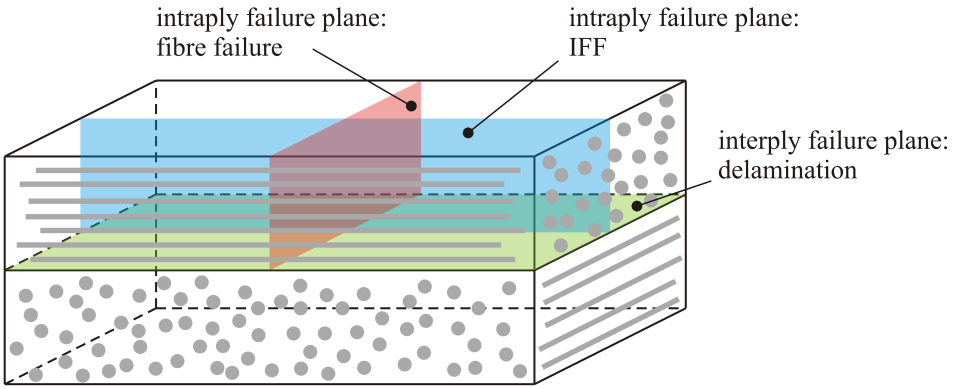


Figure 3.2: Idealised fracture planes associated with a composite's failure modes on macro scale

What follows is a condensed overview of the current state-of-the-art experimental capabilities for determining the set of strain-energy release rates of composite materials consisting of UD-reinforced laminae. A particular focus is placed on the characterisation under high-rate loading conditions. Any loading rate trend given refers to composites consisting of carbon fibres embedded in an epoxy matrix. In order to keep this overview concise, fracture mode III and any interactions between modes are not

considered.

Delamination. Standards for testing under quasi-static loading are available for both, mode I [8, 72] and mode II [9, 73]. In contrast, standards for the dynamic testing of these two fracture modes do not yet exist, despite there being a plethora of literature sources available. In an extensive review of the available literature on dynamic mode I testing, *May (2016)* [99] identified several issues that need to be overcome. For dynamic mode I testing, the majority of research suggests rate-insensitive behaviour (e.g. [74, 100]). For dynamic mode II testing, there is no clear consensus in the literature, with examples of increasing [77], decreasing [94, 128], as well as rate-insensitive [15, 148] trends reported against increases in the loading rate.

IFF. Compared to delamination, crack propagation under IFF has received only limited coverage in existing literature. The research that has been carried out has focused, almost exclusively, on mode I testing under quasi-static loading conditions, as well as a subsequent comparison of the obtained results against the corresponding value for delamination. These studies show that the initiation value of G_{Ic} is similar for IFF and delamination, however, the effect of *fibre bridging* is more pronounced in the case of IFF, thus resulting in a higher energy release rate over the course of crack propagation [34, 36, 108]. The only source covering fracture mode II is *Garg (1986)* [46], who compared the fracture surface morphologies for delamination and IFF. In undertaking this work, however, *Garg* did not calculate any energy release rate values. There were no sources found in the literature for testing under dynamic loading for either mode.

Fibre failure. Up until recently, the capability to obtain the energy release rate for

compression testing in fibre direction was limited to its initiation value due to the inability to suppress undesired additional failure modes during crack propagation in *compact compression* specimens [23, 112]. This issue has been overcome recently by *Catalanotti et al. (2014)* [25] by using a *double edge notched* specimen design in conjunction with a data reduction methodology based on the *size-effect law* to determine G_{Ic}^{f-} under quasi-static loading conditions. *Kuhn et al. (2017)* [80] then employed said methodology to determine the respective energy release rate under dynamic loading conditions, finding G_{Ic}^{f-} to increase substantially under an elevated loading rate regime. Although the determination of the energy release rate for tensile failure in fibre direction under quasi-static loading is standardised [10], many researchers have deviated from the standard's recommendations by employing a different specimen design (e.g. [25, 112]) and/or by utilising a different data reduction approach (e.g. [25, 84, 112]). For dynamic tensile loading in fibre direction, merely a single source can be found in literature (*McCarroll (2011)* [100]). Using a modification of the above mentioned *size-effect law*-based data reduction scheme, *Catalanotti et al. (2015)* [24] recently obtained the energy release rate for shearing across fibres using a cross-ply specimen and employing an *Iosipescu* test fixture. No dynamic testing has been carried out yet for fracture mode II.

A concise summary of the above overview is given in **Table 3.1**.

Table 3.1: Summary of the current state-of-the-art capabilities for determining the (dynamic) strain-energy release rate values of UD-reinforced carbon-fibre/epoxy composites

		QS dyn.	rate-dependent trend
delamination	mode I		majority suggests rate-insensitivity
	mode II		no clear consensus
IFF	mode I		-
	mode II		-
fibre failure	compression		increasing trend; only source: [80]
	tension		rate-insensitivity; only source: [100]
	mode II		-

colour code:

- standard available
- moderate to broad coverage; not standardised
- very low to low coverage
- no coverage

With the above overview in mind, the present study was motivated to focus on the determination of the energy release rate for tensile failure in fibre direction under dynamic loading conditions based on the following factors:

Dearth of literature. In marked contrast to the extensive literature covering dynamic delamination, there is merely a single literature source examining dynamic tensile failure in fibre direction, which is *McCarroll (2011)* [100]. An overview of *McCarroll*'s approach alongside an assessment of its shortcomings that merited the renewed attempt to determine $G^{f+}_{Ic,dyn}$ in the present work will be given in **Chapter 3.2.4**.

Magnitude of energy released and the implications of its change with loading rate. When compared to the matrix-dominated failure modes, the energy re-

leased for failure in fibre direction is by several orders of magnitude larger (compare $G_{Ic,QS}^{del} = 0.28$ kJ/m^2 [105] to $G_{Ic,QS}^{f+} = 147$ kJ/m^2 [84]). A direct consequence of this salient discrepancy is the necessity to correctly reflect the amount of energy released by failure in fibre direction based on its significant contribution to a composite structure's energy dissipation capability. Against the background of the dynamic nature of many design-critical loading events, it is furthermore imperative to adequately capture the composite's changing energy dissipation behaviour with increasing loading rate so as to avoid over-dimensioning in case of a positive strain-rate trend, or running the risk of not fulfilling the desired load bearing capability in case of a negative strain-rate trend, respectively.

CDM consideration. As will be described in **Chapter 4.5.1**, the constitutive model proposed in the present study employs a *continuum damage mechanics*-based (CDM) approach for modelling the composite's strain-softening behaviour. In the context of an accompanying study to illustrate the limitations of a CDM-based approach (see **Chapter 4.8**), it will be shown that, in comparison to the matrix-dominated failure modes, fibre failure is much less prone to requiring substitution of the experimentally-obtained energy release rate with an artificial value in order to ensure numerical stability. Hence, from the perspective of aiming at physically-based modelling, it appeared much more expedient to focus on the energy released for fibre failure for the present work.

3.2 Literature review

The aim of this subchapter is to present a review of: (i) the micro-mechanical mechanisms associated with the energy dissipation under tensile failure in fibre direction, (ii) the various influences on the measured value of G_{Ic}^{f+}, and, (iii) the range of data reduction approaches documented in literature for determining G_{Ic}^{f+}, particularly in light of their respective suitability for testing under high-rate loading conditions. In addition, this subchapter also presents a brief overview and critical assessment of the only other existing study for determining $G_{Ic,dyn}^{f+}$, which was undertaken by *McCarroll (2011)* [100].

3.2.1 Micro-mechanical background

Behaviour of an isolated fibre vs. behaviour of a fibre in a composite. The energy release rate of a single carbon fibre under quasi-static tensile loading was measured to be approximately 8 J/m^2 [66]. This value is in stark contrast to the energy release rate of a fibre-reinforced composite under similar loading conditions, which for example for *IM7/8552* was determined to be 147,000 J/m^2 [84]. This salient rise in the measured energy release rate for the composite can be explained by the more complex succession of failure mechanisms on micro scale. This succession involves matrix cracking, debonding of fibres from the matrix, rupturing of fibres, and finally, fibre pull-out (e.g. [69]). A depiction of these mechanisms is presented in **Figure 3.3**.

The tensile strength and modulus of carbon fibres are known to be rate-insensitive (e.g. [58, 136, 150]); the energy release rate of a single rupturing carbon fibre under

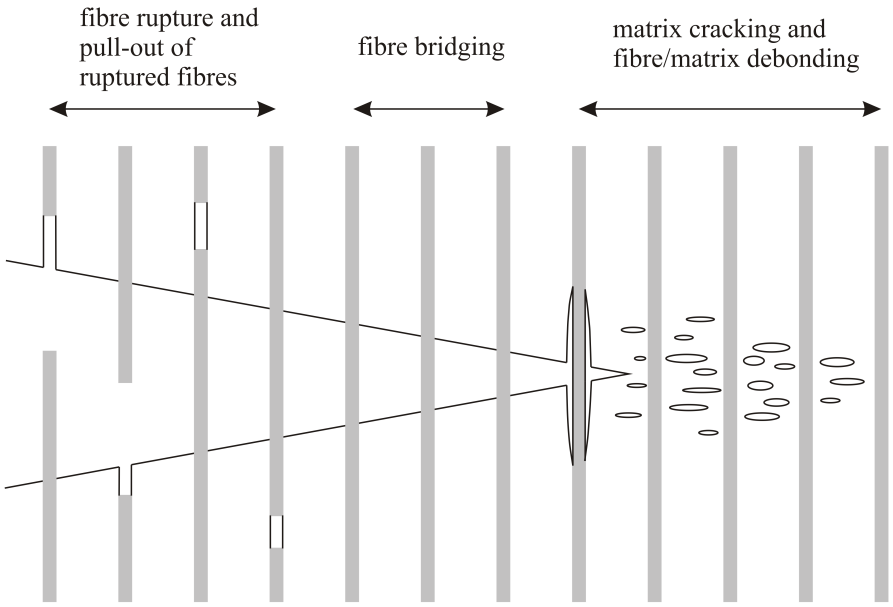


Figure 3.3: Energy dissipation mechanisms on micro scale of a composite under tensile loading in fibre direction (following the depiction in *Hou et al. (2014)* [69])

an elevated loading rate has not yet been determined experimentally. Against the background of the micro-mechanical processes outlined above, however, the carbon-fibre-reinforced composite may very well exhibit a rate-dependent energy release rate due to the matrix and fibre/matrix interface-related fracture and friction processes, even though the energy released by fibre rupture itself might prove to be rate-insensitive in the future.

Loading rate dependency. Sources addressing the dynamic fibre pull-out process in the order of magnitude of *meters per second* displacement rate are very scarce, with merely two studies documented in existing literature: *Greenfield et al. (2000)* [55], and *Tamrakar et al. (2016)* [135]. The former, *Greenfield et al.*, employed a *fibre fragmentation test* to characterise the rate-dependent nature of the *interfacial shear strength* (IFSS) of S-2 glass-fibre/PC, E-glass-fibre/PC, and carbon-fibre/PC systems. The latter, *Tamrakar et al.*, were able to show that the IFSS and the energy required to

debond an S-2 glass-fibre from an epoxy matrix droplet in a *microdroplet test* exhibits a marked dependency on the applied loading rate.

A more detailed insight into the loading rate dependency of the various energy dissipation mechanisms can be obtained from dynamic experiments at a much lower displacement rate (in the order of magnitude of *millimetres per second*). Using a specially designed testing apparatus termed *DILA* ('*dynamic interphase loading apparatus*') based on the push-out of a single fibre, *Tanoglu et al. (2000)* [137] and *(2001)* [138], and *Foley et al. (2002)* [41] demonstrated for an E-glass-fibre/epoxy-amine and an E-glass fibre/vinyl-ester system, respectively, that:

- The energy required to debond a fibre from the matrix as well as the frictional sliding process of the fibre subsequent to debonding exhibit a clear dependency on the applied loading rate.
- The energy dissipated over the course of the frictional sliding process is significantly higher than the corresponding energy for fibre/matrix debonding.
- The frictional sliding of a fibre being pushed out of its surrounding matrix exhibits a more pronounced sensitivity to loading rate than the fibre/matrix debonding process.

Even though the findings of the literature sources outlined above are based on material systems other than carbon-fibre/epoxy and/or were tested at a much lower loading rate regime, they provide, in the least, an indication of the rate-dependent nature of the fibre/matrix debonding and subsequent frictional sliding process.

3.2.2 Known influences on the measured value of G_{Ic}^{f+}

Apart from being a function of loading rate and environmental conditions (for the latter, see, for instance, [31, 95, 113]), the experimentally-determined value of G_{Ic}^{f+} has been shown to exhibit further dependencies as follows:

Ply thickness (which also involves grouping multiple individual plies). Thinner plies have been found to exhibit a lower value of G_{Ic}^{f+}. This, in turn, has been attributed to the increased ability of adjacent 90° plies to constrain the fracture plane such that the overall level of fibre pull-out decreases (*Prewo (1978)* [115], *Laffan et al. (2010)* [83], *Teixeira et al. (2016)* [140]). *Laffan et al. (2010)* [83] tested *T300/920* carbon-fibre/epoxy laminates with a ply-book of $[(90_2, 0)_8, 90]_{symm.}$ and $[(90, 0_2)_8, 90]_{symm.}$, respectively, hence effectively doubling the thickness of the 0° plies. This resulted in G_{Ic}^{f+} rising from 60 to 132 kJ/m^2, thus corresponding to an increase of 118%. *Teixeira et al. (2016)* [140] employed specimens made of *TR50s/K51* carbon-fibre/epoxy. In the most extreme case, the increase of G_{Ic}^{f+} amounted to 227% for the 'thick ply configuration' ($G_{Ic}^{f+} = 49$ kJ/m^2 for $t_{ply} = 0.031$ mm in a $[90_3, (90, 0)_{24}, 90_2]_{symm.}$ laminate; $G_{Ic}^{f+} = 160$ kJ/m^2 for $t_{ply} = 0.109$ mm in a $[90_2, (90_2, 0_2)_8, 90]_{symm.}$ laminate).

Laminate thickness. *Harris et al. (1984)* [59] and *Laffan et al. (2010b)* [83] tested laminates of different total thicknesses (sub-laminate composition remained constant). Both found G_{Ic}^{f+} to decrease slightly with increasing laminate thickness.

Notch tip radius. *Laffan et al. (2011)* [84] studied the influence of the notch tip radius on the initiation value for G_{Ic}^{f+} for a carbon-fibre/epoxy composite. It was concluded that the notch tip radius should be below 250 µm in order for the initiation

value of G_{Ic}^{f+} not to be artificially elevated.

Data reduction methodology. *Laffan et al. (2010)* [82] investigated the influence of the data reduction approach on the obtained value of G_{Ic}^{f+}. An experimental dataset was analysed using the *area method*, *ASTM E399*, the *compliance calibration* (CC) and the *modified compliance calibration method* (MCC), and an FE-based evaluation of the J-integral. Slight but noticeable differences were found in terms of the obtained mean value for G_{Ic}^{f+} and the extent of the associated experimental scatter. A more in-depth discussion on the topic of data reduction methodologies will be provided in the subsequent section.

The above overview showed that there are various influences on the measured value of G_{Ic}^{f+} besides loading rate and environmental conditions. In particular, the parameter 'ply thickness' has been demonstrated to have a pronounced effect. It is thus important to keep in mind that the value of the energy release rate G_{Ic}^{f+} determined in the present study is only valid for laminates composed of plies of identical thickness to the ones employed here.

3.2.3 Approaches to obtaining G_{Ic}^{f+}

This section presents an overview of the various approaches documented in literature to obtain G_{Ic}^{f+}.[1] Special emphasis is placed on each approach's potential suitability for testing under high-rate loading conditions. An essential aspect of this assessment

[1]More accurately speaking, G_{Ic}^{f+} is not obtained directly, but instead the laminate's strain-energy release rate G_{Ic}^{lam} is measured. The deduction of G_{Ic}^{f+} on the basis of the experimentally-obtained G_{Ic}^{lam} will be outlined in **Chapter 3.5.2**.

was the exclusion of any approach relying on the composite material's elastic properties for the data reduction process. This constraint was motivated by the following considerations: (i) The majority of the elastic properties of a carbon-fibre/epoxy composite exhibits a pronounced strain-rate dependency (e.g. see **Chapter 2** and **Chapter 5.1**). Without a sufficiently precise quantification of this dependency for each relevant deformation mode, any inaccuracy reflecting the elastic properties' rate-dependency would have directly affected the determined value of G_{Ic}^{f+}. (ii) The majority of data reduction schemes are not capable of accounting for the non-homogeneity of the strain-rate field, and thus the (rate-dependent) elastic material response, across the specimen.

ASTM E399 [11]. The calculation of the *critical stress intensity factor* K_{Ic} is based on **Equ. 3.1**, which, in turn, requires the experimental measurement of force and crack tip propagation history.

$$K_{Ic} = \frac{F_c}{t_{lam}\sqrt{w}} f\Big(\frac{a}{w}\Big) \tag{3.1}$$

In the above equation, F_c denotes the (critical) force causing crack propagation, a the accumulated crack length, t_{lam} the specimen's thickness, and w the distance between the 'load introduction line' and the specimen's back edge (see [11] for illustration), respectively. The function $f(\frac{a}{w})$, as defined in **Equ. 3.2**, introduces the *finite width correction factor* which allows to account for the specimen's finite dimensions.

$$f\Big(\frac{a}{w}\Big) = \frac{2+\frac{a}{w}}{\sqrt[1.5]{1-\frac{a}{w}}}\left[0.886 + 4.64\Big(\frac{a}{w}\Big) - 13.32\Big(\frac{a}{w}\Big)^2 + 14.72\Big(\frac{a}{w}\Big)^3 - 5.6\Big(\frac{a}{w}\Big)^4\right] \tag{3.2}$$

Based on the *critical stress intensity factor* K_{Ic} and the composite's elastic properties, the laminate's strain-energy release rate G_{Ic}^{lam} is then calculated as follows [82]:

$$G_{Ic}^{lam} = \frac{K_{Ic}^2}{\sqrt{2E_{11}E_{22}}}\sqrt{\sqrt{\frac{E_{11}}{E_{22}}} + \frac{E_{11}}{2G_{12}} - \nu_{12}} \; . \tag{3.3}$$

As pointed out by several researchers (see *Pinho et al. (2006)* [112] or *Laffan et al. (2010)* [82]), a major drawback of this data reduction scheme is its inaccuracy caused by the composite's orthotropic nature. More specifically, for the ply configuration used in the present study, *Laffan et al. (2010)* [82] determined this deviation from the reference value of G_{Ic}^{lam} obtained via FEM for an *T300/920* material system to amount to 13.2%; higher degrees of orthotropy yielded even more pronounced levels of inaccuracy.

With regard to testing under high-rate loading conditions, data reduction according to *ASTM E399* was considered unsuitable for the present study as it relies on the composite material's elastic properties.

Area method. The basic concept behind this approach is to directly relate the dissipated energy ΔU resulting from the advancing crack tip to the newly generated surface area ΔA according to

$$G_{Ic}^{lam} = \frac{\Delta U}{\Delta A} \; . \tag{3.4}$$

The energy ΔU can be obtained based on the force vs. opening displacement data, as shown for *stable crack propagation* in **Figure 3.4(a)**. For a linear elastic material exhibiting *stick-slip crack propagation*, such as the composite material tested in the present study, an approximation of G_{Ic}^{lam} can be obtained according to **Equ. 3.5** [67].

The corresponding illustration for this case is provided in **Figure 3.4(b)**.

$$G_{Ic}^{lam} = \frac{1}{2t_{lam}\Delta a}(F_1 x_2 - F_2 x_1) \tag{3.5}$$

Averaging the strain-energy release rate value over a series of N individual crack propagations Δa can be achieved via [125]

$$G_{Ic}^{lam} = \frac{1}{2t_{lam}N\Delta a}\sum_{i=1}^{N}(F_{1i}x_{2i} - F_{2i}x_{1i}) \ . \tag{3.6}$$

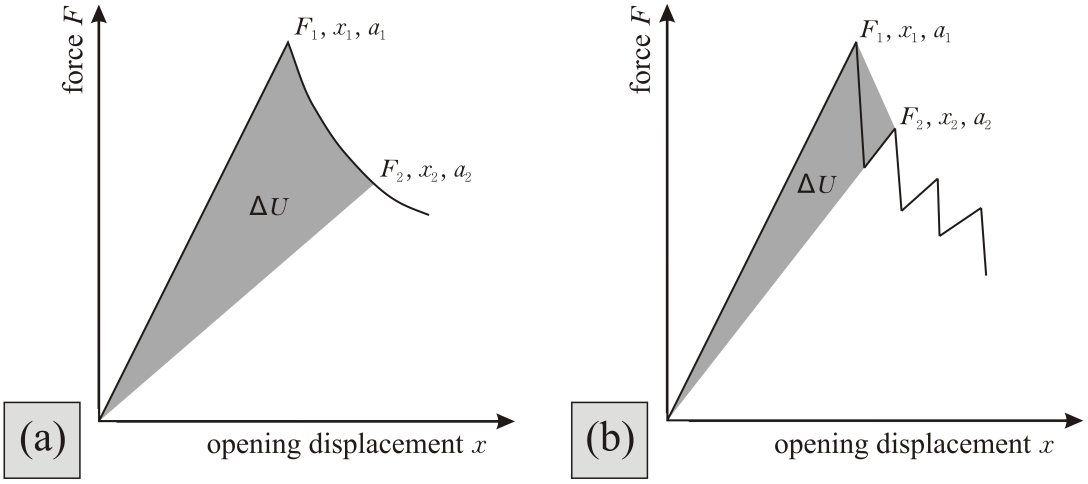


Figure 3.4: Determination of G_{Ic}^{lam} based on the *area method* for (a) stable crack propagation, and (b) stick-slip crack propagation

The *area method* was considered suitable for testing under high-rate loading conditions for the present study.

Compliance calibration. The *compliance calibration method* (CC) is motivated by the desire to bypass the necessity to measure the crack tip's position during the experiment, as obtaining this particular parameter using optical means is a known source of inaccuracy (e.g. [82]). This is achieved by experimentally determining the specimen's compliance S with increasing crack length a, and subsequently using this relationship to derive the crack tip's position on the basis of the specimen's compliance as obtained from the force vs. opening displacement curve. An extension of this technique is the

modified compliance calibration method (MCC), which aims at rendering any optical determination of the crack tip's position unnecessary, even for the calibration process. This can be achieved by using specimens featuring a range of machined crack lengths for the calibration process (e.g. [52, 83, 140]), or by employing FE modelling (as pointed out by *Laffan et al. (2010a)* [82]). The data points obtained from the calibration exercise are subsequently used to establish an appropriate fit function in order to cover the full range of $S(a)$. The laminate's strain-energy release rate G_{Ic}^{lam} can then be calculated according to [85]

$$G_{Ic}^{lam} = \frac{F_c^2}{2t_{lam}} \frac{dS}{da} \; . \tag{3.7}$$

Employing the *compliance calibration method* (CC or MCC) hinges upon the ability to extract the specimen's compliance S from the measured force vs. opening displacement curve. This can be readily achieved for testing under quasi-static loading conditions. Under high-rate loading, however, no such clear identification of 'linear curve segments' indicating the sample's compliance is possible any more, thus rendering the *compliance calibration method* unsuitable for the present study.

J-integral via **FEM**. With the aim of obtaining G_{Ic}^{lam}, *Pinho et al. (2006)* [112] employed an FE-based approach to calibrate the value of the J-integral. To this end, the authors created FE models of the specimen with unit thickness and a range of crack lengths. These models were then subjected to a unit load in order to determine the value J of their respective J-integral, see **Equ. 3.8**. Subsequently, these obtained values were parameterised using a third order polynomial.

$$f(a) = J \cdot \left(\frac{1mm}{1N} \right)^2 \tag{3.8}$$

The laminate's strain-energy release rate G_{Ic}^{lam} was then calculated according to **Equ. 3.9**, requiring the experimentally-measured force and crack tip propagation history as input.

$$G_{Ic}^{lam} = \left(\frac{F_c}{t_{lam}}\right)^2 f(a) \tag{3.9}$$

This approach was considered unsuitable for high-rate testing for the present study due to the FE model's reliance on the composite material's elastic properties.

J-integral via **DIC**. The strain-energy release rate G_{Ic}^{lam} may also be obtained by determining the value of the J-integral via a DIC-based full field analysis of the strain field surrounding the propagating crack tip (e.g. *Catalanotti et al. (2010)* [23] or *Hou et al. (2014)* [69]). A major advantage of this approach is the wide variety of parameters that can be obtained in addition to the value of the J-integral, such as the crack tip propagation history [23] or *stress intensity factor* [69]. Data reduction, however, makes use of the composite material's elastic properties, thus rendering this method unsuitable for high-rate testing for the present study.

Size-effect law. This approach, previously applied to other classes of materials [13], recently found application for testing several failure modes of composite materials: tensile failure in fibre direction [22], compressive failure in fibre direction [25], and shearing across fibres [24]. In the case of determining the strain-energy release rate for tensile failure in fibre direction, *Catalanotti et al. (2014)* [22] employed a *double edge notched* specimen design. The *size-effect law* was obtained by testing a range of specimens featuring a self-similar geometry to determine the ultimate (remote) stress σ_u causing crack propagation as a function of the specimens' geometry parameter w (representing half of the specimen's width). In addition to the *size-effect law* $\sigma_u(w)$,

a correction factor κ accounting for the specimen's geometry and orthotropy was determined employing a parametric numerical study. The calculation of the composite material's R-curve $R(\Delta a)$ was then based on **Equ. 3.10** and **Equ. 3.11**.

$$R(\Delta a) = \frac{1}{\acute{E}} w \sigma_u^2 \kappa \tag{3.10}$$

$$\frac{\partial}{\partial w}(w \sigma_u^2 \kappa) = 0 \tag{3.11}$$

In addition to the meaning of the symbols already introduced, $\acute{E}$ denotes the composite's equivalent elastic modulus (see [22] for details).

As the *size-effect law* approach relies on the composite material's elastic properties for the data reduction process, it was regarded unsuitable for testing under high-rate loading conditions for the present study.

Thermography. Determining the strain-energy release rate by employing infrared thermography is based on measuring the heat that is generated over the course of the formation and propagation of a crack (e.g. *Lisle et al. (2015)* [91]). A major drawback of this approach in general is the dearth of knowledge on the ratio of the energy converted into heat, W_{dissip}, to the energy converted into irreversible mechanical energy, W_{irrev}, mathematically expressed as $\beta = \frac{dW_{dissip}}{dW_{irrev}}$ (*Taylor-Quinney coefficient*) [91]. Moreover, this ratio β has been shown to be a function of strain and strain-rate [89, 121]. As it was not quite clear if and to what degree the time-dependent nature of the thermal diffusion process would allow for obtaining valid data under high-rate loading conditions, this methodology was not considered further for the purpose of this study.

A brief summary of the various approaches discussed above to ultimately obtain G_{Ic}^{f+}

is presented in **Table 3.2**. As is evident from this summary, the *area method* was considered to be the only viable approach for determining the strain-energy release rate under high-rate tensile loading in fibre direction for the present study. All relevant aspects concerning $F(t)$, $x(t)$, and $a(t)$ from the point of view of data acquisition will be presented in **Chapter 3.3**, and from the perspective of data reduction in **Chapter 3.5**.

Table 3.2: Summary of the approaches documented in literature to determine G_{Ic}^{f+}

method	entities to measure	additional equipment required[a]	suitability for dyn. tests in present study
ASTM E399	$F(t)$,$a(t)$	no	no
area method	$F(t)$,$x(t)$,$a(t)$	no	yes
CC	$F(t)$,$x(t)$,($a(t)$)	no	no
MCC	$F(t)$,$x(t)$	no	no
J-integral:FEM	$F(t)$,$a(t)$	yes	no
J-integral:DIC	displacement field	yes	no
size-effect law	$F(t)$	yes	no
thermography	thermography data	yes	no

[a] 'Additional' in this context refers to any equipment beyond an optical camera, and also includes commercial software packages.

3.2.4 Outline of *McCarroll*'s approach to determining $G_{Ic,dyn}^{f+}$

The only previous work documented in literature that investigated the rate-dependent nature of G_{Ic} for tensile failure in fibre direction was undertaken by *McCarroll (2011)* [100]. Said study employed *compact tension* (CT) specimens made of *IM7/8552* that were tested on a servo-hydraulic *Instron 4505* testing machine in conjunction with a *lost motion device*. This particular experimental setup, however, suffered from significant

oscillations in the machine's force reading, which, in turn, rendered the obtained force history unusable for the data reduction process.

With the aim of obtaining $G_{Ic,dyn}^{f+}$ without relying on the force history as input, *McCarroll* devised an alternative data reduction methodology. The starting point of this approach was a numerical model of the CT specimen. The crack path was reflected using cohesive elements. Both, the bulk material's elastic properties, as well as the cohesive elements' properties, were modelled as rate-insensitive. This model was then subjected to quasi-static loading. Two relationships were extracted from this simulation's results:

(i) The quotient $k(a)$ of the applied force $F_{QS}(a)$ and the compressive strain near the back end of the specimen $\epsilon_{B,QS}(a)$ (see **Figure 3.5** for illustration) according to

$$k(a) = \frac{F_{QS}(a)}{\epsilon_{B,QS}(a)} \ . \tag{3.12}$$

This quotient $k(a)$ obtained under QS loading was then assumed to remain unchanged under high-rate loading conditions, thus allowing for the substitution of the testing machine's unusable force reading for an equivalent force $F_{dyn}(a)$ based on the strain-gauge's measurement of $\epsilon_{B,dyn}(a)$ over the course of the experiment:

$$F_{dyn}(a) = k(a) \cdot \epsilon_{B,dyn}(a) \ . \tag{3.13}$$

(ii) The specimen's compliance S as a function of crack length a. Similar to the introduction of $k(a)$, $S(a)$ was obtained under QS loading and assumed to remain unchanged under high-rate loading conditions. This, in turn, then allowed to infer the specimen's compliance on the basis of the optically measured crack length a, thus 'inverting' the *compliance calibration* procedure in the sense that a measured crack

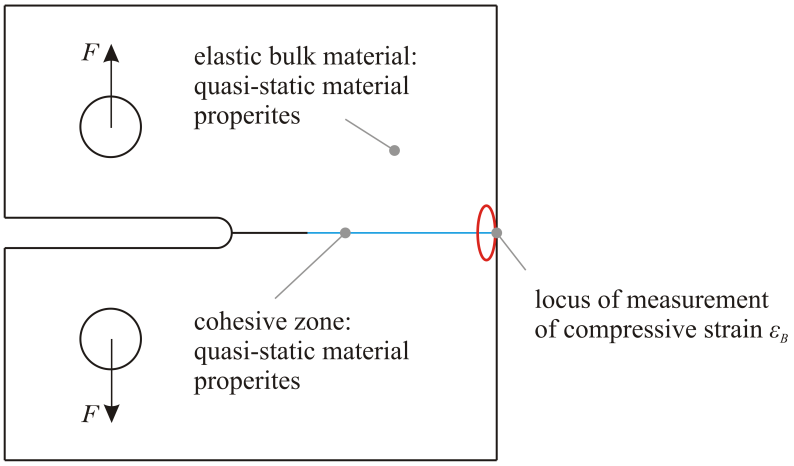


Figure 3.5: Illustration of *McCarroll*'s model of the CT specimen (specimen dimensions were identical to the ones used in the present study)

length was used to obtain the specimen's compliance as opposed to the other way around.

On the basis of these relations and their underlying assumptions, the laminate's energy release rate was finally calculated according to

$$G_{Ic,dyn}^{lam} = \frac{k^2(a) \cdot \epsilon_{B,dyn}^2(a)}{2t_{lam}} \cdot \frac{dS}{da} \,. \tag{3.14}$$

Using this data reduction methodology, *McCarroll* found the mean value of the measured energy release rate $G_{Ic,dyn}^{f+}$ to decrease very slightly with increasing loading rate, however, this decrease was still well within the experimental scatter of the quasi-static testing results.

Against the background of the issues encountered by *McCarroll* to generate a usable force signal that entailed employing a data reduction approach based on the assumption of rate-insensitivity of its key parameters, $k(a)$ and $S(a)$, the present study aims at determining $G_{Ic,dyn}^{f+}$ via an experimental setup able to yield a usable force history so as to allow for the employment of the well-established *area method* for the data

reduction process. A simple check of the validity of the assumption of rate-insensitivity of *McCarroll*'s two key data reduction parameters against the data generated in the present work will be provided in **Chapter 3.6.4**.

3.3 Specimen, experimental setup, and data acquisition

This subchapter provides all relevant information regarding the specimen, experimental setup, and data acquisition. An emphasis is placed on the high-rate tests, as this is the first study employing a modified SHTB setup for the determination of $G^{f+}_{Ic,dyn}$.

3.3.1 Specimen geometry and ply configuration

The specimen design used for the present study was the *compact tension* (CT) specimen; its dimensions, taken to be identical to those in *Pinho et al. (2006)* [112], are shown in **Figure 3.6**. The reasons for employing this particular specimen design were as follows:

- Suitability for high-rate testing on an SHTB system: (i) only minor modifications were required to be made to the bar system to accommodate the CT specimen (see **Chapter 3.3.4**), (ii) the specimen was 'compact' enough to allow for the achievement of a state of near force equilibrium over the course of crack propagation (see **Chapter 3.6.1**), and, (iii) no gripping mechanism was required that could have posed issues due to its additional inertia.

- Employing a CT specimen design ensured direct comparability with the vast majority of literature sources having investigated the energy release rate for tensile failure in fibre direction, such as [16, 23, 52, 84, 112, 140].
- As pointed out by *Laffan et al. (2012)* [85], the CT specimen design does not exhibit unstable crack propagation behaviour, thus allowing for the evaluation of multiple crack propagations per specimen to potentially derive a full R-curve.[2]

The CT specimen employed in the present study consisted of a cross-ply configuration with a ply sequence of $[(90,0)_8,90]_{symm.}$. These 34 plies added up, in total, to approx. 4.3 mm in through-thickness direction. The 90° layers in this specimen design were necessary to facilitate load introduction. A ply-book featuring two adjacent 0° layers around the specimen's mid-plane was avoided as these two 'blocked' plies would have exhibited a different energy release rate compared to that of the dispersed 'single' plies (see **Chapter 3.2.2**).

3.3.2 Specimen manufacturing, machining, and preparation

Panels were produced by stacking *IM7/8552* unidirectionally-reinforced prepreg layers by hand according to the ply-book given above; the curing process followed *Hexcel*'s recommended temperature/pressure regime [63]. By sandwiching the composite material in a metallic fixture for the machining process of the specimens' contour and through-holes, potential delaminations due to machining were avoided. The 0.4 mm wide slit was machined using a sectioning blade (*BUEHLER IsoMet 5LC*). A final notch at the end of this slit was produced by employing a 0.1 mm thick Japanese

[2] Other specimen designs sharing this feature are the extended CT ('ECT'), the three-point-bending, and four-point-bending specimen, see *Laffan et al. (2012)* [85].

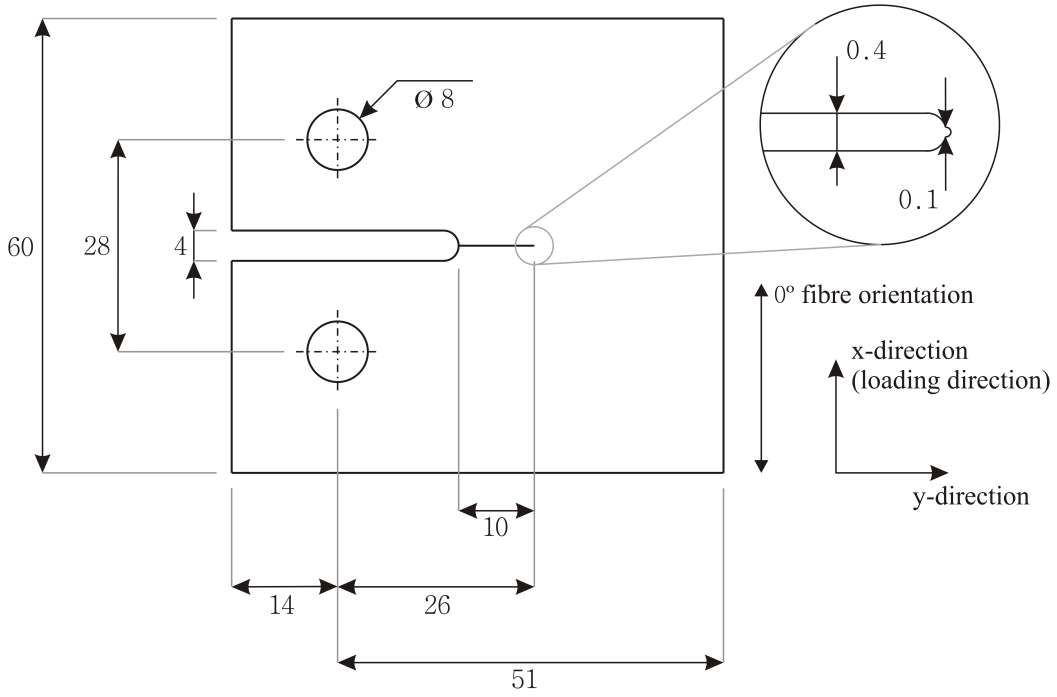


Figure 3.6: Geometry of the CT specimen (dimensions in mm)

micro saw (*'micro-dozuki'*). This last step was motivated by *Laffan et al.*'s *(2011)* [84] finding that the radius of the starter notch should be below 250 µm for the measured initial energy release rate not to exhibit an artificially elevated value (see **Chapter 3.2.2**).

In order to facilitate a DIC-based analysis of the displacement field in the vicinity of the propagating crack tip, a black speckle pattern on a white background was applied using an airbrush.

3.3.3 Setup, loading conditions, and data acquisition for quasi-static testing

Testing under quasi-static loading was carried out on a screw-driven testing machine (*Zwick/Roell Z250*). Load application was displacement-controlled at a rate of 0.5 mm/min.

The force history was measured via the testing machine's 20 kN load cell. A laser extensiometer (*EIR LE-05*) was used to measure the opening displacement history. The deformation and fracture process was recorded at a rate of 1 fps and a resolution of 1884x1520 pixels using a camera (*jAi BM-500GE*) in conjunction with a *Nikon Micro-NIKKOR* 55 mm lens. A depiction of this setup is shown in **Figure 3.8(a)**.

3.3.4 Setup, loading conditions, and data acquisition for high-rate testing

Dynamic testing was conducted using the SHTB system outlined in **Chapter 2.1.3**. In order to avoid an additional impedance mismatch, the adaptor employed to connect the bar system to the specimen was made of titanium. Additional supports made of brass mounted in the specimen's immediate vicinity were employed to complement the already existing bearings made of polyamide. Extending the SHTB setup with these additional supports was motivated by FE simulations modelling the entire experimental setup[3], which showed a transverse motion component of the bars over the course of the specimen's deformation process. The results of this study are presented in **Figure 3.7**, comparing the load introduction bolts' transverse displacement history for the setup without additional support to the setup complemented with the additional bearings made of brass. The purpose of minimising the bars' transverse motion via these brass supports was twofold: (i) prevention of any substantial bending of the bars and thus the minimisation of any spurious bending waves, and (ii) minimisation of the specimen's rotation over the course of its deformation and fracture process, which, in turn, could

[3]the FE model of the setup will be described in **Chapter 3.4.1**

otherwise have introduced an undesired fracture mode II component. The second aspect will be further discussed in the context of the next subchapter.

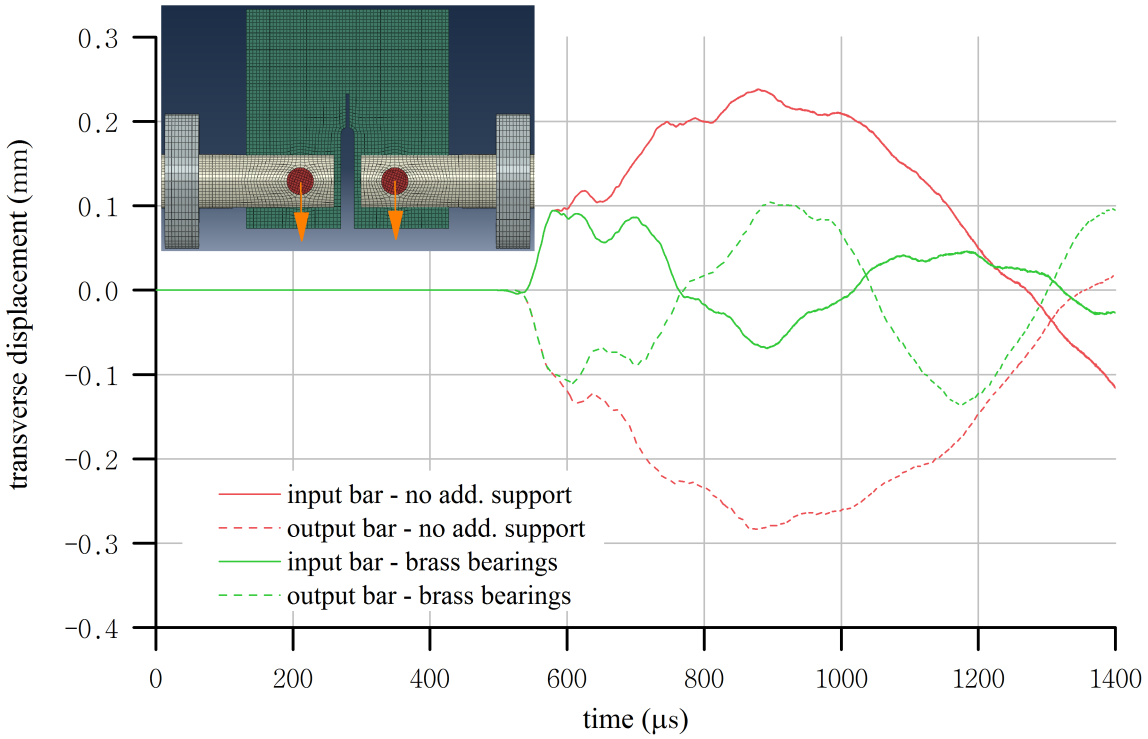


Figure 3.7: Comparison of the simulation results for the SHTB setup without any additional support to the ones employing additional brass bearings in the specimen's immediate vicinity; the plotted transverse displacement refers to the load introduction bolts' respective centre line

An additional 'separator' mechanism was employed to prevent the fractured specimen halves from coming in contact again after final failure. In this way, any undesired damage to the fracture surfaces that could have rendered the specimens unfit for fractography was avoided. A close-up view of the setup for high-rate testing is presented in **Figure 3.8(b)**.

The loading pulse was generated using a projectile velocity of 7.5 m/s in conjunction with a 2.95 mm thick neoprene rubber pulse shaper. The loading pulse was chosen such that its rising slope essentially covered the entire deformation and fracture process of the specimen; this is illustrated in **Figure 3.9**. By maintaining a reasonably constant

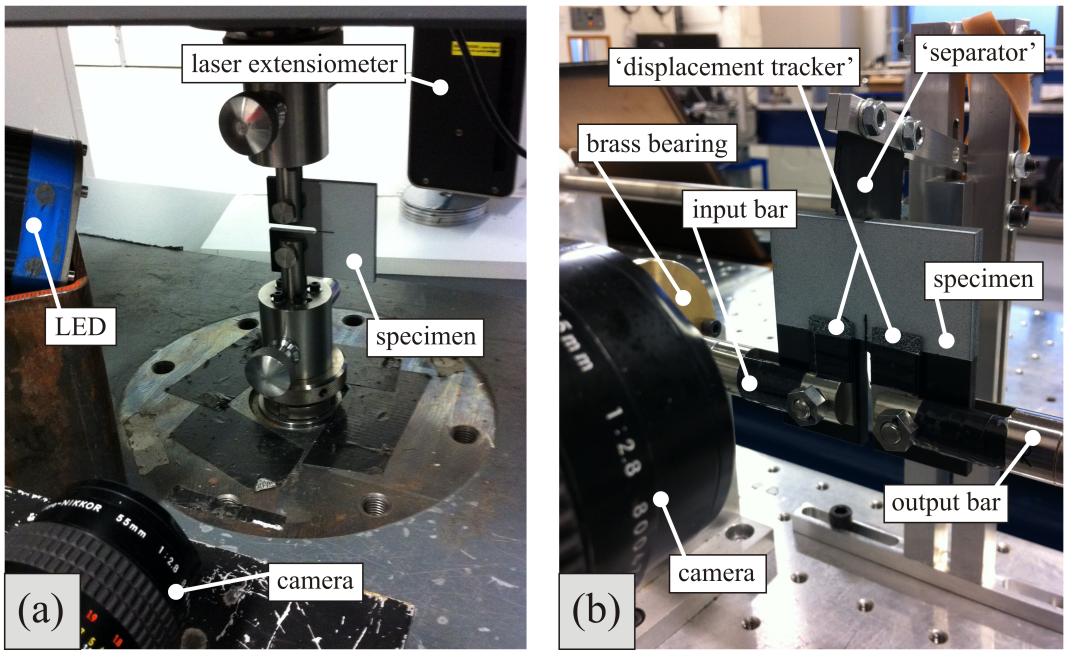


Figure 3.8: Experimental setup for the tests under (a) quasi-static, and (b) high-rate loading conditions

loading rate over the course of crack propagation, the individual crack tip advances occurred under similar loading conditions.

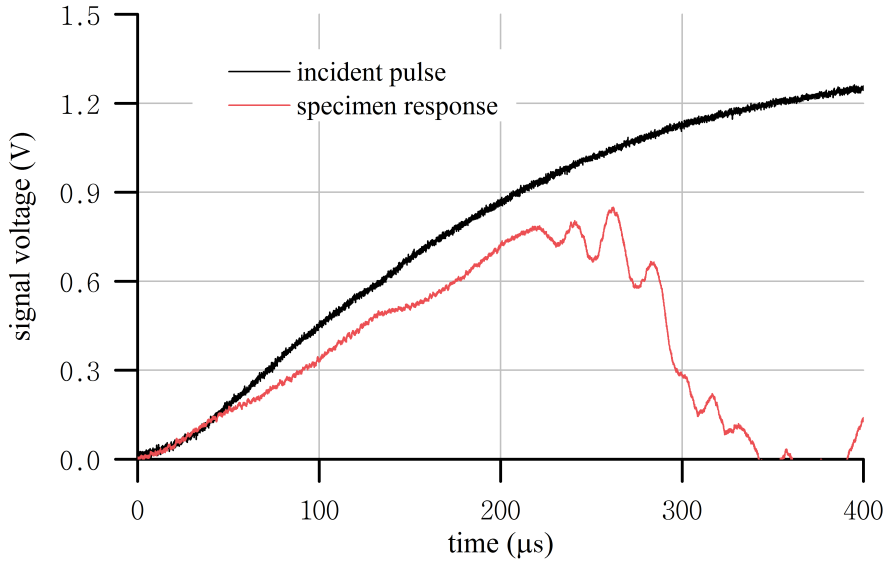


Figure 3.9: Loading pulse in conjunction with the (time-shifted) specimen response of a representative dynamic test

The bar forces acting on the specimen, F_{in} on the input bar end and F_{out} on the output bar end, were determined based via conventional SHB analysis. The force history serving as the basis for the data reduction process was calculated as the arithmetic mean of F_{in} and F_{out}.

In order to obtain the opening displacement history, two additional L-shaped sheet metal parts were mounted to the bar/specimen connector (see **Figure 3.10(a)**). The purpose of these parts was to transfer the load introduction bolts' motion into the high-speed camera's field of view close to the specimen's surface so as to roughly share a common focal plane with the latter. Each of these L-shaped parts carried a speckle pattern, thus allowing for an opening displacement measurement via a DIC-based analysis. The advantage of this approach over determining $x(t)$ via the conventional SHB analysis consisted of bypassing the loading train's considerable additional compliance, which would have distorted the obtained opening displacement history. A direct comparison between those two approaches is provided in **Figure 3.10(b)**, highlighting the necessity to employ a DIC-based measurement to obtain $x(t)$. Lastly, an additional benefit of obtaining the opening displacement history based on the high-speed camera footage lay in the simplification of the time axes alignment of the individual signals, since the measurement of opening displacement and crack tip position shared a common time axis.

The deformation and fracture process was recorded at a rate of $300,000$ fps with a resolution of 924x768 pixels using a high-speed camera (*Specialised Imaging Ltd.*, model: *Kirana*) in conjunction with a *Nikon Micro-NIKKOR* 55 mm lens and a *Nikon PK12-14* extension tube. A sketch of the complete high-rate testing setup is provided

in **Figure 3.11**.

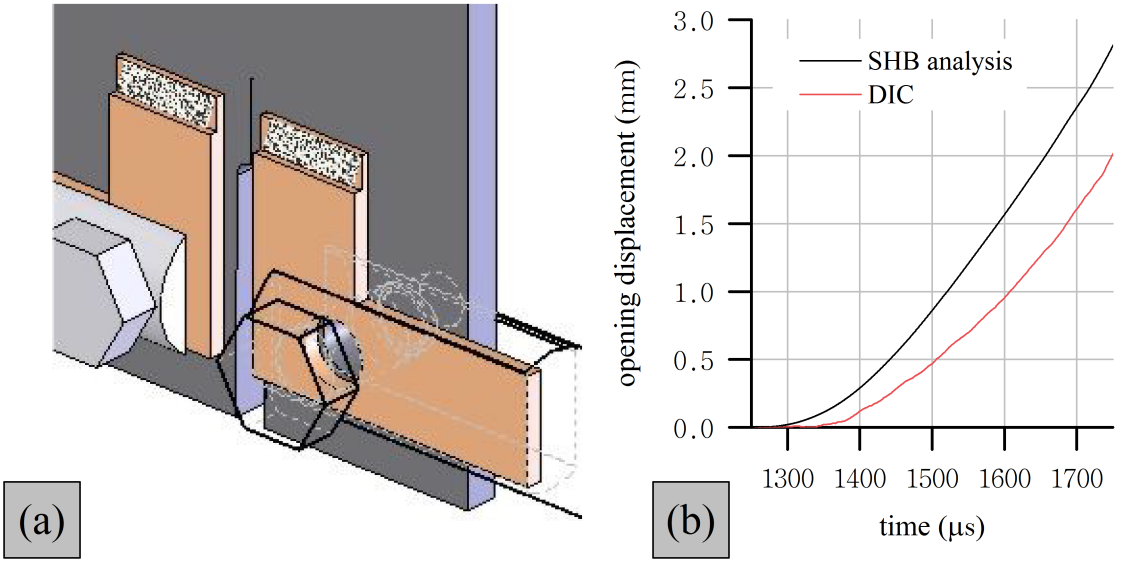


Figure 3.10: (a) 'displacement tracker' to allow for a DIC-based determination of the opening displacement; (b) comparison between an opening displacement measurement based on a conventional SHB analysis and a DIC-based approach

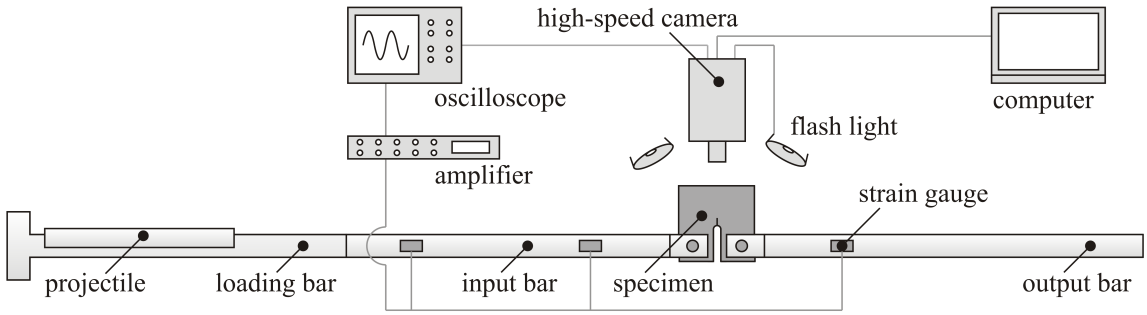


Figure 3.11: Modified split-Hopkinson tension bar and data acquisition setup for the high-rate experiments

3.4 Validity checks for the high-rate experiments

The aim of this subchapter is to provide a critical assessment of the validity of the experiments carried out under high-rate loading conditions. This evaluation covers the following aspects: (i) convergence towards a state of (near) force equilibrium, (ii)

absence of a fracture mode II component, and, (iii) appraisal of possible stress wave interferences with the crack tip stress field.

3.4.1 Convergence towards force equilibrium

The convergence towards force equilibrium with respect to the employed loading pulse was investigated via a numerical model of the experimental setup, see **Figure 3.12**. Considering that *cohesive elements* to reflect the crack path would not have captured the experimentally-observable discontinuous (i.e. 'stick-slip') nature of crack propagation for this failure mode, the aim of the FE-based model was limited to developing a qualitative understanding of the specimen's behaviour up until fracture initiation. An additional simplification to this model was the assumption of rate-insensitivity of its elastic properties.[4]

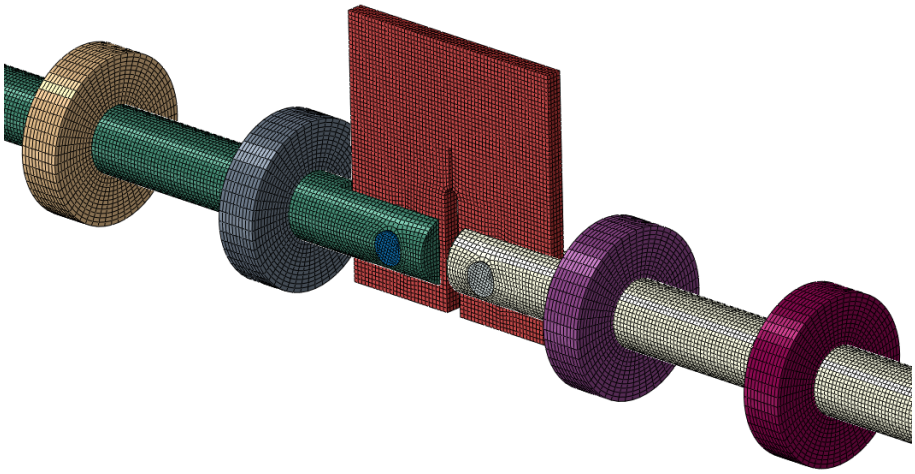


Figure 3.12: Model of the SHTB setup to investigate the specimen's convergence behaviour towards force equilibrium

[4]The material properties of the specimen were based on the relevant QS values detailed in **Chapter 5.1**.

The model was first subjected to an 'unshaped' loading pulse. The reader is referred to **Figure 2.7** in **Chapter 2.1.3** for a plot of this pulse profile's rising slope. **Figure 3.13** presents the corresponding bar forces F_{in} and F_{out} as measured at the load introduction bolts. The simulation results clearly indicated that the approximate force level associated with the onset of crack propagation was exceeded in the input bar before the loading pulse even reached the output bar. It was thus concluded that the high-rate tests necessitated shaping the incident pulse in order to provide enough time for the bar forces to converge to a reasonable level of force equilibrium prior to the onset of the fracture process.

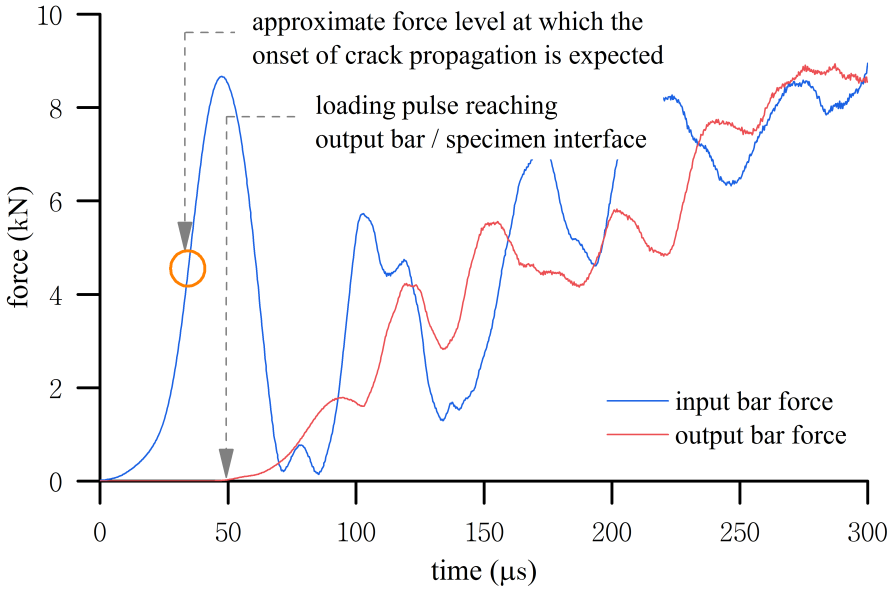


Figure 3.13: Forces measured at the load introduction bolts of input and output bar based on an FE simulation of the entire high-rate testing setup in conjunction with an unshaped incident pulse

The model was then subjected to a loading pulse corresponding to employing a 2.95 mm thick neoprene rubber pulse shaper in conjunction with a projectile velocity of 7.5 m/s. The reader is referred to **Figure 3.9** in **Chapter 3.3.4** for a plot of the resulting incident pulse profile. **Figure 3.14** presents the obtained bar forces F_{in} and F_{out}, as measured at the load introduction bolts, as well as the associated force disequilibrium (calculated according to **Equ. 2.4** in **Chapter 2.1.1**). The simulation results indicated that by the time the bar forces reached the force level associated with crack initiation (approx. 5 kN), the corresponding disequilibrium dropped to an acceptable level of about 10%.

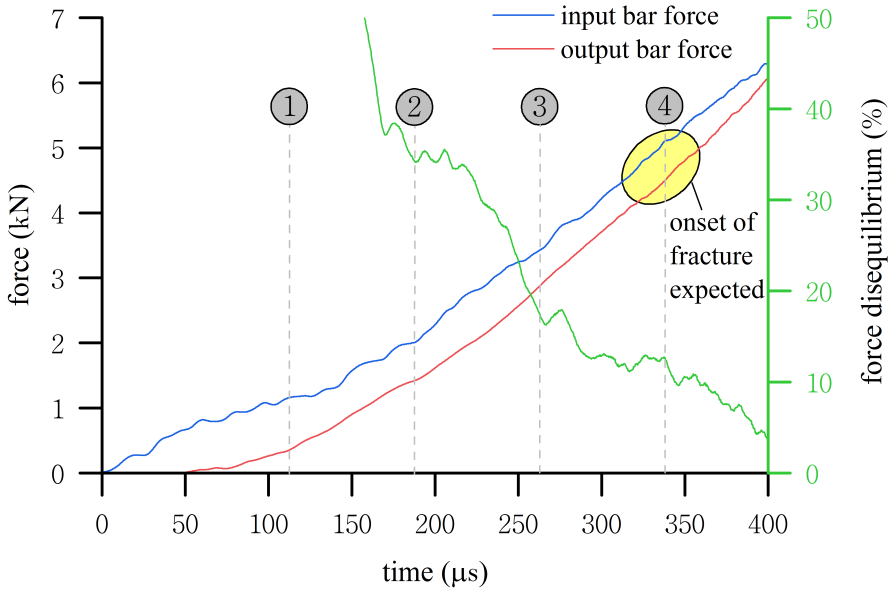


Figure 3.14: Forces measured at the load introduction bolts of input and output bar based on an FE simulation of the entire high-rate testing setup in conjunction with a shaped incident pulse (highlighted timestamps are for reference purposes for the subsequent section)

3.4.2 Mode I loading

In order to associate the experimentally-obtained energy release rate with crack opening under fracture mode I, the specimen's loading component in the bars' axial direction, σ_{xx}, had to be clearly dominant over any (in-plane) shear loading component, τ_{xy}. The presence of this additional shear loading component across the specimen was already encountered, albeit indirectly, in the context of **Chapter 3.3.4**, where those stresses caused a transverse motion component of the bars. A deeper insight into the underlying cause for the development of this additional shear loading component can be obtained from *Beguelin et al. (1997)* [14]. In said study, inertia effects due to the high acceleration of the sample material were found to cause pronounced stress field asymmetries across a CT specimen. This, in turn, resulted in a deviation from a desired (pure) mode I crack opening due to the development of a significant additional mode II component.

For the present study, the FE model outlined in the preceding section was employed to assess the stress field across the specimen. In addition to the model's limitations discussed in the previous section, it must also be kept in mind that the model's mesh density in the vicinity of the crack tip was not high enough for capturing the actual tip's geometric details. The model's scope was thus limited to the investigation of the different stress field components in a more qualitative manner as well as their respective proportion on the resulting stress field across the specimen.

Figure 3.15 presents selected stages of the stress fields pertaining to σ_{xx} and τ_{xy} with reference to the timestamps introduced in **Figure 3.14** in the preceding section. The σ_{xx} field shown in **(a)** indicates no noticeable asymmetries. In order to assess the

influence of the τ_{xy} loading component (shown in **Figure 3.15 (b)**) on the specimen's stress field, **Figure 3.16** presents a plot of the max. principal stress field for the final timestamp. The reasonable symmetry of this stress field's structure was taken as an indication that the shear loading component did not introduce a pronounced fracture mode II component. In order to further substantiate this, **Figure 3.17** presents the evaluation of the ratio of τ_{xy} to the sum of σ_{xx} and τ_{xy} according to

$$\gamma = \frac{|\sigma_{xy}|}{\sigma_{xx} + |\sigma_{xy}|} \tag{3.15}$$

for selected finite elements in direct vicinity of the crack tip. This plot shows that the ratio γ stabilised below the 10% mark after an initial 'ringing-up' period, thus providing further indication of a crack tip stress field which was dominated by the axial loading component, hence resulting in a crack opening essentially under mode I.

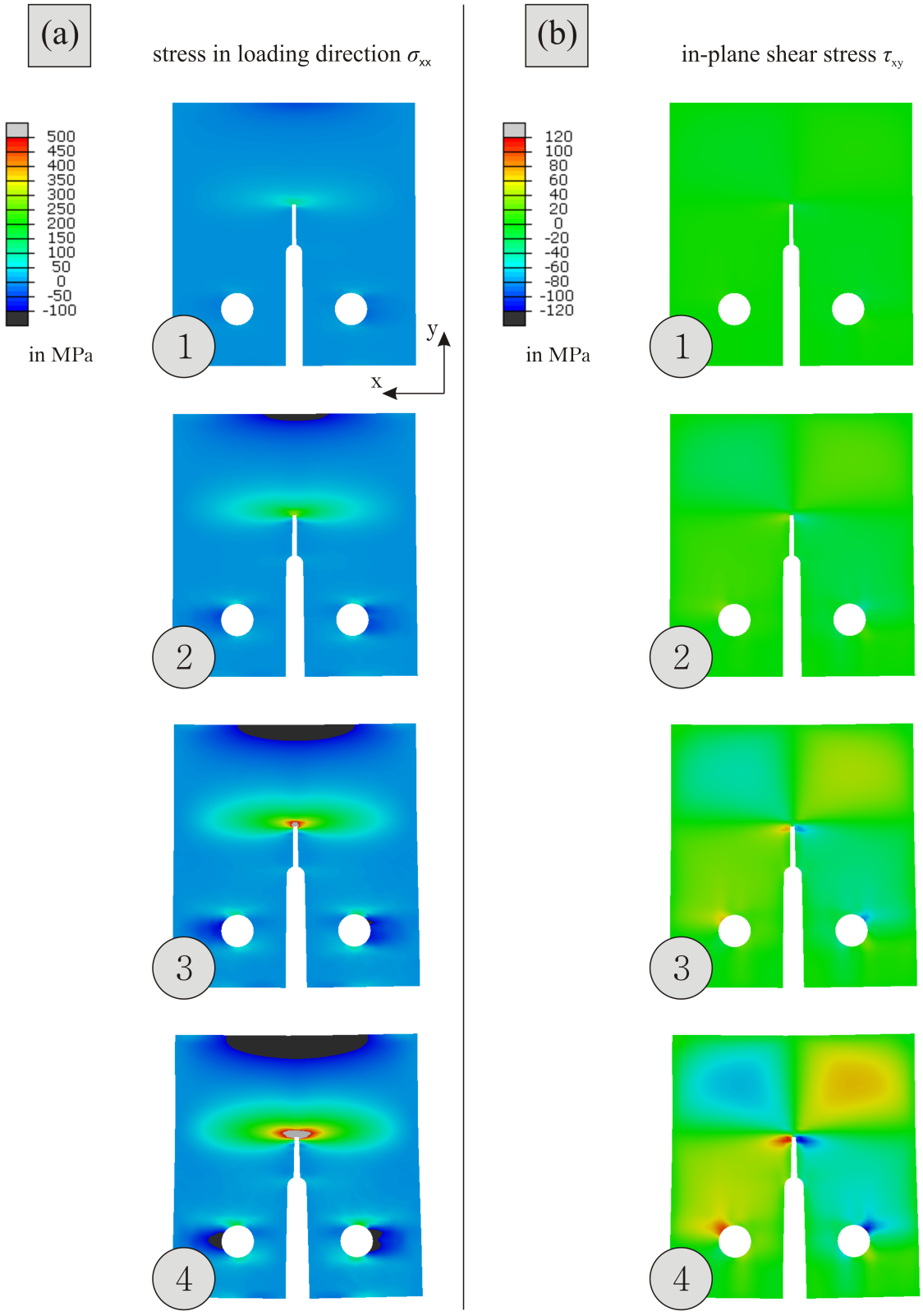


Figure 3.15: Selected states of the stress fields pertaining to (a) σ_{xx} and (b) τ_{xy} (see **Figure 3.14** for the times associated with the timestamps 1 to 4)

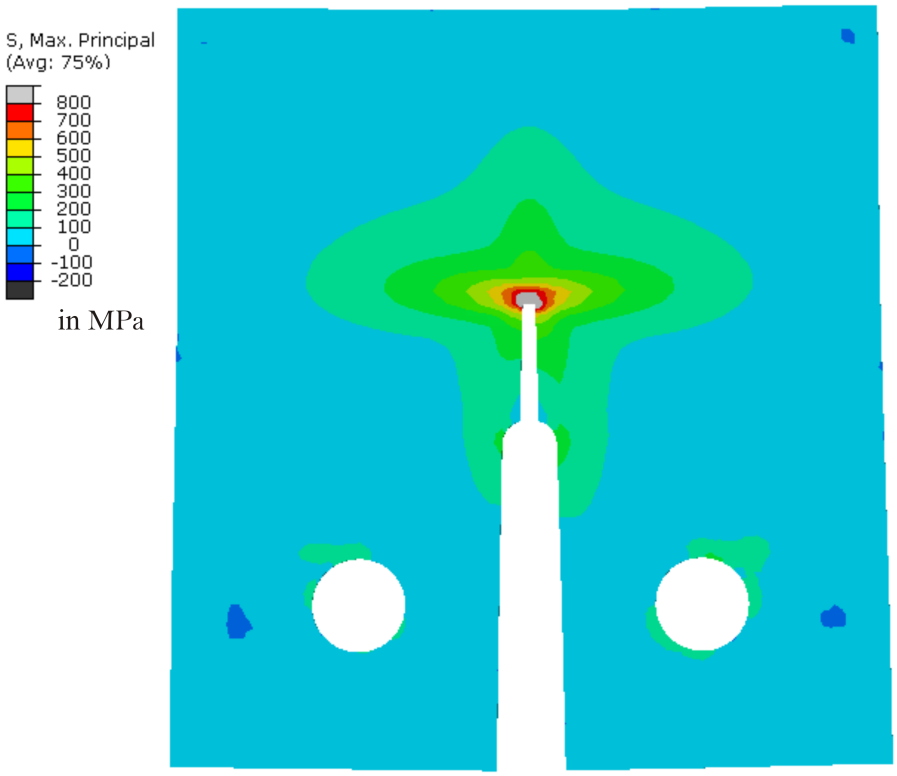


Figure 3.16: State of the max. principal stress field corresponding to 'timestamp 4' in **Figure 3.14**

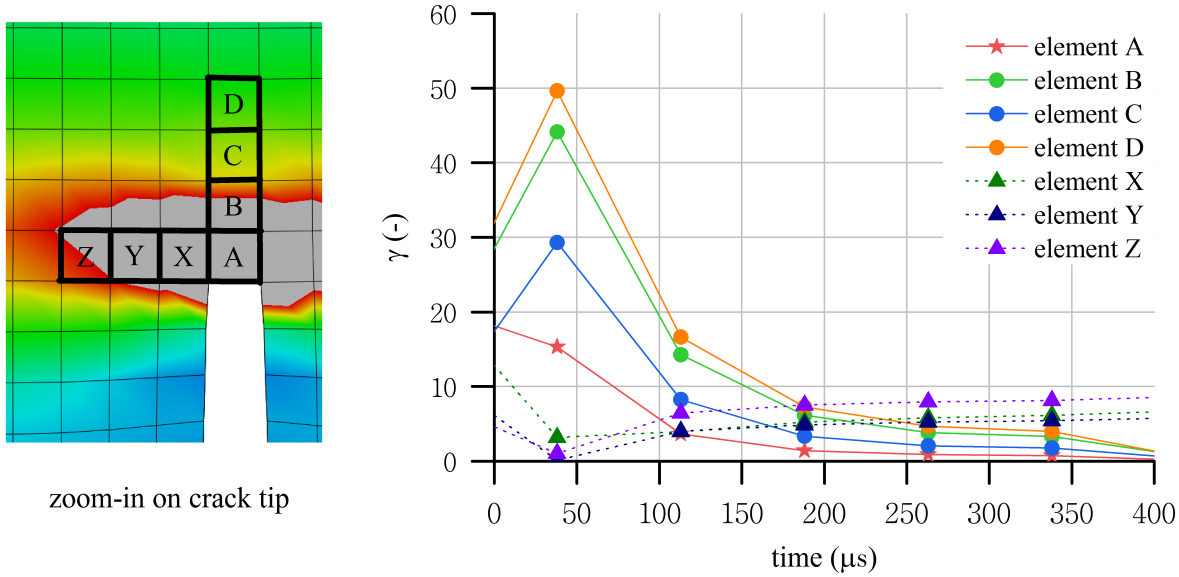


Figure 3.17: Ratio γ of shear stress to the sum of axial and shear stresses for selected elements in direct vicinity of the crack tip

3.4.3 Stress wave interferences with the crack tip stress field

The build-up of the stress field around the crack tip prior to the onset of crack propagation took place in a gradual and continuous manner.[5] Crack propagation, in contrast, occurred in a much more discontinuous manner due to its 'stick-slip' nature. This, in turn, means that crack propagation took place as a series of comparatively large energy releases, each accompanied by pronounced stress waves originating from their respective current crack tip position. These stress waves keep propagating and reverberating until a state of (new) equilibrium is reached. Ideally, any subsequent crack propagation should occur only after this state of equilibrium has been re-established. Otherwise, these reverberating stress waves may interfere with the crack tip stress field, consequently distorting the measuring process.

Unfortunately, the limited number of high-speed camera frames available in the present study did not allow for a DIC-based evaluation of this phenomenon.[6] Further, employing an FE model of the specimen featuring *cohesive elements* to reflect the crack path would not have reproduced the discontinuous nature of crack propagation, thus ruling out this option as well. However, a rough estimate of the time scale of interest was possible to make on the basis of the longest specimen dimension (65 mm, see **Chapter 3.3.1**) and the composite material's wave propagation velocity.[7] This calculation indicated that an elastic wave could have traversed the specimen approximately eight times from the time of the first to the last (usable) crack propagation. This number was

[5] This gradual build-up was observable in both, the FE-based simulation, as described in the previous section, as well as the DIC-based analysis of the specimens which will be detailed in **Chapter 3.6.2**.

[6] With the setup used here, the crack propagation process was captured by approx. 30 frames.

[7] The calculation of the composite's wave propagation velocity was based on the material's QS properties, as detailed in **Chapter 5.1**, and took the specimen's cross-ply configuration into account.

not deemed high enough to confidently rule out any unwanted interferences between reverberating stress waves and the crack tip's stress field. Hence, it must be kept in mind that this phenomenon might have affected the determined mean value of $G^{f+}_{Ic,dyn}$, and, maybe even more so, its associated experimental scatter.

3.5 Elements of the data reduction process

The aim of this subchapter is to outline the key elements of the data reduction process as follows: (i) the rationale for having determined G^{f+}_{Ic} as an averaged value over a series of crack tip propagations, (ii) the relationship between the experimentally-determined G^{lam}_{Ic} and the sought value of G^{f+}_{Ic}, and, (iii) the association of the obtained energy release rate $G^{f+}_{Ic,dyn}$ with a strain-rate measure that is relevant to the constitutive model employed in the present study.

3.5.1 Rationale for determining G^{f+}_{Ic} as an averaged value over a series of crack tip propagations

For the present study, the energy release rate was not evaluated for each of the individual crack tip propagations, but for the cumulative sum of several crack tip advances for each specimen instead. This evaluation was based on **Equ. 3.6**, which was presented in the context of outlining the *area method* in **Chapter 3.2.3**. The reasons for having determined G^{f+}_{Ic} as an averaged value over a series of individual crack jumps are as follows:

- The constitutive model employed in the present study considers only a single value of G_{Ic}^{f+} for governing its stain-softening behaviour under fibre tensile failure. A full R-curve characterisation was thus not necessary.
- The R-curve for *IM7/8552* under quasi-static loading has already been characterised by *Laffan et al. (2011)* [84], who found it to exhibit a constant propagation value. This, then, justified determining G_{Ic}^{f+} as an averaged value which approximates said constant propagation value. A consequence of averaging, however, is that the distinction between the *initiation* and *propagation value* of G_{Ic}^{f+} was lost.
- Averaging G_{Ic}^{f+} over several crack tip advances mitigated the effect of a number of factors that are prone to magnify the degree of experimental scatter, which, in turn, would have rendered the end result less representative. These factors encompass: (i) the varying degree of force disequilibrium over the course of crack propagation, which will be shown in **Chapter 3.6.1**, (ii) the unquantified effect of interfering stress waves with the crack tip stress field, which was described in **Chapter 3.4.3**, (iii) the limited number of high-speed camera frames, which contributed to a certain degree of inaccuracy for the crack tip position determination, and, (iv) the determination of the crack tip's position by means of optical measurement, which is a well-known source of inaccuracy, see *Laffan et al. (2010)* [82]. By having relied on a single crack tip position per specimen representing a comparatively large absolute crack tip propagation value, the influence of these factors was thus minimised.

As a final remark it should be mentioned that determining G_{Ic}^{f+} as an averaged value can only yield meaningful results if the loading conditions under which the crack

propagation took place remained reasonably constant throughout. This was ensured in the present study by subjecting the specimens to an approximately linearly rising incident pulse profile stretching over the whole duration of the specimens' fracture process, see **Chapter 3.3.4**.

3.5.2 Relationship between G_{Ic}^{f+} and G_{Ic}^{lam}

Evaluating the force vs. opening displacement data in conjunction with the crack tip propagation history based on the *area method* facilitated calculating the energy release rate G_{Ic}^{lam} of the cross-ply laminate. In order to extract the sought value of the 0° plies G_{Ic}^{f+} from G_{Ic}^{lam}, *Pinho et al. (2006)* [112] proposed **Equ. 3.16** based on the assumption of the negligibility of any significant interaction between the 0° and 90° plies.

$$G_{Ic}^{f+} = \frac{t_{lam}}{t_0} G_{Ic}^{lam} - \frac{t_{90}}{t_0} G_{Ic}^{IFF} \tag{3.16}$$

In the above equation, t_0 denotes the cumulative thickness of all 0° plies, and t_{90} the cumulative thickness of all 90° plies, respectively.

However, as *Pinho et al. (2006)* also pointed out in [112], the energy release rate due to matrix cracking of the 90° plies is by orders of magnitude lower than the corresponding value for failure in fibre tensile direction of the 0° plies (e.g., compare $G_{Ic,QS}^{IFF} = 0.23$ kJ/m² [34] to $G_{Ic,QS}^{f+} = 147$ kJ/m² [84]). Thus, the last term on the right-hand side of above equation was neglected for the present study.

3.5.3 Association of G_{Ic}^{f+} with strain-rate

In order to finally provide $G_{Ic}^{f+}(\dot{\epsilon})$ for constitutive model calibration, an appropriate strain-rate measure had to be determined.[8] The relevant strain-rate measure is reflected in the experiment as the strain-rate across a reference length perpendicular to the crack propagation direction, intersecting the crack tip. As this approach renders the measured strain-rate to be a function of the reference length, the strain-rate has to be determined for a range of reference lengths. The strain-rate that is then finally chosen for model calibration will be the one corresponding to the reference length that reflects the finite elements' dimension in fibre direction, thus allowing for a direct connection between model parameter and experimentally-observable material behaviour. A depiction of the reference length l_{ref} across which the strain-rate is measured in the experiments, and its representation in an FE modelling context, is given in **Figure 3.18**. As the number of high-speed camera frames capturing the crack propagation process was not enough to allow this measurement to be undertaken for any other than the initial crack tip position, the latter was taken as the reference locus for obtaining the strain-rate.

[8]The determination of a suitable strain-rate measure here assumes a *continuum damage mechanics*-based approach to in-plane damage modelling.

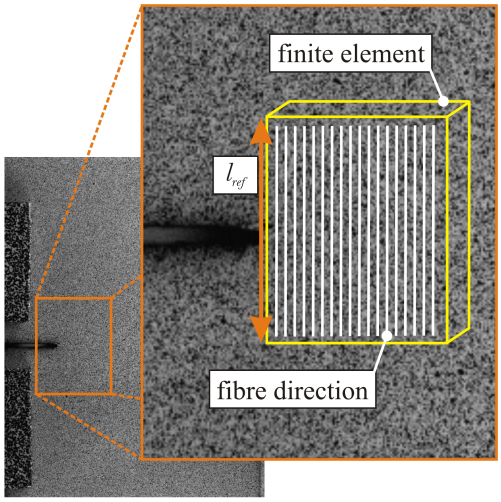


Figure 3.18: Determination of the relevant strain-rate for constitutive model calibration: experimental basis and its relation to FE modelling

3.6 Experimental results and discussion

This subchapter first presents the experimental results for the present study, which is then followed by an attempt to relate the rate-dependent trend found for G_{Ic}^{f+} across two loading rate regimes to the associated changes of the governing mechanisms on micro scale. This is achieved by evaluating the strain field surrounding the advancing crack tip employing DIC, as well as undertaking a fractographic study of the specimens' fracture surface morphology via SEM. Finally, an attempt is made to explain the discrepancy between the findings in the present and *McCarroll*'s [100] study.

3.6.1 Experimental results

Figure 3.19 presents a plot of F_{in}, F_{out}, their average F_m in conjunction with the corresponding force disequilibrium history (as introduced in **Equ. 2.4** in **Chapter**

2.1.1). As can be seen, the bar forces F_{in} and F_{out} converged up until the onset of crack propagation and remained within a range of roughly $5-20\%$ over the course of the crack propagation process. Although the bounds of this range were slightly higher than what would have been desirable, the dynamic experiments were nevertheless considered adequate for the drawing of general conclusions regarding the composite material's behaviour under high-rate loading. An appraisal of the influence of the state of slight force disequilibrium on the obtained value for $G^{f+}_{Ic,dyn}$ will be given later in this section. As a recommendation though, subsequent experiments should aim at lowering the state of force disequilibrium over the course of crack propagation.

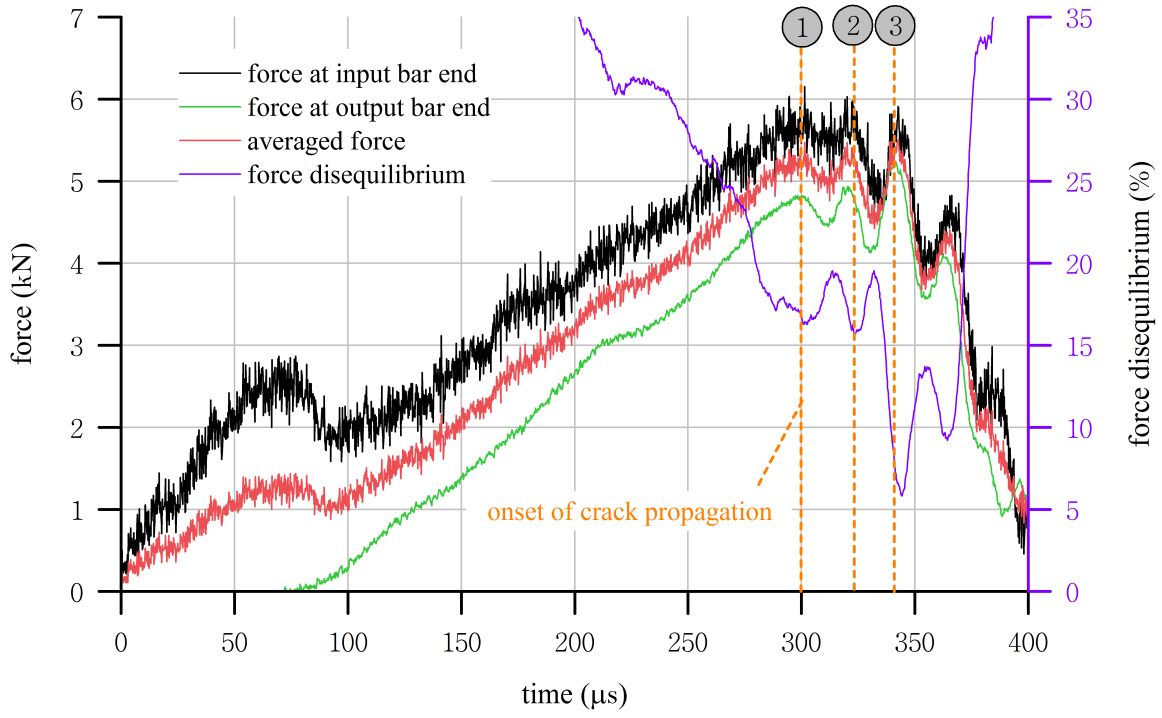


Figure 3.19: Input bar, output bar, and averaged force histories in conjunction with the corresponding force disequilibrium of a representative high-rate experiment (timestamps 1–3 will be referred to by **Figure 3.22** in the subsequent section)

Figure 3.20 presents representative force vs. opening displacement curves for both loading rate regimes. The curve obtained under quasi-static loading exhibited the

well-known stepwise degradation of force level with increasing values of opening displacement (see, for instance, [84]). Against the background of this quasi-static curve, its counterpart obtained under high-rate loading conditions featured a markedly steeper elastic slope, as well as an increase in force at the onset of crack propagation.[9] Further, the force level did not show a steady degradation for each successive crack tip advancement but remained comparatively high throughout. Lastly, as indicated in **Figure 3.20**, the opening displacement necessary to grow the total crack length to a comparable value was smaller under high-rate than for quasi-static loading.

It is worth noting that the specimens tested under high-rate loading failed to re-establish a state of reasonable force equilibrium beyond values of a_{tot} of approx. 10 mm, thus rendering the force vs. opening displacement data beyond this point unusable.

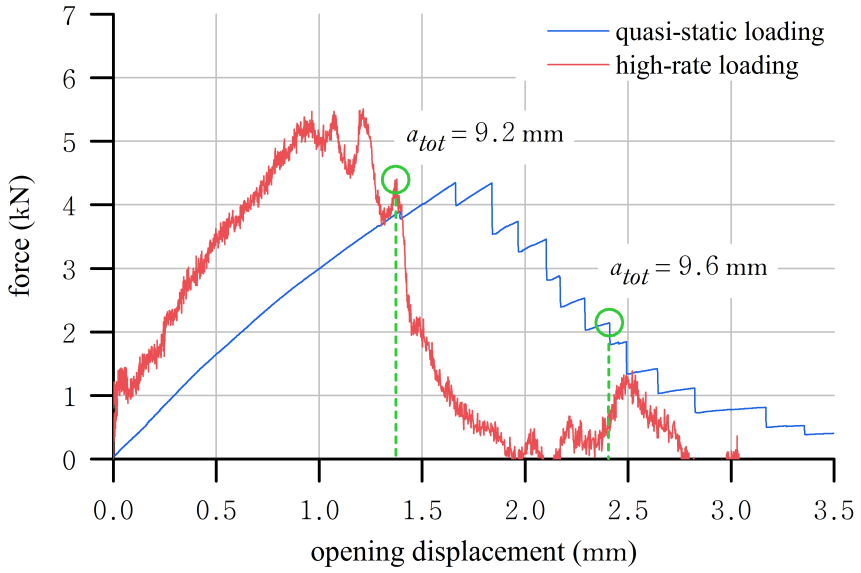


Figure 3.20: Representative force vs. opening displacement curves for both loading rate regimes

[9]It should be noted, however, that the state of slight force disequilibrium might have amplified the magnitude of these phenomena.

A summary of the energy release rate values obtained across both loading rate regimes is provided in **Table 3.3**.

Table 3.3: Summary of determined energy release rate values across both loading rate regimes

		quasi-static loading			high-rate loading		
		specimen designation	G_{Ic}^{f+} kJ/m^2	determined at a_{tot} mm	specimen designation	G_{Ic}^{f+} kJ/m^2	determined at a_{tot} mm
		201	220	14.9	212	52	7.8
		202	178	14.6	214	100	8.2
		203	197	15.5	215	92	9.2
		204	188	15.0	216	84	11.6
mean	kJ/m^2		196			82	
SD	kJ/m^2		18			21	
CV	%		9.2			25.4	

Table 3.4 presents the results of literature sources also having determined G_{Ic}^{f+} for *IM7/8552* under quasi-static loading. Even though specimen designs and/or data reduction methodologies may have deviated between the individual sources, an extraordinarily large range of determined values for $G_{Ic,QS}^{f+}$ is immediately recognisable. The results generated under quasi-static loading conditions in the present study fall within the upper segment of this range of existing data.

Table 3.4: Results of literature sources having determined G_{Ic}^{f+} for *IM7/8552* under quasi-static loading

source		mean prop. value kJ/m^2	SD kJ/m^2	CV %	specimen design	data reduction methodology
Camanho et al. (2007)	[20]	82	6	7.6	CT	not stated
Catalanotti et al. (2010)	[23]	134	-	-	CT	DIC-based
Laffan et al. (2011)	[84]	147	12	8.2	CT	MCC
McCarroll (2011)	[100]	75	7	9.1	CT	**Chapter 3.2.4**
Catalanotti et al. (2014)	[22]	205	-	-	DEN	size-effect law

When comparing the value of G_{Ic}^{f+} determined under high-rate loading to its quasi-static counterpart, a salient decrease was observed. Furthermore, the magnitude of experimental scatter associated with the high-rate tests was much more pronounced.

As the micro-mechanisms involved in a composite's failure in fibre tensile direction (see **Chapter 3.2.1**) resemble, to some extent, those governing the pull-out process of z-pins, it is noteworthy that the dynamic mode I z-pin pull-out experiments carried out by *Cui et al. (2017)* [33] similarly showed a pronounced decrease in their corresponding energy release rate value under high-rate loading.

In light of the state of slight force disequilibrium present over the course of crack propagation, the sensitivity of the obtained value for $G_{Ic,dyn}^{f+}$ with respect to the measured force history was assessed by calculating $G_{Ic,dyn}^{f+}$ based on each of the two force signals individually. In the case of F_{in}, $G_{Ic,dyn}^{f+}$ was found to increase by 10.2% with respect to the value given in **Table 3.3**; the corresponding calculation based on F_{out} resulted in a decrease by 6.2%. These deviations from the reference value (based on the arithmetic mean of F_{in} and F_{out}) were taken as an indication that the state of slight

force disequilibrium over the course of crack propagation did not excessively influence the value obtained for $G^{f+}_{Ic,dyn}$, especially against the background of the pronounced experimental scatter experienced for the high-rate tests.

The association of strain-rate with the determined values of G^{f+}_{Ic} for both loading rate regimes followed the approach outlined in **Chapter 3.5.3**. **Figure 3.21** presents the obtained strain-rate values for a range of reference lengths. This range attempted to roughly cover commonly used in-plane finite element dimensions.

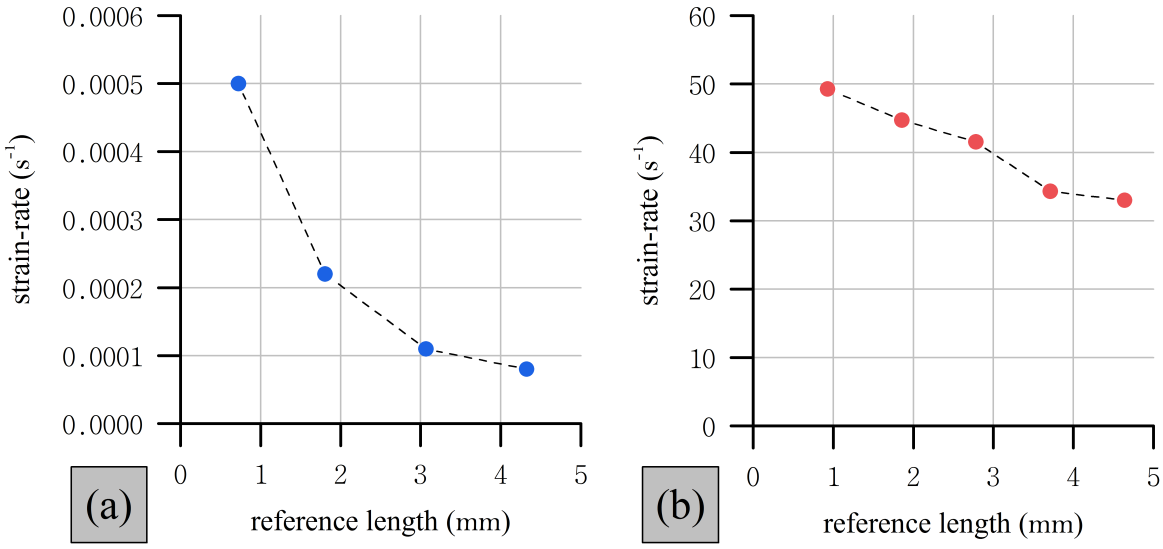


Figure 3.21: Determined strain-rate values for (a) quasi-static loading, and (b) high-rate loading for a range of reference lengths

3.6.2 Strain field analysis via DIC

The shape, extent, and magnitude of the strain field surrounding the advancing crack tip was investigated via DIC using *GOM Aramis*. The main goal of this analysis was to study the effect of the applied loading rate on the strain experienced by the critical load-bearing 0° fibres perpendicular to the crack tip.

As the DIC investigation is based on analysing the speckle pattern applied to the 90°

surface layer, the 0° plies' behaviour cannot be studied directly. However, the strain field on the specimens' outer surface in loading direction (i.e. along the x-direction in **Figure 3.22**) is dominated by the behaviour of the 0° plies due to their much higher stiffness compared to that of the 90° layers. This stiffness discrepancy, however, also means that the strain field parallel to the crack plane (i.e. along the y-direction in **Figure 3.22**) is majorly influenced by the mechanical behaviour of the surface 90° ply. This ultimately means that, on the one hand, the strain field obtained *in loading direction* can be assumed to be a viable reflection of the state of strain experienced by the critical load-bearing 0° fibres, but, on the other hand, the strain field *transverse to the loading direction* should not be taken to be a direct representation of the strain experienced by these fibres.

Select frames pertaining to a representative DIC analysis of a specimen tested under quasi-static and high-rate loading, respectively, are provided in **Figure 3.22**. The plots show the strain field surrounding the crack tip immediately prior to crack tip advancement.

The DIC analysis of a representative specimen tested under quasi-static loading showed an extensive and sharply defined high-strain zone (colour code: red and orange). This is in salient contrast to the strain field under high-rate loading, which showed a very compact, less defined, and less intense high-strain zone.

The key conclusion that was drawn from the DIC analysis presented here was that a larger section of the length of the critical load-carrying fibres orthogonal to the crack tip was involved in the fracture process under quasi-static compared to high-rate loading. This, in turn, was taken as an indication of the fracture process under high-rate loading

being a more locally confined phenomenon, involving a smaller material volume.

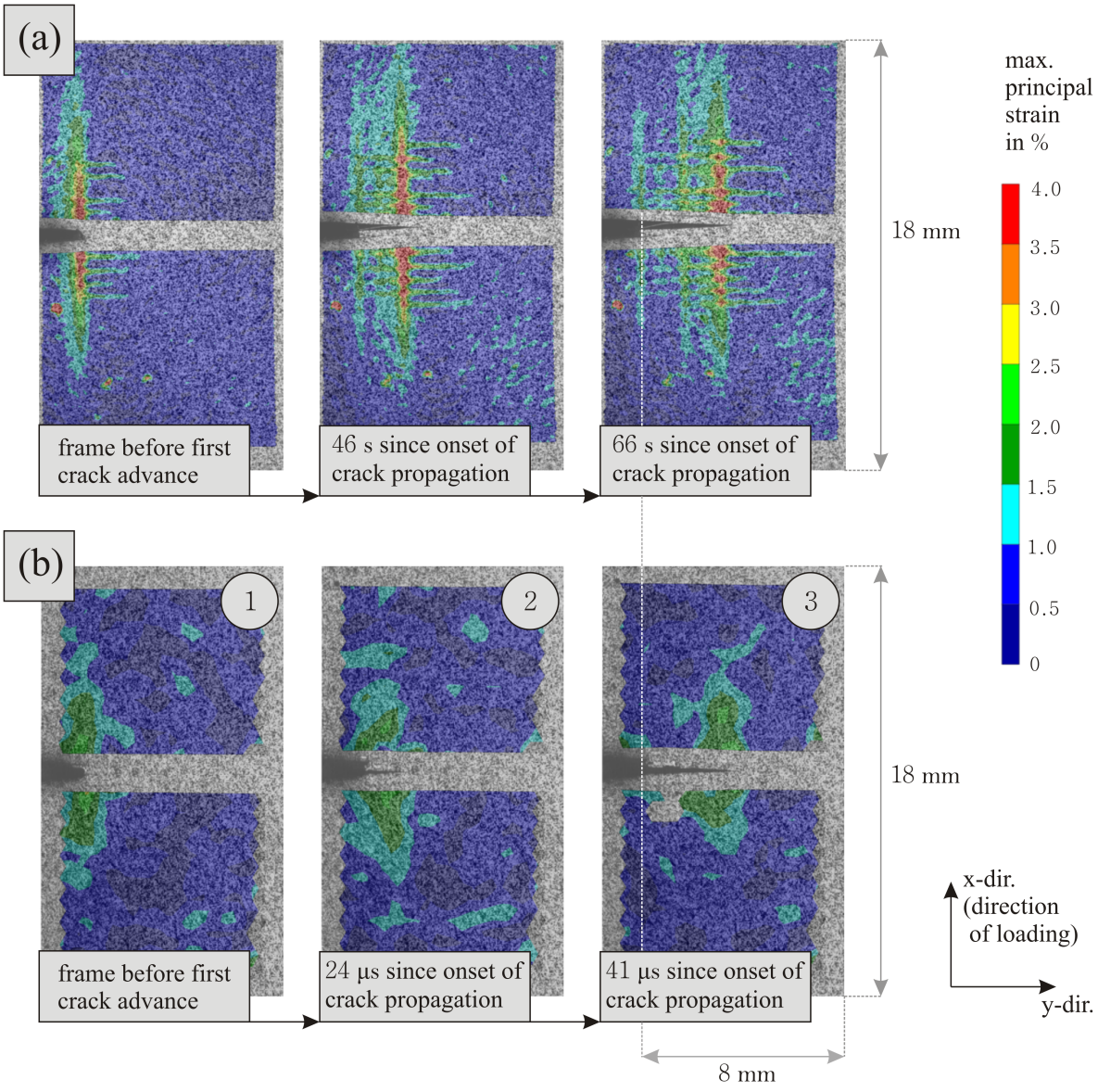


Figure 3.22: Strain field surrounding the crack tip for several stages of crack tip advancement under (a) quasi-static loading, and (b) high-rate loading (the times associated with the timestamps 1–3 for the latter can be found in **Figure 3.19** in the preceding section)

3.6.3 Fractography via SEM

As was described in the context of introducing a composite's failure in fibre tensile direction on micro scale, there are several mechanisms that are involved in the energy dissipation process: matrix cracking, fibre/matrix debonding, fibre rupture, and fibre pull-out (see **Chapter 3.2.1**). Of these, investigating the fracture surface morphology via SEM may allow assessing the overall level of fibre length involved in the fibre/matrix debonding and subsequent fibre pull-out process. The samples were coated prior to scanning to prevent the electrically non-conductive matrix material to build up charge. This process employed palladium/gold as coating material (thickness: approx. 3 nm).

Figures 3.23 and **3.24** show representative images of multiple 0° plies across the specimen's through-thickness direction for loading under quasi-static conditions; **Figures 3.25** and **3.26** depict the corresponding images for high-rate loading. No obvious differences in the fracture surface morphologies across the two loading rate regimes could be detected. In particular, no difference in terms of the overall level of the length of fibres protruding from the specimens' fracture plane could be observed. This result is congruent with *McCarroll*'s *(2011)* [100] SEM-based post-mortem study, even though the specimens tested under high-rate loading in said study were subjected to a loading pulse profile differing from the one employed in the present work.

At a higher magnification level capturing the fracture surface morphology of a single 0° ply, the tendency of a greater fibre length protruding from the fracture plane with increasing distance from the adjacent 90° plies was consistently observed in the SEM scans of specimens of both loading rate regimes, see **Figure 3.27**. This phenomenon

can be interpreted as the adjacent 90° plies' increased ability to constrain the level of fibre pull-out in the 0° plies with increasing proximity, see **Chapter 3.2.2**.

Even though fractography was not able to yield any direct indications regarding the micro-mechanical origin of the change of G_{Ic}^{f+} under high-rate loading, it should, however, be mentioned that the absence of any obvious changes in fracture surface morphology in itself does not allow for the drawing of any 'final conclusions', as the energy dissipated by each failure mechanism on micro scale is also dependent on the respective forces involved. Against this background, in the above-mentioned study carried out by *Cui et al. (2017)* [33], the measured negative strain-rate trend of G_{Ic}^{del} was linked to a decrease in frictional resistance to pull-out between the carbon-fibre/epoxy z-pins and the composite laminate under high-rate loading conditions. Provided that this mechanism, observed on a 'fibre-bundle level', similarly affects the fibre pull-out of single fibres (or small groups of fibres), this decrease in frictional resistance under high-rate loading could thus provide a (partial) explanation for the strongly negative strain-rate trend found for G_{Ic}^{f+} in the present study.

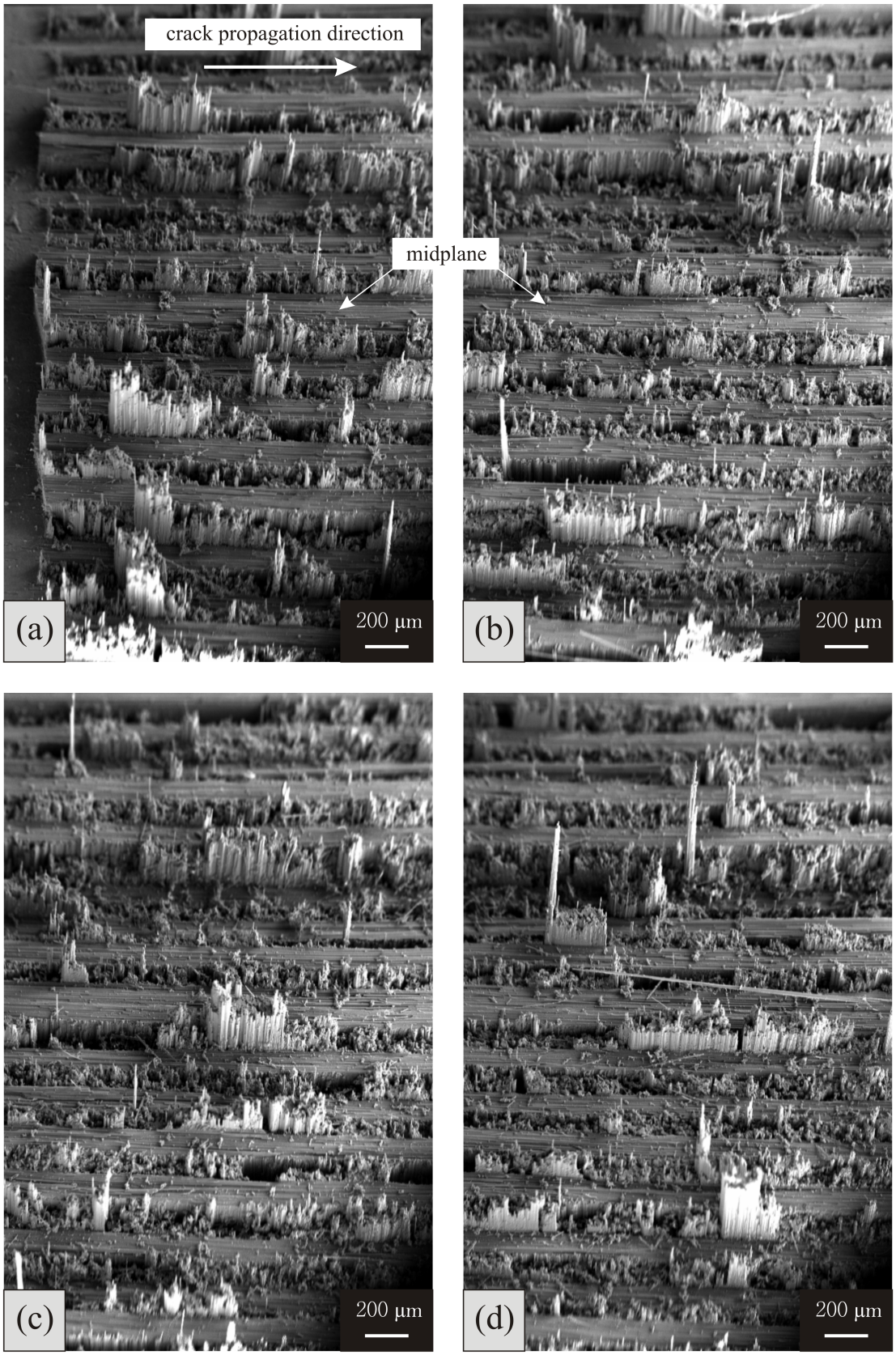


Figure 3.23: SEM images of multiple 0° plies across the specimen's through-thickness direction for quasi-static loading (covering the total crack length from approx. 0 to 10 mm from image (a) to (d))

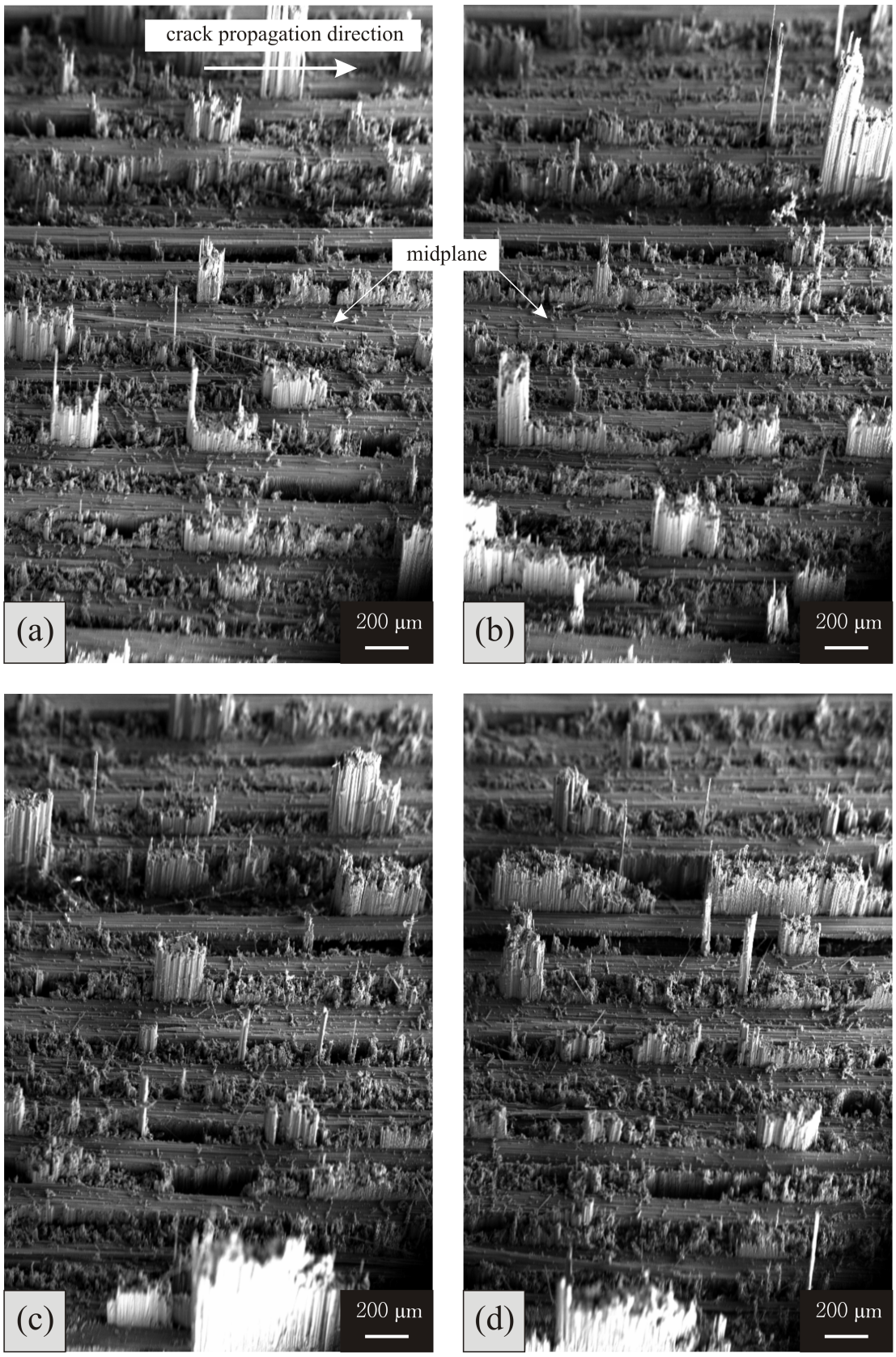


Figure 3.24: SEM images of multiple 0° plies across the specimen's through-thickness direction for quasi-static loading (covering the total crack length from approx. 10 to 20 mm from image (a) to (d))

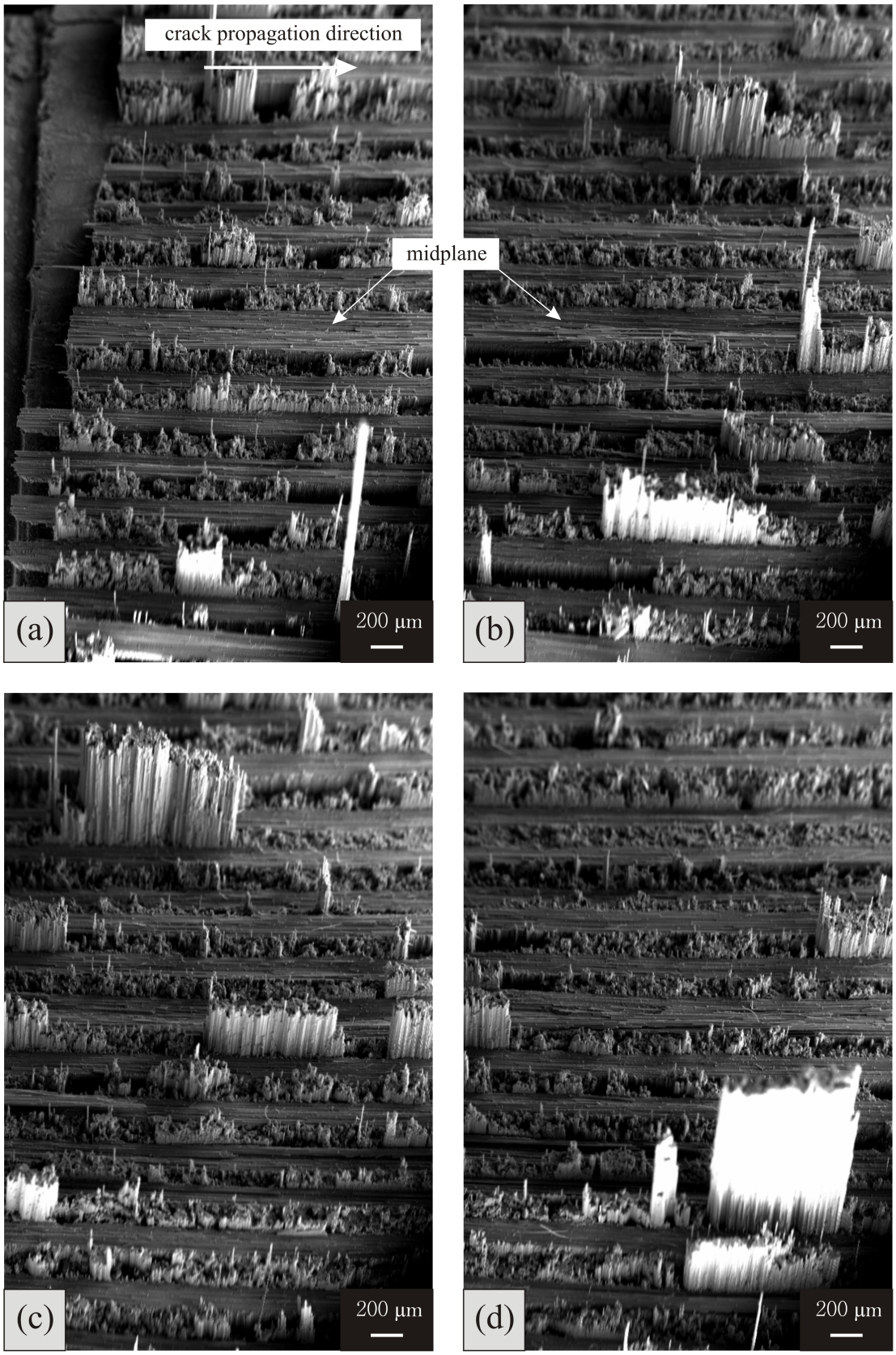


Figure 3.25: SEM images of multiple 0° plies across the specimen's through-thickness direction for high-rate loading (covering the total crack length from approx. 0 to 10 mm from image (a) to (d))

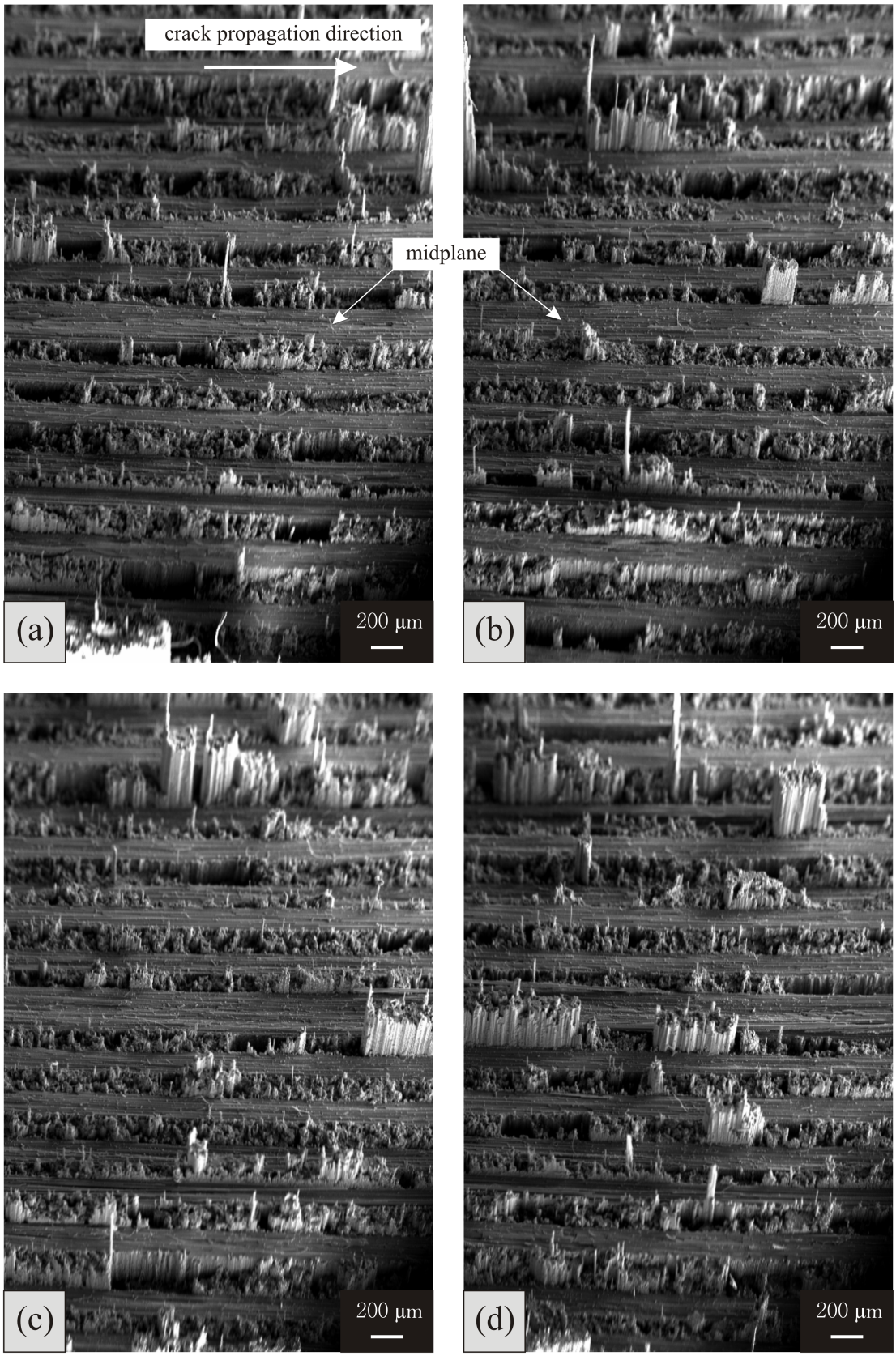


Figure 3.26: SEM images of multiple 0° plies across the specimen's through-thickness direction for high-rate loading (covering the total crack length from approx. 10 to 20 mm from image (a) to (d))

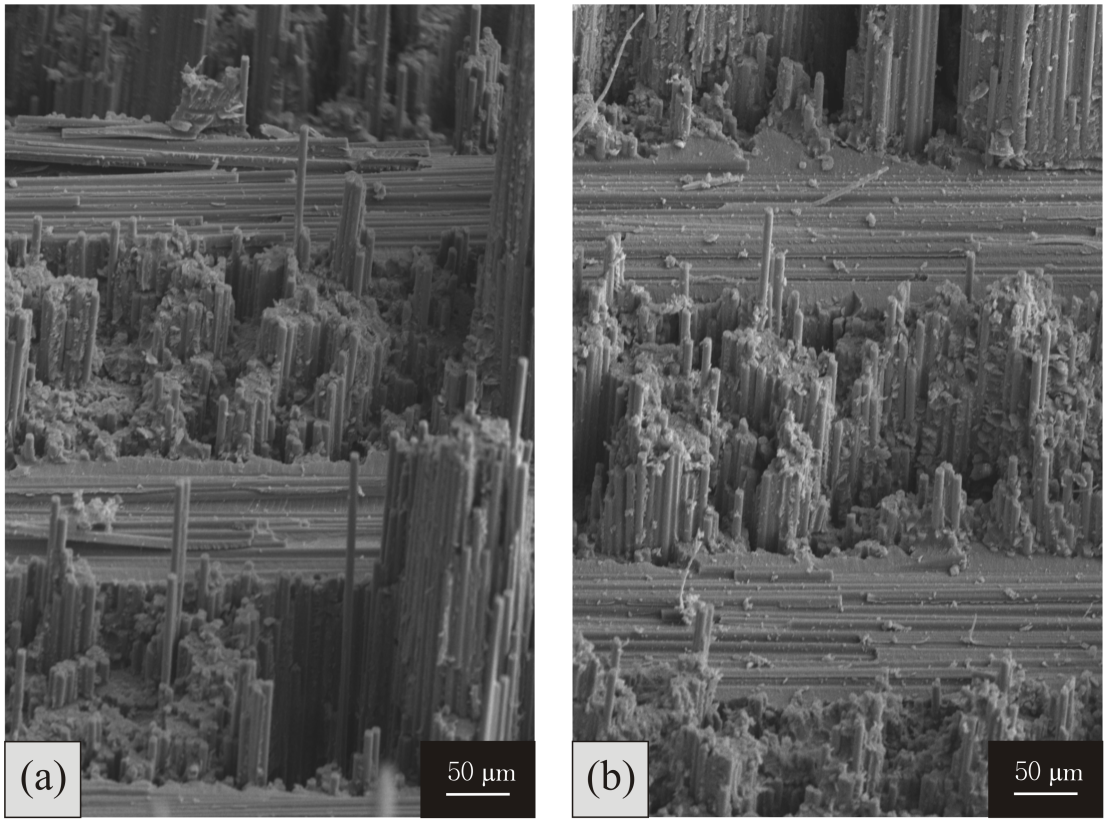


Figure 3.27: SEM images of a single 0° ply, showing the constraining effect of 90° layers on adjacent 0° plies for (a) quasi-static loading, and (b) high-rate loading

3.6.4 Attempt to explain the discrepancy between the present and *McCarroll*'s study

In contrast to the present work, *McCarroll (2011)* [100] found G_{Ic}^{f+} to exhibit a nearly rate-insensitive behaviour.[10] In order to provide a possible explanation for this discrepancy, the assumption of rate-insensitivity of the key parameters k and S in *McCarroll*'s data reduction approach was examined against the background of the data generated in the context of the present work.

As a simple check, both parameters were evaluated for each loading rate regime based

[10]The reader is referred to **Chapter 3.2.4** for an outline of *McCarroll*'s study.

on the force vs. opening displacement curve's elastic slope in the immediate vicinity of the specimen's elastic limit. Beyond this point, a meaningful interpretation of the results of this evaluation proved difficult in case of the high-rate tests due to severe fluctuations of the obtained values caused by the stick-slip nature of crack propagation. When approaching the sample's elastic limit, the value for k under high-rate loading exhibited a decrease of approx. 17% compared to its counterpart for quasi-static loading. Similarly, the value for S showed a decrease of approx. 50% compared to the quasi-static loading case.

On the basis of these discrepancies, albeit mildly distorted due to the existing state of slight force disequilibrium, it could be argued that the rate-dependent nature of the composite material's properties has a considerable effect on the sample's deformation behaviour, thus necessitating a data reduction approach that takes this into account (or, alternatively, as was done in the present study, that does not rely on the material's properties in the first place). *McCarroll*'s assumption of rate-insensitivity for these two central data reduction parameters might thus explain the discrepancy in the findings between [100] and the present study.

3.7 Recommendations for improvements for further high-rate testing

On the basis of the material characterisation carried out in the present study to determine $G^{f+}_{Ic,dyn}$, several recommendations that aim to improve the quality of the obtained results or their interpretation are made:

- **Reducing the steepness of the incident pulse's rising slope**. This is considered to be the most pressing modification for the high-rate determination of $G_{Ic,dyn}^{f+}$ in subsequent studies. On the one hand, this would allow for the determination of a more accurate value of $G_{Ic,dyn}^{f+}$ as inertia forces would have a lesser influence on the material's response. On the other hand, the potential influence of reverberating stress waves on the crack tip's stress field could be reduced, ideally ruling out their influence altogether. However, addressing those two issues could also potentially be accomplished by employing a loading pulse featuring a constant velocity 'plateau' over the course of the crack propagation process (similar to the loading pulse employed by *McCarroll (2011)* [100]) instead of a linearly rising pulse profile.
- **Increasing the number of high-speed camera frames**, especially for the crack propagation stage. This refined temporal resolution of the fracture process would facilitate a more precise association of the measured peaks of the force vs. opening displacement plot with the corresponding crack tip position $a(t)$. Furthermore, the strain field build-up process around the crack tip, as was discussed in **Chapter 3.6.2**, could be studied more comprehensively. Finally, an increased number of high-speed camera frames in conjunction with a fracture process closer to force equilibrium (see previous bullet point) are deemed necessary for a meaningful establishment of an R-curve for $G_{Ic,dyn}^{f+}$ in future studies.
- **Refined post-mortem analysis** so as to allow for a more exhaustive insight into the relationship between the measured material properties on macro scale and the corresponding changes in the governing mechanisms on micro scale. On the one hand, this could involve a more in-depth investigation of a (potentially) more

extensive damage zone for testing under quasi-static than for testing under high-rate loading conditions, as was indicated by the DIC-based analysis of the strain-field surrounding the advancing crack tip in **Chapter 3.6.2**. On the other hand, the SEM-based fractography undertaken in **Chapter 3.6.3** did not show any substantial difference in the fracture surface morphology across the two loading rate regimes. In particular, the pull-out length did not seem to noticeably differ. In order to gain more insight into the rate-sensitivity of the governing mechanisms on micro scale, it is thus recommended to study the single fibre pull-out behaviour at very high loading rates for a carbon-fibre/epoxy material system to quantify the change in dissipated energy due to fibre/matrix debonding and subsequent fibre pull-out as a function of loading rate.

- **Additional high-rate tests**. The number of tested specimens for the present study was comparatively low. Additional tests under high-rate loading conditions would thus be desirable in order to increase the results' representative nature.
- **Reproducibility**. As is evident against the background of the summary of all available sources in literature having obtained $G_{Ic,QS}^{f+}$ in **Table 3.4** in **Chapter 3.6.1**, the determined energy release rate for identical material systems can differ substantially depending on the source: compare $G_{Ic,QS}^{f+} = 75$ kJ/m^2 obtained by *McCarroll (2011)* [100] to $G_{Ic,QS}^{f+} = 205$ kJ/m^2 determined by *Catalanotti et al. (2014)* [22]. As the experimental scatter, where quoted, was within reasonable bounds, and differing data reduction schemes cannot (solely) explain the magnitude of this discrepancy (see *Laffan et al. (2010)* [82]), it becomes clear that it is essential to explore the nature of this currently poor reproducibility. A general lack of reproducibility would otherwise put the experimental results' status as

a *material property* and thus, by extension, their usefulness as a model input parameter, in question.

- **Embedding the high-rate testing results in a dataset obtained over a more densely populated loading rate spectrum**. For the purpose of parameterising $G_{Ic}^{f+}(\dot{\epsilon})$ for constitutive model input, additional data points would significantly increase the ability to establish a qualitatively and quantitatively appropriate fit function. As the loading conditions employed in the present study already marked (or even slightly exceeded) the upper end of the testable strain-rate spectrum[11], at a bare minimum, an additional data point for $G_{Ic}^{f+}(\dot{\epsilon})$ in the order of magnitude of 0.1 to 1 s^{-1} would be desirable.[12]
- **Higher accuracy for crack tip position determination**. The crack tip detection based on optical means is a well-known source of inaccuracy (e.g. *Laffan et al. (2010)* [82]). Similar to the existing methods of addressing this issue for testing under quasi-static loading, such as bypassing the measurement of the advancing crack tip in the experiment via the CC or MCC method (see **Chapter 3.2.3**), or employing X-ray tomography in order to *in-situ* track the crack tip's advance within the material's volume, see *Nikiskov et al. (2016)* [105]), it would be desirable to develop means that could allow for a higher accuracy for the determination of the position of the advancing crack tip under high-rate loading conditions.

[11] assuming the specimen design, material, and qualitative loading pulse profile employed in the present study

[12] referring to the strain-rate measure outlined in **Chapter 3.5.3**

3.8 Summary and conclusion

The contents of this chapter may be summarised as follows:

- In order to allow for a successful design and analysis process of aerospace composite components against critical impact loading events, such as *bird strike*, the material's rate-dependent behaviour must be adequately accounted for. In contrast to delamination failure, the rate-dependent nature of the energy release rate for tensile failure in fibre direction has barely been addressed in existing literature.
- This study employed a *compact tension* specimen design consisting of a cross-ply configuration of *IM7/8552* unidirectionally-reinforced prepreg layers. Quasi-static loading tests were carried out on a screw-driven test machine. High-rate loading tests were conducted on a modified SHTB system. In contrast to the only previous attempt to characterise $G_{Ic}^{f+}(\dot{\epsilon})$ (*McCarroll (2011)* [100]), this high-rate testing setup was able to provide clear force history data. The incident pulse profile was shaped using a pulse shaper, resulting in a linearly rising incident pulse profile covering the specimens' entire deformation and fracture process.
- The force vs. opening displacement curve for high-rate testing showed a markedly different behaviour when juxtaposed against its quasi-static counterpart. The most salient differences included: (i) a steeper rising flank, (ii) a higher force at the onset of crack propagation, and, (iii) an overall higher force level over the course of crack propagation. The averaged energy release rate, obtained using the *area method*, amounted to 196 ± 18 kJ/m^2 for quasi-static testing ($\dot{\epsilon} \approx 0.0001$ s^{-1}) and 82 ± 21 kJ/m^2 for high-rate testing ($\dot{\epsilon} \approx 40$ s^{-1}), thus re-

vealing a significant drop of G_{Ic}^{f+} when the composite material was subjected to an elevated loading rate.

- A DIC-based analysis of the strain field surrounding the propagating crack tip indicated the involvement of a more extensive length of the critical load-carrying 0° fibres in the fracture process under quasi-static than high-rate loading. This observation, in turn, was taken as an indication of a less extensive material volume being involved in the fracture process under a high-rate loading regime. An SEM-based fractographic study did not show any readily detectable differences between the fracture surface morphologies across the two loading rate regimes.

The findings generated in the context of the present chapter bear a significant implication for the design and dimensioning process of aerospace composite components threatened by impact loading entailing fibre tensile failure. Considering that the energy release rate G_{Ic}^{f+} suffers a salient drop under high-rate loading conditions, a simulation-based design and dimensioning process that does not account for this strongly negative loading rate trend might not be able to provide a realistic basis on which an accurate assessment of a composite component's ability to withstand a specific design-critical impact loading case is possible.

Chapter 4

Constitutive model

This chapter presents a description of the purpose, algorithm, merits and limitations of the constitutive model developed to reflect the rate-dependent mechanical behaviour of a composite laminate. First, the model's motivation and aim is introduced, followed by a description of its main premise and high-level structure. Then, the model's calculation of the state of stress, the detection of all relevant failure modes, and its damage evolution behaviour are outlined and the corresponding governing equations presented. Thereafter, the incorporation of rate-effects on the various material properties is described, followed by the development of a suitable strain-rate smoothing algorithm to enforce numerical stability. Lastly, a study is presented which seeks to quantify the finite element dimensions that limit the usage of the experimentally-determined set of energy release rates for the constitutive model's damage evolution algorithm.

Main contributions to the body of knowledge contained in the present chapter at a glance:

- Development of an economical constitutive model that reflects the rate-dependent elastic, failure, and damage evolution behaviour of a composite laminate.
- Development of a strain-rate smoothing algorithm that seeks to enforce numerical stability whilst preserving the 'high strain-rate nature' of an impact loading event.
- The constitutive model has been adopted as part of the production code for the design and analysis process of a turbofan engine fan blade at *Rolls-Royce plc*.

4.1 Motivation and aim of the model

Simulating design-critical impact loading events on large aerospace composite material components, such as a fan blade of a turbofan engine subjected to *bird strike*, poses considerable challenges. A major difficulty in this context is the very large number of finite elements required for reflecting the laminated composite structure. In case of employing a conventional composite constitutive model representing the laminate in a ply-by-ply manner, this number of elements, and, by extension, the effort required to solve the corresponding numerical model, may easily lead to prohibitively high run times. An additional issue of representing the laminate by employing (at least) one finite element in each ply's through-thickness direction is that the corresponding FE mesh usually features very poor edge length ratios due to the elements' typically much larger in-plane dimensions. This poor mesh quality due to these very 'flat' elements, in turn, is a well-known cause of reductions in accuracy of the finite element method (e.g. [93]). In the foreseeable future, these issues are likely to become even more pressing,

as ultra-thin plies have been demonstrated to exhibit superior mechanical properties over the current generation of prepregs (e.g. [2, 127, 140]).

In order to address the issues resulting from a modelling approach that represents each lamina separately, the constitutive model presented in this chapter aims at facilitating a reflection of the composite's behaviour across a multitude of unidirectionally-reinforced plies of arbitrary orientation within a single *representative volume element* (RVE). This, in turn, then allows for employing a coarser finite element mesh, resulting in economically viable model run times for the design and dimensioning process of large composite aerospace structures subjected to impact loading.

The constitutive model presented in this chapter was implemented as a user-defined material model in the SMP version of *LS-Dyna 7.1.2* for *single integration point hexahedral elements*. The modelling work carried out in the context of the present thesis built upon the original version of this constitutive model coded by *Jens Wiegand* [145]. The improvements over this original version mainly focussed on the implementation of all rate-dependent aspects of the model, including a strain-rate smoothing algorithm.

4.2 Main premise of the model and overview of its structure

Within the framework of a finite element algorithm, the main purpose of a constitutive model is to calculate the elements' stress tensor components on the basis of the corresponding (incremental) strain tensor components that enter the constitutive model subroutine. Against the background of its representation of a multitude of individual

plies within a single RVE, the constitutive model described in the present chapter rests on the main premise that the delamination between those individual plies is entirely driven by the RVE's out-of-plane stresses σ_{33}, σ_{23}, and σ_{31}, whereas any failure and damage evolution within the plies is exclusively linked to the RVE's in-plane stresses σ_{11}, σ_{22}, and σ_{12}. This, in turn, allows for the RVE's treatment on the basis of two separate 'submodels': A *delamination model* for its out-of-plane and a *ply model* for its in-plane behaviour. As a consequence, the constitutive model describing the RVE's behaviour incorporates considerations made on two length scales:[1]

- The delamination model operates on macro scale within the laminate coordinate system. Its deformation and failure analysis is based on a homogenised stiffness tensor in order to reflect the RVE's behaviour across a multitude of plies.
- The ply model operates on meso scale within each ply's material coordinate system. Its deformation and failure analysis for the set of its governing failure modes, fibre tensile and compressive failure, and IFF, is based on the stiffness tensor of each individual ply. The RVE's homogenised in-plane stress tensor components are ultimately obtained via the sum of their appropriately rotated relevant counterparts, taking into account the respective ratio μ_k of their ply thickness t_k to the total thickness of the N plies contained in the RVE:[2]

[1] See **Chapter 1.2** for an introduction to the length scales and corresponding coordinate systems commonly employed in the context of composite material modelling.

[2] What is referred to as 'plies' throughout the present chapter may also be understood in a more general sense as 'the entirety of plies of a particular orientation'.

$$\begin{aligned}\sigma_{11} &= \sum_{k=1}^{N} \mu_k \sigma_{11}^k \ , \\ \sigma_{22} &= \sum_{k=1}^{N} \mu_k \sigma_{22}^k \ , \\ \sigma_{12} &= \sum_{k=1}^{N} \mu_k \sigma_{12}^k \ ,\end{aligned} \tag{4.1}$$

with

$$\mu_k = \frac{t_k}{\sum_{p=1}^{N} t_p} \ . \tag{4.2}$$

For the remainder of this chapter, all vectorial and tensoral entities, including their constituent elements, will be denoted by an additional *tilde* symbol if they refer to the analysis in the ply coordinate system on meso scale.

Figure 4.1 presents a graphical representation of the constitutive model's main premise of obtaining the RVE's out-of-plane stresses via a delamination and the in-plane stresses via a ply model.

Figure 4.2 provides an overview of the structure of the constitutive model subroutine, highlighting the two separate branches for calculating the RVE's out-of-plane and in-plane stress tensor components. Each of the model's key elements will be described in the subsequent subchapters: the elastic properties and stiffness tensors in **Chapter 4.3**, the stress update and failure analysis in **Chapter 4.4**, the damage evolution in **Chapter 4.5**, and all rate-dependent aspects in **Chapter 4.6** and **4.7**.

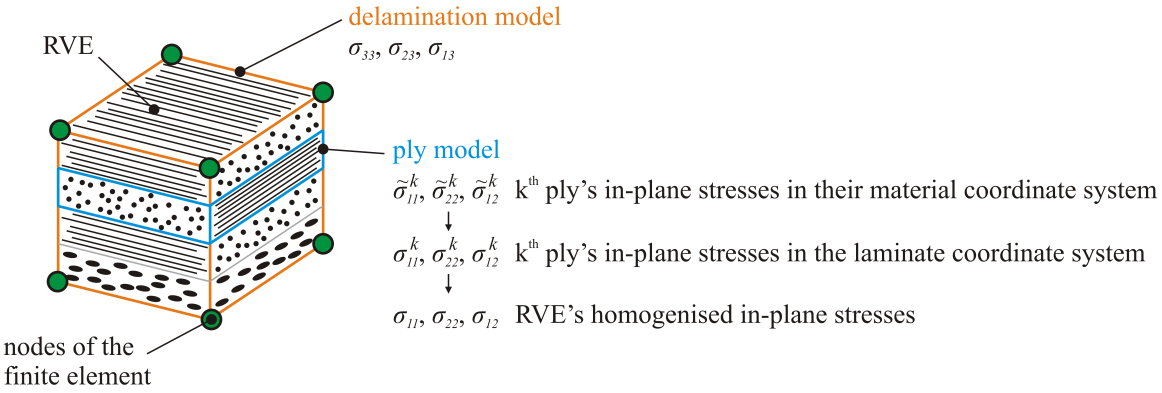


Figure 4.1: Graphical representation of the constitutive model's main premise of obtaining the RVE's out-of-plane stresses via a delamination and the in-plane stresses via a ply model

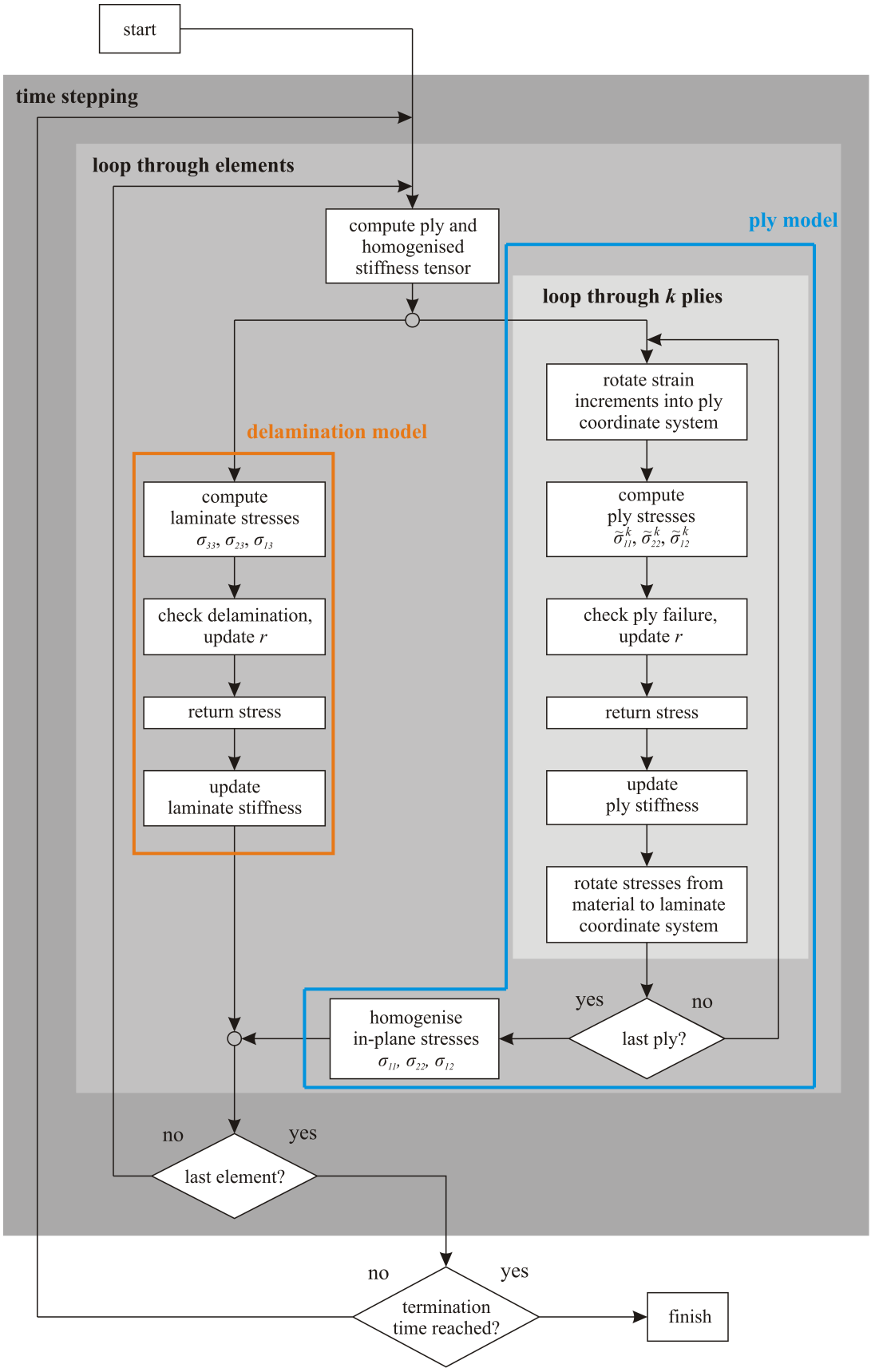


Figure 4.2: Flowchart of the constitutive algorithm's main elements

4.3 Elastic properties, ply and homogenised stiffness tensors

Elastic properties. With the exception of in-plane shear deformation, the composite material's elastic behaviour is assumed to follow a linear stress-strain relationship up to failure. For *11-t* (e.g. [136]), *22-t* (e.g. [124] or **Chapter 2.3.1**), *33-t* (e.g. [38] or **Chapter 2.4**), *11-c* (e.g. [114]), and *23-shear* (e.g. [53]) this assumption reflects the experimentally-measurable stress-strain relationship exactly or very nearly so. In case of *22-c* (e.g. [79] or **Chapter 2.2**), this assumption neglects the slight non-linearity of the stress-strain curve leading up to failure. Any non-linearity of the *31-shear* deformation mode is not considered by the model.

Loading a material from an unstressed state in either tensile or compressive direction is associated with the identical modulus, see, for instance, *Ashby et al.* [4]. The experimentally-obtained mean values of a particular normal deformation mode's Young's modulus for testing in tensile and compressive direction, however, may still feature a slight discrepancy. This discrepancy can be caused by a range of reasons:

- The limited number of specimens tested for each dataset.
- Employing different batches of material and/or semi-finished products for the specimens' production.
- The differing extent to which unaccounted influences associated with the specimens' design affect the desired homogeneous and one-dimensional stress state in their respective gauge volume (in case the specimen design deviates for testing in tensile and compressive direction).

- Differing methodologies for determining the Young's modulus across the datasets. This may involve: (i) the range of strain values across which the modulus is obtained, (ii) basing its value on a linear fit to a series of data points or determining the chord modulus between two data points, and (iii) differing approaches to obtaining the stress-strain data, which, in turn, affects the determined modulus.

In case of the existence of two datasets, one for tensile and one for compression testing of the same deformation mode, and there is no particular reason to prefer the obtained Young's modulus of one over the other, then the model allows for the accounting of both values by permitting the assignment of differing Young's moduli for the tensile and compressive domain associated with each normal deformation mode.

The composite's deformation under in-plane shear loading features a pronounced non-linear behaviour prior to reaching its ultimate strength S_m (see, for instance, the corresponding stress-strain curves generated in the context of **Chapter 5.1.2**). The constitutive model captures in-plane shear deformation and failure as follows:

- Damage is assumed to initiate only after the ultimate strength S_m is exceeded. It must be noted that this assumption is a simplification of the experimentally-observable material behaviour, which exhibits a cumulative growth of micro cracks prior to reaching S_m (e.g. [40]).
- Deformation below the yield strength S_Y is assumed to be linear elastic with $G_{12} = G_{12,0}$. Above this threshold, a plastic deformation component ϵ_p governs the monotonic decrease of the tangent modulus, which is ultimately limited to a minimum value $G_{12,f}$:

$$G_{12} = max\left(G_{12,0} \cdot e^{-\frac{G_{12,0} \cdot \epsilon_p}{S_{Yp} - S_Y}}, G_{12,f}\right) . \tag{4.3}$$

Figure 4.3 presents a sketch of the qualitative stress-strain behaviour under in-plane shear deformation and failure. In contrast to the material's initial modulus $G_{12,0}$ and its ultimate strength S_m, the parameters S_Y, S_{Yp}, and $G_{12,f}$ are, to varying degrees, empirical in nature. Their purpose is to facilitate a satisfactory fit of the modelled in-plane shear stress-strain curve to the experimentally-observable material behaviour. In order to allow for a suitable fit to curves obtained across a range of loading rates, the parameters $G_{12,0}$, S_Y, S_{Yp}, $G_{12,f}$, and S_m are each independently a function of strain-rate. The calibration of the composite's in-plane shear behaviour against experimentally-determined stress-strain curves across two loading rate regimes will be presented in **Chapter 5.1.2**.

- The diminishment of stiffness and strength due to damage evolution in the strain-softening domain will be discussed in the context of **Chapter 4.5**.
- Unloading the material in the elastoplastic domain is associated with $G_{12,0}$ due to the assumption of the absence of damage accumulation prior to reaching S_m. The modulus once again changes if the stress state associated with plastic flow is exceeded in the former or opposite ('reverse loading') direction of loading. Unloading is handled similarly in the strain-softening domain, except that the modulus upon unloading here corresponds to the appropriately reduced value of $G_{12,0}$ due to damage accumulation, and further damage evolution requires exceeding the stress state associated with last state of damage propagation. **Figure 4.4** shows the unloading and 'reverse loading' behaviour in the elastoplastic and strain-softening domain, respectively.

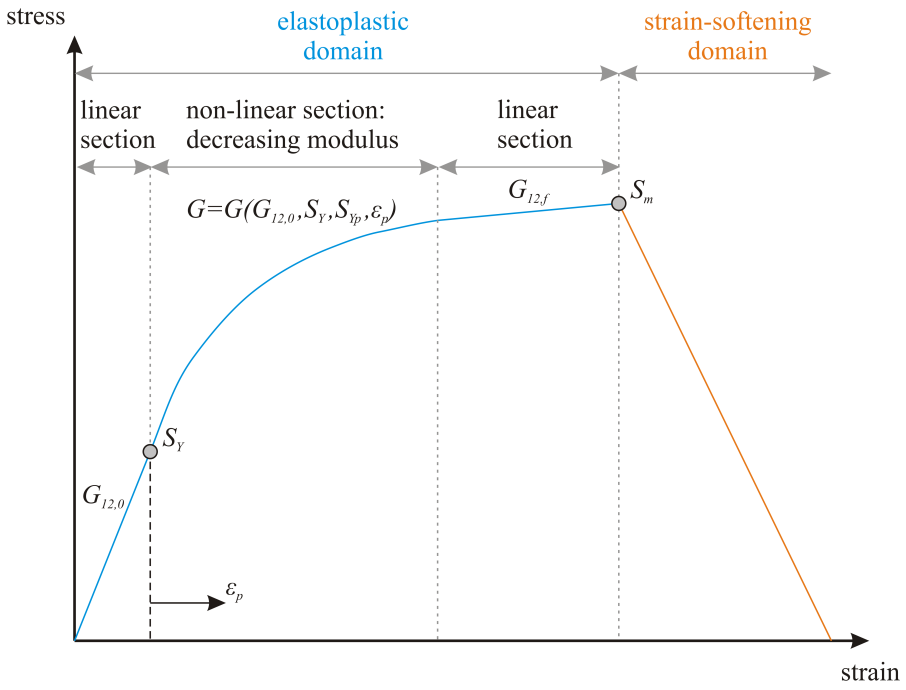


Figure 4.3: Qualitative shape of the modelled stress-strain curve under in-plane shear deformation

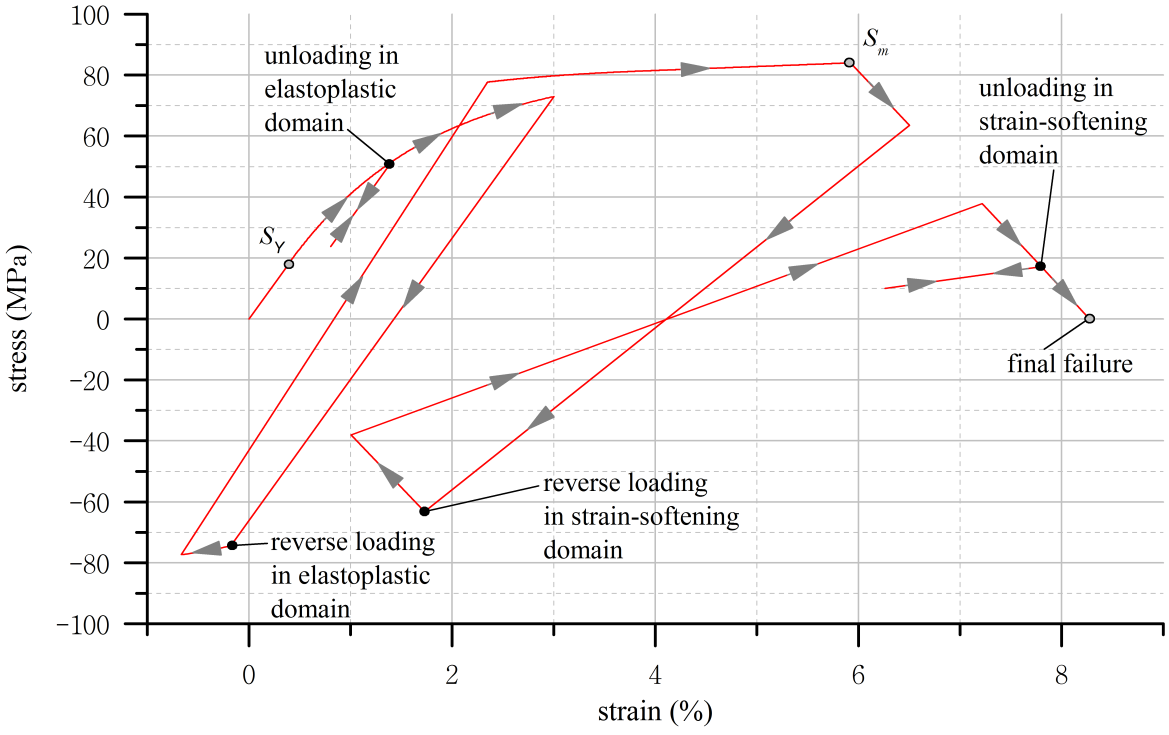


Figure 4.4: Shear stress-strain behaviour for unloading and reverse loading in the elastoplastic and strain-softening domain

Ply stiffness tensor. The individual ply's stiffness tensor is obtained based on the set of its elastic properties (see, for instance, [120]). The resulting *orthotropic*[3] stiffness tensor of an individual ply, $\tilde{\boldsymbol{C}}$, connects a ply's stress and strain tensor components as follows [120]:

$$\begin{pmatrix} \tilde{\sigma}_{11} \\ \tilde{\sigma}_{22} \\ \tilde{\sigma}_{33} \\ \tilde{\sigma}_{12} \\ \tilde{\sigma}_{23} \\ \tilde{\sigma}_{31} \end{pmatrix} = \begin{pmatrix} \tilde{C}_{11} & \tilde{C}_{12} & \tilde{C}_{13} & 0 & 0 & 0 \\ \tilde{C}_{12} & \tilde{C}_{22} & \tilde{C}_{23} & 0 & 0 & 0 \\ \tilde{C}_{13} & \tilde{C}_{23} & \tilde{C}_{33} & 0 & 0 & 0 \\ 0 & 0 & 0 & \tilde{C}_{44} & 0 & 0 \\ 0 & 0 & 0 & 0 & \tilde{C}_{55} & 0 \\ 0 & 0 & 0 & 0 & 0 & \tilde{C}_{66} \end{pmatrix} \cdot \begin{pmatrix} \tilde{\epsilon}_{11} \\ \tilde{\epsilon}_{22} \\ \tilde{\epsilon}_{33} \\ 2\tilde{\epsilon}_{12} \\ 2\tilde{\epsilon}_{23} \\ 2\tilde{\epsilon}_{31} \end{pmatrix} \tag{4.4}$$

Homogenised stiffness tensor. In order to arrive at the homogenised stiffness tensor governing the RVE's elastic behaviour, the individual plies' stiffness tensors are rotated from their respective ply to the laminate coordinate system and then combined in accordance with the relative proportion of each ply to the total set of plies reflected by the RVE. For the corresponding set of equations linking the plies' stiffness tensor components to the components of the homogenised stiffness tensor, see [28, 29, 132]. As the RVE's composition of plies is not restricted to *balanced* lay-ups, the RVE's behaviour is, in the general case, *monoclinic*. This, in turn, means that an in-plane shear deformation may also entail normal stresses. The RVE's homogenised stiffness

[3] In case *transverse isotropy* is assumed, the number of independent stiffness tensor components reduces from 9 to 5.

tensor, $\boldsymbol{C}$, connects the RVE's stress and stain tensor components as follows:

$$\begin{pmatrix} \sigma_{11} \\ \sigma_{22} \\ \sigma_{33} \\ \sigma_{12} \\ \sigma_{23} \\ \sigma_{31} \end{pmatrix} = \begin{pmatrix} C_{11} & C_{12} & C_{13} & C_{14} & 0 & 0 \\ C_{12} & C_{22} & C_{23} & C_{24} & 0 & 0 \\ C_{13} & C_{23} & C_{33} & C_{34} & 0 & 0 \\ C_{14} & C_{24} & C_{34} & C_{44} & 0 & 0 \\ 0 & 0 & 0 & 0 & C_{55} & C_{56} \\ 0 & 0 & 0 & 0 & C_{56} & C_{66} \end{pmatrix} \cdot \begin{pmatrix} \epsilon_{11} \\ \epsilon_{22} \\ \epsilon_{33} \\ 2\epsilon_{12} \\ 2\epsilon_{23} \\ 2\epsilon_{31} \end{pmatrix} \tag{4.5}$$

4.4 Stress calculation and detection of failure

This subchapter provides a description of the stress calculation and detection of failure first from a conceptual point of view and then, in detail, for the delamination and ply model.

4.4.1 Conceptual considerations

The stress state is determined by employing a *predictor-corrector* approach. Within the framework of an incremental stress update, this means that the predicted stress state, also called *trial stress state*, $\boldsymbol{\sigma^{tr}}$, is calculated as the sum of the stress value pertaining to the previous calculation cycle, $\boldsymbol{\sigma^{pr}}$, and its incremental change $\Delta\boldsymbol{\sigma}$. The latter, in turn, is derived on the basis of the increments of the strain tensor components entering the constitutive subroutine for the current calculation cycle in conjunction with the appropriate stiffness tensor:

$$\boldsymbol{\sigma^{tr}} = \boldsymbol{\sigma^{pr}} + \Delta\boldsymbol{\sigma} \ , \tag{4.6}$$

with

$$\Delta\boldsymbol{\sigma} = \boldsymbol{C} : \Delta\boldsymbol{\epsilon} \, . \tag{4.7}$$

Failure, or, in other words, the impermissibility of the trial stress state, is then determined via calculating the *material exposure* e for each failure mode, i.e. for fibre tensile and compressive failure, IFF, and delamination. Within the framework of the failure criterion for each of these failure modes, the material exposure provides a scalar measure which reflects the impermissibility of $\boldsymbol{\sigma}^{\boldsymbol{tr}}$ if its value is greater or equal to unity, i.e. $e \geq 1$.

4.4.2 Delamination model

Trial stress calculation. The trial stress state, $\boldsymbol{\sigma}^{\boldsymbol{tr}}$, pertaining to the out-of-plane stress tensor components is calculated as the sum of the stress state after the previous time step, $\boldsymbol{\sigma}^{\boldsymbol{pr}}$, and the predicted stress increment associated with the current calculation cycle: $\boldsymbol{\sigma}^{\boldsymbol{tr}} = \boldsymbol{\sigma}^{\boldsymbol{pr}} + \Delta\boldsymbol{\sigma}$. The equations corresponding to the calculation of $\Delta\boldsymbol{\sigma}$ are given as follows:

$$\begin{aligned}
\Delta\sigma_{33} &= (1-\omega_3^{pr})(C_{13}\Delta\epsilon_{11} + C_{23}\Delta\epsilon_{22} + C_{33}\Delta\epsilon_{33} + +C_{34}\Delta\epsilon_{12}) \, , \\
\Delta\sigma_{23} &= (1-\omega_5^{pr})(C_{55}\Delta\epsilon_{23} + C_{56}\Delta\epsilon_{31}) \, , \\
\Delta\sigma_{31} &= (1-\omega_6^{pr})(C_{56}\Delta\epsilon_{23} + C_{66}\Delta\epsilon_{31}) \, .
\end{aligned} \tag{4.8}$$

The above equations take into account the accumulated stiffness damage, ω, associated with each deformation mode. For out-of-plane normal deformation, a distinction is made between tensile and compressive loading in order to reflect the material's un-

impaired ability to transmit forces in compression due to crack closure:

$$\omega_3^{pr} = \begin{cases} \omega_3^{pr} & \text{if } \sigma_{33}^{pr} \geq 0 \ , \\ 0 & \text{otherwise} \ . \end{cases} \tag{4.9}$$

Failure criterion. The failure envelope associated with delamination is defined based on the set of equations proposed by *Hou et al. (2001)* [70]. In order to achieve a more satisfactory reflection of the composite's experimentally-observable behaviour, however, the corresponding equation governing the normal compressive domain was modified. This modification took the experimental data generated by *Gan et al. (2013)* [45] as a reference, who tested an *IM7/8552* laminate under combined out-of-plane normal compressive and shear loading. A comparison between the failure envelopes in σ_{33}-σ_{31}^{+}-space based on *Hou et al.*'s original formulation and its modification for the present work, and *Gan et al.*'s experimentally-generated data points is presented in **Figure 4.5**. Finally, the set of equations employed for obtaining the material exposure associated with delamination reads

$$e_{del} = \begin{cases} \sqrt{\left(\frac{\sigma_{33}^{tr}}{Z_t(1-r_d)}\right)^2 + \left(\frac{\sigma_{23}^{tr}}{S_d(1-r_d)}\right)^2 + \left(\frac{\sigma_{31}^{tr}}{S_d(1-r_d)}\right)^2} & \text{for } 0 \leq \sigma_{33}^{tr} \ , \\ \sqrt{\left(\frac{\sigma_{23}^{tr}+\sigma_{31}^{tr}}{S_d(1-r_d)}\right)^2 - 0.3\left(\frac{\sigma_{33}^{tr}}{S_d(1-r_d)}\right)^2} & \text{for } -350\text{MPa} < \sigma_{33}^{tr} < 0 \ , \\ 0 & \text{otherwise} \ . \end{cases} \tag{4.10}$$

In the above set of equations, the strength associated with each of the two out-of-plane shear deformation modes is assumed to be identical, i.e. $S_{23} = S_{31} = S_d$. In order to allow for a direct comparison between *Hou et al.*'s original equation governing the normal compressive domain and its modified version employed for the present study,

the former is given as

$$e_{del} = \sqrt{\left(\frac{\sigma_{23}^{tr} + \sigma_{31}^{tr}}{S_d(1-r_d)}\right)^2 - 8\left(\frac{\sigma_{33}^{tr}}{S_d(1-r_d)}\right)^2} \text{ for } -\sqrt{\frac{\left(\sigma_{23}^{tr}\right)^2 + \left(\sigma_{31}^{tr}\right)^2}{8}} < \sigma_{33}^{tr} < 0\ . \tag{4.11}$$

Lastly, it deserves to be mentioned that the above failure criterion was specifically chosen in view of featuring stress terms of identical order. This, in turn, allows for a numerically efficient inversion of the failure criterion in the context of determining the *reserve factor* for the *stress return*, see **Chapter 4.5.2**.

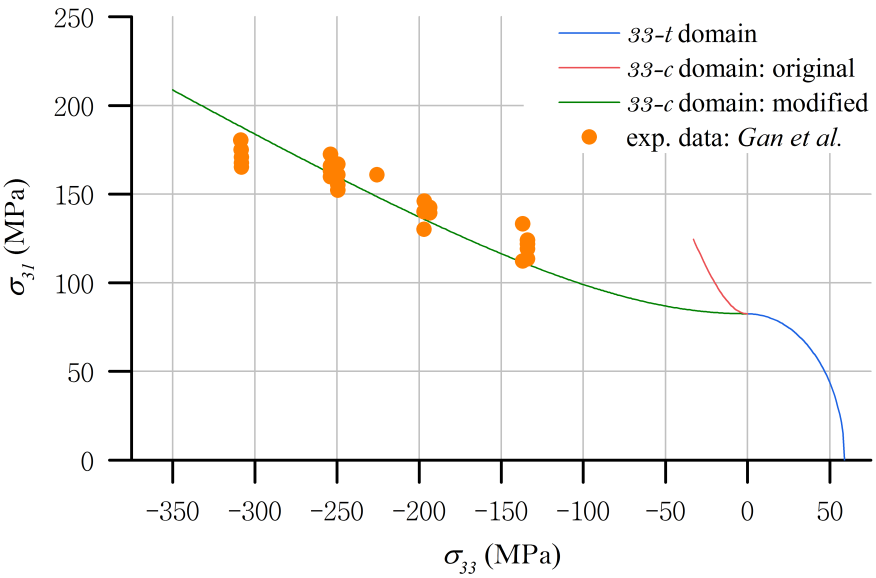


Figure 4.5: Comparison between the delamination failure criterion proposed by *Hou et al.* and its modification for the present study against the background of *Gan et al.*'s experimentally-generated data points in σ_{33}-σ_{31}^{+}-space

4.4.3 Ply model

Trial stress calculation. The trial stress state, $\tilde{\boldsymbol{\sigma}}^{\boldsymbol{k,tr}}$, pertaining to the kth ply's in-plane stress tensor components is calculated as the sum of the stress state after the previous time step, $\tilde{\boldsymbol{\sigma}}^{\boldsymbol{k,pr}}$, and the predicted stress increment associated with the current calculation cycle: $\tilde{\boldsymbol{\sigma}}^{\boldsymbol{k,tr}} = \tilde{\boldsymbol{\sigma}}^{\boldsymbol{k,pr}} + \Delta\tilde{\boldsymbol{\sigma}}^{\boldsymbol{k}}$. The equations corresponding to the

calculation of $\Delta\tilde{\boldsymbol{\sigma}}^{\boldsymbol{k}}$ are as follows:

$$\begin{aligned}
\Delta\tilde{\sigma}_{11}^{k} &= \left(1-\omega_1^{k,pr}\right)\left(\tilde{C}_{11}\Delta\tilde{\epsilon}_{11}^{k}+\tilde{C}_{12}\Delta\tilde{\epsilon}_{22}^{k}+\tilde{C}_{13}\Delta\tilde{\epsilon}_{33}^{k}\right) , \\
\Delta\tilde{\sigma}_{22}^{k} &= \left(1-\omega_2^{k,pr}\right)\left(\tilde{C}_{12}\Delta\tilde{\epsilon}_{11}^{k}+\tilde{C}_{22}\Delta\tilde{\epsilon}_{22}^{k}+\tilde{C}_{23}\Delta\tilde{\epsilon}_{33}^{k}\right) , \\
\Delta\tilde{\sigma}_{12}^{k} &= \left(1-\omega_4^{k,pr}\right)\left(\tilde{C}_{44}\Delta\tilde{\epsilon}_{12}^{k}\right) .
\end{aligned} \tag{4.12}$$

The above equations take into account the accumulated stiffness damage, ω, associated with each deformation mode. For the in-plane normal deformation modes, a distinction is made between tensile and compressive loading in order to reflect the material's unimpaired ability to transmit forces in compression due to crack closure:

$$\omega_1^{k,pr} = \begin{cases} \omega_1^{k,pr} & \text{if } \tilde{\sigma}_{11}^{k,pr} \geq 0 , \\ 0 & \text{otherwise} , \end{cases} \tag{4.13}$$

and

$$\omega_2^{k,pr} = \begin{cases} \omega_2^{k,pr} & \text{if } \tilde{\sigma}_{22}^{k,pr} \geq 0 , \\ 0 & \text{otherwise} . \end{cases} \tag{4.14}$$

Failure criteria. The experimental data documented in literature for multi-axial testing involving tensile loading in fibre direction superimposed by loading in further directions is very scarce. The data found in the only two available sources, *Zinoview et al. (2001)* [151] for testing under a hydrostatic stress state, and *Soden et al. (2002)* [129] for testing under a σ_{11}-σ_{21} and σ_{11}-σ_{22}-stress state, respectively, however, does not suggest a pronounced influence of any stress tensor component other than σ_{11} on fibre tensile failure. Failure in fibre tensile direction is thus reflected by employing a *maximum stress criterion*:

$$e_{f+}^{k} = \frac{\tilde{\sigma}_{11}^{k,tr}}{X_t} \qquad \text{for} \qquad \tilde{\sigma}_{11}^{k,tr} \geq 0 . \tag{4.15}$$

In case of failure in fibre compressive direction, the available experimental data indicates an influence of stress tensor components other than σ_{11}. A review conducted by *Gutkin et al. (2016)* [56], which juxtaposed the experimental data in σ_{11}-σ_{21}-stress space generated by various sources, however, concluded that there was no clear common failure envelope between these datasets. On this basis, and considering the substantial experimental scatter featured by those datasets, failure in fibre compressive direction is reflected by a *maximum stress criterion*:

$$e_{f-}^{k} = \frac{\left|\tilde{\sigma}_{11}^{k,tr}\right|}{X_c} \qquad \text{for} \qquad \tilde{\sigma}_{11}^{k,tr} < 0 \; . \tag{4.16}$$

Failure of the composite in a plane orthogonal to the fibre direction is modelled via employing *Puck et al.*'s [116] (2D) inter-fibre failure (IFF) criterion, which, analogous to the delamination criterion discussed in **Chapter 4.4.2**, reflects the composite's increasing apparent shear strength under a simultaneously acting normal compressive stress. This particular IFF criterion has been proven to provide an appropriate prediction of the failure envelope under superimposed σ_{21} and σ_{22} loading in the context of the *world-wide failure exercise* (WWFE) [64] for quasi-static loading, and by *Koerber et al. (2010)* [79] and *Kuhn et al. (2015)* [81] for high-rate loading in the normal compressive and normal tensile domain, respectively. *Puck et al.*'s IFF criterion [116] is defined over three domains as follows:

Mode A, valid in the domain fulfilling the condition $\tilde{\sigma}_{22}^{k,tr} \geq 0$:

$$e_{IFF}^{k} = \sqrt{\left(\frac{\tilde{\sigma}_{12}^{k,tr}}{R_1}\right)^2 + \left(1 - \frac{p_1 Y_t}{R_1}\right)^2 \left(\frac{\tilde{\sigma}_{22}^{k,tr}}{Y_t}\right)^2} + \frac{p_1 \tilde{\sigma}_{22}^{k,tr}}{R_1} \; . \tag{4.17}$$

Mode B, fulfilling the conditions $\tilde{\sigma}_{22}^{k,tr} < 0$ and $\left|\frac{\tilde{\sigma}_{22}^{k,tr}}{\tilde{\sigma}_{12}^{k,tr}}\right| \leq \frac{R_2}{R_1\sqrt{1+2p_2}}$:

$$e_{IFF}^{k} = \left(\frac{1}{R_1}\right) \cdot \left(\sqrt{\left(\tilde{\sigma}_{12}^{k,tr}\right)^2 + \left(p_1 \tilde{\sigma}_{22}^{k,tr}\right)^2} + p_1 \tilde{\sigma}_{22}^{k,tr}\right) \; . \tag{4.18}$$

Mode C, fulfilling the conditions $\tilde{\sigma}_{22}^{k,tr} < 0$ and $\left|\frac{\tilde{\sigma}_{12}^{k,tr}}{\tilde{\sigma}_{22}^{k,tr}}\right| \leq \frac{R_1\sqrt{1+2p_2}}{R_2}$:

$$e_{IFF}^{k} = \left(\left(\frac{\tilde{\sigma}_{12}^{k,tr}}{2R_1(1+p_2)} \right)^2 + \left(\frac{\tilde{\sigma}_{22}^{k,tr}}{Y_c} \right)^2 \right) \cdot \frac{Y_c}{-\tilde{\sigma}_{22}^{k,tr}} \, . \tag{4.19}$$

In the above equations, R_1 denotes the in-plane shear strength, i.e. $R_1 = S_{12}$, and p_1 the in-plane inclination parameter (see [116] for details), respectively. The remaining parameters, R_2, the out-of-plane shear strength, and p_2, the out-of-plane inclination parameter, are defined as follows [116]:

$$R_2 = \frac{R_1}{2p_1} \left(\sqrt{1 + \frac{2p_1 Y_c}{R_1}} - 1 \right) , \tag{4.20}$$

$$p_2 = p_1 \frac{R_2}{R_1} \, . \tag{4.21}$$

Similar to the failure criterion for delamination, the criterion for IFF was specifically chosen in view of featuring stress terms of identical order, thus allowing for a numerically efficient calculation of the corresponding *reserve factor*, see **Chapter 4.5.3**.

4.5 Damage evolution

This subchapter provides a description of the model's reflection of damage evolution first from a conceptual point of view and then, in detail, for the delamination and ply model.

4.5.1 Conceptual considerations

The effect of damage on the RVE's mechanical behaviour is twofold: (i) the RVE's ability to transfer load decreases, or, in other words, its strength diminishes, and (ii) the RVE's resistance to elastic deformation decreases, or, in other words, its stiffness

diminishes. These two effects are reflected in the constitutive model by employing a *continuum damage mechanics* (CDM) approach to the damage evolution pertaining to both, ply and delamination failure. Damage in the RVE is thus reflected not explicitly but via its effect on the finite elements' deformation and failure behaviour, i.e. in a 'smeared' manner over the RVE's volume.

Conceptually, damage is represented in the model by introducing the damage evolution parameter r. This damage evolution parameter is linked to the strain-softening domain, which is assumed to feature a linear slope, such that $r = 0$ until the incident of first failure, and $r = 1$ at final failure, with a linear slope connecting these two points.

If a particular failure criterion is exceeded in the current calculation cycle, i.e. $e \geq 1$, a corresponding increment of the damage evolution parameter, Δr, is calculated. This increment is proportional to the strain increment driving the damage evolution, $\Delta\epsilon$, and the damage evolution parameter's slope m:

$$r = r^{pr} + \Delta r = r^{pr} + m\Delta\epsilon \, . \tag{4.22}$$

In order to ensure that the energy dissipation process associated with each failure mode is physically sound, the damage evolution parameter's slope m is associated with the 'scaled' value of the corresponding strain-energy release rate. This 'scaling' introduces the *characteristic element length* l_c, which reflects the finite element's dimension orthogonal to the fracture plane associated with a particular failure mode. This link between the element's geometry and the energy released over the course of fracture can be understood as 'smearing' the energy release rate over the element's volume, which, in turn, considerably reduces the CDM approach's well-known mesh dependency, see, for

instance, [111, 144]. With the calculation of ϵ_f as

$$\epsilon_f = \frac{2G}{\sigma_0 l_c} \,, \tag{4.23}$$

the damage evolution parameter's slope m is then obtained according to

$$m = \frac{1}{\epsilon_f - \epsilon_0} \,. \tag{4.24}$$

This calculation of m is carried out at the first instance when a particular failure mode exceeds its elastic limit; its value is then assumed to remain constant thereon. A well-known limitation of a CDM-based damage evolution approach is its inability to employ the experimentally-determined energy release rate value once a finite element's dimensions exceed a certain threshold (e.g. [111]). A more detailed discussion of this limitation will be undertaken in **Chapter 4.8** where the results of a study that aimed at quantifying these dimensions for the material system employed for the present study will be presented. Should a physically-based energy dissipation process not be possible, the calculation of m is based on setting $\epsilon_f = 1.5 \cdot \epsilon_0$ instead.

With the determination of the updated value of r, the RVE's decreased ability to transfer load is then reflected by transferring the impermissible *trial stress state* to a *corrected stress state*, or, in other words, to return the trial stress state to the exceeded failure criterion's 'shrunken' failure envelope. The RVE's diminished stiffness is subsequently derivable on the basis of these two stress states, the trial and corrected stress state, see [144].

4.5.2 Delamination model

Calculation of the damage evolution parameter's slope m. The parameters for the determination of $\epsilon_f = 2G\sigma_0^{-1}l_c^{-1}$, and, ultimately, the damage evolution parameter's slope $m_d = (\epsilon_f - \epsilon_0)^{-1}$ are calculated as follows:

The mixed-mode energy release rate is obtained as (see [144] for details):

$$G = \left(\left(\frac{cos^2\eta}{G_{IIc}^{del}} \right)^{\alpha} + \left(\frac{sin^2\eta}{G_{Ic}^{del}} \right)^{\alpha} \right)^{-\frac{1}{\alpha}} . \tag{4.25}$$

In the above equation, G_{Ic}^{del} and G_{IIc}^{del} denote the energy release rate under fracture mode I and II, respectively, α the *mixed mode coefficient*, and η the *mixed mode ratio* as follows:

$$\eta = arccos\left(\frac{\epsilon_{shr}}{\epsilon_{tot}} \right) , \tag{4.26}$$

with

$$\epsilon_{shr} = \sqrt{\epsilon_{23}^2 + \epsilon_{31}^2} \tag{4.27}$$

and

$$\epsilon_{tot} = \sqrt{\epsilon_{33}^2 + \epsilon_{shr}^2} . \tag{4.28}$$

The stress at the onset of damage propagation is obtained as

$$\sigma_0 = \begin{cases} \sqrt{\sigma_{33}^2 + \sigma_{23}^2 + \sigma_{31}^2} & \text{for } \sigma_{33} \geq 0 , \\ \sqrt{\sigma_{23}^2 + \sigma_{31}^2} & \text{otherwise} , \end{cases} \tag{4.29}$$

and the corresponding strain as

$$\epsilon_0 = \sqrt{\epsilon_{33}^2 + \epsilon_{23}^2 + \epsilon_{31}^2} . \tag{4.30}$$

Update of the damage evolution parameter r. If the trial stress state exceeds the failure envelope in the current calculation cycle, the damage evolution parameter

$r_d = r_d^{pr} + m_d \Delta\epsilon$ is updated based on:

$$\Delta\epsilon = \begin{cases} \sqrt{\Delta\epsilon_{33}^2 + \Delta\epsilon_{23}^2 + \Delta\epsilon_{31}^2} & \text{for } \sigma_{33}^{tr} \geq 0 \ , \\ \sqrt{\Delta\epsilon_{23}^2 + \Delta\epsilon_{31}^2} & \text{otherwise} \ . \end{cases} \tag{4.31}$$

Strength degradation. The 'return' of the stress vector from an impermissible trial stress state to one that corresponds to the updated failure envelope is based on the following equations:

For $\sigma_{33}^{tr} \geq 0$:

$$f_{res} = \frac{1}{\sqrt{\left(\frac{\sigma_{33}^{tr}}{Z_t(1-r_d)}\right)^2 + \left(\frac{\sigma_{23}^{tr}}{S_d(1-r_d)}\right)^2 + \left(\frac{\sigma_{31}^{tr}}{S_d(1-r_d)}\right)^2}} \tag{4.32}$$

resulting in

$$\begin{aligned} \sigma_{33} &= f_{res}\sigma_{33}^{tr} \ , \\ \sigma_{23} &= f_{res}\sigma_{23}^{tr} \ , \\ \sigma_{31} &= f_{res}\sigma_{31}^{tr} \ , \end{aligned} \tag{4.33}$$

and for $\sigma_{33}^{tr} < 0$:

$$f_{res} = \sqrt{\frac{\big(S_d(1-r_d)\big)^2 + 0.3\big(\sigma_{33}^{tr}\big)^2}{\big(\sigma_{23}^{tr} + \sigma_{31}^{tr}\big)^2}} \tag{4.34}$$

resulting in

$$\begin{aligned} \sigma_{33} &= \sigma_{33}^{tr} \ , \\ \sigma_{23} &= f_{res}\sigma_{23}^{tr} \ , \\ \sigma_{31} &= f_{res}\sigma_{31}^{tr} \ . \end{aligned} \tag{4.35}$$

The above equations distinguish between a stress state which exceeds the failure envelope in the normal tensile domain and one that does so in the normal compression domain. In contrast to the former, the latter does not entail a reduced load bearing

capability for the normal stress tensor component σ_{33}. **Figure 4.6** provides an illustration of the differing treatment of the stress return depending on a stress state in the normal tensile or compression domain.

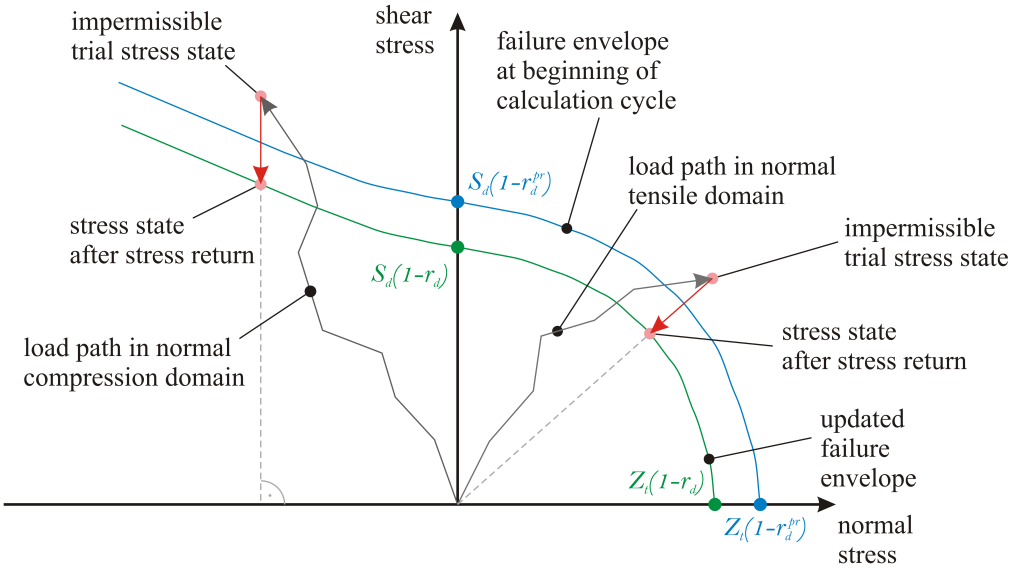


Figure 4.6: Differing treatment of the stress return to the updated failure envelope depending on a stress state in the normal tensile or compression domain

Stiffness degradation. The stiffness damage increment is calculated as follows:

$$\begin{aligned}
\Delta\omega_3 &= \frac{\left(1-\omega_3^{pr}\right)\left(\sigma_{33}^{tr}-\sigma_{33}\right)}{\sigma_{33}^{tr}}\,, \\
\Delta\omega_5 &= \frac{\left(1-\omega_5^{pr}\right)\left(\sigma_{23}^{tr}-\sigma_{23}\right)}{\sigma_{23}^{tr}}\,, \\
\Delta\omega_6 &= \frac{\left(1-\omega_6^{pr}\right)\left(\sigma_{31}^{tr}-\sigma_{31}\right)}{\sigma_{31}^{tr}}\,.
\end{aligned} \tag{4.36}$$

The accumulated stiffness damage is finally updated according to:

$$\omega_i = \omega_i^{pr} + \Delta\omega_i \qquad \text{for} \qquad i = 3,5,6\,. \tag{4.37}$$

4.5.3 Ply model

Calculation of the damage evolution parameter's slope m. For the fibre failure modes, $\epsilon_f = 2G\sigma_0^{-1}l_c^{-1}$, and, ultimately, the damage evolution parameter's slope $m = (\epsilon_f - \epsilon_0)^{-1}$, are calculated based on the values of σ and ϵ when the failure envelope is first exceeded, and the corresponding value of G_{Ic}^{f+} or G_{Ic}^{f-}, respectively. For IFF, ϵ_f and m are calculated as follows:

The mixed-mode energy release rate is obtained as (see [144] for details):

$$G = \left(\left(\frac{cos^2\eta}{G_{IIc}^{IFF}} \right)^{\alpha} + \left(\frac{sin^2\eta}{G_{Ic}^{IFF}} \right)^{\alpha} \right)^{-\frac{1}{\alpha}} . \tag{4.38}$$

In the above equation, G_{Ic}^{IFF} and G_{IIc}^{IFF} denote the energy release rate under fracture mode I and II, respectively, α the *mixed mode coefficient*, and η the *mixed mode ratio* as follows:

$$\eta = arccos\left(\frac{\epsilon_{shr}}{\epsilon_{tot}} \right) , \tag{4.39}$$

with

$$\epsilon_{shr} = \tilde{\epsilon}_{12}^{k} \tag{4.40}$$

and

$$\epsilon_{tot} = \sqrt{\left(\tilde{\epsilon}_{22}^{k}\right)^2 + \left(\tilde{\epsilon}_{12}^{k}\right)^2} . \tag{4.41}$$

The stress at the onset of damage propagation is obtained as

$$\sigma_0 = \begin{cases} \sqrt{\left(\tilde{\sigma}_{22}^{k}\right)^2 + \left(\tilde{\sigma}_{12}^{k}\right)^2} & \text{for } \tilde{\sigma}_{22}^{k} \geq 0 , \\ \tilde{\sigma}_{12}^{k} & \text{otherwise} , \end{cases} \tag{4.42}$$

and the corresponding strain as

$$\epsilon_0 = \begin{cases} \sqrt{\left(\tilde{\epsilon}_{22}^k\right)^2 + \left(\tilde{\epsilon}_{12}^k\right)^2} & \text{for } \tilde{\sigma}_{22}^k \geq 0 \ , \\ \tilde{\epsilon}_{12}^k & \text{otherwise} \ . \end{cases} \tag{4.43}$$

Update of the damage evolution parameter r. If the trial stress state exceeds the failure envelope for a particular ply failure mode in the current calculation cycle, its damage evolution parameter $r = r^{pr} + m\Delta\epsilon$ is updated based on $\Delta\epsilon_{11}^k$ for fibre tensile failure, $|\Delta\epsilon_{11}^k|$ for fibre compressive failure, and for IFF according to

$$\Delta\epsilon = \begin{cases} \sqrt{\left(\Delta\tilde{\epsilon}_{22}^k\right)^2 + \left(\Delta\tilde{\epsilon}_{12}^k\right)^2} & \text{for } \tilde{\sigma}_{22}^k \geq 0 \ , \\ \Delta\tilde{\epsilon}_{12}^k & \text{otherwise} \ . \end{cases} \tag{4.44}$$

Strength degradation. The 'return' of the stress vector from an impermissible trial stress state to one that corresponds to the updated failure envelope is dependent on the failure mode. The corresponding set of equations for fibre tensile failure, which reflects this failure mode's 'catastrophic' nature affecting all in-plane stress tensor components, reads as follows:

$$\begin{aligned} \tilde{\sigma}_{11}^k &= (1 - r_f^k) X_t \ , \\ \tilde{\sigma}_{22}^k &= (1 - r_f^k) \tilde{\sigma}_{22}^{k,tr} \ , \\ \tilde{\sigma}_{12}^k &= (1 - r_f^k) \tilde{\sigma}_{12}^{k,tr} \ , \end{aligned} \tag{4.45}$$

and for fibre compressive failure, which is modelled analogous to perfect plasticity:

$$\begin{aligned} \tilde{\sigma}_{11}^k &= -X_c \ , \\ \tilde{\sigma}_{22}^k &= \tilde{\sigma}_{22}^{k,tr} \ , \\ \tilde{\sigma}_{12}^k &= \tilde{\sigma}_{12}^{k,tr} \ , \end{aligned} \tag{4.46}$$

and for IFF:

Mode A:

$$f_{res} = \frac{1}{\sqrt{\left(\frac{\tilde{\sigma}_{12}^{k,tr}}{R_1}\right)^2 + \left(1 - \frac{p_1 Y_t}{R_1}\right)^2 \left(\frac{\tilde{\sigma}_{22}^{k,tr}}{Y_t}\right)^2} + \frac{p_1 \tilde{\sigma}_{22}^{k,tr}}{R_1}} \tag{4.47}$$

resulting in

$$\begin{aligned} \tilde{\sigma}_{22}^{k} &= f_{res} \tilde{\sigma}_{22}^{k,tr} \ , \\ \tilde{\sigma}_{12}^{k} &= f_{res} \tilde{\sigma}_{12}^{k,tr} \ , \end{aligned} \tag{4.48}$$

Mode B:

$$f_{res} = \sqrt{\frac{\left(R_1\right)^2 - 2 R_1 p_1 \tilde{\sigma}_{22}^{k,tr}}{\left(\tilde{\sigma}_{12}^{k,tr}\right)^2}} \ , \tag{4.49}$$

and Mode C:

$$f_{res} = \sqrt{\frac{\left(1 + \frac{\tilde{\sigma}_{22}^{k,tr}}{Y_c}\right) 4 \left(R_1\right)^2 \left(1 + p_2\right)^2 \left(- \tilde{\sigma}_{22}^{k,tr}\right)}{Y_c \left(\tilde{\sigma}_{12}^{k,tr}\right)^2}} \tag{4.50}$$

resulting in

$$\begin{aligned} \tilde{\sigma}_{22}^{k} &= \tilde{\sigma}_{22}^{k,tr} \ , \\ \tilde{\sigma}_{12}^{k} &= f_{res} \tilde{\sigma}_{12}^{k,tr} \ . \end{aligned} \tag{4.51}$$

Similar to the delamination model, the stress return for IFF distinguishes between a stress state which exceeds the failure envelope in the normal tensile domain and one that does so in the normal compression domain. The reader is referred to **Chapter 4.5.2** for an illustration of this differing treatment of the stress return.

Stiffness degradation. The stiffness damage increment is calculated as follows:

$$\begin{aligned} \Delta\omega_1^k &= \frac{\left(1 - \omega_1^{k,pr}\right)\left(\tilde{\sigma}_{11}^{k,tr} - \tilde{\sigma}_{11}^{k}\right)}{\tilde{\sigma}_{11}^{k,tr}} \ , \\ \Delta\omega_2^k &= \frac{\left(1 - \omega_2^{k,pr}\right)\left(\tilde{\sigma}_{22}^{k,tr} - \tilde{\sigma}_{22}^{k}\right)}{\tilde{\sigma}_{22}^{k,tr}} \ , \\ \Delta\omega_4^k &= \frac{\left(1 - \omega_4^{k,pr}\right)\left(\tilde{\sigma}_{12}^{k,tr} - \tilde{\sigma}_{12}^{k}\right)}{\tilde{\sigma}_{12}^{k,tr}} \ . \end{aligned} \tag{4.52}$$

The accumulated stiffness damage is finally updated according to:

$$\omega_i^k = \omega_i^{k,pr} + \Delta\omega_i^k \qquad \text{for} \qquad i = 1, 2, 4 \ . \tag{4.53}$$

4.6 Rate-dependency

The rate-dependency of the composite material's elastic and strength properties is reflected by scaling the corresponding base values obtained under quasi-static loading. The scale factors associated with the elastic properties, κ, see **Equ. 4.54**, are a function of the deformation mode, its respective strain-rate fit function parameters, and the relevant strain-rate value of the current calculation cycle. Analogous to the elastic properties, the scale factors associated with the strength properties, λ, are given in **Equ. 4.55**. Both sets of equations already incorporate the assumptions made with respect to the reflection of the composite's rate-dependent nature, which will be discussed in more detail in the context of **Chapter 5.1.1** and **5.1.2**. The reflection of the rate-dependency for the set of energy release rate values is based on a linear interpolation between the scarce available data points (see **Chapter 5.1.3** for discussion).

$$\begin{aligned}
E_{22t}^{dyn} &= \kappa_{22t} \cdot E_{22t}^{QS} \ , \\
E_{22c}^{dyn} &= \kappa_{22c} \cdot E_{22c}^{QS} \ , \\
E_{33t}^{dyn} &= E_{33c}^{dyn} = \kappa_{22t} \cdot E_{22t}^{QS} \ , \\
G_{12,0}^{dyn} &= \kappa_{12,0} \cdot G_{12,0}^{QS} \ , \\
G_{23}^{dyn} &= G_{31}^{dyn} = \kappa_{12,0} \cdot G_{31}^{QS} \ , \\
G_{12,f}^{dyn} &= \kappa_{12,f} \cdot G_{12,f}^{QS}
\end{aligned} \tag{4.54}$$

$$
\begin{aligned}
X_c^{dyn} &= \lambda_{11c} \cdot X_c^{QS} \ , \\
Y_t^{dyn} &= \lambda_{22t} \cdot Y_t^{QS} \ , \\
Y_c^{dyn} &= \lambda_{22c} \cdot Y_c^{QS} \ , \\
Z_t^{dyn} &= \lambda_{22t} \cdot Y_t^{QS} \ , \\
S_{12}^{dyn} &= \lambda_{12} \cdot S_{12}^{QS} \ , \\
S_{23}^{dyn} &= S_{31}^{dyn} = \lambda_{12} \cdot S_{31}^{QS} \ , \\
S_Y^{dyn} &= \lambda_Y \cdot S_Y^{QS} \ , \\
S_{Yp}^{dyn} &= \lambda_{Yp} \cdot S_{Yp}^{QS}
\end{aligned}
\tag{4.55}
$$

The calibration of both sets of scale factors, κ and λ, against the available data points for the composite material system *IM7/8552* will be described in **Chapter 5.1**. The treatment of the other crucial component for capturing rate-dependent effects, i.e. the strain-rate value of the current calculation cycle, will be investigated in the following subchapter.

4.7 Strain-rate smoothing

This subchapter first provides the motivation for smoothing the strain-rate value(s) obtained on the basis of the strain increments and the time step size entering the constitutive model subroutine. Thereafter, a strain-rate smoothing algorithm mimicking the characteristics of a *low-pass filter* is developed and contrasted against the commonly used *running average* approach. Finally, the results of a numerical study are presented which aimed at directly comparing the effect of the *low-pass filter* with the

running average approach, and to determine a suitable starting point for setting the arbitrary parameters of the former.

4.7.1 Motivation

The constitutive model subroutine calculates the strain-rate for each deformation mode based on the corresponding component $\Delta\epsilon_t$ of the vector of strain increments, and the time step size Δt, which enter the subroutine for the current calculation cycle, according to $\dot{\epsilon}_{t,raw} = \frac{\Delta\epsilon_t}{\Delta t}$. The strain-rate history experienced locally by a structure, however, is not only a result of the high-rate loading event, but also due to causes inherent in the explicit finite element method. These causes most notably involve the method's time stepping scheme and the employed contact algorithms. As a result, a structure's local strain-rate history can feature a very high level of 'noise' as well as pronounced strain-rate peaks, both of which are caused rather by the numerical method than the high-rate loading event itself. This effect is further amplified in case of accounting for the material's rate-dependent stiffness properties. **Figure 4.7** provides an example of the strain-rate history experienced by a finite element featuring pronounced and rapid changes across small numbers of calculation cycles due to the reasons outlined above.[4] As these pronounced and rapid strain-rate changes are prone to trigger numerical instabilities, $\dot{\epsilon}_{t,raw}$ must be processed in order to enforce a stable model calculation whilst still facilitating a realistic reflection of a material's rate-dependent phenomena.

[4]The data presented in **Figure 4.7** was taken from one of the simulations in the context of the numerical study described in **Chapter 4.7.3**.

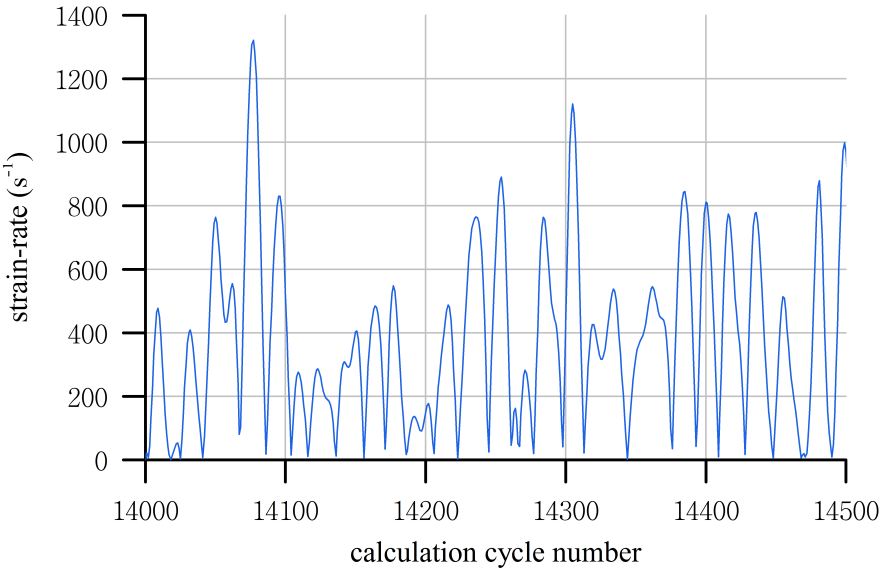


Figure 4.7: Unprocessed out-of-plane normal strain-rate history of a finite element in direct vicinity of a projectile impacting on a panel

4.7.2 A *low-pass filter*-like algorithm for smoothing the strain-rate

The commonly employed method for transforming $\dot{\epsilon}_{t,raw}$ into a processed (i.e. smoothed) strain-rate value $\dot{\epsilon}_{proc}$ is to base its calculation on a *running average*. The two parameters to influence this calculation are: (i) the number of considered strain-rate values n, which corresponds to accounting for the strain-rate values across the previous $n-1$ calculation cycles, and (ii) the weights w associated with each of these strain-rate values. The formula to compute the *running average* is given as

$$\dot{\epsilon}_{proc} = \frac{\sum_{i=1}^{n} w_i \dot{\epsilon}_{t-(i-1)\Delta t}}{\sum_{i=1}^{n} w_i} \tag{4.56}$$

with

$$\dot{\epsilon}_{t-(i-1)\Delta t}\big|_{i=1} = \dot{\epsilon}_{t,raw} \ . \tag{4.57}$$

Examples for the implementation of this approach can be found in a plethora of standard material models in *LS-Dyna*, e.g. *MAT 54/55*, *MAT 58* or *MAT 34* [92].

Against the background of the *running average* approach's indiscriminate transformation of $\dot{\epsilon}_{t,raw}$ into a smoothed strain-rate value $\dot{\epsilon}_{proc}$, however, concerns were raised in the present study regarding its ability to retain a realistic strain-rate level that reflects the 'nature' of a given high-rate loading case. In other words, the question was: *Does the lack of any condition for smoothing the strain-rate impede a constitutive model's ability to capture the full succession of rate-dependent deformation and failure phenomena?*

In order to address this concern, an alternative algorithm for calculating $\dot{\epsilon}_{proc}$ was developed. The key concept behind this algorithm consists of controlling the magnitude of smoothing based on the strain-rate jump across the previous, $\dot{\epsilon}_{t-\Delta t}$, and the current time step, $\dot{\epsilon}_{t,raw}$, i.e.:

$$\Delta\dot{\epsilon}_{raw} = \left|\dot{\epsilon}_{t,raw} - \dot{\epsilon}_{t-\Delta t}\right| . \tag{4.58}$$

Mapping $\Delta\dot{\epsilon}_{raw}$ onto the smoothed strain-rate jump, $\Delta\dot{\epsilon}_{proc}$, then, mimicks the behaviour of a *low-pass filter* according to:

$$\Delta\dot{\epsilon}_{proc} = \begin{cases} \Delta\dot{\epsilon}_{raw} & \text{for } \Delta\dot{\epsilon}_{raw} \leq \Delta\dot{\epsilon}_{tsh} , \\ \Delta\dot{\epsilon}_{tsh} + (\Delta\dot{\epsilon}_{lim} - \Delta\dot{\epsilon}_{tsh}) \cdot \left(1 - e^{-\frac{\Delta\dot{\epsilon}_{raw} - \Delta\dot{\epsilon}_{tsh}}{\Delta\dot{\epsilon}_{lim} - \Delta\dot{\epsilon}_{tsh}}}\right) & \text{for } \Delta\dot{\epsilon}_{raw} > \Delta\dot{\epsilon}_{tsh} . \end{cases} \tag{4.59}$$

Figure 4.8 presents an illustration of the mapping of $\Delta\dot{\epsilon}_{raw}$ onto $\Delta\dot{\epsilon}_{proc}$ for $\Delta\dot{\epsilon}_{tsh} = 30$ s^{-1} and $\Delta\dot{\epsilon}_{lim} = 80$ s^{-1}.

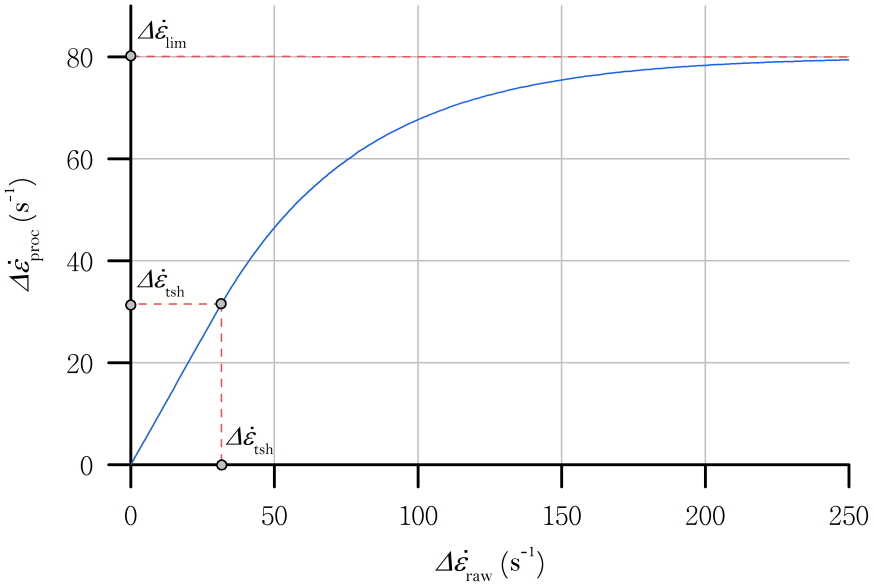


Figure 4.8: Illustration of a *low-pass filter*-like algorithm for preventing the strain-rate from deviating excessively across successive time steps

Finally, the smoothed strain-rate for the current calculation cycle is obtained as follows:

$$\dot{\epsilon}_{proc} = \begin{cases} \dot{\epsilon}_{t-\Delta t} + \Delta\dot{\epsilon}_{proc} & \text{if } \dot{\epsilon}_{t,raw} \geq \dot{\epsilon}_{t-\Delta t} \ , \\ \dot{\epsilon}_{t-\Delta t} - \Delta\dot{\epsilon}_{proc} & \text{if } \dot{\epsilon}_{t,raw} < \dot{\epsilon}_{t-\Delta t} \ . \end{cases} \tag{4.60}$$

4.7.3 Numerical study

A numerical study was undertaken to investigate the effect of employing different approaches to strain-rate smoothing on the force vs. deflection output of a ball/plate impact model. Three approaches for obtaining $\dot{\epsilon}_{proc}$ were examined: (i) an unweighted *running average* considering the stain-rate values across the previous m calculation cycles (with $m = 1..8$), (ii) a weighted *running average* based on the identical range of strain-rate values across previous calculation cycles, but halving the weight associated with each successive strain-rate value, and, (iii) the *low-pass filter*-like algorithm

described in the preceding section considering a comprehensive range of combinations of its two governing parameters, $\Delta\dot{\epsilon}_{tsh}$ and $\Delta\dot{\epsilon}_{lim}$.

The numerical model employed for this study consisted of a sphere impacting a panel. The projectile's initial velocity and mass were set to 3.85 m/s and 0.5 kg, respectively, thus generating a load case that was severe enough to potentially cause the emergence of numerical instabilities. The panel's nodes along its rim were fully constrained. Its material behaviour was modelled employing the constitutive model that was outlined earlier within the present chapter.

The simulations developed severe numerical instabilities for: (i) the unweighted *running average* runs for $m = 1..4$, (ii) all runs employing the weighted *running average*, and, (iii) the *low-pass filter* runs for $\Delta\dot{\epsilon}_{lim} > 120$ s^{-1}. The resulting force vs. deflection curves obtained from the remaining stable simulation runs are presented in **Figure 4.9** with only the curves' rising branch shown for the sake of clarity. An additional simulation was run with all the model's rate-dependent features disabled (denoted as 'QS' in the chart's legend) in order to provide a reference for assessing the magnitude of the influence of employing the different strain-rate smoothing approaches. Furthermore, with the aim of rendering the convergence behaviour of the force vs. deflection data more graspable, the force values at an arbitrarily chosen constant deflection of 2 mm are plotted in **Figure 4.10** with the *low-pass filter* data grouped once for $\Delta\dot{\epsilon}_{lim} = const.$, and then for $\Delta\dot{\epsilon}_{tsh} = const.$, respectively.

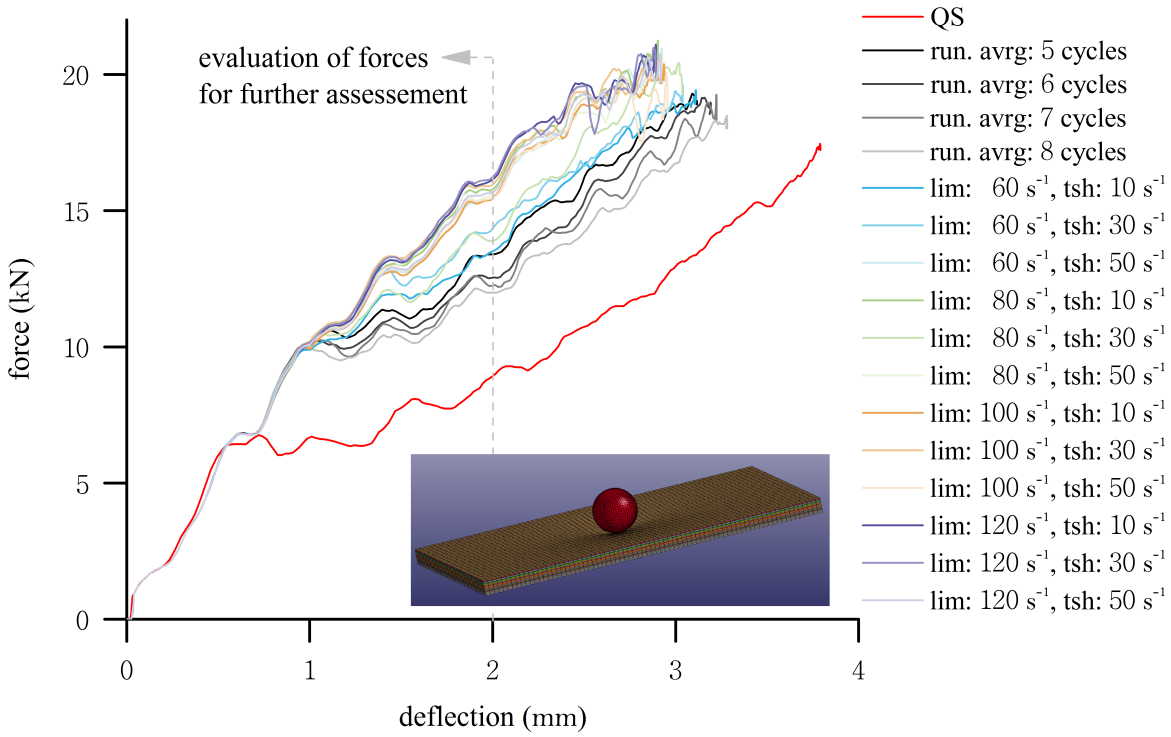


Figure 4.9: Force vs. deflection curves for a ball/plate impact model employing a range of strain-rate smoothing approaches

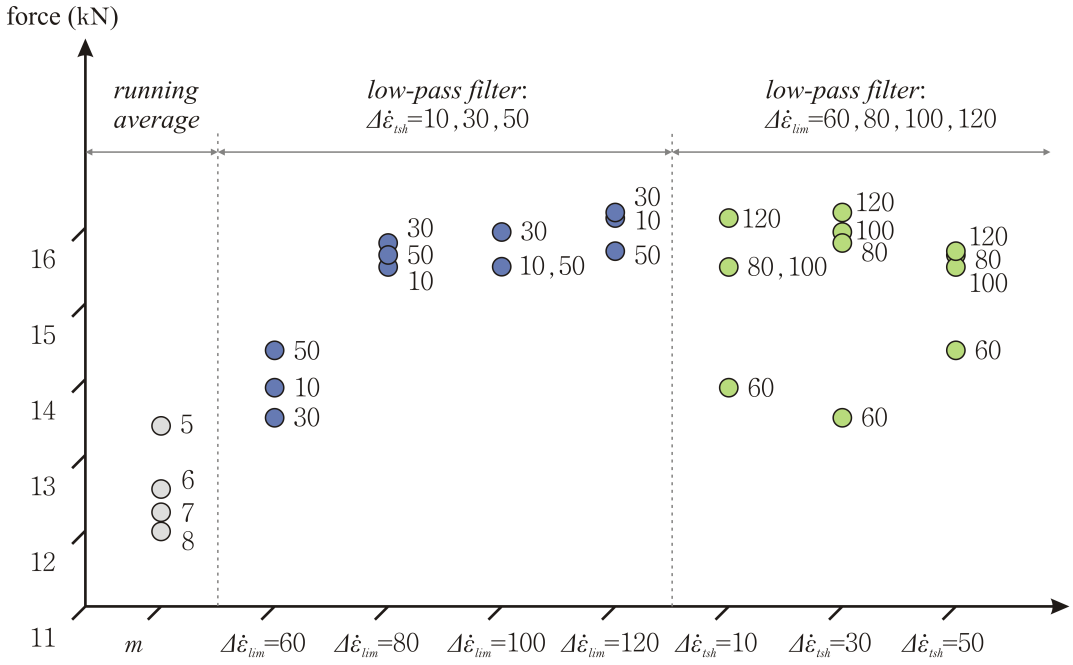


Figure 4.10: Force values at a deflection of 2 mm for all rate-smoothing approaches to highlight the convergence behaviour in case of an appropriate choice of the *low-pass filter*-like algorithm's governing parameters $\Delta\dot{\epsilon}_{tsh}$ and $\Delta\dot{\epsilon}_{lim}$ (strain-rate values in s^{-1}; running average values in number of cycles)

The evaluation of the simulations' results was based on the assumption that a less 'restrictive' algorithm for obtaining $\dot{\epsilon}_{proc}$ would result in a force vs. deflection curve that is less influenced by its rate-smoothing algorithm, or, in other words, in a model behaviour closer to the 'real' solution. The key conclusions that were drawn from this numerical study are as follows: (i) the approach chosen for obtaining $\dot{\epsilon}_{proc}$ had a profound influence on the obtained force vs. deflection curve, (ii) the more 'restrictive' this chosen algorithm, the closer the simulation result tended to be shifted towards the rate-insensitive solution, (iii) the *low-pass filter*-like algorithm, in conjunction with an appropriate set of its governing parameters, performed better than the *running average* approach, (iv) the solutions employing the *low-pass filter*-like algorithm tended to converge beyond a certain point, which seemed to be essentially governed by $\Delta\dot{\epsilon}_{lim}$, see **Figure 4.10**. For the simulations carried out in the present study, the value of the second governing parameter, $\Delta\dot{\epsilon}_{tsh}$, appeared to be of minor importance for the resulting model output, provided $\Delta\dot{\epsilon}_{lim}$ was set to min. 80 s^{-1}.

In conclusion, it is recommended to employ a *low-pass filter*-like algorithm rather than a *running average* approach for the purpose of strain-rate smoothing. Against the background of the numerical study presented in this section it is further recommended to set the *low-pass filter*-like algorithm's governing parameters to $\Delta\dot{\epsilon}_{lim} = 80$ s^{-1} and $\Delta\dot{\epsilon}_{tsh} = 30$ s^{-1}. It should be kept in mind, however, that the underlying assumption behind this particular set of values is the reasonable generalizability of the simulation results generated in the context of the present study. It must be mentioned that this is a working hypothesis and it is thus recommended to extend the scope of this study to considerably lower and higher impact velocities, and to also employ additional impact loading models, in order to explore the load case sensitivity of the *low-pass filter*-like

algorithm's governing parameters.

4.8 Quantification of the limitations of damage modelling via CDM

This subchapter first provides the background regarding the source of the limitations of a CDM-based damage modelling approach. Thereafter, the results of a study that aimed at quantifying these limitations in terms of the finite element dimensions for each failure mode are presented.

4.8.1 Background and motivation

As outlined in **Chapter 4.5**, the constitutive model's CDM-based reflection of damage propagation is based on the set of experimentally-determined energy release rate values. This link between model behaviour and a physically measurable quantity, however, is well-known to be limited by the finite element mesh's topology (e.g. [111]). The aim of this subchapter is thus to quantify this limitation with respect to the individual failure modes and the composite material employed in the present study.

Considering that, in the general case, increasing the edge length dimensions of a finite element entails the element's volume to grow more quickly than its cross-sectional area associated with a certain failure mode, the element's elastically stored energy at the onset of failure becomes too large to be dissipated using the experimentally-determined energy release rate value beyond a certain threshold. This particular case

corresponds to the end point of the softening slope dropping below the strain value at the onset of damage evolution, ϵ_0. Further, the stress-strain curve's slope in the softening domain must not fall too abruptly in order to avoid numerical instabilities, thus practically limiting the end point of the softening slope to ϵ_{tsh}. **Figure 4.11** provides an illustration of this dependence of the stress-strain curve's strain-softening slope on an increasing finite element's volume.

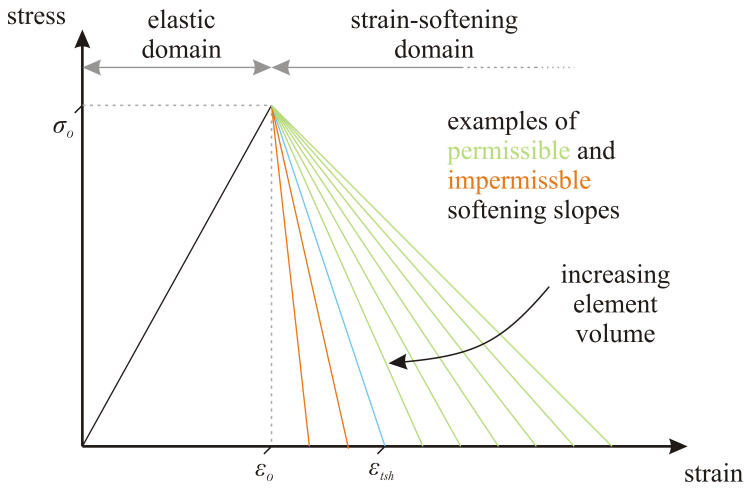


Figure 4.11: Illustration of the dependency of the stress-strain curve's softening slope on the finite element's volume for a given energy release rate value

4.8.2 Study outline, results, and conclusions

In order to quantify the finite element size limitations that arise in conjunction with a CDM-based damage modelling approach, a single element study was carried out based on the following parameters: (i) quasi-static material properties of *IM7/8552* were assumed (see **Chapter 5.1**), (ii) fracture mode I was assumed, (iii) a rectangular finite element geometry with deformation along its principal axes was assumed, and, (iv) ϵ_{tsh} was set to 1.5 times the value of ϵ_0. Two finite element shapes were considered: a cubical and a 'tile' geometry; the latter being of special importance to the majority

of practical application cases as these typically employ an FE mesh featuring elements with in-plane dimensions considerably larger than the elements' through-thickness dimension. The range of values for the latter was chosen to correspond to a stacking of 1, 2, 4, and 8 prepreg plies (with $t_{ply} = 0.125$ mm).

The results of this study are presented in **Figure 4.12**, showing the energy ratio r_E, defined as

$$r_E = \frac{\frac{G}{l_c}}{1.5 \cdot 0.5 \cdot \epsilon_0 \cdot \sigma_0} \ , \tag{4.61}$$

plotted against the element edge length dimension (for cube: all edge lengths; for tile: in-plane edge lengths). This energy ratio, describing the quotient of the energy dissipated over the course of crack propagation to the elastically stored energy at the onset of failure (multiplied by 1.5), must be equal to or greater than unity in order to permit an element's strain-softening behaviour to be based on the experimentally-determined energy release rate value G for a particular failure mode.

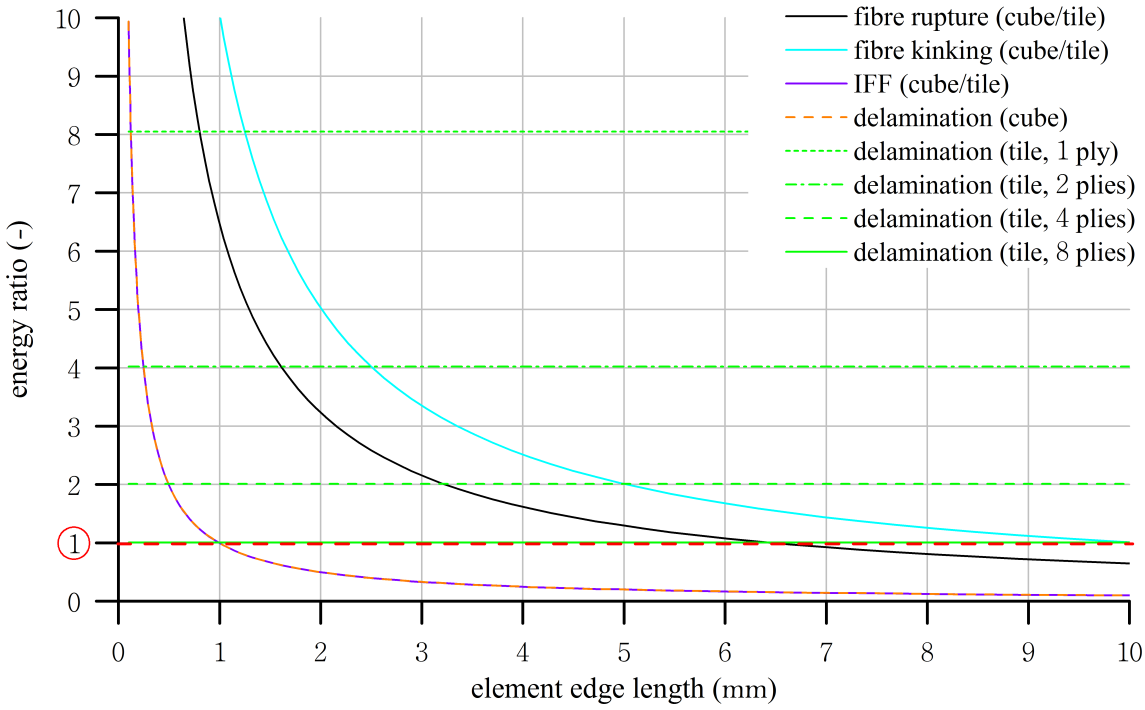


Figure 4.12: Quantification of the limiting finite element dimensions for basing the damage evolution process on the experimentally-determined energy release rate value for each failure mode

The following key conclusions were drawn from the study results presented above: (i) the fibre-dominated failure modes are fairly unproblematic with critical edge length dimensions well above 6 mm, and (ii) the critical edge length dimensions for the matrix-dominated failure modes are relatively low (around 1 mm), which, in turn, means that the model's strain-softening behaviour for these failure modes will most likely not reflect the experimentally-determined energy release rate values for the vast majority of typical application cases. An exception to this, however, is delamination failure in tile-shaped elements.

4.9 Key merits and limitations of the model

Key merits. The constitutive model's key merits may be summarised as follows:

- Enabling the usage of a comparatively coarse FE mesh. This is facilitated by representing the mechanical behaviour of a multitude of arbitrarily oriented plies within a single RVE. The resulting reduction in required finite elements to discretise a large composite material structure then ultimately leads to a considerably reduced model run time, as will be demonstrated in **Chapter 5.3**.
- Reflection of the elastic, failure, and damage evolution behaviour of all relevant failure modes, i.e. fibre tensile and compressive failure, inter-fibre failure, and delamination.
- Consideration of the rate-dependency of the composite's elastic behaviour, strength properties, and energy release rate values.

Limitations. The constitutive model's main limitations may be summarised as follows:

- The information on the position of each individual ply within the RVE is lost as a consequence of the homogenisation procedure. Thus, the model reflects the ply-book within each RVE only with respect to the individual plies' orientations and relative fraction on the entirety of contained plies, not, however, its sequence.
- Due to the model's reflection of a multitude of plies, the number of potential delamination planes between these individual plies must be assumed *a priori*. This constraint of basing the delamination process, and thus the energy dissipated over its course, on a fixed number of planes, in turn, introduces a degree

of uncertainty with respect to what would be the composite's experimentally-observable behaviour.

- Employing the experimentally-determined set of strain-energy release rates in the context of a CDM-based damage modelling approach is known to be limited by the finite elements' dimensions. A quantification of this limitation with respect to each failure mode was presented in **Chapter 4.8**.

4.10 Summary

Conventionally, design-critical impact loading events involving large aerospace composite material structures, such as a composite fan blade subjected to *bird strike*, are modelled by employing a ply-by-ply representation of the composite laminate. This approach typically results in FE meshes featuring a very large number of elements, which, in turn, are prone to lead to model run times which are uneconomically high for a component's design and dimensioning process. In order to address this issue, a numerically efficient yet accurate constitutive model was developed which is able to represent the composite's mechanical behaviour across a multitude of plies of arbitrary orientation. This, then, allows for a comparatively coarse FE mesh to be employed which ultimately leads to a reduction in the model's run time.

The version of the constitutive model described in this chapter built upon an existing model. This particular model was extended by enabling the reflection of the composite's rate-dependency for the whole range of its mechanical behaviour, i.e. elastic deformation, failure, and damage evolution. Particular attention was placed on an appropriate stain-rate smoothing algorithm, which seeks to prevent the development of numerical

instabilities caused by excessively high strain-rate changes across subsequent calculation cycles. This algorithm, which mimicks the characteristics of a *low-pass filter*, was shown to allow for an improved representation of high-rate phenomena compared to a conventional *running average* approach.

Lastly, a study was presented which aimed at providing a reference point for the critical finite element dimensions beyond which the experimentally-obtained set of energy release rates can no longer be reflected by a CDM-based damage modelling approach. This study found the fibre failure modes to be fairly unproblematic. In contrast, the matrix-dominated failure modes, i.e. IFF and delamination, featured very small critical element dimensions, thus rendering the respective energy release rates prone to be internally overwritten to enforce numerical stability for typical application cases.

Chapter 5

Model calibration and validation

This chapter first presents the constitutive model's calibration against rate-dependent datasets for: (i) its elastic and strength properties under normal deformation, (ii) its elastic and strength properties under shear deformation, and (iii) its set of energy release rates. Then, an outline of a 'panel impact' validation experiment is provided, followed by a description of the corresponding FE model alongside the results of the associated mesh sensitivity analysis. The constitutive model's validation exercise covers the following aspects: (i) a study comparing the model's performance as a function of the chosen discretisation level to the experimental database as well as a state-of-the-art composite material model (*MAT 261* in *LS-Dyna*), and (ii) a study of the influence of accounting for the model's individual rate-dependent effects.

Main contributions to the body of knowledge contained in the present chapter at a glance:

- Demonstration of the proposed constitutive model's ability to reflect a composite laminate's mechanical behaviour with sufficient accuracy whilst requiring only a fraction of the computing time compared to a state-of-the-art ply-by-ply model.

5.1 Model calibration

This subchapter presents the constitutive model's calibration against experimental data for: (i) its rate-dependent behaviour under normal deformation and failure, (ii) its rate-dependent behaviour under shear deformation and failure, and (iii) its set of rate-dependent energy release rates.

5.1.1 Calibration of the model's rate-dependent behaviour under normal deformation and failure

The fit function employed for the parameterisation of the experimentally-obtained sets of data points to calibrate the rate-dependent scale factors κ and λ, see **Chapter 4.6**, is based on an extended version of a function originally employed by *Wiegand (2008)* [144], see **Equ. 5.1**. This extended formulation, as given in **Equ. 5.2**, introduces an additional degree of freedom in order to allow for a more accurate fit to the experimental data.

$$\kappa = 1 + \sqrt{K \cdot \dot{\epsilon}} \tag{5.1}$$

$$\kappa = 1 + \left(K \cdot \dot{\epsilon}\right)^{\frac{1}{H}} \tag{5.2}$$

In the above equations, K and H denote the arbitrary parameters of the fitting function, and $\dot{\epsilon}$ the strain-rate associated with the appropriate deformation mode, respectively. An identical function is used for the calibration of λ.

For reasons of consistency, the above fit function was also employed for datasets containing merely two data points.

The calibration of the composite's normal deformation modes and their respective interactions were based on the following sources and assumptions:

- ***11-t* deformation**. The Young's modulus and strength of carbon-fibre-based composites are known to be rate-insensitive for deformation in fibre tensile direction [58, 136, 150]. The quasi-static values for both properties were taken from [96].
- ***11-c* deformation**. The Young's modulus for this deformation mode has been shown to be rate-insensitive [78, 114]. The data points used to calibrate the strain-rate-dependent strength were taken from *Ploeckl et al. (2017)* [114].
- ***22-t* deformation**. The data points used to calibrate the strain-rate-dependent Young's modulus and strength were taken from *Schaefer et al. (2014)* [124], *Kuhn et al. (2015)* [81], and the experimental results generated in the context of **Chapter 2.3.1**.
- ***22-c* deformation**. The data points used to calibrate the strain-rate-dependent Young's modulus and strength were taken from *Koerber et al. (2010)* [79], *Schaefer et al. (2014)* [124], and the experimental results generated in the context of **Chapter 2.2**.
- ***33* deformation**. The model's elastic behaviour in *33*-direction does not dis-

tinguish between deformation in its tensile or compressive domain, and, further, neglects any rate-dependency. Its tensile strength is assumed to be identical to its counterpart under *22-t* deformation; no failure is assumed under pure compressive loading.

- **Poisson's ratios**. The values of the composite's Poisson's ratios $\nu_{23} = 0.5$ [76], $\nu_{12} = 0.316$ [96], and $\nu_{13} = \nu_{12}$ are assumed to be rate-insensitive.

The least-square-fit-based calibration of the fit function against the individual sets of rate-dependent data points for each relevant Young's modulus is presented in **Figure 5.1**, and for the relevant strength properties under normal deformation in **Figure 5.2**. **Table 5.1** provides the numerical values of the quasi-static properties and their corresponding fit function parameters for all Young's moduli, and **Table 5.2** for all strength properties under normal deformation. For purposes of numerical stability, scale factor values associated with strain-rates above $10,000$ s^{-1} are capped.

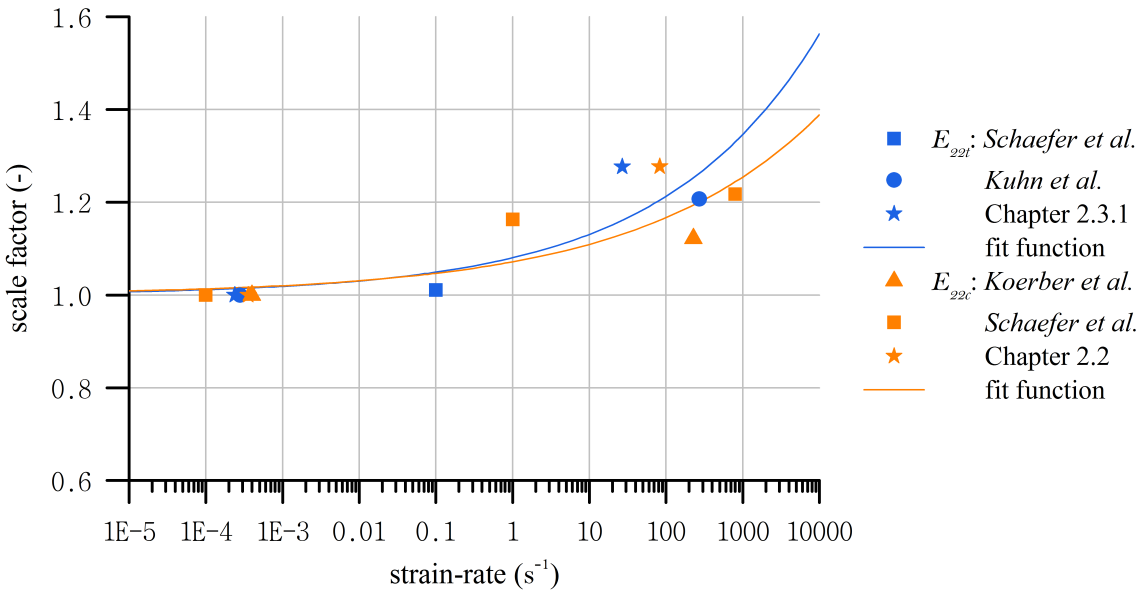


Figure 5.1: Normalised sets of data points and their corresponding fit functions for each relevant Young's modulus reflecting the composite's rate-dependent normal deformation behaviour

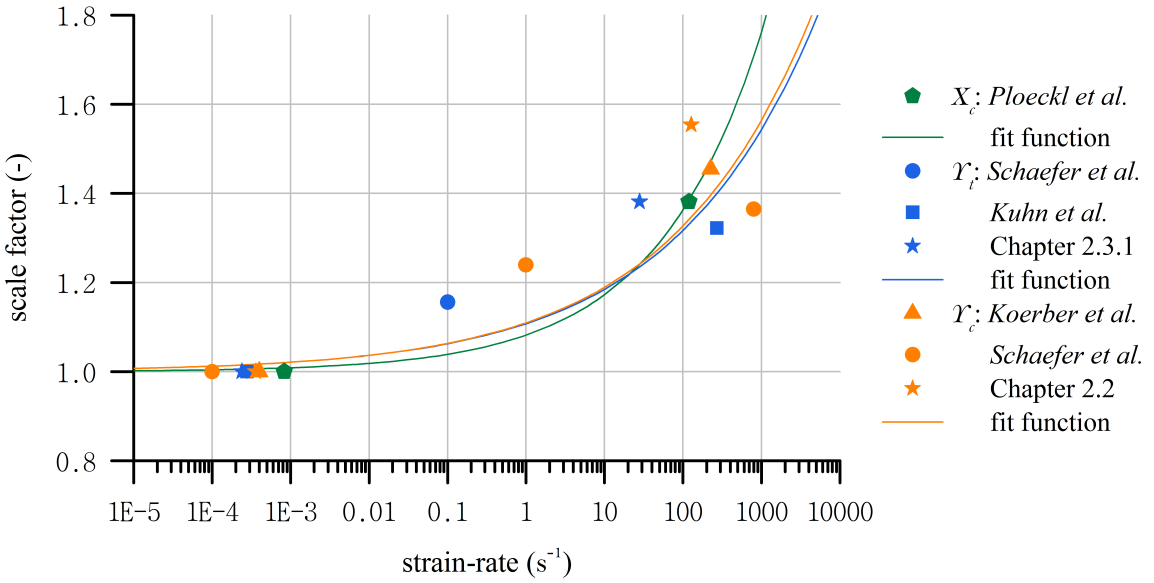


Figure 5.2: Normalised sets of data points and their corresponding fit functions for each relevant strength parameter reflecting the composite's rate-dependent normal deformation behaviour

Table 5.1: Quasi-static material properties and their corresponding fit function parameters to reflect the composite's rate-dependent Young's moduli under normal deformation

material property	QS value GPa	source	fit function parameter K	H
E_{11t}	162	*NIAR report* [96]	no rate-dependency	
E_{11c}	155	*Ploeckl et al. (2017)* [114]	no rate-dependency	
E_{22t}	9.4	**Chapter 2.3.1**	$6.62E-06$	4.729
E_{22c}	8.5	**Chapter 2.2**	$2.53E-07$	5.661
E_{33}	9.4	$E_{33} = E_{22t}$ assumed	rate-dependency neglected	

Table 5.2: Quasi-static material properties and their corresponding fit function parameters to reflect the composite's strength properties under normal deformation

material property	QS value MPa	source	fit function parameter K	H
X_t	2557	*NIAR report* [96]	no rate-dependency	
X_c	1454	*Ploeckl et al. (2017)* [114]	$4.30E-04$	3.100
Y_t	59	**Chapter 2.3.1**	$7.39E-05$	4.266
Y_c	266	**Chapter 2.2**	$8.92E-05$	4.218
Z_t	59	$Z_t = Y_t$ assumed	identical to Y_t assumed	

5.1.2 Calibration of the model's rate-dependent behaviour under shear deformation and failure

Shear in *12*-direction. The constitutive model's reflection of in-plane shear deformation and failure was introduced in **Chapter 4.3**. In order to calibrate its rate-dependent governing parameters, the composite material was characterised across two strain-rate regimes. To this end, a laminate composed of 12 unidirectionally-reinforced *IM7/8552* plies was produced according to the ply book $[(+45, -45)_3]_{symm.}$. From this laminate, dog-bone-type specimens were manufactured, which were then adhesively bonded to threaded mild steel 'end sleeves'. Subsequently, a black speckle pattern on a white background was applied in order to allow for a DIC-based analysis of the specimens' deformation behaviour. Testing under quasi-static loading was carried out on a screw-driven testing machine (*Zwick/Roell Z250*) under displacement control (0.008 mm/s); the high-rate experiments employed an SHTB setup (see **Chapter 2.1.3**) in conjunction with a neoprene rubber pulse shaper ($t = 2.1$ mm) and a projectile velocity of 5.8 m/s. Following *ASTM D3518/D3518M* [7], the stress-strain

curves were truncated at 5% strain due to the excessive influence of *fibre scissoring* beyond this level of strain. In accordance with the same standard, the ultimate strength was determined to $S_m = \frac{F_{max}}{2A_0}$, with F_{max} denoting the maximum load and A_0 the sample's initial cross-section, respectively; the initial shear modulus $G_{12,0}$ was obtained as the chord modulus between the strain values 0.2 and 0.6%. All further parameters governing the model's in-plane shear behaviour were determined via a fit to the experimentally-obtained stress-strain curves. With respect to the high-rate characterisation experiments, it must be mentioned that the initial sample deformation did not occur under a sufficiently low state of force disequilibrium along the specimen's gauge section. Thus, the parameters obtained on the basis of the samples' initial deformation, $G_{12,0}$ and S_Y, should be considered with caution as they are not truly representative of the material's intrinsic behaviour. It is recommended to repeat the high-rate experiments employing an even lower steepness of the incident pulse's rising slope in order to ultimately achieve a sufficiently quick establishment of force equilibrium which would then allow to obtain more representative high-rate data points for those two parameters. **Figure 5.3** presents the sets of stress-strain curves obtained under quasi-static and high-rate loading in conjunction with their respective reflection by the constitutive model.

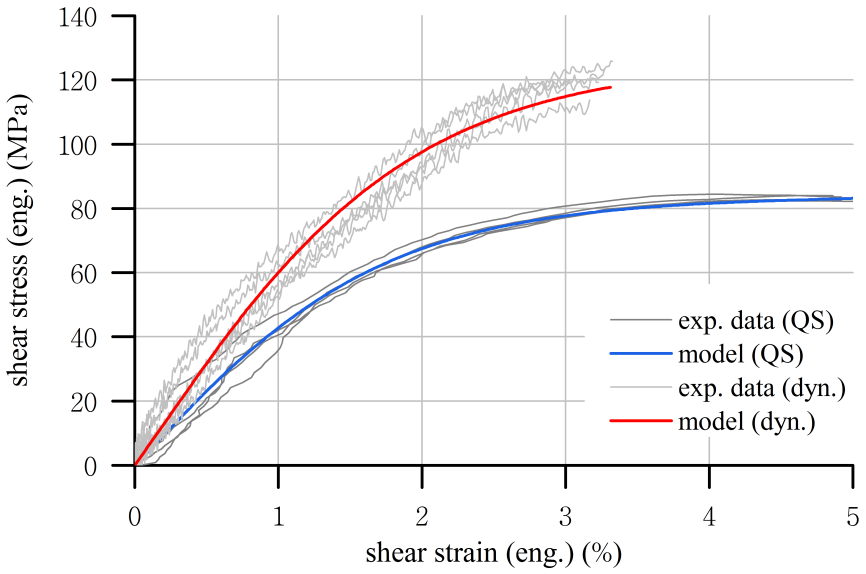


Figure 5.3: Sets of stress-strain curves obtained under in-plane shear deformation across two loading rate regimes and their respective reflection by the constitutive model

Figure 5.4 presents the rate-dependent sets of data points obtained for the in-plane shear model's material properties, $G_{12,0}$ and S_m, its empirical parameters, S_Y, S_{Yp}, and $G_{12,f}$, and their corresponding fit functions to reflect their individual rate-dependency. In order to avoid excessive scaling beyond the experimentally-generated data range, scale factor values associated with strain-rate values above $1,000$ s^{-1} are capped for the in-plane shear model. **Table 5.3** provides the quasi-static values and their corresponding fit function parameters for all material properties and empirical parameters under in-plane shear deformation.

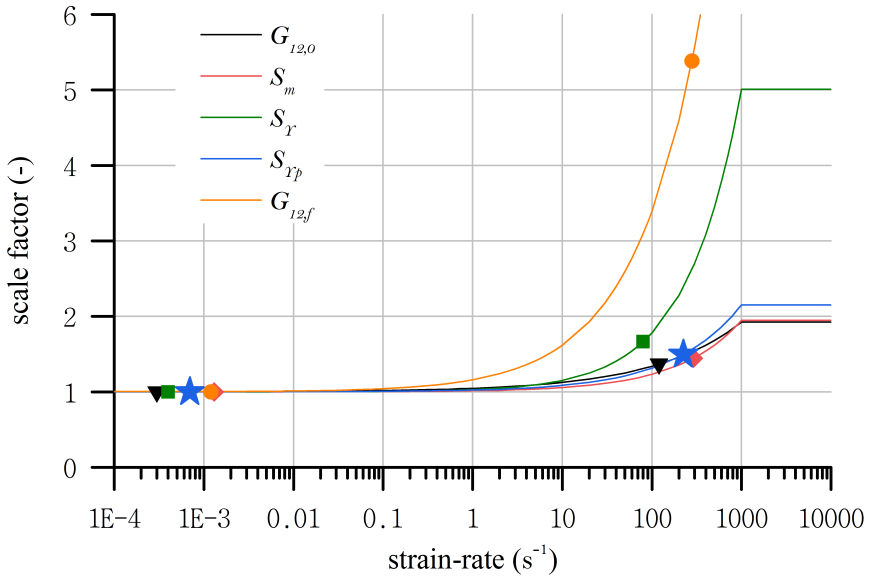


Figure 5.4: Normalised sets of data points and their corresponding fit functions for each material property and empirical parameter reflecting the composite's rate-dependent in-plane shear behaviour

Table 5.3: Quasi-static values and their corresponding fit function parameters for all material properties and empirical parameters under in-plane shear deformation

material property or empirical parameter	QS value	fit function parameter	
	MPa	K	H
$G_{12,0}$	4634	0.0008329	2.297
S_m	83	0.000915	1.637
S_Y	18	0.00705	1.406
S_{Yp}	137	0.001283	1.774
$G_{12,f}$	130	0.04413	1.701

Lastly, **Figure 5.5** presents an example of an array of stress-strain curves of the modelled in-plane shear behaviour across the full range of relevant strain-rate values.

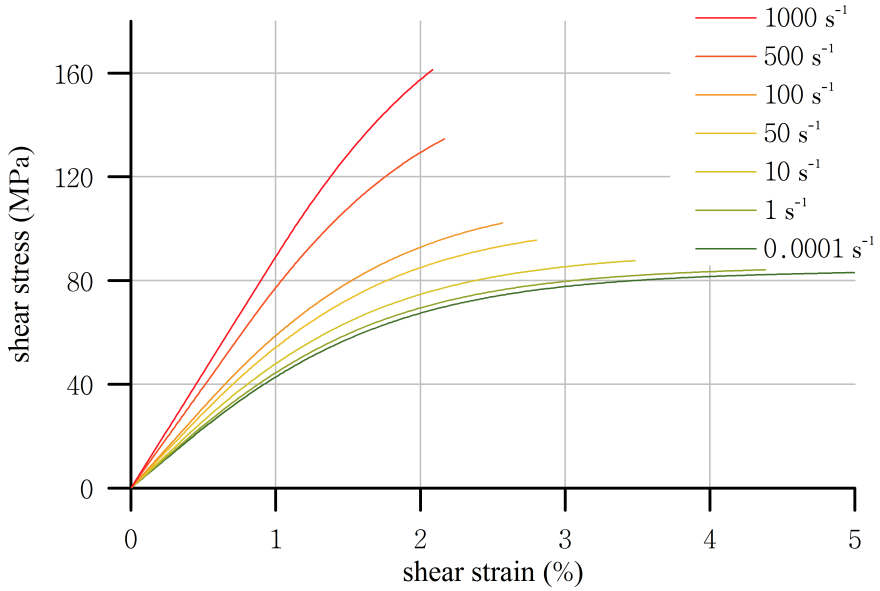


Figure 5.5: Example of an array of stress-strain curves of the modelled in-plane shear behaviour across the full range of relevant strain-rate values

Shear in *31*-direction. The values for the Young's modulus and strength for *31-shear* deformation under quasi-static loading were taken from *Kaddour et al. (2013)* [76]: $G_{31} = 5600$ MPa, $S_{31} = 90$ MPa. The Young's modulus' rate-dependency is neglected. The rate-dependent trend pertaining to S_{31} is assumed to be identical to the one for shear deformation in *12*-direction, i.e. $\lambda_{31} = \lambda_{12}$.

Shear in *23*-direction. Identical behaviour to *31-shear* is assumed.

5.1.3 Calibration of the set of rate-dependent energy release rates

Delamination. G_{Ic}^{del} has been shown to be rate-insensitive [18, 100]; its quasi-static value was taken from *Camanho et al. (2007)* [20]. In contrast, G_{IIc}^{del} has been demonstrated to be a function of the applied loading rate (see discussion in the context of

Chapter 3.1). However, as no high-rate data for *IM7/8552* was found in the literature, an identical rate-sensitivity trend as for *AS6/8552* [18] is assumed. This assumption is based on both composites featuring the identical matrix material, which, in turn, is furthermore assumed to essentially govern the fracture process under delamination failure. The value of $G^{del}_{IIc,QS}$ was taken from *Camanho et al. (2007)* [20]. The reference strain-rates for the quasi-static and high-rate values of G^{del}_{IIc} could not be deduced from their corresponding literature sources, and were thus assumed to be identical to the ones associated with $G^{f+}_{Ic}(\dot{\epsilon})$ (see **Chapter 3**).

IFF. The energy release rate values associated with IFF are assumed to be identical to their corresponding counterparts for delamination (see discussion in **Chapter 3.1** for justification).

Fibre failure. In contrast to delamination and IFF, damage evolution involving fibre failure considers only fracture mode I. The rate-dependent energy release rate values for fibre tensile failure were taken from the characterisation experiments carried out in the context of **Chapter 3**. The values for $G^{f-}_{Ic}(\dot{\epsilon})$ were taken from *Kuhn et al. (2017)* [80]. The corresponding quasi-static reference strain-rate value was assumed; its high-rate counterpart was taken to be identical to the strain-rate value quoted in the context of the associated SHB analysis.

As merely two data points were available for each of the rate-dependent energy release rate values, and no further indication regarding their qualitative change under increasing loading rate conditions could be deduced from the available literature, a linear interpolation between the respective sets of data points was chosen. For strain-rate values above the reference high-rate value, the corresponding energy release rate is

capped.

A summary of the model input parameters defining the composite's set of rate-dependent energy release rate values is provided in **Table 5.4**. Delamination and IFF are subsumed under the term 'matrix failure'.

Table 5.4: Calibration of the model's set of rate-dependent energy release rates

	quasi-static loading		high-rate loading	
	energy release rate kJ/m^2	reference strain-rate s^{-1}	energy release rate kJ/m^2	reference strain-rate s^{-1}
matrix failure: mode I	0.28	no rate-dependency		
matrix failure: mode II	0.79	0.0001	0.98	40
fibre tensile failure	196	0.0001	82	40
fibre compressive failure	102	0.0001	166	100

5.2 Validation experiment and its model

This subchapter first presents an outline of the experiment that formed the basis of the constitutive model validation exercise. Subsequently, the numerical model that represented this experiment is described and the results of the corresponding mesh sensitivity study are presented.

5.2.1 Experimental setup

The experimental database against which the constitutive model described in **Chapter 4** was validated had been generated by *Hao Cui* at the *Impact Engineering Laboratory* at the *University of Oxford* [32]. The experiment employed composite panels consisting of

a quasi-isotropic layup of *IM7/8552* prepreg laminae (ply-book: $[0, 45, 90, -45]_{5,symm.}$). The panels' dimensions were 200 x 200 x 5 mm. These panels were subjected to an impact by a $\varnothing$20 mm steel ball bearing which was accelerated using a gas gun (bore: 70 mm). The panels' support consisted of four steel ball bearings identical to the projectile. The experimental setup's essential dimensions are provided in **Figure 5.6**. A black speckle pattern on a white background was applied to the projectile in order to allow for a DIC-based determination of its motion. The series of images required for this analysis was obtained employing a high-speed camera (*Photron SA5*).

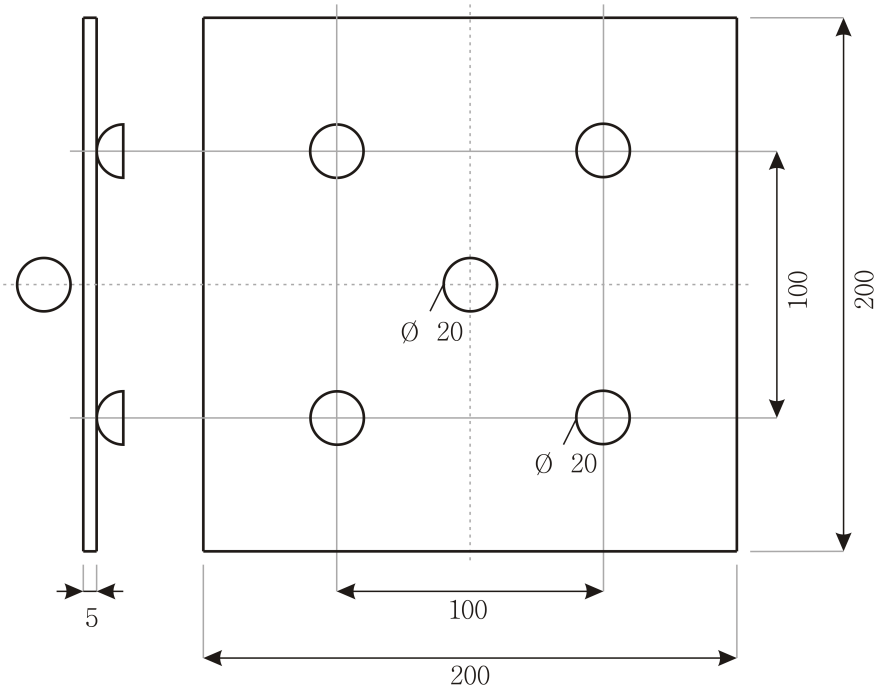


Figure 5.6: Essential geometric dimensions of the validation experiment (in mm)

5.2.2 Model of the validation experiment

Outline of the model. The individual parts were meshed employing a *structured mesh* of *single integration point solid elements*. The projectile's and support's mesh consisted of elements with an approximate element edge length of 1 mm; both were

modelled as *rigid* with $E = 205$ GPa and $\rho = 7.85$ g/cm^3. The panel's mesh will be discussed in the subsequent paragraph. Loading conditions consisted of applying the impact velocity to the projectile's nodes; boundary conditions consisted of restricting the support's appropriate nodes' degrees of freedom. *LS-Dyna*'s *eroding surface to surface* contact was used to model the interaction between projectile and panel; the interaction between panel and support was modelled employing an *automatic surface to surface* contact.

Mesh sensitivity study: Setup. As a finite element mesh's topology influences its deformation behaviour, a mesh sensitivity study for the panel was carried out. This study was based on a projectile velocity of 20 m/s and a purely elastic and isotropic material behaviour of the panel ($E = 70$ GPa and $\rho = 2.7$ g/cm^3). A mesh bias was employed for the panel's FE mesh to achieve a higher spatial resolution in the immediate impact area, see **Figure 5.7(a)**.

In order to investigate the effect of the panel's in-plane mesh density on the deflection history of its centre, the following meshes were employed: element dimensions ranging from min. 0.5 to max. 1.2 mm (*mesh A*), from 0.75 to 1.8 mm (*mesh B*), from 1.0 to 2.4 mm (*mesh C*), from 1.25 to 3.0 mm (*mesh D*), and from 1.5 to 3.6 mm (*mesh E*). The panel's out-of-plane discretisation was kept constant across the range of these meshes (40 elements).

In order to then investigate the effect of the panel's out-of-plane mesh density on the deflection history of its centre, *mesh C* was discretised using 5, 10, 20, and 40 elements, respectively, in its through-thickness direction. This range directly reflected the discretisation levels employed for the constitutive model validation exercise.

Mesh sensitivity study: Results and discussion. As shown in **Figure 5.7(b)**, the deflection history monotonically converged against the 'accurate' solution for increasing in-plane mesh densities. However, as displayed in **Figure 5.7(c)**, the gain in accuracy decreased drastically whilst the numerical cost increased substantially for meshes denser than *mesh C*. Said mesh was thus chosen as the in-plane mesh topology for the model validation exercise.

Employing *mesh C* in conjunction with a range of out-of-plane mesh densities revealed a considerable dependency of the panel's deflection history on the latter, see **Figure 5.7(d)**. Moreover, no clear convergence behaviour existed as it was the case for increasing in-plane mesh densities. This, in turn, may have been caused by the superposition of two competing mechanisms. On the one hand, a higher spatial discretisation allowed for a more realistic capturing of pronounced stress field gradients, which tendentially yields a more compliant deformation behaviour. On the other hand, a higher spatial discretisation also entailed a higher moment of resistance, which tendentially yields a stiffer structural response. This higher moment of resistance originates from the increasing distance of the outer elements' integration points from the panel's neutral plane with increasing levels of discretisation in its through-thickness direction, see illustration in **Figure 5.8**. Consequently, as a second important outcome of this mesh sensitivity study, it must be noted that varying discretisation levels in the panel's through-thickness direction inevitably play a role in the modelled component's deformation behaviour beyond the influence of the assigned constitutive model.

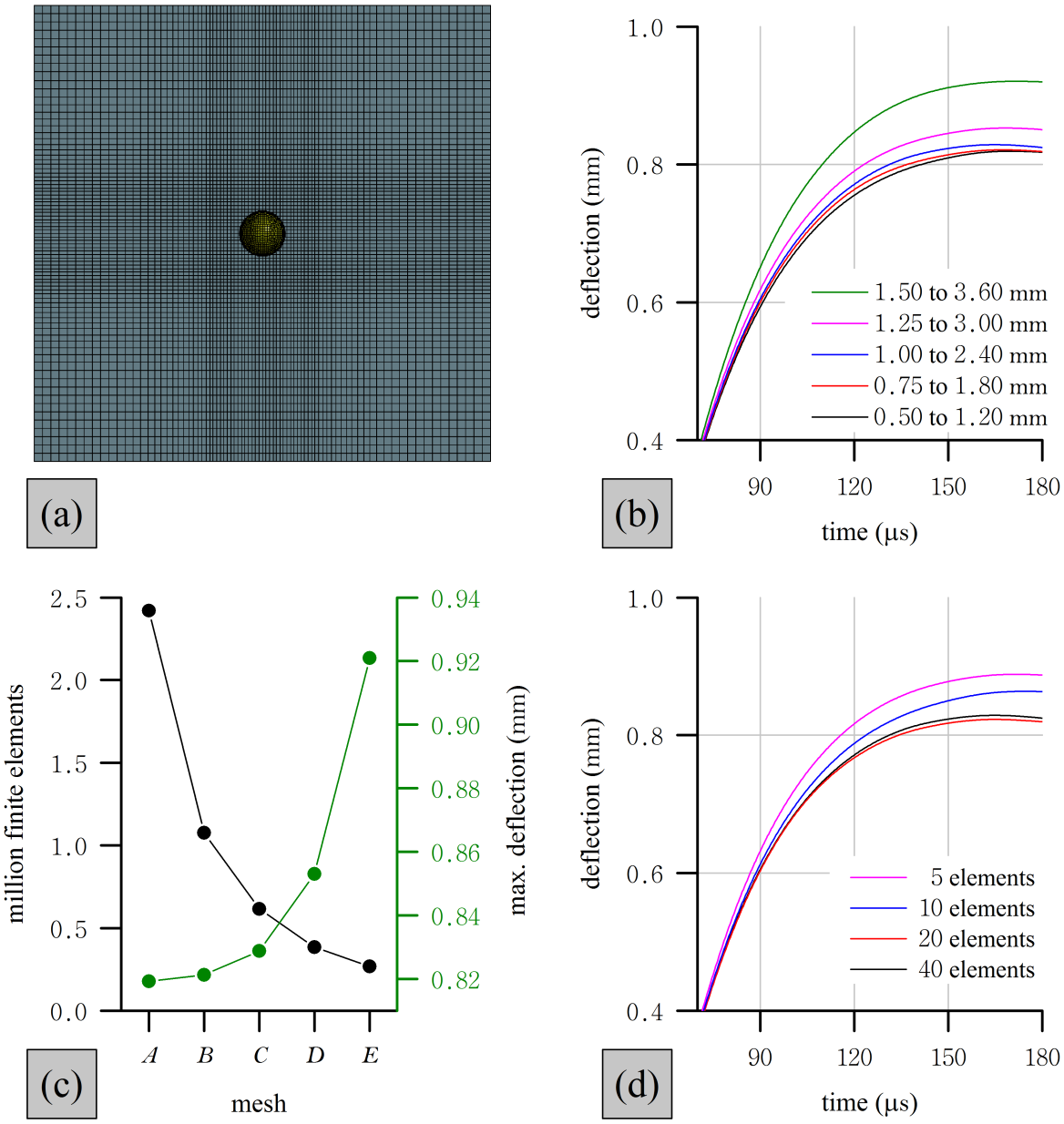


Figure 5.7: (a) mesh bias for the FE mesh of the panel; (b) deflection history for the range of investigated in-plane mesh densities; (c) juxtaposition of the meshes' maximum deflection against the number of finite elements for the range of investigated in-plane mesh densities; (d) deflection histories for the range of investigated out-of-plane discretisations

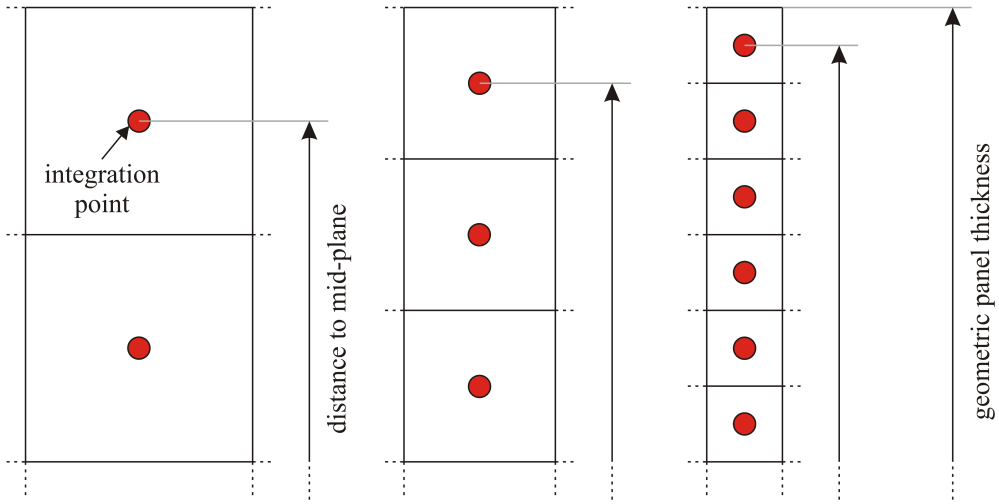


Figure 5.8: Increasing moment of resistance caused by higher levels of discretisation in the panel's through-thickness direction

5.3 Constitutive model validation

This subchapter first provides an outline of *LS-Dyna MAT 261*, followed by an assessment of the performance of the constitutive model proposed in this thesis against the experimental database described in **Chapter 5.2** and aforementioned *MAT 261*. This assessment encompasses a study of the following aspects of the model: (i) the employed discretisation level of the composite panel, and (ii) the individual effects of taking into account the composite's rate-dependent elastic, failure, and damage evolution behaviour.

5.3.1 Outline of *LS-Dyna MAT 261*

In order to allow for a more comprehensive assessment of the predictive quality and numerical cost of the constitutive model proposed in **Chapter 4**, the model's valida-

tion exercise also incorporates a comparison with a state-of-the-art composite material model, namely *LS-Dyna MAT 261*.[1] This material model operates on meso scale, i.e. it reflects the mechanical behaviour of an individual composite material ply. Its governing equations are based on the work of *Pinho et al. (2006)* [110, 111].

The material exposure pertaining to IFF is formulated in terms of the normal traction σ_n, and two shear tractions τ_T and τ_L, acting on the potential fracture plane with its normal oriented orthogonally to the fibre direction. **Figure 5.9** provides a depiction of these tractions in the material coordinate system.

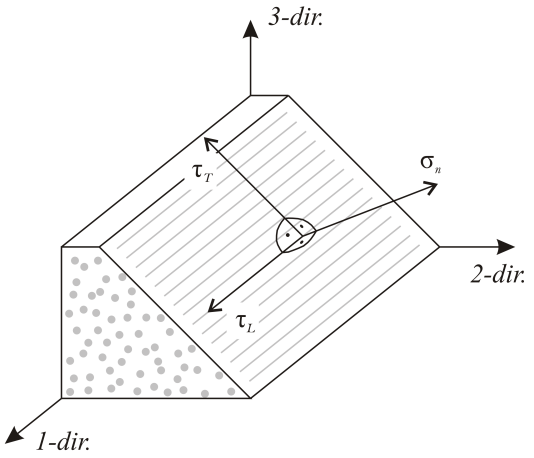


Figure 5.9: Tractions acting on the potential fracture plane associated with IFF (following the depiction in *Pinho et al. (2006)* [110])

The model reflects a Mohr/Coulomb-type material behaviour under normal compressive load on the fracture plane. The set of equations pertaining to the material exposure associated with IFF reads as follows:

$$e_{IFF} = \begin{cases} \left(\frac{\sigma_n}{Y_t}\right)^2 + \left(\frac{\tau_T}{S_T}\right)^2 + \left(\frac{\tau_L}{S_L}\right)^2 & \text{if } \sigma_n \geq 0 \ , \\ \left(\frac{\tau_T}{S_T - \mu_T \sigma_n}\right)^2 + \left(\frac{\tau_L}{S_L - \mu_L \sigma_n}\right)^2 & \text{if } \sigma_n < 0 \ . \end{cases} \tag{5.3}$$

In the above equation, S_L denotes the longitudinal shear strength (i.e. S_{12}), S_T the

[1] *MAT 261* is available *LS-Dyna* versions above R7.0.

transverse shear strength, and μ_L and μ_T the friction coefficients associated with longitudinal and transverse shear, respectively. With the fracture angle obtained under pure transverse compression, ϕ_0, the last three of the aforementioned parameters are then determined according to

$$S_T = \frac{Y_c}{2tan(\phi_0)}, \qquad \mu_T = -\frac{1}{tan(2\phi_0)}, \qquad \mu_L = S_L \frac{\mu_T}{S_T} \; . \tag{5.4}$$

In order to find the set of tractions associated with the potential fracture plane of highest material exposure, the model evaluates the full three-dimensional stress space.

Fibre compressive failure is modelled as the kinking of misaligned fibres. Fibre kinking, in turn, is assumed to be driven by IFF in the vicinity of those fibres. Consequently, fibre compressive failure also employs above IFF criterion. In order to find the plane associated with the highest material exposure, however, additional stress tensor rotations are performed. The reader is referred to the original sources [110, 111] for an in-depth description of the individual operations required. Lastly, fibre tensile failure is reflected by a maximum stress criterion.

Important additional features of *MAT 261* are its ability to account for the non-linearity of the in-plane shear stress-strain relationship, as well as its consideration of the experimentally-determined set of energy release rates for its strain-softening behaviour.

The key differences between *MAT 261* and the constitutive model proposed in **Chapter 4** are as follows: (i) *MAT 261* represents the behaviour of a single composite ply as opposed to that of multiple laminae, (ii) it takes the full stress tensor into account for the calculation of the material exposure for IFF and fibre kinking opposed to assuming

a state of plane stress, and (iii) no rate-dependent material properties are considered opposed to an extensive consideration of the composite's rate-dependency.

5.3.2 Influence of the model's level of homogenisation and comparison to *MAT 261*

The study of the influence of the model's level of homogenisation and its comparison to *MAT 261* was based on the following setup and parameters:

- The metric employed to gauge the models' performance was the energy dissipated by the panel over the course of its interaction with the projectile. This parameter, E_{dissip}, was derived from the experimental data on the basis of the projectile's initial and residual velocity according to

$$E_{dissip} = E_{init} - E_{resid} = \frac{1}{2} m_{proj} (v_{init}^2 - v_{resid}^2) \; . \tag{5.5}$$

  Any kinetic energy stored in the panel after its interaction with the projectile was neglected. Three sub-critical impact velocities were evaluated ($v_{init} = 36$, 62, and 72 m/s) and one super-critical (i.e. causing panel perforation; $v_{init} = 164$ m/s).
- The panel's in-plane mesh was kept constant throughout all model configurations (*mesh C* in **Chapter 5.2.2**); its out-of-plane mesh density was dependent on the number of composite plies represented by each FE layer.
- Two constitutive models were assessed: (i) the model proposed in **Chapter 4**, employing a *2*, *4*, and *8 ply homogenisation*, with all rate-dependencies enabled, and (ii) *MAT 261* (see **Chapter 5.3.1** for details). The latter was used without any additional *cohesive elements*, which means that this model configuration

could not reflect delamination failure. Both constitutive models were calibrated against the data collected in **Chapter 5.1**. In order to allow for the panel's perforation, *element erosion* was enabled in case of fibre tensile or compressive failure. Additionally, erosion was triggered for a value of the deviatoric strain tensor reaching 0.07. This value was found to prevent the simulation time step from excessively diminishing and is about equal to other sources, e.g. [17]. A major drawback of this additional erosion criterion, however, was that the elements' strain-softening domain could be 'cut off' by the erosion, thus resulting in a discarding of elements which still had elastic energy stored in them.

- Each simulation was run on 20 cores of a *Linux Workstation* featuring 24 *Intel Xeon* CPUs @ 2.30 GHz and 62.9 GB of RAM.

Figure 5.10 presents the results of the *MAT 261* and the *2*, *4*, and *8 ply homog.* model simulations for the range of simulated impact velocities; in **(a)** the panel's dissipated energy is given, and in **(b)** the models' run time is displayed. **Figure 5.11** shows the panel's perforation for the super-critical impact velocity $v_{init} = 164$ m/s.

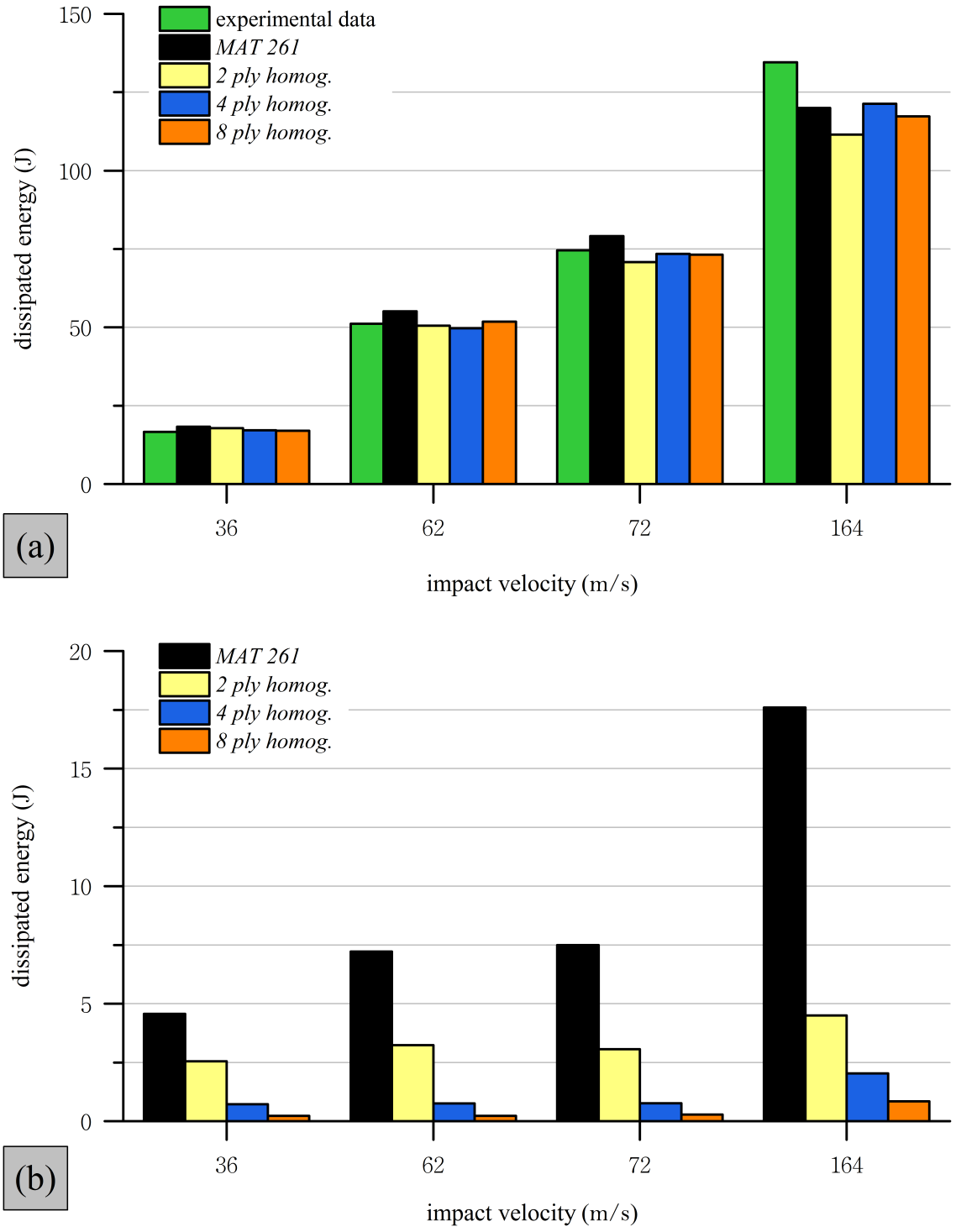


Figure 5.10: (a) energy dissipated by the panel against impact velocity, and (b) model run time against impact velocity

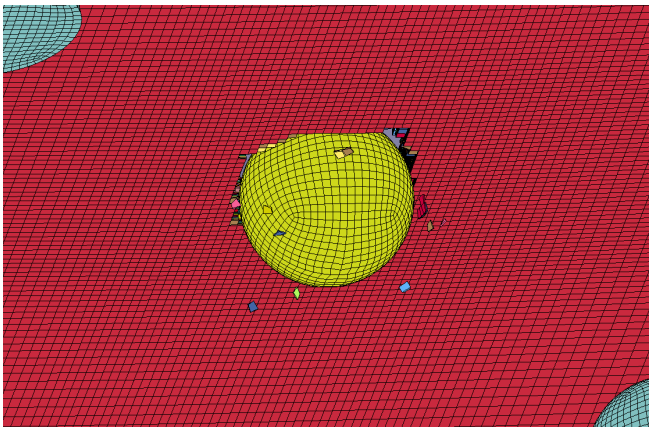


Figure 5.11: Perforation of the panel for the super-critical impact velocity $v_{init} = 164$ m/s

Across all simulated impact velocities, the developed constitutive model showed a response comparable to that of *MAT 261*. In case of the sub-critical impact velocities, the proposed model demonstrated a satisfying level of accuracy; the slight inaccuracy of *MAT 261* was likely caused by not reflecting delamination damage. In case of the super-critical impact velocity, both, the proposed model and *MAT 261*, showed a lower level of energy dissipation than what was observable in the experiment. This discrepancy, however, might be explained by the shortcomings associated with the erosion of finite elements in order to reflect the emergence of discontinuities over the course of the panel's interaction with the projectile. As was explained above, erosion might have triggered before the finite elements could 'shed' all their elastically stored energy, thus effectively removing energy that could then no longer be part of the dissipation process.

In terms of the calculation time required to solve each model, **Figure 5.10(b)** indicates a vastly superior performance of the developed model over *MAT 261*. In particular, higher levels of homogenisation showed a very significant reduction in the model's run time.

Lastly, it is recommended to extend above study by complementing the *MAT 261* simulations with cohesive elements. This would ultimately provide an even clearer picture in terms of the corresponding model's ability, but also of its required run time.

5.3.3 Influence of the model's individual rate-dependent effects

The influence of the model's individual rate-dependent effects was examined by employing the *4 ply homog.* model and running it in the following (additional) configurations: (i) switching *all* rate-dependent effects off, (ii) accounting for the rate-dep. strength and toughness, but switching the rate-dep. elasticity off, (iii) accounting for the rate-dep. elasticity and toughness, but switching the rate-dep. strength off, (iv) accounting for the rate-dep. elasticity and strength, but switching the rate-dep. toughness off, and (v) accounting for all rate-dependencies except for the one associated with G_{Ic}^{f+}. All remaining simulation parameters were kept identical to the preceding section. **Figure 5.12** presents the results of this study for the range of impact velocities.

For the lowest impact velocity, $v_{init} = 36$ m/s, accounting for the composite's rate-dependency did not show a significant effect on the panel's dissipated energy E_{dissip}. For $v_{init} = 62$ and 72 m/s, in contrast, a clear but moderate effect on E_{dissip} was observable. This effect, however, seemed to be majorly driven by accounting for the rate-dependency of the strength properties. In comparison, accounting for the rate-dependency of the composite's elastic and toughness properties appeared to have an almost negligible effect on E_{dissip}. For the highest impact velocity, $v_{init} = 164$ m/s,

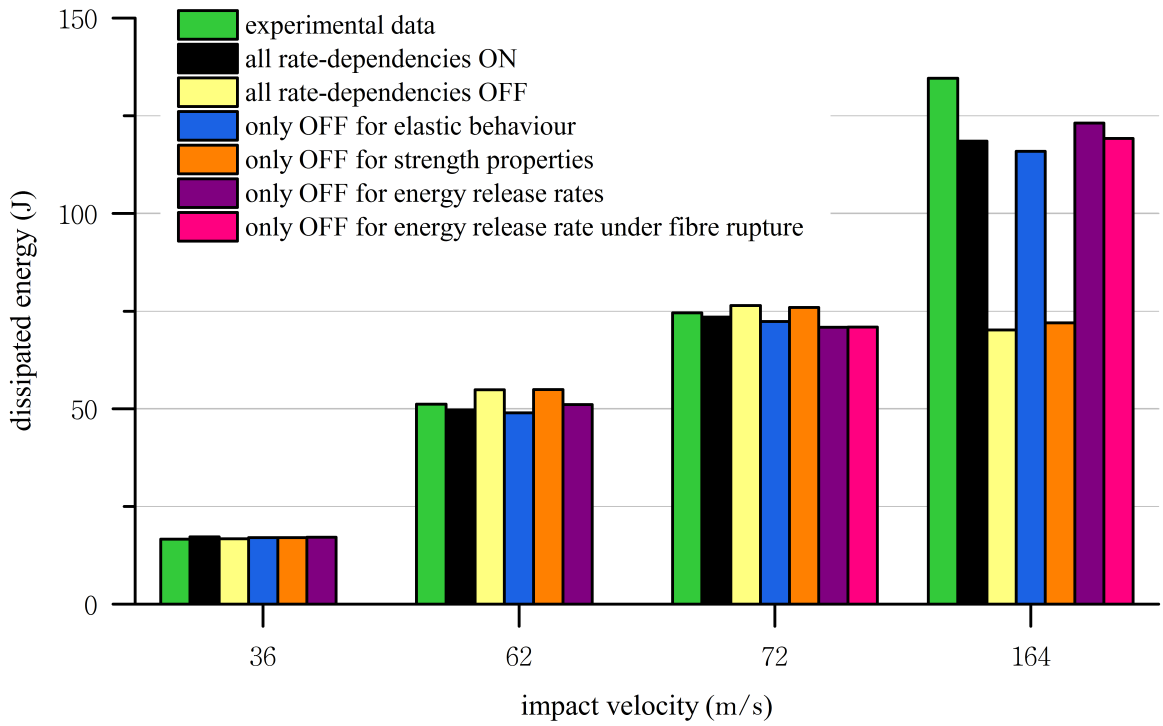


Figure 5.12: Dissipated energy against impact velocity for taking into account the individual rate-dependency of the model's elastic, failure, and damage evolution behaviour

accounting for the composite's rate-dependency significantly improved the model's capability to reflect the experimental data. Again, however, this improvement appeared to be essentially driven by accounting for the composite's rate-dependent strength properties.

Lastly, the model's behaviour did not show a marked change of E_{dissip} when taking into account the rate-dependent nature of G_{Ic}^{f+}. This, however, was not unexpected, as the impact velocities up to and including $v_{init} = 72$ m/s did not entail any significant fibre damage in the model (or the experiment). For $v_{init} = 164$ m/s, the model's element erosion resulted in a 'cut-off' of the elements' strain-softening domain under fibre failure (see **Chapter 5.3.2**), thus masking a potential effect of $G_{Ic}^{f+}(\dot{\epsilon})$ on the model's response.

5.4 Summary

Model calibration. The model was calibrated against rate-dependent datasets for *IM7/8552* for: (i) its elastic and strength properties under normal deformation, (ii) its elastic and strength properties under shear deformation, and (iii) its set of energy release rates. A particular focus was placed on the composite's non-linear in-plane shear behaviour, which was characterised across two strain-rate regimes in order to calibrate the rate-dependent arbitrary parameters of its governing equation.

Model validation. First, a brief overview of the validation experiment and the corresponding finite element model was presented. This was followed by an outline of the state-of-the-art model *MAT 261* in *LS-Dyna*, which was selected to serve as a direct comparison to the developed constitutive model. The metric chosen for the validation exercise was the energy dissipated by the panel over the course of its interaction with the projectile, E_{dissip}. The following key conclusions were drawn from this exercise:

- Overall, the developed constitutive model demonstrated a predictive ability comparable to that of *MAT 261*. Maintaining this level of accuracy, however, was achieved whilst *drastically* reducing the required simulation run time. For high levels of homogenisation, the proposed model merely required a fraction of the run time of the ply-by-ply model *MAT 261*.
- The effect of the composite's rate-dependency on E_{dissip} appeared to be essentially governed by its rate-dependent strength; its rate-dependent elastic and toughness properties, in comparison, exerted only a minor influence on E_{dissip}.

Chapter 6

Summary, conclusions, and suggestions for future work

The aim of the present thesis was to develop a fully rate-dependent composite material model operating on macro scale to eventually aid the design and analysis process of a CFRP fan blade. In order to facilitate a qualitatively and quantitatively accurate reflection of the composite's rate-dependency by the model, the modelling work was complemented by experiments addressing selected gaps and shortcomings in the data and procedures documented in literature. This chapter presents a summary for each of the objectives of the experimental and modelling work, emphasising the contributions made to the body of knowledge, and finally providing suggestions for future work.

6.1 Experimental work

The experimental work's purpose was twofold: (i) to establish unavailable or extend existing rate-dependent model input datasets for chosen relevant material properties, and (ii) to address critical aspects of the (high-rate) material characterisation procedure of selected deformation, failure, or fracture modes in order to ultimately obtain material properties generated under valid testing conditions. In the following, the appropriate aspects are first covered for the characterisation of the high-rate modulus and strength for the deformation modes *22-c*, *22-t*, *33-t*, and *12-shear*, and thereafter for the strain-energy release rate under high-rate tensile loading in fibre direction, $G^{f+}_{Ic,dyn}$.

6.1.1 High-rate modulus and strength for *22-c*, *22-t*, *33-t*, and *12-shear*

22-c. The following facets of this deformation mode's characterisation were addressed:

- *Specimen design.* An experimental study was undertaken to quantify the deviation of the measured (initial) modulus and strength from their correct values when employing the most commonly used *block* specimen design opposed to a *waisted block* design. It was demonstrated that the deviations from a reasonably one-dimensional stress field along a *block* design specimen's gauge volume result in non-negligible inaccuracies in the obtained material properties. Consequently, it was recommended to favour a *waisted block* over a *block* specimen design.
- *Material characterisation.* The composite's (initial) modulus and strength for

this deformation mode were determined under quasi-static and high-rate loading as follows: $E_{22c,0}^{QS} = 8.5 \pm 0.2$ GPa and $Y_c^{QS} = 266 \pm 9$ MPa at $\dot{\epsilon} = 0.00036$ s^{-1}, $E_{22c,0}^{dyn} = 10.9 \pm 0.6$ GPa at $\dot{\epsilon} = 83$ s^{-1}, and $Y_c^{dyn} = 413 \pm 15$ MPa at $\dot{\epsilon} = 127$ s^{-1}. Both properties thus showed a significant dependency on the applied loading rate.

- A comprehensive simulation-based study was undertaken to investigate the influence of key SHB setup and testing parameters on the achievability of valid high-rate testing conditions. This study's key findings were as follows: (i) the conventional SHB analysis provides a very conservative measure for the determination of the establishment of SE compared to a direct force measurement at the gauge volume's end faces, (ii) fluctuations and disturbances in the incident pulse exert a pronounced influence on the force disequilibrium and strain-rate history of the sample's gauge section, and, (iii) the influence of the choice of bar material and diameter has an almost negligible influence on the establishment of SE, but a pronounced effect on reaching a deformation state satisfying CSR.

22-t. The following facets of this deformation mode's characterisation were addressed:

- *Material characterisation.* The composite's modulus and strength for this deformation mode were determined under quasi-static and high-rate loading as follows: $E_{22t}^{QS} = 9.4 \pm 0.6$ GPa and $Y_t^{QS} = 59 \pm 14$ MPa at $\dot{\epsilon} = 0.00024$ s^{-1}, $E_{22t}^{dyn} = 12.0 \pm 0.5$ GPa at $\dot{\epsilon} = 27$ s^{-1}, and $Y_t^{dyn} = 82 \pm 16$ MPa at $\dot{\epsilon} = 28$ s^{-1}. Both properties thus showed a significant dependency on the applied loading rate.
- A comprehensive simulation-based study was undertaken to investigate the influence of key SHB setup and testing parameters on the achievability of valid

high-rate testing conditions. The key findings of this modelling study were similar to the corresponding *22-c* study's findings for its statements (i), (ii), and the first aspect of (iii). With respect to the establishment of a deformation state satisfying CSR for high-rate *22-t* testing, however, it was found that this condition cannot be met, irrespective of the material employed for bars and end sleeves.

33-t. Motivated by the goal of overcoming adhesive bond failure observed when employing a conventional *adhesively-bonded waisted block* specimen design in conjunction with testing a composite featuring a comparatively inert matrix material, a form-fit specimen design was developed for (high-rate) out-of-plane tensile testing. This form-fit design was shown to be an appropriate substitute for the conventional *adhesively-bonded waisted block* design and its suitability for testing under high-rate loading conditions was demonstrated. Apart from not relying on an adhesive bond between 'end caps' and specimen, the form-fit design offers additional advantages: (i) a substantially reduced material volume requirement, (ii) a simplification and foreshortening of the specimen assembly process, and (iii) the reusability of the grips connecting the specimen to the testing machine.

12-shear. The composite's non-linear in-plane shear behaviour was characterised across two strain-rate regimes in order to generate the rate-dependent dataset against which the constitutive model's *12-shear* behaviour could be calibrated. One shortcoming of the generated dataset which merits further attention is that the determination of the high-rate properties associated with the stress-strain curve's initial section, $G_{12,0}$ and S_Y, did not satisfy the condition of a reasonable force equilibrium along the specimens' gauge section. This, in turn, means that these two high-rate properties cannot

be regarded as being truly representative of the material's intrinsic behaviour. It is thus recommended to seek for improved methods to characterise these properties at high rates of loading.

6.1.2 Strain-energy release rate under high-rate tensile loading in fibre direction

In contrast to the dynamic energy release rates associated with fibre compressive failure, delamination, and IFF, which have either been successfully determined experimentally or can be reasonably approximated, the one pertaining to failure in fibre tensile direction, $G^{f+}_{Ic,dyn}$, has not yet been *satisfactorily* addressed. The only attempt so far was undertaken by *McCarroll (2011)* [100], however, the experimental setup employed in said study suffered from an unusable force signal, which, in turn, necessitated the incorporation of far-reaching assumptions in the data reduction process. It was thus the goal of the present study to determine $G^{f+}_{Ic,dyn}$ by employing a modified SHTB setup, which was able to yield a clear force signal. This, then, allowed for employing the well-established *area method* for the data reduction process. Across the examined loading rate spectrum, G^{f+}_{Ic} was found to drop from 196 ± 18 kJ/m^2 at a strain-rate of about 0.0001 s^{-1} to 82 ± 21 kJ/m^2 at a strain-rate of about 40 s^{-1}. A DIC-based analysis of the strain field surrounding the crack tip indicated that a larger section of the length of the critical load-carrying fibres orthogonal to the crack tip is involved in the fracture process under quasi-static compared to high-rate loading. This observation, in turn, was taken as an indication of the fracture process under high-rate loading being a more locally confined phenomenon, involving a smaller material volume. Thus,

considering that the energy release rate G_{Ic}^{f+} suffers a salient drop under high-rate loading conditions, a simulation-based design and dimensioning process that does not account for this strongly negative loading rate trend might not be able to provide a realistic basis on which an accurate assessment of a composite component's ability to withstand a specific design-critical impact loading case is possible.

The work on the determination of $G_{Ic,dyn}^{f+}$ makes two contributions to the existing body of knowledge: (i) the employment of a modified SHTB setup for the characterisation process, involving refinements on aspects of the experimental setup, loading conditions, and data reduction, and (ii) the rate-dependent dataset obtained as a result of the material characterisation process.

The main aspects under which the work on characterising $G_{Ic,dyn}^{f+}$ may be continued are: (i) the reduction of the existing slight force disequilibrium still present in this study, and (ii) the extension and refinement of the specimens' post-mortem analysis in order to investigate the existence of a potentially larger damage zone under quasi-static than high-rate loading, as indicated by the results of the DIC-based analysis of the strain field surrounding the advancing crack tip. For a more detailed and comprehensive outline of possible improvements for characterising $G_{Ic,dyn}^{f+}$, the reader is referred to **Chapter 3.7**.

6.2 Constitutive model

Summary and key conclusions. This thesis developed an economical, fully rate-dependent model for the reflection of the deformation, failure, and damage evolution

behaviour of composite laminates. A baseline model, coded by *Jens Wiegand* [145], was taken as a starting point, and extended by all necessary features required in order to render the model adequate for the design and analysis process of a CFRP fan blade. The individual modelling objectives thus covered the implementation of: (i) the non-linearity of the in-plane shear behaviour, (ii) the reflection of the rate-dependency of the elastic, strength, and energy release rate properties, and, (iii) a strain-rate smoothing algorithm, which enforces numerical stability without impairing the 'high loading rate nature' of a simulated impact scenario.

The constitutive model is able to reflect the mechanical response of a multitude of plies within a single RVE. Its key premise is that delamination between those individual plies is entirely driven by the RVE's out-of-plane stresses σ_{33}, σ_{23}, and σ_{31}, whereas any failure and damage evolution within the plies is exclusively linked to the RVE's in-plane stresses σ_{11}, σ_{22}, and σ_{12}. This, in turn, then allows for the RVE's treatment on the basis of two separate 'submodels': A *delamination model* for its out-of-plane, and a *ply model* for its in-plane behaviour. The delamination model operates on the macro scale within the laminate coordinate system, and the ply model on meso scale within each individual plies' material coordinate system.

The two novelties generated in the context of the constitutive modelling work are: (i) a *low-pass filter*-like strain-rate smoothing algorithm, which was shown to exceed the performance of a conventional *running average* approach, and, (ii) the constitutive model's range of capabilities as a whole in conjunction with its substantially reduced computation time requirements when compared to a conventional ply-by-ply representation of a laminate.

Potential improvements. The following model aspects are considered to merit further attention:

With regard to **deformation modes** and **failure criteria**:

- The current model version employs a simple, linear elastic reflection of *31-shear*. This could be refined by reflecting this deformation mode's experimentally-observable non-linearity.
- The reflection of fibre compressive failure in the present model version is very pragmatic. Both, the onset of failure, particularly under multi-axial loading, and damage evolution of this failure mode could be refined, provided that a sound and convincing experimental basis could be generated for the corresponding calibration of that model aspect.
- The model for capturing the ply behaviour currently operates under a *plane stress* assumption. This simplification could be dropped by also taking into account the out-of-plane stress tensor components in the context of determining the material exposure for each of the plies' governing failure modes.

With regard to **rate-dependency**:

- The model in its current version does not take into account the out-of-plane moduli's rate-dependency. This effect should be added in subsequent versions.
- In order to allow for a more accurate reflection of the composite's rate-dependency by the model, the generation of more densely populated datasets for all relevant material properties would be desirable, especially in the high-rate regime. It is recommended to address the following properties first: X_c, G_{Ic}^{f+}, G_{Ic}^{f-}, and G_{IIc}^{IFF}. Furthermore, an extended dataset for the in-plane shear model's calibra-

tion would be desirable. Finally, the reason for the glaring discrepancy among the determined values for $G^{f+}_{Ic,QS}$ across several literature sources, see **Table 3.4** in **Chapter 3.6.1**, should be examined, as this lack of reproducibility currently puts the representative nature of this material property in question.

- In the context of **Chapter 3.5.3**, an appropriate strain-rate measure associated with the determined energy release rate G^{f+}_{Ic} was outlined in order to allow for the calibration of the damage evolution behaviour of a CDM-based damage modelling approach. No other literature source was found associating the determined energy release rate value with a similar strain-rate measure. It would thus be desirable to find a way to link data from already existing literature sources having determined other energy release rates, such as G^{f-}_{Ic}, to an analogous strain-rate measure.

Strain-rate smoothing algorithm. The proposed *low-pass filter*-like algorithm is governed by two arbitrary parameters, $\Delta\dot{\epsilon}_{tsh}$ and $\Delta\dot{\epsilon}_{lim}$. Under the assumption of a reasonable generalizability, an accompanying numerical study determined sensible values for these parameters. This hypothesis should be further examined by subjecting the strain-rate smoothing algorithm to a broader range of high-rate loading scenarios, and assessing the arbitrary parameters' potential sensitivity.

General approach to damage modelling. The constitutive model currently employs a *continuum damage mechanics*-approach to reflect damage evolution, and, upon reaching the end of its stress-strain curve, ϵ_f, (conditional) *element erosion* for the post-*final failure* treatment. One shortcoming of a CDM-based damage modelling approach, its inability to reflect the experimentally-obtained energy release rate value above a certain element size threshold, has already been detailed in **Chapter 4.8**.

Another shortcoming is encountered when ϵ_f is comparatively large, as it is particularly the case for the fibre-dominated failure modes. There, the elements can deform substantially prior to reaching ϵ_f, potentially resulting in very small calculation steps as a consequence. This, in turn, then necessitates eroding the elements in question *before* reaching ϵ_f in order to ensure the simulation's completion within a reasonable timeframe. **Chapter 5.3.2** briefly touched on this issue in the context of the model's validation exercise. A consequence of this 'premature' element erosion, however, is that it also removes a part of the elements' elastically stored energy from the dissipation process, thus counteracting the effort of linking the damage evolution to an experimentally-obtained material property. Lastly, the mechanism itself of deleting finite elements, especially in the region directly in the projectile's path, does not actually reflect the composite's perforation behaviour in the experiment. A particular issue in this context arises when elements that may have been damaged by a matrix-, but not a fibre-dominated failure mode, have to be eroded in order to avoid highly deformed elements, which, in turn, could otherwise excessively reduce the time step.

In order to address the abovementioned issues associated with employing a CDM-based approach in conjunction with element erosion, it is, as a long-term perspective, recommended to develop an FEM framework that allows for inserting *cohesive elements* during run time once damage evolution initiates. This would then facilitate the damage evolution process to take place solely at the elements' interfaces, whereas the composite's elastic (and plastic) deformation would be captured by the bulk elements.

Bibliography

[1] Aboudi, J., Arnold, S., and Bednarcyk, B. (2013). *Micromechanics of Composite Materials: A Generalized Multiscale Analysis Approach*. Elsevier Science.

[2] Amacher, R., Cugnoni, J., Botsis, J., Sorensen, L., Smith, W., and Dransfeld, C. (2014). Thin ply composites: Experimental characterization and modeling of size-effects. *Composites Science and Technology*, 101:121–132.

[3] Amoo, L. M. (2013). On the design and structural analysis of jet engine fan blade structures. *Progress in Aerospace Sciences*, 60:1–11.

[4] Ashby, M., Shercliff, H., and Cebon, D. (2010). *Materials: Engineering, Science, Processing and Design*. Butterworth-Heinemann.

[5] ASM International Handbook Committee (2000). *ASM Handbook: Mechanical testing and evaluation*. ASM Handbook. ASM International.

[6] ASTM D3410/D3410M-16 (2016). Standard test method for compressive properties of polymer matrix composite materials with unsupported gage section by shear loading. Standard, ASTM International, West Conshohocken, PA.

[7] ASTM D3518/D3518M-94 (1994). Standard test method for in-plane shear response of polymer matrix composite materials by tensile test of a $\pm 45^\circ$ laminate. Standard, ASTM International, West Conshohocken, PA.

[8] ASTM D5528-13 (2013). Standard test method for mode I interlaminar fracture toughness of unidirectional fiber-reinforced polymer matrix composites. Standard, ASTM International, West Conshohocken, PA.

[9] ASTM D7905/D7905M-14 (2014). Standard test method for determination of the mode II interlaminar fracture toughness of unidirectional fiber-reinforced polymer matrix composites. Standard, ASTM International, West Conshohocken, PA.

[10] ASTM E1922-04 (2015). Standard test method for translaminar fracture toughness of laminated and pultruded polymer matrix composite materials. Standard, ASTM International, West Conshohocken, PA.

[11] ASTM E399-17 (2017). Standard test method for linear-elastic plane-strain fracture toughness KIc of metallic materials. Standard, ASTM International, West Conshohocken, PA.

[12] Baranowski, P., Malachowski, J., Gieleta, R., Damaziak, K., Mazurkiewicz, L., and Kolodziejczyk, D. (2013). Numerical study for determination of pulse shaping

design variables in SHPB apparatus. *Bulletin of the Polish Academy of Sciences: Technical Sciences*, 61(2):459–466.

[13] Bažant, Z. and Planas, J. (1997). *Fracture and Size Effect in Concrete and Other Quasibrittle Materials*. New Directions in Civil Engineering. Taylor & Francis.

[14] Beguelin, P., Fond, C., and Kausch, H. (1997). Fracture mechanics at intermediate rates of loading: The influence of the acceleration on compact tension tests. *Le Journal de Physique IV*, 7(C3):C3–867.

[15] Blackman, B., Kinloch, A., Wang, Y., and Williams, J. (1996). The failure of fibre composites and adhesively bonded fibre composites under high rates of test. *Journal of Materials Science*, 31(17):4451–4466.

[16] Bullegas, G., Pinho, S. T., and Pimenta, S. (2016). Engineering the translaminar fracture behaviour of thin-ply composites. *Composites Science and Technology*, 131:110–122.

[17] Byar, A. D., Iqbal, J. S., Pang, J., and Rassaian, M. (2018). Determination of ballistic limit for IM7/8552 using MAT261. In *2018 AIAA/ASCE/AHS/ASC Structures, Structural Dynamics, and Materials Conference*, page 1702.

[18] Cairns, D. S. (1992). Static and dynamic mode II strain energy release rates in toughened thermosetting composite laminates. *Journal of Composites, Technology and Research*, 14(1):37–42.

[19] Camanho, P. and Lambert, M. (2006). A design methodology for mechanically fastened joints in laminated composite materials. *Composites Science and Technology*, 66(15):3004–3020.

[20] Camanho, P., Maimí, P., and Dávila, C. (2007). Prediction of size effects in notched laminates using continuum damage mechanics. *Composites Science and Technology*, 67(13):2715–2727.

[21] Carbajal, N. and Mujika, F. (2011). Determination of transverse compressive strength of long fibre composites by three-point bending of [90m/0n] cross-ply laminated strips. *Polymer Testing*, 30(5):578–584.

[22] Catalanotti, G., Arteiro, A., Hayati, M., and Camanho, P. (2014a). Determination of the mode I crack resistance curve of polymer composites using the size-effect law. *Engineering Fracture Mechanics*, 118:49–65.

[23] Catalanotti, G., Camanho, P., Xavier, J., Dávila, C., and Marques, A. (2010). Measurement of resistance curves in the longitudinal failure of composites using digital image correlation. *Composites Science and Technology*, 70(13):1986–1993.

[24] Catalanotti, G. and Xavier, J. (2015). Measurement of the mode II intralaminar fracture toughness and R-curve of polymer composites using a modified Iosipescu specimen and the size-effect law. *Engineering Fracture Mechanics*, 138:202–214.

[25] Catalanotti, G., Xavier, J., and Camanho, P. (2014b). Measurement of the compressive crack resistance curve of composites using the size-effect law. *Composites Part A: Applied Science and Manufacturing*, 56:300–307.

[26] Charrier, J.-S., Laurin, F., Carrere, N., and Mahdi, S. (2016). Determination of the out-of-plane tensile strength using four-point bending tests on laminated L-angle specimens with different stacking sequences and total thicknesses. *Composites Part A: Applied Science and Manufacturing*, 81:243–253.

[27] Chen, D., Lu, F., and Jiang, B. (2012). Tensile properties of a carbon fiber 2D woven reinforced polymer matrix composite in through-thickness direction. *Journal of Composite Materials*, 46(26):3297–3309.

[28] Chen, H.-J. and Tsai, S. W. (1996). Three-dimensional effective moduli of symmetric laminates. *Journal of Composite Materials*, 30(8):906–917.

[29] Chou, P., Carleone, J., and Hsu, C. (1972). Elastic constants of layered media. *Journal of Composite Materials*, 6(1):80–93.

[30] Christensen, R., Swanson, S., and Brown, W. (1972). Split-Hopkinson-bar tests on rock under confining pressure. *Experimental Mechanics*, 12(11):508–513.

[31] Cowley, K. D. and Beaumont, P. W. (1997). The interlaminar and intralaminar fracture toughness of carbon-fibre/polymer composites: The effect of temperature. *Composites Science and Technology*, 57(11):1433–1444.

[32] Cui, H. and Thomson, D. (2017). Report on plate impact tests. Internal report, University of Oxford, Department of Engineering Science.

[33] Cui, H., Yasaee, M., Kalwak, G., Pellegrino, A., Partridge, I. K., Hallett, S. R., Allegri, G., and Petrinic, N. (2017). Bridging mechanisms of through-thickness reinforcement in dynamic mode I and II delamination. *Composites Part A: Applied Science and Manufacturing*, 99:198–207.

[34] Czabaj, M. W. and Ratcliffe, J. G. (2013). Comparison of intralaminar and interlaminar mode I fracture toughnesses of a unidirectional IM7/8552 carbon/epoxy composite. *Composites Science and Technology*, 89:15–23.

[35] Davies, E. and Hunter, S. (1963). The dynamic compression testing of solids by the method of the split Hopkinson pressure bar. *Journal of the Mechanics and Physics of Solids*, 11(3):155–179.

[36] De Moura, M., Campilho, R. D., Amaro, A., and Reis, P. (2010). Interlaminar and intralaminar fracture characterization of composites under mode I loading. *Composite Structures*, 92(1):144–149.

[37] Ellwood, S., Griffiths, L., and Parry, D. (1982). Materials testing at high constant strain rates. *Journal of Physics E: Scientific Instruments*, 15(3):280.

[38] Ferguson, R., Hinton, M., and Hiley, M. (1998). Determining the through-thickness properties of FRP materials. *Composites Science and Technology*, 58(9):1411–1420.

[39] Field, J. E., Walley, S., Proud, W., Goldrein, H., and Siviour, C. (2004). Review of experimental techniques for high rate deformation and shock studies. *International Journal of Impact Engineering*, 30(7):725–775.

[40] Fleck, N. and Jelf, P. (1995). Deformation and failure of a carbon fibre composite under combined shear and transverse loading. *Acta metallurgica et materialia*, 43(8):3001–3007.

[41] Foley, M., Obaid, A. A., Huang, X., Tanoglu, M., Bogetti, T., McKnight, S., and Gillespie, J. (2002). Fiber/matrix interphase characterization using the dynamic interphase loading apparatus. *Composites Part A: Applied Science and Manufacturing*, 33(10):1345–1348.

[42] Frew, D., Forrestal, M. J., and Chen, W. (2001). A split Hopkinson pressure bar technique to determine compressive stress-strain data for rock materials. *Experimental Mechanics*, 41(1):40–46.

[43] Frew, D., Forrestal, M. J., and Chen, W. (2002). Pulse shaping techniques for testing brittle materials with a split Hopkinson pressure bar. *Experimental Mechanics*, 42(1):93–106.

[44] Gama, B. A., Lopatnikov, S. L., and Gillespie, J. W. (2004). Hopkinson bar experimental technique: A critical review. *Applied Mechanics Reviews*, 57(4):223–250.

[45] Gan, K. W., Wisnom, M. R., and Hallett, S. R. (2014). Effect of high through-thickness compressive stress on fibre direction tensile strength of carbon/epoxy composite laminates. *Composites Science and Technology*, 90:1–8.

[46] Garg, A. C. (1986). Interlaminar and intralaminar fracture surface morphology in graphite/epoxy laminates. *Engineering Fracture Mechanics*, 23(6):1031–1050.

[47] Gay, D., Hoa, S., and Tsai, S. (2002). *Composite Materials: Design and Applications*. CRC Press.

[48] Gerlach, R., Kettenbeil, C., and Petrinic, N. (2012a). A new split Hopkinson tensile bar design. *International Journal of Impact Engineering*, 50:63–67.

[49] Gerlach, R., Sathianathan, S. K., Siviour, C., and Petrinic, N. (2011). A novel method for pulse shaping of split Hopkinson tensile bar signals. *International Journal of Impact Engineering*, 38(12):976–980.

[50] Gerlach, R., Siviour, C. R., Wiegand, J., and Petrinic, N. (2012b). In-plane and through-thickness properties, failure modes, damage and delamination in 3D woven carbon fibre composites subjected to impact loading. *Composites Science and Technology*, 72(3):397–411.

[51] Ghidossi, P., El Mansori, M., and Pierron, F. (2004). Edge machining effects on the failure of polymer matrix composite coupons. *Composites Part A: Applied Science and Manufacturing*, 35(7-8):989–999.

[52] Gigliotti, L. and Pinho, S. (2016). Translaminar fracture toughness of NCF composites with multiaxial blankets. *Materials and Design*, 94:410–416.

[53] Gipple, K. L. and Hoyns, D. (1994). Measurement of the out-of-plane shear response of thick section composite materials using the V-notched beam specimen. *Journal of Composite Materials*, 28(6):543–572.

[54] Gorham, D. (1983). A numerical method for the correction of dispersion in pressure bar signals. *Journal of Physics E: Scientific Instruments*, 16(6):477.

[55] Greenfield, M., Pedicini, A., and Penn, L. (2000). Development of a single fiber fragmentation test for high strain rates. *International Journal of Adhesion and Adhesives*, 20(5):403–407.

[56] Gutkin, R. and Pinho, S. T. (2016). Review on failure of laminated composites: Experimental perspective and modelling.

[57] Hale, J. (2006). Boeing 787 from the Ground Up. *AERO Magazine QRT 04*, pages 18–19.

[58] Harding, J. and Welsh, L. M. (1983). A tensile testing technique for fibre-reinforced composites at impact rates of strain. *Journal of Materials Science*, 18(6):1810–1826.

[59] Harris, C. E. and Morris, D. (1984). Fracture behavior of thick, laminated graphite/epoxy composites. Technical report, Virginia Polytechnic Institute.

[60] Hartung, D., Aschenbrenner, L., and Teßmer, J. (2007). Analysis of the through-thickness material and failure behaviour of textile composites. In *ECCOMAS Thematic Conference on Mechanical Response of Composites, Porto, Portugal*.

[61] Haselbach, F., Newby, A., and Parker, R. (2015). Next generation of large civil aircraft engines: Concepts & technologies. In *European Conference on Turbomachinery Fluid dynamics and Thermodynamics (ETC), Madrid, Spain*.

[62] Heimbs, S. (2011). Computational methods for bird strike simulations: A review. *Computers & Structures*, 89(23-24):2093–2112.

[63] Hexcel Corporation (2016). Hexply 8552. Product datasheet, Hexcel Corporation.

[64] Hinton, M., Kaddour, A., and Soden, P. (2004). A further assessment of the predictive capabilities of current failure theories for composite laminates: Comparison with experimental evidence. *Composites Science and Technology*, 64(3):549–588.

[65] Hoffmann, M., Zimmermann, K., Bautz, B., and Middendorf, P. (2015). A new specimen geometry to determine the through-thickness tensile strength of composite laminates. *Composites Part B: Engineering*, 77:145–152.

[66] Honjo, K. (2003). Fracture toughness of PAN-based carbon fibers estimated from strength-mirror size relation. *Carbon*, 41(5):979–984.

[67] Hosford, W. (2010). *Mechanical Behavior of Materials*. Cambridge University Press.

[68] Hosur, M., Alexander, J., Vaidya, U., and Jeelani, S. (2001). High strain rate compression response of carbon/epoxy laminate composites. *Composite Structures*, 52(3-4):405–417.

[69] Hou, F. and Hong, S. (2014). Characterization of R-curve behavior of translaminar crack growth in cross-ply composite laminates using digital image correlation. *Engineering Fracture Mechanics*, 117:51–70.

[70] Hou, J., Petrinic, N., and Ruiz, C. (2001). A delamination criterion for laminated composites under low-velocity impact. *Composites Science and Technology*, 61(14):2069–2074.

[71] Hufenbach, W., Hornig, A., Zhou, B., Langkamp, A., and Gude, M. (2011). Determination of strain rate dependent through-thickness tensile properties of textile reinforced thermoplastic composites using L-shaped beam specimens. *Composites Science and Technology*, 71(8):1110–1116.

[72] ISO 15024:2001 (2001). Fibre-reinforced plastic composites – determination of mode I interlaminar fracture toughness, GIc, for unidirectionally reinforced materials. Standard, International Organization for Standardization, Geneva, Switzerland.

[73] ISO 15114:2014 (2014). Fibre-reinforced plastic composites – determination of the mode II fracture resistance for unidirectionally reinforced materials using the calibrated end-loaded split (C-ELS) test and an effective crack length approach. Standard, International Organization for Standardization, Geneva, Switzerland.

[74] Jacob, G. C., Starbuck, J. M., Fellers, J. F., Simunovic, S., and Boeman, R. G. (2005). The effect of loading rate on the fracture toughness of fiber reinforced polymer composites. *Journal of Applied Polymer Science*, 96(3):899–904.

[75] Jiang, B. and Zhang, R. (2006). Tensile properties in the through-thickness direction for a carbon fiber woven reinforced composite at impact loading rate. In *Journal de Physique IV (Proceedings)*, volume 134, pages 1071–1075. EDP sciences.

[76] Kaddour, A., Hinton, M. J., Smith, P. A., and Li, S. (2013). Mechanical properties and details of composite laminates for the test cases used in the third world-wide failure exercise. *Journal of Composite Materials*, 47(20-21):2427–2442.

[77] Kageyama, K. and Kimpara, I. (1991). Delamination failures in polymer composites. *Materials Science and Engineering: A*, 143(1-2):167–174.

[78] Koerber, H. and Camanho, P. (2011). High strain rate characterisation of unidirectional carbon-epoxy IM7-8552 in longitudinal compression. *Composites Part A: Applied Science and Manufacturing*, 42(5):462–470.

[79] Koerber, H., Xavier, J., and Camanho, P. (2010). High strain rate characterisation of unidirectional carbon-epoxy IM7-8552 in transverse compression and in-plane shear using digital image correlation. *Mechanics of Materials*, 42(11):1004–1019.

[80] Kuhn, P., Catalanotti, G., Xavier, J., Camanho, P., and Koerber, H. (2017). Fracture toughness and crack resistance curves for fiber compressive failure mode in polymer composites under high rate loading. *Composite Structures*, 182:164–175.

[81] Kuhn, P., Ploeckl, M., and Koerber, H. (2015). Experimental investigation of the failure envelope of unidirectional carbon-epoxy composite under high strain rate transverse and off-axis tensile loading. *EPJ Web of Conferences*, 94:01040.

[82] Laffan, M., Pinho, S., Robinson, P., and Iannucci, L. (2010a). Measurement of the in situ ply fracture toughness associated with mode I fibre tensile failure in FRP. Part I: Data reduction. *Composites Science and Technology*, 70(4):606–613.

[83] Laffan, M., Pinho, S., Robinson, P., and Iannucci, L. (2010b). Measurement of the in situ ply fracture toughness associated with mode I fibre tensile failure in FRP. Part II: Size and lay-up effects. *Composites Science and Technology*, 70(4):614–621.

[84] Laffan, M., Pinho, S., Robinson, P., and McMillan, A. (2011). Translaminar fracture toughness: The critical notch tip radius of 0° plies in CFRP. *Composites Science and Technology*, 72(1):97–102.

[85] Laffan, M., Pinho, S., Robinson, P., and McMillan, A. (2012). Translaminar fracture toughness testing of composites: A review. *Polymer Testing*, 31(3):481–489.

[86] Leong, M., Overgaard, L. C., Daniel, I. M., Lund, E., and Thomsen, O. T. (2013). Interlaminar/interfiber failure of unidirectional glass fiber reinforced composites used for wind turbine blades. *Journal of Composite Materials*, 47(3):353–368.

[87] Li, X., Lok, T., and Zhao, J. (2005). Dynamic characteristics of granite subjected to intermediate loading rate. *Rock Mechanics and Rock Engineering*, 38(1):21–39.

[88] Li, X., Lok, T., Zhao, J., and Zhao, P. (2000). Oscillation elimination in the Hopkinson bar apparatus and resultant complete dynamic stress–strain curves for rocks. *International Journal of Rock Mechanics and Mining Sciences*, 37(7):1055–1060.

[89] Li, Z. and Lambros, J. (2001). Strain rate effects on the thermomechanical behavior of polymers. *International Journal of Solids and Structures*, 38(20):3549–3562.

[90] Lifshitz, J. and Leber, H. (1994). Data processing in the split Hopkinson pressure bar tests. *International Journal of Impact Engineering*, 15(6):723–733.

[91] Lisle, T., Bouvet, C., Hongkarnjanakul, N., Pastor, M.-L., Rivallant, S., and Margueres, P. (2015). Measure of fracture toughness of compressive fiber failure in composite structures using infrared thermography. *Composites Science and Technology*, 112:22–33.

[92] Livermore Software Technology Corporation (2014). LS-Dyna keyword user's manual R7.1.

[93] Logan, D. (2016). *A First Course in the Finite Element Method*. Cengage Learning.

[94] Maikuma, H., Gillespie Jr, J. W., and Wilkins, D. J. (1990). Mode II interlaminar fracture of the center notch flexural specimen under impact loading. *Journal of Composite Materials*, 24(2):124–149.

[95] Marín, L., González, E., Maimí, P., Trias, D., and Camanho, P. (2016). Hygrothermal effects on the translaminar fracture toughness of cross-ply carbon/epoxy laminates: Failure mechanisms. *Composites Science and Technology*, 122:130–139.

[96] Marlett, K. (2011). Hexcel 8552 IM7 unidirectional prepreg 190 gsm & 35% RC qualification material property data report. Data report, National Institute for Aviation Research, Wichita State University, USA.

[97] Marsh, G. (2015). Composites in commercial jets. *Reinforced Plastics*, 59(4):190–193.

[98] Marsh, G. (2016). Composites consolidate in commercial aviation. *Reinforced Plastics*, 60(5):302–305.

[99] May, M. (2016). Measuring the rate-dependent mode I fracture toughness of composites: A review. *Composites Part A: Applied Science and Manufacturing*, 81:1–12.

[100] McCarroll, C. A. (2011). *High rate fracture toughness measurement of laminated composites*. PhD thesis, Imperial College London, Department of Aeronautics.

[101] Medina, J. and Harding, J. (2000). The effect of strain rate on the through-thickness tensile stiffness and strength properties of fibre-reinforced epoxy composites. *Le Journal de Physique IV*, 10(PR9):Pr9–275.

[102] Naghdabadi, R., Ashrafi, M., and Arghavani, J. (2012). Experimental and numerical investigation of pulse-shaped split Hopkinson pressure bar test. *Materials Science and Engineering: A*, 539:285–293.

[103] Naik, N. K., Yernamma, P., Thoram, N. M., Gadipatri, R., and Kavala, V. R. (2010). High strain rate tensile behavior of woven fabric E-glass/epoxy composite. *Polymer Testing*, 29(1):14–22.

[104] Nakai, K. and Yokoyama, T. (2015). Dynamic tensile stress–strain characteristics of carbon/epoxy laminated composites in through-thickness direction. In *EPJ Web of Conferences*, volume 94, page 01039. EDP Sciences.

[105] Nikishkov, Y., Seon, G., Makeev, A., and Shonkwiler, B. (2016). In-situ measurements of fracture toughness properties in composite laminates. *Materials and Design*, 94:303–313.

[106] Olsson, R. (2011). A survey of test methods for multiaxial and out-of-plane strength of composite laminates. *Composites Science and Technology*, 71(6):773–783.

[107] Pan, Y., Chen, W., and Song, B. (2005). Upper limit of constant strain rates in a split Hopkinson pressure bar experiment with elastic specimens. *Experimental Mechanics*, 45(5):440–446.

[108] Pappas, G. and Botsis, J. (2016). Intralaminar fracture of unidirectional carbon/epoxy composite: Experimental results and numerical analysis. *International Journal of Solids and Structures*, 85:114–124.

[109] Parry, D., Walker, A., and Dixon, P. (1995). Hopkinson bar pulse smoothing. *Measurement Science and Technology*, 6(5):443.

[110] Pinho, S., Iannucci, L., and Robinson, P. (2006a). Physically-based failure models and criteria for laminated fibre-reinforced composites with emphasis on fibre kinking. Part I: Development. *Composites Part A: Applied Science and Manufacturing*, 37(1):63–73.

[111] Pinho, S., Iannucci, L., and Robinson, P. (2006b). Physically based failure models and criteria for laminated fibre-reinforced composites with emphasis on fibre kinking. Part II: FE implementation. *Composites Part A: Applied Science and Manufacturing*, 37(5):766–777.

[112] Pinho, S., Robinson, P., and Iannucci, L. (2006c). Fracture toughness of the tensile and compressive fibre failure modes in laminated composites. *Composites Science and Technology*, 66(13):2069–2079.

[113] Pinto, R., Catalanotti, G., and Camanho, P. (2016). Measuring the intralaminar crack resistance curve of fibre reinforced composites at extreme temperatures. *Composites Part A: Applied Science and Manufacturing*, 91:145–155.

[114] Ploeckl, M., Kuhn, P., Grosser, J., Wolfahrt, M., and Koerber, H. (2017). A dynamic test methodology for analyzing the strain-rate effect on the longitudinal compressive behavior of fiber-reinforced composites. *Composite Structures*, 180:429–438.

[115] Prewo, K. M. (1978). The effect of ply lay-up sequence on the fracture toughness of boron aluminum. *Journal of Composite Materials*, 12(1):40–52.

[116] Puck, A. (1996). *Festigkeitsanalyse von Faser-Matrix-Laminaten: Modelle für die Praxis*. Hanser.

[117] Puck, A. and Schürmann, H. (2002). Failure analysis of FRP laminates by means of physically based phenomenological models. *Composites Science and Technology*, 62(12):1633–1662.

[118] Ramírez, H. and Rubio-Gonzalez, C. (2006). Finite-element simulation of wave propagation and dispersion in Hopkinson bar test. *Materials & Design*, 27(1):36–44.

[119] Ravichandran, G. and Subhash, G. (1994). Critical appraisal of limiting strain rates for compression testing of ceramics in a split Hopkinson pressure bar. *Journal of the American Ceramic Society*, 77(1):263–267.

[120] Reddy, J. (2004). *Mechanics of Laminated Composite Plates and Shells: Theory and Analysis, Second Edition*. CRC Press.

[121] Rittel, D. (1999). On the conversion of plastic work to heat during high strain rate deformation of glassy polymers. *Mechanics of Materials*, 31(2):131–139.

[122] Roesler, J., Harders, H., and Baeker, M. (2007). *Mechanical Behaviour of Engineering Materials: Metals, Ceramics, Polymers, and Composites*. Springer Berlin Heidelberg.

[123] Rolls-Royce plc (2019). UltraFan engine generation. `https://www.rolls-royce.com/products-and-services/civil-aerospace/future-products.aspx#section-overview`.

[124] Schaefer, J., Werner, B., and Daniel, I. (2014). Strain-rate-dependent failure of a toughened matrix composite. *Experimental Mechanics*, 54(6):1111–1120.

[125] Sela, N. and Ishai, O. (1989). Interlaminar fracture toughness and toughening of laminated composite materials: A review. *Composites*, 20(5):423–435.

[126] Shokrieh, M. M. and Omidi, M. J. (2011). Investigating the transverse behavior of glass–epoxy composites under intermediate strain rates. *Composite Structures*, 93(2):690–696.

[127] Sihn, S., Kim, R. Y., Kawabe, K., and Tsai, S. W. (2007). Experimental studies of thin-ply laminated composites. *Composites Science and Technology*, 67(6):996–1008.

[128] Smiley, A. and Pipes, R. (1987). Rate sensitivity of mode II interlaminar fracture toughness in graphite/epoxy and graphite/PEEK composite materials. *Composites Science and Technology*, 29(1):1–15.

[129] Soden, P., Hinton, M., and Kaddour, A. (2002). Biaxial test results for strength and deformation of a range of E-glass and carbon fibre reinforced composite laminates: Failure exercise benchmark data. *Composites Science and Technology*, 62(12):1489–1514.

[130] Soutis, C. (2005a). Carbon fiber reinforced plastics in aircraft construction. *Materials Science and Engineering: A*, 412(1-2):171–176.

[131] Soutis, C. (2005b). Fibre reinforced composites in aircraft construction. *Progress in Aerospace Sciences*, 41(2):143–151.

[132] Sun, C. and Li, S. (1988). Three-dimensional effective elastic constants for thick laminates. *Journal of Composite Materials*, 22(7):629–639.

[133] Takeda, T., Narita, F., Shindo, Y., and Sanada, K. (2015). Cryogenic through-thickness tensile characterization of plain woven glass/epoxy composite laminates using cross specimens: Experimental test and finite element analysis. *Composites Part B: Engineering*, 78:42–49.

[134] Talreja, R. and Singh, C. (2012). *Damage and Failure of Composite Materials*. Cambridge University Press.

[135] Tamrakar, S., Haque, B. Z. G., and Gillespie, J. W. (2016). High rate test method for fiber-matrix interface characterization. *Polymer Testing*, 52:174–183.

[136] Taniguchi, N., Nishiwaki, T., and Kawada, H. (2007). Tensile strength of unidirectional CFRP laminate under high strain rate. *Advanced Composite Materials*, 16(2):167–180.

[137] Tanoglu, M., McKnight, S., Palmese, G., and Gillespie Jr, J. (2000). A new technique to characterize the fiber/matrix interphase properties under high strain rates. *Composites Part A: Applied Science and Manufacturing*, 31(10):1127–1138.

[138] Tanoglu, M., McKnight, S., Palmese, G., and Gillespie Jr, J. (2001). The effects of glass-fiber sizings on the strength and energy absorption of the fiber/matrix interphase under high loading rates. *Composites Science and Technology*, 61(2):205–220.

[139] Tao, Y., Chen, H., Yao, K., Lei, H., Pei, Y., and Fang, D. (2017). Experimental and theoretical studies on inter-fiber failure of unidirectional polymer-matrix composites under different strain rates. *International Journal of Solids and Structures*, 113:37–46.

[140] Teixeira, R., Pinho, S., and Robinson, P. (2016). Thickness-dependence of the translaminar fracture toughness: Experimental study using thin-ply composites. *Composites Part A: Applied Science and Manufacturing*, 90:33–44.

[141] Teßmer, J., Hartung, D., and Aschenbrenner, L. (2008). Mechanics of composites in lightweight structures: Efficient testing and computation accounting for complex 3D behaviour. In *Proceedings of 26th Congress of International Council of the Aeronautical Sciences. Anchorage, Alaska, USA*.

[142] University of Cambridge, Department of Engineering (2002). Material selection charts. `http://www-materials.eng.cam.ac.uk/mpsite/interactive_charts/`.

[143] Vecchio, K. S. and Jiang, F. (2007). Improved pulse shaping to achieve constant strain rate and stress equilibrium in split-Hopkinson pressure bar testing. *Metallurgical and Materials Transactions A*, 38(11):2655–2665.

[144] Wiegand, J. (2008). *Constitutive modelling of composite materials under impact loading*. PhD thesis, University of Oxford, Department of Engineering Science.

[145] Wiegand, J. (2012). Documentation of multi-directional composites damage model for LS-DYNA. Technical note, University of Oxford, Department of Engineering Science.

[146] Wiegand, J. and Hoffmann, J. (2014). Characterisation of strain-rate dependent out-of-plane tension material properties by means of rate dependent experiments on RARDE type specimens. Internal report, University of Oxford, Department of Engineering Science.

[147] Yokozeki, T., Aoki, Y., and Ogasawara, T. (2008). Experimental characterization of strength and damage resistance properties of thin-ply carbon fiber/toughened epoxy laminates. *Composite Structures*, 82(3):382–389.

[148] Zabala, H., Aretxabaleta, L., Castillo, G., and Aurrekoetxea, J. (2016). Dynamic 4 ENF test for a strain rate dependent mode II interlaminar fracture toughness characterization of unidirectional carbon fibre epoxy composites. *Polymer Testing*, 55:212–218.

[149] Zhang, Q. B. and Zhao, J. (2014). A review of dynamic experimental techniques and mechanical behaviour of rock materials. *Rock Mechanics and Rock Engineering*, 47(4):1411–1478.

[150] Zhou, Y., Wang, Y., Jeelani, S., and Xia, Y. (2007). Experimental study on tensile behavior of carbon fiber and carbon fiber reinforced aluminum at different strain rate. *Applied Composite Materials*, 14(1):17–31.

[151] Zinoviev, P. A., Tsvetkov, S. V., Kulish, G. G., van den Berg, R. W., and Schepdael, L. J. V. (2001). The behavior of high-strength unidirectional composites under tension with superposed hydrostatic pressure. *Composites Science and Technology*, 61(8):1151–1161.